IntechOpen

Thermal Power Plants

New Trends and Recent Developments

Edited by Paweł Madejski

THERMAL POWER PLANTS - NEW TRENDS AND RECENT DEVELOPMENTS

Edited by **Paweł Madejski**

Thermal Power Plants - New Trends and Recent Developments
http://dx.doi.org/10.5772/intechopen.69696
Edited by Paweł Madejski

Contributors

Ming-Chuan Zhang, Zhu Zhang, Youjun Lu, Liping Wei, Jikai Huang, Teresa Kurek, Konrad Wojdan, Konrad Świrski, Daniel Nabagło, Łukasz Śladewski, Enas Shouman, Kw Guo, Mariusz Banaszkiewicz, Maciej Zyrkowski, Piotr Zymelka, Maciej Bujalski, Paweł Madejski

Notice

First published in London, United Kingdom, 2018 by IntechOpen
eBook (PDF) Published by IntechOpen, 2019
IntechOpen is the global imprint of INTECHOPEN LIMITED, registered in England and Wales, registration number: 11086078, The Shard, 25th floor, 32 London Bridge Street
London, SE19SG – United Kingdom
Printed in Croatia

British Library Cataloguing-in-Publication Data
A catalogue record for this book is available from the British Library

Additional hard and PDF copies can be obtained from orders@intechopen.com

Thermal Power Plants - New Trends and Recent Developments
Edited by Paweł Madejski

p. cm.

Print ISBN 978-1-78923-078-9

Online ISBN 978-1-78923-079-6

eBook (PDF) ISBN 978-1-83881-408-3

Meet the editor

Paweł Madejski, MSc, PhD, is a senior specialist for Thermodynamic Research in Research and Development Department of PGE Energia Ciepła Group. His current research activities are mainly focused on the studies of the steam boiler operation, combustion processes and heat transfer analysis, CFD modeling of boilers and heat exchangers, development of models and systems to monitor boiler performances, improvement of the efficiency and optimization of large steam boilers in thermal power plants. In 2014, he was awarded a doctoral degree in Mechanical Engineering—Power Machines and Equipment—at AGH University of Science and Technology in Kraków. In years 2011–2013, he was a scholar of scholarship program organized by Małopolska Centre of Entrepreneurship. He has co-authored over 40 papers, has supervised and co-supervised master students and industrial interns, and has also lectured on Fuel Combustion as well as Steam Boilers at Cracow University of Technology.

Contents

Preface

The demand for electricity and heat production is still largely covered by conventional thermal power plants based on fossil fuel combustion. Thermal power stations face a big challenge to meet the environmental requirements constantly keeping high process efficiency and avoiding lifetime shortening of critical components. In recent years, many activities have been observed to reduce pollutant emissions and optimize performance in thermal power plants.

Increased share of renewable sources of energy in domestic markets enforces flexible operation of plant units and fast adjustment to actual electricity demand. Gas power plants start to play a very important role in this process, allowing for rapid change of load and to reduce emission of gas pollutants. Operation under changing load together with keeping emissions at the accurate level requires constantly introducing new solutions and technologies as well as carrying out many research and development activities for optimization of the electricity and heat production process.

The present edited book intends to cover recent research and development activities dedicated to thermal power plants, new approaches and future perspectives. This book consists of 8 chapters covering research issues as analysis of coal-fired power unit operation for flexibility improvement, algorithm dedicated to detect certain abnormal conditions and malfunctions of coal mills, numerical analysis of creep-fatigue damage in a steam turbine rotor. The book also includes work on new potential solutions to enhance fluid flow and heat exchange, modelling of dilute phase transportation, engineering approach for fast fluidization dynamics and also recent trends and discussions about a concept strategy for concentrating solar power management.

The editor is indebted to all the colleagues who have contributed to this volume and presented results of latest research, to InTechOpen for the opportunity to work on this book and to its members for the help and support.

Paweł Madejski
PGE Energia Ciepła S.A.
Research and Development
Kraków, Poland

Chapter 1

Introductory Chapter: New Trends and Recent Developments for Thermal Power Plants

Paweł Madejski

Additional information is available at the end of the chapter

http://dx.doi.org/10.5772/intechopen.74723

1. New trends and challenges

The largest share of sources for electricity generation still belongs to fossil fuels such as coal, natural gas, and oil. Conventional thermal power plants based on the fossil fuel combustion are currently facing new challenges. The challenges and recent activities mainly result from the development of technologies that use renewable energy sources and activities aimed at reducing the emission of harmful substances into the atmosphere.

The new challenges are a decisive impulse for introducing changes in power plants and combined heat and power plants, as well as for the implementation and continuous development of new technologies allowing for the electricity and heat production in the least harmful way to the environment. In recent years, many activities have been observed to reduce pollutant emissions and optimize the performance of thermal power plants. Ensuring a continuous supply of electricity and heat is necessary and requires a continuous monitoring of all processes and conduct of maintenance and optimization works.

Based on the data provided by International Energy Agency [1], we can observe how electricity generation during almost last 50 years is changing (**Figure 1**). Total electricity generation was increased almost 6 times, reaches in 2015 value 24,255 TWh, with the share of fossil fuel on the level around 66% (75% in 1973). The share of renewable energy sources (**Figure 1**) includes mainly geothermal, solar, wind, ocean, biofuels, and waste was increased from 0.6 to 7.1% of total electricity generation sources. Despite these changes and the intensive development of technologies based on renewable energy sources, fossil fuels still dominate. The values presented in **Figure 1** confirm current trends indicating the continuous use of coal (39.3% in 2015) as the main source and a large increase of natural gas utilization (22.9% in 2015).

The use of various sources for the electricity generation is strongly diversified and depends on the geographical location which determines the possibility of using renewable resources, as

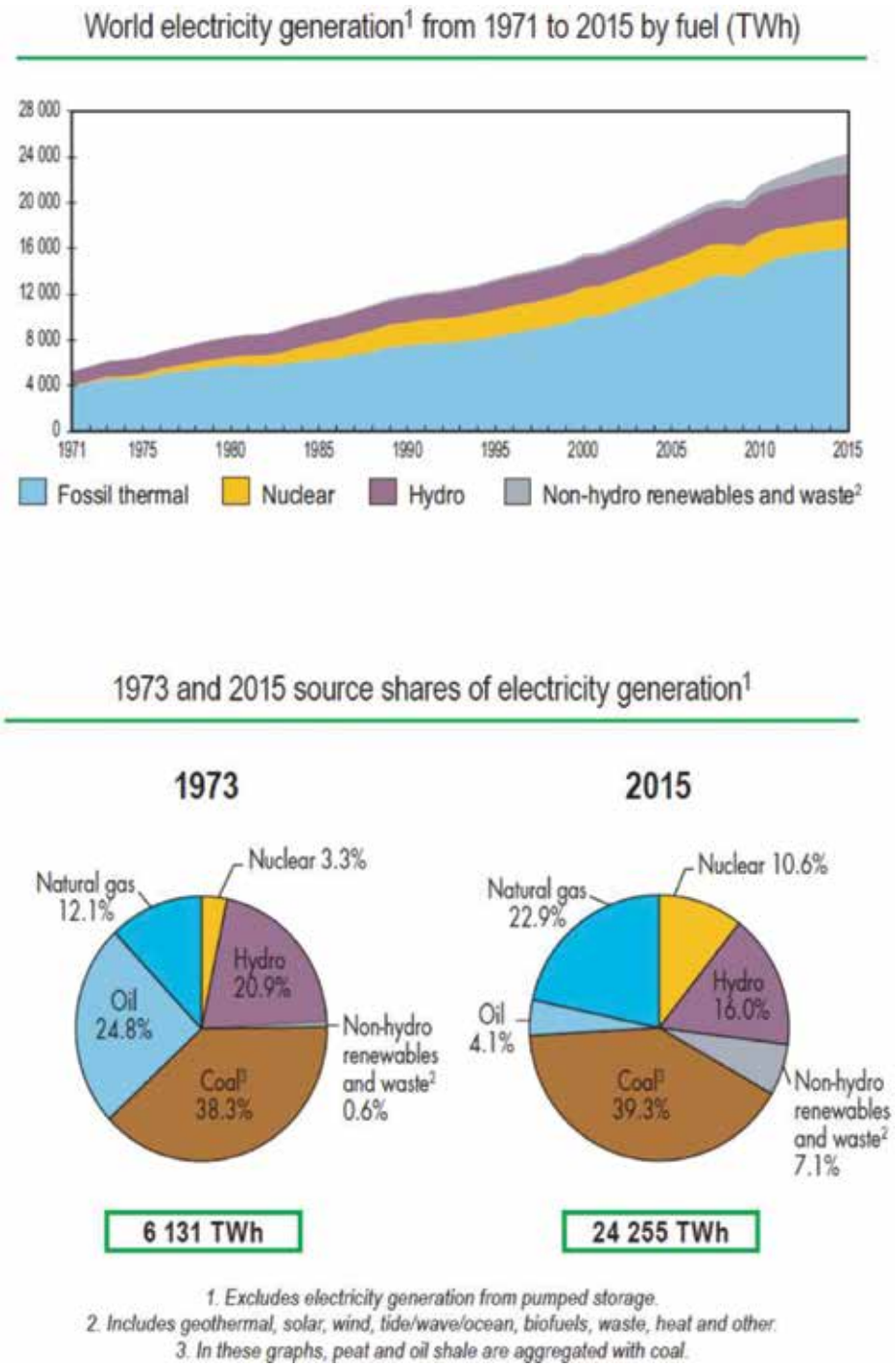

Figure 1. World electricity generation by fuel between 1971 and 2015 [1].

well as on the availability of fossil fuels (coal, gas). The next very important factor is the change in the demand for electricity, which is conditioned by the development dynamics of individual regions of the world. **Figure 2** presents data illustrating changes in the quantities of electricity produced in particular regions of the world. It is noticeable that in recent years, the increase in electricity generation has changed in many regions of the world with different rates. Organization for Economic Co-operation and Development (OECD) countries have the largest share all the time (44.7% in 2015), but for some time the rate of growth has decreased and this level is almost constant.

Coal-fired power plants currently face a big challenge to reduce the level of gaseous pollutants and to adopt new flue-gases treatment methods and devices. Regulations for reducing NO_x, So_x, and dust emissions become more strict [2], and the required limits of gas emission levels are different for old and for new units. In case of old units, with the fuel power above 300 MW, permitted emission levels have been changed during last year's [2]. The upper limits of the average annual values for pulverized coal-fired boilers and for sources above 300 MWt are presented in **Figure 3**. In addition to these values, the future regulations can also include limits of emission levels for HCl, HF, Hg, and NH_3, as well as CO indicator levels. Emission limit values are developed every few years based on the best available techniques (BATs) that exist or will be available in the future.

Due to mandatory environmental regulations, coal-fired power stations in many countries need to install denitrification plants ($DeNO_x$) for nitrogen oxide (NO_x) and desulphurization plants ($DeSO_x$) for sulfur oxide (SO_x) removal from the flue gases. The most popular methods for removing sulfur oxides from exhaust gases are calcium methods. There are several types of this calcium method such as dry, semi-dry, but the Wet Flue Gas Desulfurization (WFGD) method is the most common technology for SO_x control. The reduction of NO_x emission levels is currently possible using primary and secondary measures. Primary measures are used inside the combustion chamber including methods as proper selection of the excess air ratio and temperature, modification of combustion techniques (re-burning, exhaust gas recirculation, air staging, cooling the flame and burners re-design). The use of primary measures allows to reduce NO_x emission with an efficiency about 35%, so in many cases is not enough to meet the environmental concerns. The other solution is to use secondary measures of NO_x reduction, such as Selective Non-Catalytic Reduction (SNCR) and Selective Catalytic Reduction (SCR). These techniques based on the auxiliary installations are located behind the boiler combustion zone. Secondary measures are more effective than primary methods and NO_x reduction efficiency can reach about 50 and 95% for SNCR and SCR techniques, respectively. Many research activities are currently focused on the developed methodology of prediction and assessment [3–6], optimization [7–10], and improving the efficiency of NO_x reduction using primary as well as secondary measures.

However, to avoid efficiency reduction of the production process by applying these methods, the thermal efficiency of the boiler needs to be constantly at a high level. It is necessary to perform optimization work of combustion process using dedicated and novel measurement techniques, optimization algorithms, consequently developed by many researchers and boilers

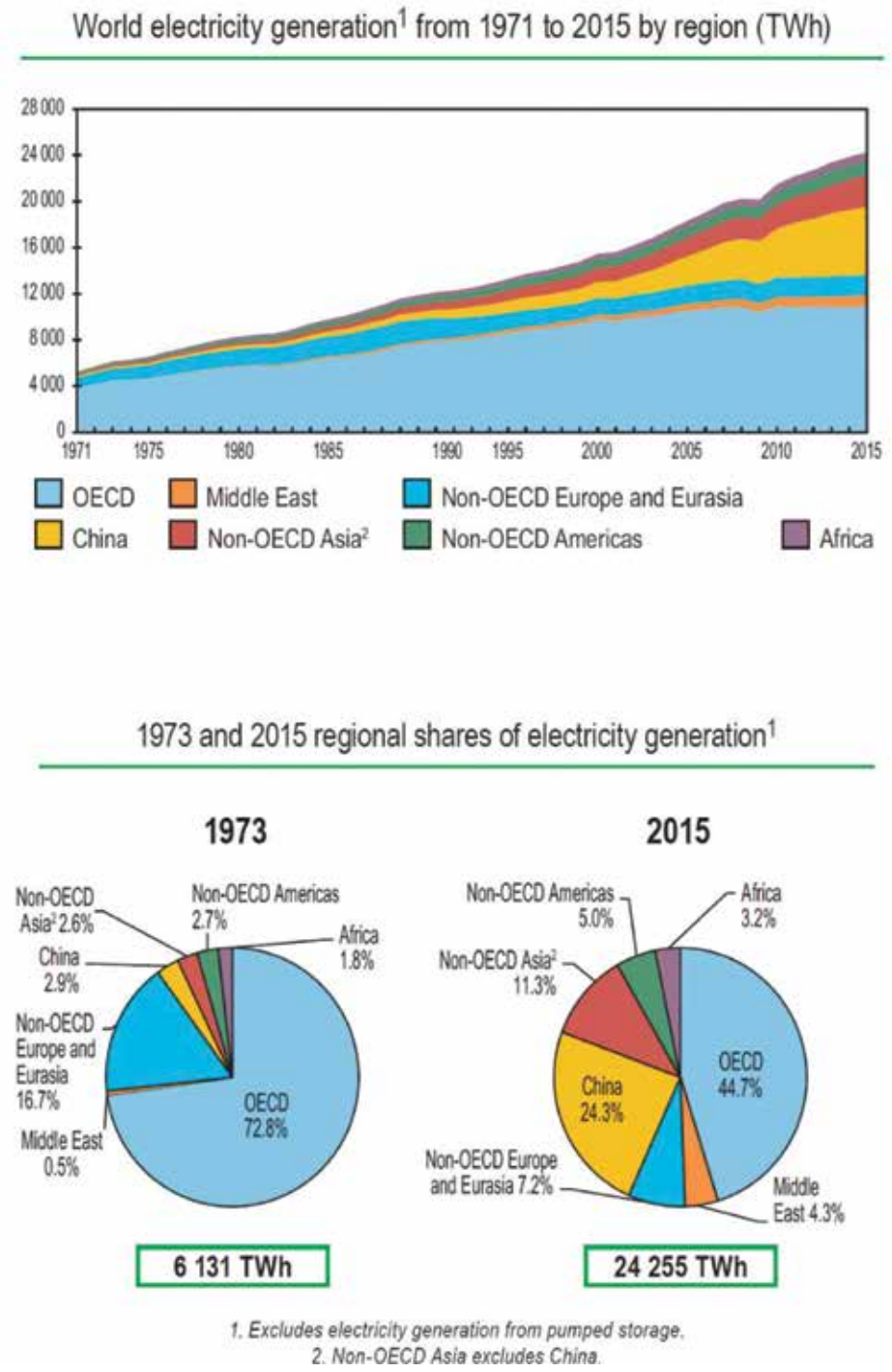

Figure 2. World electricity generation by region between 1971 and 2015 [1].

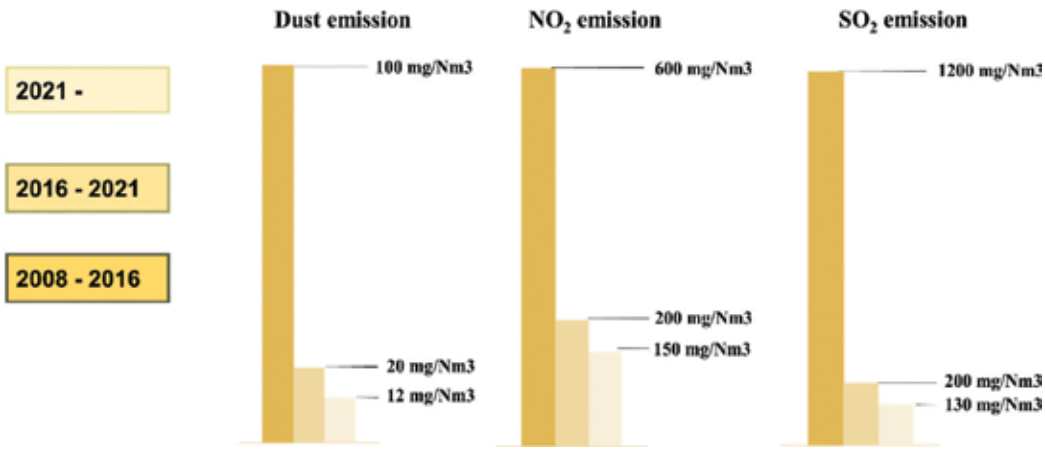

Figure 3. Emission limit values (mg/Nm^3) for SO_2, NO_2, and dust for fossil fuel-fired power plants using solid or liquid fuels with the exception of gas turbines and gas engines, and for the total nominal power delivered in fuel >300 MW.

manufacturers [11–18]. Introduction of primary and secondary measures for NO_x reduction can result in a higher level of carbon in fly ash. Many research activities are observed regarding the quality of fly ash [19, 20] and its potential utilization [21, 22] as well as ash monitoring and optimization of cleaning methods of ash deposits formation inside the boilers [23–30].

Currently, one of the big challenges is to assess the possibilities of CO_2 capture and to develop a technology that allows limiting the emission of this greenhouse gas. For this reason, many theoretical studies, as well as experimental work, have been carried out, among others in order to evaluate the possibilities of CO_2 capture, and the impact of applying technology on production efficiency in both old production units and newly built [31–35].

The increased share of electricity produced from renewable energy sources [36] requires from coal-fired power plants more flexible operation to balance power grids and compensate the variable electricity demand [37]. Coal-fired power plants need to adopt these requirements and to operate in the flexible regime. Flexibility in the power plants operation is characterized by the necessity of frequent load changes, the need to work outside the nominal operating conditions, and the need of more frequent power units start-ups as well as shortening the time of start-up, shutdown or changing a partial load. The necessary flexibility can be achieved with acceptable impacts on component life, efficiency, and emissions but it needs continuous monitoring and controlling of basic operating parameters [38–47]. In **Figure 4**, the forecasted electricity generation (2012–2040) based on renewable energy sources is presented.

In recent years, an intense increase in the use of gas-fired systems can be observed. Gas-fired plants are characterized by high efficiency and the ability to provide fast response to variable electricity demand. Production of electricity and heat using gas technology is widely used in the power industry, and from year to year more and more units start the operation [48–50]. The efficiency of the gas turbine is mainly responsible for the high efficiency of the system, as well as the ability to quickly change the load and operate under high flexible regime [51, 52]. Ensuring

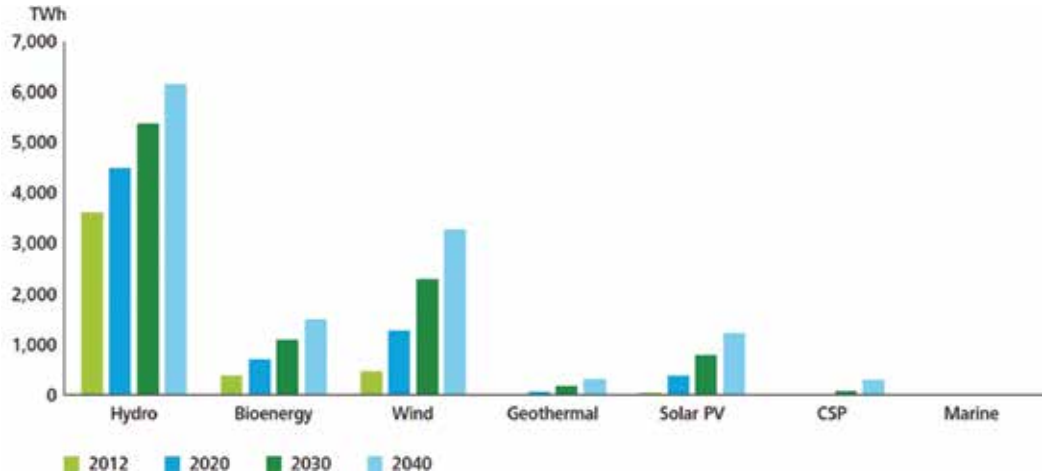

Figure 4. Electricity generation by sources (2012–2040) [36].

Figure 5. Shale gas resources [36].

the optimal operating conditions together with the changing demand requires the use of proper tools for monitoring and optimizing the production process.

For several years, it has been observed a great interest in the growing possibilities of obtaining gas from the unconventional gas resources. The shale gas supply can play an important role and lead to a substitution of a coal-fired plant by gas-fired plants. In **Figure 5**, the technically recoverable shale gas resources are presented.

Shale gas deposits belong to unconventional resources (tight gas, shale gas) and are under detailed consideration as a chance for replacing fuels from conventional resources. Finding of shale formations is easier than conventional, but exploitation of hydrocarbons is more difficult [53–56]. Nevertheless, on the basis of the data presented in **Figure 5**, it can be observed that the gas resources are located in every region of the world.

2. Conclusions

Nowadays, power companies need to modify their management method and models and adapt to strongly changing requirements and regulation on the electricity generation and sale market. Development of more marketable approaches focused on high-quality services needs to be prepared in a careful way. All activities need to be scheduled taking into account upcoming requirements maintaining optimal parameters and efficiency of all processes. The demand for electricity and heat production is still largely covered by conventional Thermal Power Plants which face a big challenge to meet the environmental requirements. Constant keeping high efficiency of processes, avoiding shortening of a critical component lifetime is one of the most important tasks to accomplish. Increased share of renewable energy sources enforces more flexible operation of existing Thermal Power Plants and the necessity to provide fast response to variable electricity demand. Because of these limitations, Gas Power Plants can start to play an important role, allowing for rapid change of load and to reduce the emission of harmful gas pollutants. New environmental restrictions together with the need for operation under changing load, requires constantly introducing new solutions and technologies, as well as carrying out research and development activities to create and implement new optimal solutions.

Author details

Paweł Madejski

Address all correspondence to: pawel.madejski@gkpge.pl

PGE Energia Ciepła S.A., Research and Development, Kraków, Poland

References

[1] International Energy Agency. Key World Energy Statistics 2017. Paris. https://www.iea.org/publications/freepublications/publication/KeyWorld2017.pdf

[2] Directive 2010/75/EU of the European Parliament and of the Council of 24 November 2010 on Industrial Emissions (integrated pollution prevention and control, Recast). Official Journal of the European Union. 2010;**334**:17-119

[3] Stupar G, Tucakovic D, Zivanovic T, Belosevic S. Assessing the impact of primary measures for NO_x reduction on the thermal power plant steam boiler. Applied Thermal Engineering. 2015;**78**:397-409. DOI: 10.1016/j.applthermaleng.2014.12.074

[4] Chui EH, Gao H. Estimation of NO_x emissions from coal-fired utility boilers. Fuel. 2010; **89**:2977-2984. DOI: 10.1016/j.fuel.2010.05.008

[5] Backreedy RI, Jones JM, Ma L, Pourkashanian M, Williams A, Arenillas A, Arias B, Pis JJ, Rubiera F. Prediction of unburned carbon and NO_x in a tangentially fired power station using single coals and blends. Fuel. 2005;**84**:2196-2203. DOI: 10.1016/j.fuel.2005.05.022

[6] Modliński N. Numerical simulation of SNCR (selective non-catalytic reduction) process in coal fired grate boiler. Energy. 2015;**92**:67-76. DOI: 10.1016/j.energy.2015.03.124

[7] Zheng L-G, Zhou H, Cen K-F, Wang C-L. A comparative study of optimization algorithms for low NO_x combustion modification at a coal-fired utility boiler. Expert Systems with Applications. 2009;**36**:2780-2793. DOI: 10.1016/j.eswa.2008.01.088

[8] Tan P, Ji X, Zhang C, Fang Q, Chen G. Modeling and reduction of NO_x emissions for a 700 MW coal-fired boiler with the advanced machine learning method. Energy. 2016;**94**:672-679. DOI: 10.1016/j.energy.2015.11.020

[9] Smrekar J, Potocnik P, Senegacnik A. Multi-step-ahead prediction of NO_x emissions for a coal-based boiler. Applied Energy. 2013;**106**:89-99. DOI: 10.1016/j.apenergy.2012.10.056

[10] Song J, Romero CE, Yao Z, He B. Improved artificial bee colony-based optimization of boiler combustion considering NO_x emissions, heat rate and fly ash recycling for on-line applications. Fuel. 2016;**172**:20-28. DOI: 10.1016/j.fuel.2015.12.065

[11] Łukasz Ś, Konrad W, Konrad Ś, Tomasz J, Daniel N, Jerzy C. Optimization of combustion process in coal-fired power plant with utilization of acoustic system for in-furnace temperature measurement. Applied Thermal Engineering 2017;**123**:711-720. DOI: 10.1016/j.applthermaleng.2017.05.078.

[12] Alamoodi N, Daoutidis P. Nonlinear control of coal-fired steam power plants. Control Engineering Practice 2017;**60**:63-75. DOI: 10.1016/j.conengprac.2016.12.005

[13] Campbell R. Increasing the Efficiency of Existing Coal-Fired Power Plant. Congressional Research Service Report, December 2013. R43343. Available from: www.crs.gov

[14] Madejski P, Janda T, Modliński N, Nabagło D. A combustion process optimization and numerical analysis for the low emission operation of pulverized coal-fired boiler. In: Konstantinos G, Skvaril J, editors. Developments in Combustion Technology. IntechOpen; 2016

[15] Żymełka P, Nabagło D, Janda T, Madejski P. Online monitoring system of air distribution in pulverized coal-fired boiler based on numerical modeling. Archives of Thermodynamics. 2017;**38**:109-125. DOI: 10.1515/aoter-2017-0027

[16] Baldi S, Le Quang T, Holub O, Endel P. Real-time monitoring energy efficiency and performance degradation of condensing boilers. Energy Conversion and Management 2017;**136**:329-339. DOI: 10.1016/j.enconman.2017.01.016

[17] Badur J, Ziółkowski P, Sławiński D, Kornet S. An approach for estimation of water wall degradation within pulverized-coal boilers. Energy. 2015;**92**:142-152. DOI: 10.1016/j.energy.2015.04.061

[18] Cho B, Choi G, Uruno Y, Kim H, Chung J, Kim H, Lee K. One-dimensional simulation for attemperator based on commissioning data of coal-fired steam power plant. Applied Thermal Engineering. 2017;**113**:508-518. DOI: 10.1016/j.applthermaleng.2016.11.069

[19] Barranco R, Gong M, Thompson A, Cloke M, Hanson S, Gibb W, Lester E. The impact of fly ash resistivity and carbon content on electrostatic precipitator performance. Fuel. 2007;**86**:2521-2527. DOI: 10.1016/j.fuel.2007.02.022

[20] Hower JC, Trimble AS, Eble CF. Temporal and spatial variations in fly ash quality. Fuel Processing Technology. 2001;**73**:37-58. DOI: 10.1016/S0378-3820(01)00193-X

[21] Blissett RS, Rowson NA. A review of the multi-component utilisation of coal fly ash. Fuel. 2012;**97**:1-23. DOI: 10.1016/j.fuel.2012.03.024

[22] Ahmaruzzaman M. A review on the utilization of fly ash. Progress in Energy and Combustion Science. 2010;**36**:327-363. DOI: 10.1016/j.pecs.2009.11.003

[23] Shi Y, Wang J, Liu Z. On-line monitoring of ash fouling and soot-blowing optimization for convective heat exchanger in coal-fired power plant boiler. Applied Thermal Engineering. 2015;**78**:39-50. DOI: 10.1016/j.applthermaleng.2014.12.002

[24] Madejski P, Taler D. Analysis of temperature and stress distribution of superheater tubes after attemperation or sootblower activation. Energy Conversion and Management. 2013;**71**:131-137. DOI: 10.1016/j.enconman.2013.03.025

[25] Madejski P, Janda T, Taler J, Nabagło D, Węzik R, Mazur M. Analysis of fouling degree of individual heating surfaces in a pulverized coal fired boiler. Journal of Energy Resources Technology – ASME 2018. 2018;**140**:1-8. DOI: 10.1115/1.4037936

[26] Taler J, WeRglowski B, Taler D, Trojan M, Sobota T, Dzierwa P, Pilarczyk M, Madejski P, Nabagło D. Method of determination of thermo-flow parameters for steam boiler. Journal of Power Technologies. 2015;**95**(4):309-316

[27] Bilirgen H. Slagging in PC boilers and developing mitigation strategies. Fuel. 2014;**115**:618-624. DOI: 10.1016/j.fuel.2013.07.034

[28] Pronobis M. The influence of biomass co-combustion on boiler fouling and efficiency. Fuel. 2006;**85**(4):474-480. DOI: 10.1016/j.fuel.2005.08.015

[29] Taler J, Trojan M, Taler D. Chapter 1. Monitoring of Ash Fouling and Internal Scale Deposits in Pulverized Coal Fired Boilers. New York: Nova Science Publishers; 2012

[30] Taler J, Taler D, Ludowski P. Measurements of local heat flux to membrane water walls of combustion chambers. Fuel. 2014;**115**:70-83. DOI: 10.1016/j.fuel.2013.06.033

[31] Arias B, Abanades JC, Criado YA, Moreno J, Spoerl R, Romano M, Casella F, de Lena E, Díaz L, Lorenzo M, Madejski P, Czupryński P. Improving the flexibility of coal power plants with

CO_2 capture by calcium looping. In: 7th IEAGHG Network Meeting and Technical Workshop on High Temperature Solid Looping Cycles. Luleå, Sweden: Kulturens Hus; Sep 4–5, 2017

[32] Abanades JC, Arias B, Lyngfelt A, Mattisson T, Wiley DE, Li H, Ho MT, Mangano E, Brandani S. Emerging CO_2 capture systems. International Journal of Greenhouse Gas Control. 2015;**40**:126-166. DOI: 10.1016/j.ijggc.2015.04.018

[33] Arias B, Diego ME, Abanades JC, Lorenzo M, Diaz L, Martínez D, Alvarez J, Sánchez-Biezma A. Demonstration of steady state CO_2 capture in a 1.7 MWth calcium looping pilot. International Journal of Greenhouse Gas Control. 2013;**18**:237-245. DOI: 10.1016/j.ijggc.2013.07.014

[34] Bryngelsson M, Westermark M. CO_2 capture pilot test at a pressurized coal fired CHP plant. Energy Procedia. 2009;**1**:1403-1410. DOI: 10.1016/j.egypro.2009.01.184

[35] Korkmaz Ö, Oeljeklaus G, Görner K. Analysis of retrofitting coal-fired power plants with carbon dioxide capture. Energy Procedia. 2009;**1**:1289-1295. DOI: 10.1016/j.egypro.2009.01.169

[36] Deloitte Global Services Limited. The Future of the Global Power Sector. London, Deloitte: The Creative Studio; 2015

[37] Henderson C. Increasing the Flexibility of Coal-fired Power Plants. London: IEA Clean Coal Centre Park House; 2014. Available from: www.iea-coal.org

[38] Alizadeh MI, Parsa Moghaddam M, Amjady N, Siano P, Sheikh-El-Eslami MK. Flexibility in future power systems with high renewable penetration: A review. Renewable and Sustainable Energy Reviews. 2016;**57**:1186-1193. DOI: 10.1016/j.rser.2015.12.200

[39] Belderbos A, Delarue E. Accounting for flexibility in power system planning with renewables. Advanced Materials Research – Switzerland. 2015;**71**:33-41. DOI: 10.1016/j.ijepes.2015.02.033

[40] Zapata Riveros J, Donceel R, Van Engeland J, D'haeseleer W. A new approach for near real-time micro-CHP management in the context of power system imbalances – A case study. Energy Conversion and Management. 2015;**89**:270-280. DOI: 10.1016/j.enconman.2014.09.076

[41] Zhao H, Qiuwei W, Shuju H, Honghua X, Rasmussen CN. Review of energy storage system for wind power integration support. Applied Energy. 2015;**137**:545-553. DOI: 10.1016/j.apenergy.2014.04.103

[42] Mikkola J, Lund PD. Modeling flexibility and optimal use of existing power plants with large-scale variable renewable power schemes. Energy. 2016;**112**:364-375. DOI: 10.1016/j.energy.2016.06.082

[43] Sun L, Liu C. Reliable and flexible steam and power system design. Applied Thermal Engineering. 2015;**79**:184-191. DOI: 10.1016/j.applthermaleng.2014.11.076

[44] Taler J, Węglowski B, Taler D, Sobota T, Dzierwa P, Trojan M, Madejski P, Pilarczyk M. Determination of start-up curves for a boiler with natural circulation based on the

analysis of stress distribution in critical pressure components. Energy. 2015;**92**:153-159. DOI: 10.1016/j.energy.2015.03.086

[45] Taler J, Węglowski B, Dzierwa P, Czupryński P, Madejski P, Nabagło D, Żyrkowski C. Analysis to speed up of the start-up of steam boiler OP-380. Journal of Power Technologies. 2014;**94**(2):1-8

[46] Trojan M, Taler D. Thermal simulation of superheaters taking into account the processes occurring on the side of the steam and flue gas. Fuel. 2015;**150**(10):75-87. DOI: 10.1016/j.fuel.2015.01.095

[47] Madejski P, Taler D, Taler J. Numerical model of a steam Superheater with a complex shape of the tube cross section using control volume based finite element method. Energy Conversion and Management. 2016;**118**:179-192. DOI: 10.1016/j.enconman.2016.03.069

[48] Olumayegun O, Wanga M, Kelsall G. Closed-cycle gas turbine for power generation: A state-of-the-art review. Fuel. 2016;**180**:694-717. DOI: 10.1016/j.fuel.2016.04.074

[49] Sabouhi H, Abbaspour A, Fotuhi-Firuzabad M, Dehghanian P. Reliability modeling and availability analysis of combined cycle power plants. Advanced Materials Research – Switzerland. 2016;**79**:108-119

[50] Thamir k. Ibrahim, Mohammed Kamil Mohammed, Omar I. Awad, Rahman MM, Najafi G, Firdaus Basrawi, Ahmed N. Abd Alla, Rizalman Mamat. The optimum performance of the combined cycle power plant: A comprehensive review. Renewable and Sustainable Energy Reviews. 2017;**79**:459-474. DOI: 10.1016/j.rser.2017.05.060

[51] Meherwan P. Boyce: Gas Turbine Engineering Handbook. 2nd ed. Huston, USA: Butterworth-Heinemann; 2002

[52] Cohen H, Rogers GFC, Saravanamuttoo HIH. Gas Turbine Theory. 3rd ed. UK: Longman Group Limited; 1987

[53] Jarzyna JA, Bała M, Krakowska P, Puskarczyk E, Strzępowicz A, Wawrzyniak-Guz K, Więcław D, Ziętek J. Shale gas in Poland. In: Al-Megren HA, Altamimi RH, editors. Advances in Natural Gas Emerging Technologies. Rijeka: InTech; 2017. pp. 191-210. DOI: 10.5772/67301

[54] Saussay A. Can the US shale revolution be duplicated in continental Europe? An economic analysis of European shale gas resources. Energy Economics. 2018;**69**:295-306. DOI: 10.1016/j.eneco.2017.10.002

[55] Bilgen S, Sarıkaya İ. New horizon in energy: Shale gas. Journal of Natural Gas Science and Engineering. 2016;**35**:637-645. DOI: 10.1016/j.jngse.2016.09.014

[56] Wang Q, Li R. Research status of shale gas: A review. Renewable and Sustainable Energy Reviews. 2017;**74**:715-720. DOI: 10.1016/j.rser.2017.03.007

Chapter 2

Analysis of Coal-Fired Power Unit Operation in Reduced Minimum Safe Load Regime

Piotr Żymełka, Maciej Żyrkowski and Maciej Bujalski

Additional information is available at the end of the chapter

http://dx.doi.org/10.5772/intechopen.72954

Abstract

Large coal-fired power plants were typically designed as a base load units. Any changes in load level, as well as start-up time, are noticeably slow on that kind of units. However, in order to adapt to changing market conditions with increasing number of renewable energy sources, coal-fired power plants need to improve their flexibility. In the paper, 200 MWe class unit has been taken into consideration. During the test campaign, a minimum safe load of the unit was decreased from 60 to 40%. Paper presents results of a model that was made using Ebsilon®Professional software. The simulation model is comprised of boiler and turbine part of the power unit. Obtained results were validated using measurements collected from the test campaign. Parameters important from the technical and economical point of view were investigated. Results revealed that simulation model can be utilised successfully to scrutinise coal-fired units under off-design operation conditions. As the outcome of the performed analysis, a number of issues related to low load operation of the coal-fired unit are presented and discussed. Paper indicates sensitive areas that need to be addressed when operation in decreased safe load is considered. Finally, overall potential for flexibility improvement for 200 MWe class coal-fired units has been evaluated.

Keywords: flexibility, simulation modelling, power plant, power production, coal

1. Introduction

Large coal-fired power plants used to be designed as a base load unit for electricity market. Power units in such power plants can only change their load level in limited range. What is more, any load changes as well as start-up periods, are considerably slow. That has not been the case for many years, currently though, power units require much more flexibility in operation. The reason for that is a growing number of intermittent energy sources, like wind or

PV units. Due to the currents EU's policy, they are privileged on the electricity market, therefore other units role is to balance power level in the system. Power plants with the highest ability to balance renewable energy sources are those equipped with gas turbines, because of a very high speed of load changes as well as short start-up time they are able to provide. However, many energy markets still rely on large coal-fired plants and therefore they need to increase their flexibility. Two aspects of the flexible operation are taken into consideration. The first is the ability to start and change load faster. The second aspect is related to load level of considered units and possibility of its extension [1]. Paper refers to the latter case and tries to evaluate the potential for flexibility improvement of 200 MWe class coal-fired power unit, including both turbine and boiler part.

Flexibility issues with the steam turbine are mostly related to start-up periods. Material limitations impose a maximum temperature gradient that is allowed when the turbine warms up, which for saturated steam is equal to about 1 K/min and for superheated steam about 5 K/min [2]. Minimum power output that steam turbine can produce depends on the pressure in the condenser, which must be kept close to zero. Much more problems however, are associated with the boiler. In case of the reference unit, the most critical element in terms of thermal stress is a drum, for which maximum allowed temperature gradient for is equal to about 4.5 K/min [2]. Next flexibility limitation is related to combustion process itself, which in case of large-scale boilers cannot be controlled too fast. In fact, any changes in boiler operation must be done gradually. When it comes to the boiler load range, it mainly depends on its water circulation technology. Natural circulation boilers have limited flexibility, due to the fact that certain level of heat from combustion process must be delivered to the evaporator, to maintain water circulation. Boilers with forced circulation can operate with much lower minimum safe load. In the reference unit, that is natural circulation boiler, the minimum safe load was designed to 60%, which is equal roughly to 390 t/h of steam flow and 135 MWe of power output. As a matter of fact, minimum safe load operation of the boiler is crucial in this investigation as it indicates overall minimum load of the entire unit. That is because steam turbine has typically wider range of operation than the boiler. Decreasing minimum safe load of the boiler would subsequently allow to decrease the electric power output of the unit. This, in turn, can be strongly beneficial during periods with low energy consumption, when coal-fired units are often forced to shut down. Avoiding the latter, by ability to decrease the power production, is highly desirable by power plant operators. The reason for that, is because shutting down and starting-up coal fired power plants is a rather costly and time consuming process. In the chapter, authors present outcomes of in situ tests as well as simulation modelling of reference unit operation at 40% load level that is below its safe design minimum.

2. Flexibility of reference coal-fired power unit

Reference coal-fired units were produced between 1970 and 1974 in Poland. It is comprised of 225 MWe condensing steam turbine and pulverised coal boiler with a nominal steam output of 650 t/h. Turbine consists of the high, medium and low-pressure part. Inlet steam pressure equals to about 13.5 MPa. The boiler has natural water circulation and is equipped with the drum as well as front wall burners configuration with additional over fire air nozzles. Fuel mixed with primary air is supplied by six coal mills to low-NOx burners and steam nominal

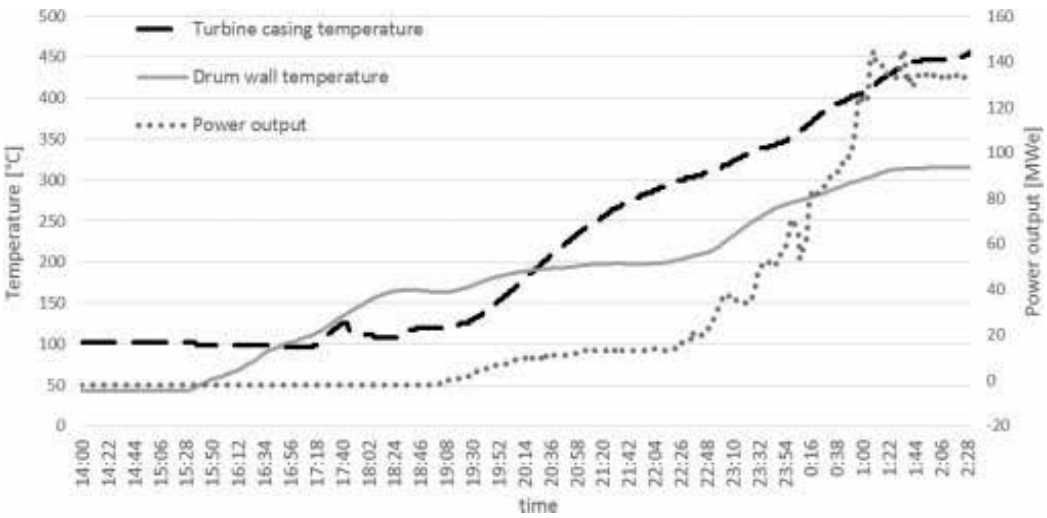

Figure 1. Reference unit cold start-up.

outlet temperature is equal to 540°C. The boiler is comprised of 5 superheaters and 2 reheaters as well as double water heater and three rotary air preheaters. At the boiler's outlet, there is one electrostatic precipitation unit (ESP).

For coal-fired units, it is important if the start-up is being done from the cold, warm or hot state [2, 3]. **Figures 1** and **2** present parameter like electric power output and critical factors (drum wall and turbine casing temperatures) of reference unit during cold and warm start-ups. According to presented data, the warm start-up time of the unit is equal to about 7 h 20 min, while cold start-up is equal to about 10 h 40 min. Typical load variation of the reference unit is presented in **Figure 3** and it changes from about 140 to 220 MWe. The minimum safe load for the reference unit is equal to 60%.

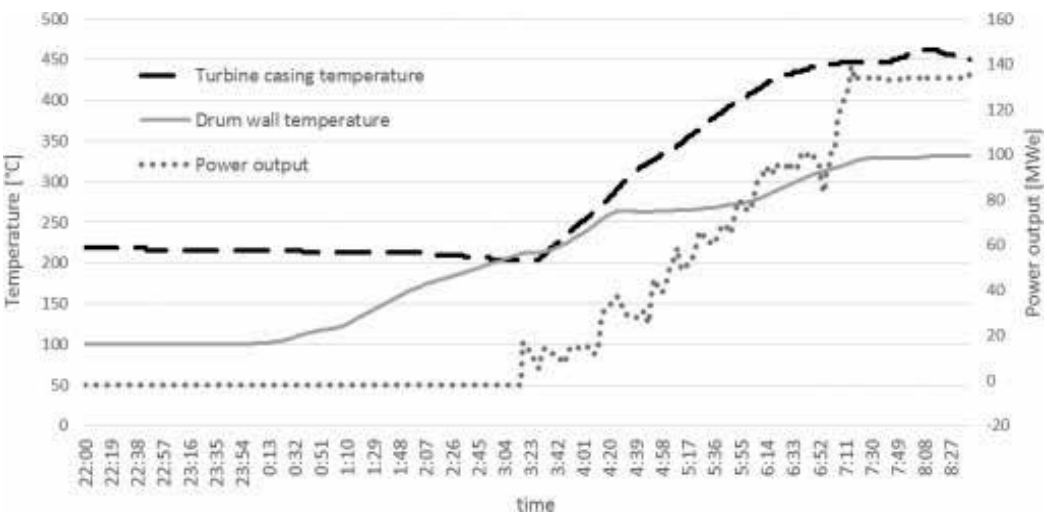

Figure 2. Reference unit warm start-up.

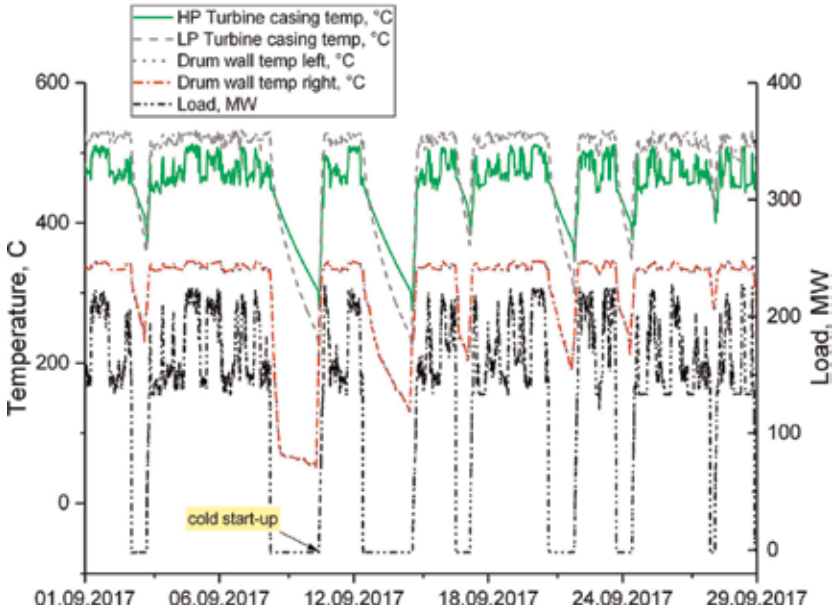

Figure 3. Reference unit critical operation parameters (during September 2017).

The output load of the reference unit has been studied between January and October 2017. Histogram of the electric power is presented in **Figure 4**. During this period, the unit was under flexible operation with frequent load changes over a single day. Most of the time the unit worked with output power below 180 MW which corresponds to the load level below 80%. The unit worked almost 30 h with maximum capacity—225 MW and was shut down several

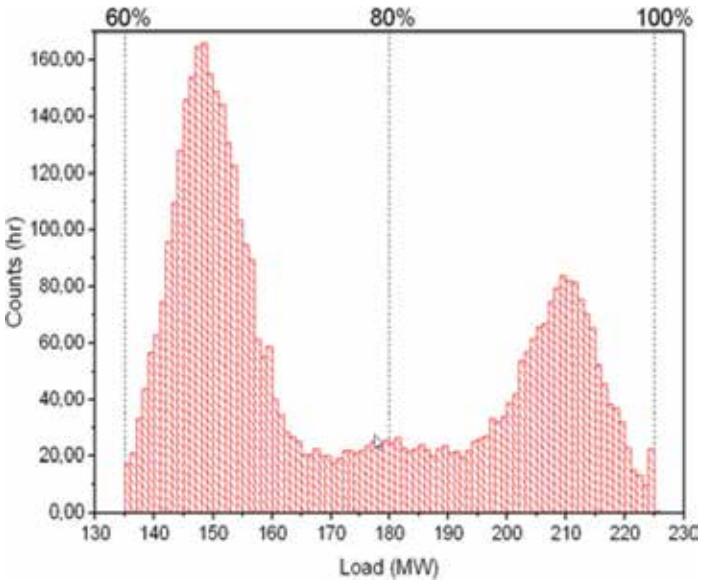

Figure 4. Histogram of the output power (from 1 January to 30 October 2017).

Month	Avg. start-up time, h	No. of cold start-ups, –	No. of warm start-ups, –	Stand-by time, h
January	7.3	1.0	2.0	227.7
February	9.9	1.0	0	520
March	7.0	1.0	2.0	225.7
April	0	0	0	0
May	10.1	1.0	0	571.5
June	9.6	2.0	0	106.0
July	8.1	1.0	1.0	63.0
August	7.9	1.0	2.0	111.3
September	6.0	1.0	6.0	183.2
October	5.1	0	6.0	230.6

Table 1. A number of different start-ups of the reference unit between January and October 2017.

times a month. **Table 1** shows the number of start-ups with the start-up type (from the cold or warm state) during individual months. Aggregated stand-by and average start-up time are also provided. Until the end of October, the unit was launched 28 times. The critical factors (load, drum wall and casing turbine temperatures) of the reference unit during September are presented in **Figure 3**. Over this month, the unit was launched 7 times in total (including one cold start-up).

3. Turbine modelling

3.1. Description of simulation model

Steam turbine of a 225 MW power unit is considered for the simulation analysis. The mathematical model of the coal-fired power unit was developed using the Ebsilon®Professional computer software [4], including detailed models of turbine and boiler part. Boiler model description and simulation results are presented in the next chapter.

The subcritical steam cycle structure of analysed power unit is presented in **Figure 5**. The hatched areas show the main components of analysed thermal system: steam boiler, three casing turbine (consisting of a high-pressure part HP, an intermediate-pressure part IP and a low-pressure part LP), eight regenerative heat exchangers (consisting of three high-pressure HPH and five low-pressure LPH), two-part condenser (CO-1 and CO-2), an electric generator (G), a feed-water tank with deaerator (FW), condensate pumps (CP-1 and CP-2) and feed water pump (FWP).

The superheated steam from the steam boiler at 535°C temperature under 12.17 MPa pressure and 180.6 kg/s mass flow feed the high-pressure turbine. The steam after the expansion process in HP part is reduced to the pressure equal to 2.67 MPa. The HP turbine part supplies two regenerative heat exchangers (HPH-3 and HPH-2) and at the outlet of HP section, the mass flow rate is reduced to 158.8 kg/s. After the HP part, the steam is reheated from 324 to 535°C. The nominal pressure drop in the reheated system is equal to 0.36 MPa. The reheated steam at

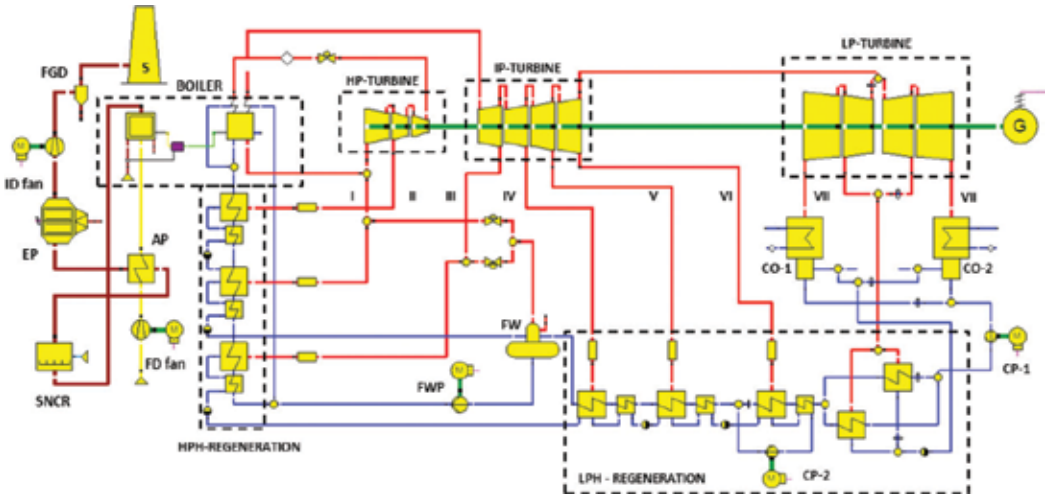

Figure 5. A simulation model of the power unit.

535°C and with 2.31 MPa pressure enters the intermediate-pressure (IP) turbine. In the IP turbine part, the steam is expanded to the of temperature 188.0°C and the pressure of 0.13 MPa. The IP section has four extractions to the regeneration system (HPH-1, LPH-5, LPH-4 and LPH-3). The steam mass flow leaving the IP part of the turbine is reduced to 134.9 kg/s. Steam from the IP turbine section feeds the low-pressure LP part. The LP section has one extraction to the low-pressure regeneration heat exchangers (LPH-1/2), so the mass flow rate at the outlet of LP part of the turbine is equal to 129.4 kg/s. The low-pressure steam from the outlet of LP turbine part goes to condensers where is subcooled and then is pumped to the LPH regeneration system. In the LPH section water is reheated to the temperature of 146°C and then enters the deaerator and feed water tank. The water pressure after the deaerator is increased to 16.7 MPa and then it flows to the HPH regeneration system. In the HPH section water is reheated to the 250°C under 15.5 MPa and then feeds the steam boiler. The design steam parameters (pressure, temperature and mass flow rate) at selected turbine extractions are presented in **Table 2**.

The steam expansion line for nominal conditions of the analysed power unit is presented in **Figure 6**. The numerical designation on the expansion curves correspond with the steam parameters in the following locations in turbine system: 1—after shut-off valve, 2—HP-regulating stage, 3—exhaust I (to HPH-3), 4—exhaust II (to HPH-2), 5—before IP stage, 6—exhaust III (to HPH-1), 7—exhaust IV (to LPH-5), 8—exhaust V (to LPH-4), 9—exhaust VI (to LPH-3), 10—exhaust VII (to LPH-1/2), 11—turbine outlet.

The structure of simulation model of 225 MW power unit was developed on the basis of information and data included in the turbine operational manual and performance documentation (power unit energy balance). In the design phase, the average numerical values from thermal measurements included in the in the performance measurements report were used for the unit power load equal to 225 MW. Additionally, values of thermal parameters according to operational data from the measuring system were assumed during the simulation model preparation. The efficiencies of main power plant components (turbine, pumps, generator)

Extraction	Bleed number	Pressure, MPa	Temperature, °C	Mass flow rate, kg/s
I	9	4.03 (3.72)	376.4 (368.0)	8.56 (7.64)
II	12	2.70 (2.48)	324.0 (317.0)	13.17 (11.83)
III	15	1.23 (1.14)	447.0 (447.0)	7.50 (6.72)
IV	19	0.51 (0.47)	334.0 (334.0)	3.72 (3.31)
V	21	0.28 (0.26)	268.0 (268.0)	5.28 (4.78)
VI	23	0.13 (0.12)	188.0 (188.0)	7.39 (6.75)
VII	25	0.026 (0.025)	63.0 (64.6)	5.50 (4.89)

Table 2. Design steam parameters at selected turbine extractions.

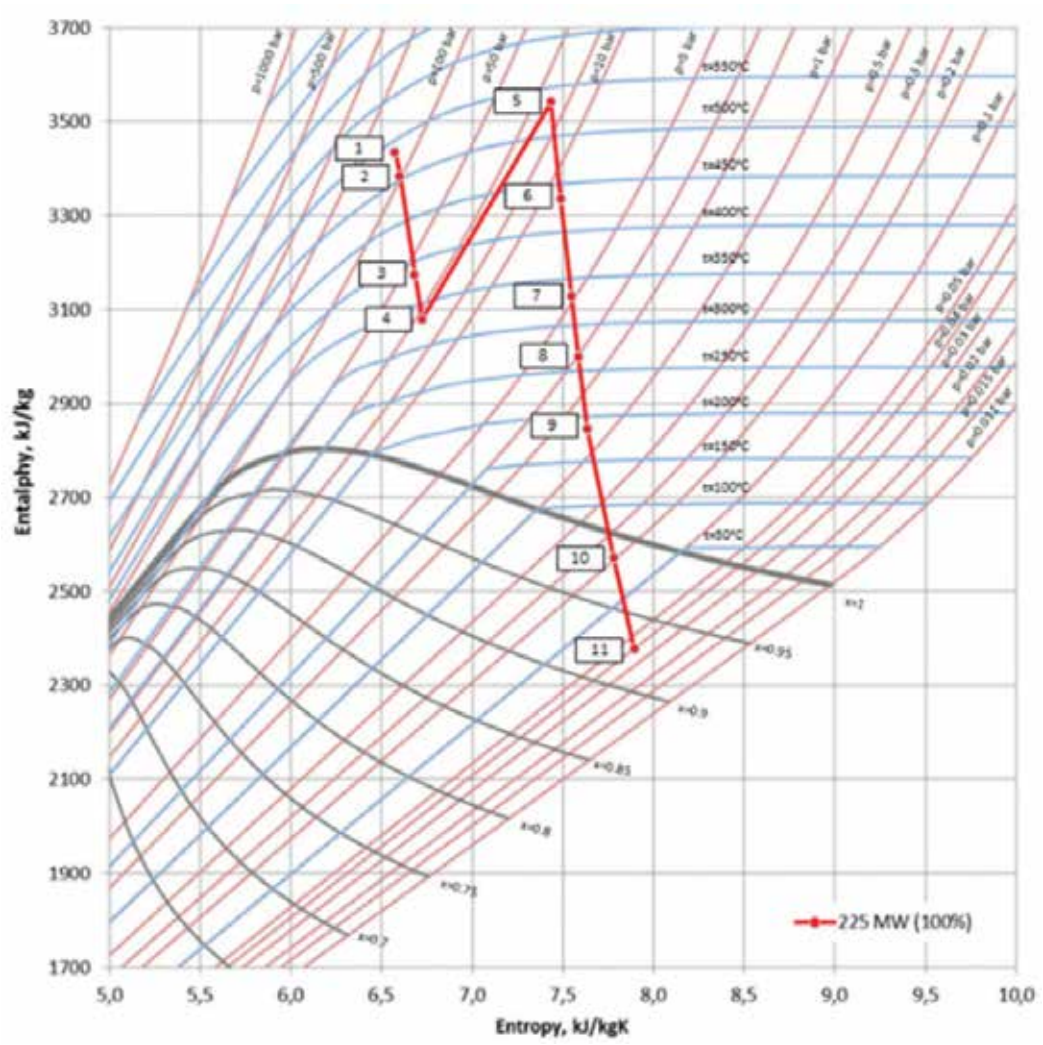

Figure 6. Course of steam expansion line for nominal load of power unit.

were assumed to achieve the nominal operating conditions (in the design mode) and are presented in **Table 3**. The topology constructing process of the analysed power unit thermal cycle was conducted with the following simplifications:

- deaerator is supplied from the third turbine extraction (IP turbine section) for power load above 190 MW, whereas for power load below 190 MW—from the second turbine extraction (HP turbine section),
- steam distribution in the outer glands of the turbine shaft and the turbine sealing system were not included in the simulation model calculations.

The steam turbine simulation model was developed as a number of turbine stages. The number of turbine sections was determined in terms of main inlets and outlets (extractions) in steam turbine cycle. The simulation model of steam turbine was divided into the high-pressure part, intermediate-pressure part and low-pressure part in accordance with its actual construction. The steam turbine model is based on the variable isentropic efficiency, what allows to receive accurate results of simulation calculations for the different load operation. This is very important in part load modelling of steam turbine which is working in sliding pressure mode. The performance operation of steam turbine cycle dependents from many operational parameters, e.g. the temperature, pressure and speed of the working medium. This fact also applies to other elements in the thermal cycle of power systems. The characteristics are used in simulation modelling for an accurate thermodynamic description of components behaviour under part load operation. The characteristic lines describing steam turbine performance were developed for each of turbine stage and then implemented in a simulation model of power unit [4, 5].

The local design mode was assumed for high and low-pressure feed water heaters during the model constructing phase in the design mode. The special off-design mode was used for HPH and LPH regeneration sections in the off-design calculations (at different load levels). The regeneration heat exchangers of HP/LP sections and also the condenser system was developed in separate files for design values and then was subsequently transferred to the simulation model of the power unit. The special off-design mode enables maintenance of constant rated values for given components during the development of the whole power unit designing without the possibility of such values overwriting after operation parameters change of the components directly influencing their functioning [5]. The nominal parameters of HP and LP regeneration system developed in the local design mode are presented in **Figures 7** and **8**, respectively.

Efficiency, %	**Turbine**			**Pumps**	**Generator**
	HP	**IP**	**LP**		
Isentropic	0.852	0.837	0.823	0.800	–
Mechanical	0.996	0.996	0.996	0.985	0.996
Electrical	–	–	–	–	0.986

Table 3. Power unit components efficiency.

3.2. Verification of steam turbine simulation model

The simulation model of power unit was verified with available measurements from the DCS system and also with the performance documentation which contains the results of power unit energy balances. Results obtained from simulation calculations in the design mode were compared to results of the guarantee measurements for four different load levels: 100% (225 MW), 80% (180 MW), 60% (135 MW) and 40% (90 MW). In the verification process of simulation model built in the Ebsilon®Professional software, over 50 measurement points (temperature, pressure and mass flow rate) were used at the characteristic points of the thermal structure of analysed power unit. The off-design calculations were performed by entering the required generator active power (power load) and the external (ambient) conditions for the temperature of cooling water inlet to the steam turbine condenser. The characteristic lines were developed for each of steam turbine stages based on the turbine performance data. The real characteristics of a turbine stage group allow to determine the

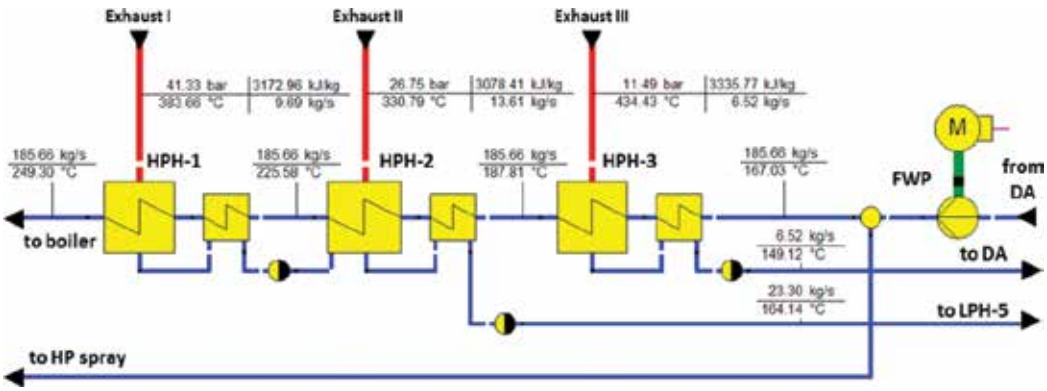

Figure 7. High-pressure regeneration system in the local design mode.

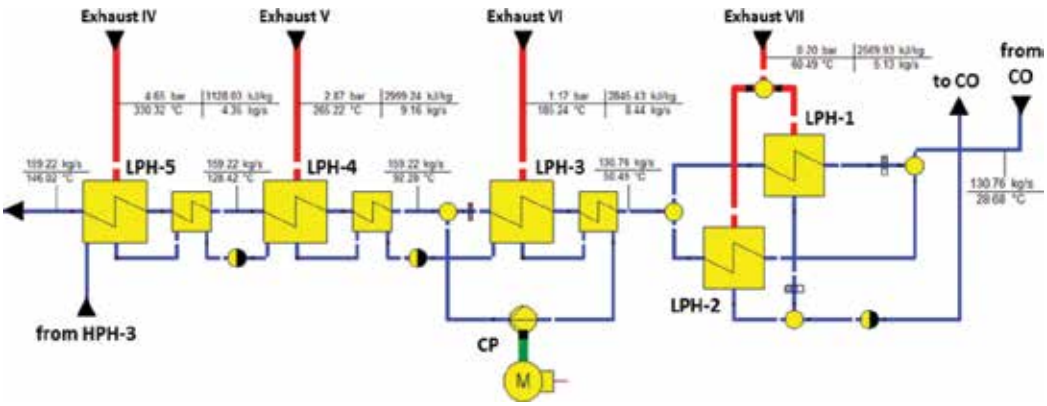

Figure 8. Low-pressure regeneration system in the local design mode.

changes of the isentropic efficiencies in part load calculations and to obtain the reliable results of thermodynamic parameters in steam turbine system.

The relative error for different parameters at the characteristic points in the power unit thermal cycle was used to assess the quality of the developed simulation model. The values of relative error δx_i of selected parameters were calculated according to the following formula:

$$\delta x_i = \frac{|x_{i\ REF} - x_{i\ EBS}|}{x_{i\ REF}} \tag{1}$$

where:

$x_{i\ REF}$—reference value of the i-th parameter,

$x_{i\ EBS}$—simulation model value of the i-th parameter.

The values of relative errors calculated using Eq. (1) for different groups of the parameter at part load conditions are presented in **Table 3**. The values of relative errors obtained from the verification process of steam turbine cycle confirm the correctness and accuracy of the simulation model. The analysis shows that the difference between simulation model results and measured data varying from 1.94 to 6.17%. Based on the obtained results it can be concluded that the simulation model of steam turbine cycle may be used for off-design investigation of the analysed 225 MWe power unit. Results in **Table 4** show that with the decrease of power unit load the average relative error increases. This means that the accuracy of the simulation model is the highest for nominal conditions and in the steam turbine part load operation the precision decreases. The main cause of this is the various simulation model assumptions and the accuracy of the developed characteristics of turbine stages. However, it must be also taken into account the uncertainties of measured data used in the verification process.

3.3. Thermodynamic analysis of power unit in off-design conditions

Through simulation analysis, it is possible to determine the specific parameters of thermal power systems under conditions which are different from the nominal. In this chapter, the thermodynamic analysis was carried out to demonstrate the impact of changes in power unit performance under part load operation. One-dimensional simulation modelling is sufficient to obtain the detailed results of power systems behaviour in steady-state conditions. However, it does not give any information about the effects of dynamic changes in power system operation. This type of thermodynamic modelling is a perfect engineering tool to give a global view of the thermal cycle performance [5–7].

	100% load	**80% load**	**60% load**	**40% load**
Pressure	2.40%	3.78%	4.47%	5.08%
Temperature	2.89%	4.97%	5.38%	6.17%
Mass flow	1.94%	4.32%	5.24%	5.23%
Average	2.42%	4.24%	4.72%	5.48%

Table 4. Relative errors in the verification process of power unit under different load.

To determine the technical-operational parameters of the power unit in off-design conditions the following indices were determined based on the results of simulation calculations: gross power of steam turbine generator, isentropic efficiency of steam turbine, isentropic efficiency of HP, IP and LP part of steam turbine, gross thermal efficiency of power unit, heat supplied to the steam cycle and specific consumption of heat. The mathematical formulas concerning quantities and indices specified above are presented below [8].

The gross power of steam turbine generator is defined as follows:

$$N_{el,G} = (N_{i,HP} + N_{i,IP} + N_{i,LP}) \cdot \eta_{mS,T} \cdot \eta_G \tag{2}$$

where:

$N_{i,HP}$—internal power of the HP section of the steam turbine, MW

$N_{i,IP}$—internal power of the IP section of the steam turbine, MW

$N_{i,LP}$—internal power of the LP section of the steam turbine, MW

$\eta_{mS,T}$—mechanical efficiency of the steam turbine,

η_G—generator efficiency.

The isentropic efficiency of the steam turbine is calculated from the following equation:

$$\eta_i = \frac{i_1 - i_2}{i_1 - i_{2s}} \tag{3}$$

where:

i_1—enthalpy at the inlet to the turbine, kJ/kg

i_2—enthalpy at the outlet from the turbine, kJ/kg

i_{2s}—enthalpy at the outlet from the turbine after isentropic expansion, kJ/kg

The values of the gross thermal efficiency of power unit result from the following equation:

$$\eta_{el,G} = \frac{N_{el,G}}{\dot{Q}_{ch}} \tag{4}$$

where:

$\dot{Q}_{ch}$—the flux of chemical energy of the fuel, MW

The values of the flux of chemical energy of fuel were taken from the simulation calculations of boiler performance in off-design conditions. The amount of heat supplied to the steam cycle in coal-fired boiler result from the equation:

$$\dot{Q}_{sc} = \dot{m}_{LS} \cdot (i_{LS} - i_{FW}) + \dot{m}_{RH} \cdot (i_{HRH} - i_{CRH}) \tag{5}$$

where:

$\dot{m}_{LS}$—live steam mass flow rate, kg/s

i_{LS}—live steam enthalpy at the outlet from the boiler, kJ/kg

i_{FW}—feed water enthalpy at the inlet to the boiler, kJ/kg

$\dot{m}_{RH}$—reheat steam mass flow rate, kg/s

i_{HRH}—hot reheat steam enthalpy at the outlet from the intermediate superheater, kJ/kg

i_{CRH}—cold reheat steam enthalpy at the inlet to the intermediate superheater, kJ/kg

The specific consumption of heat in a steam turbine is calculated from the following equation:

$$q_{h,ST} = 3600 \cdot \frac{\dot{Q}_{sc}}{N_{el,G}} \tag{6}$$

The values of selected characteristic indices obtained from the simulation modelling of steam turbine system are presented in **Table 4**. The part load calculations were performed for four different loads of power unit: 100%, 80%, 60% and 40%. For each of off-design conditions, the simulation results were compared with the data obtained from the performance documentation of the steam turbine. The *EBS* and *REF* abbreviations used in **Table 5** mean the calculation results from the Ebsilon®Professional simulation model and the values of selected parameters from the reference documentation, respectively. The obtained results show that with the decrease in power load, the gross thermal efficiency decreases from 40.0% (for 100% load) to 36.8% (40% load). This means that for 40% part load of the power unit, the gross thermal efficiency is 3.2% less than for the nominal conditions. The steam turbine heat rate of 100% load is equal to 8119 kJ/kWh. The steam turbine heat rate increase with power load drop and for 40% load is 9021 kJ/kWh. On this basis, it can be concluded that for 40% load of power unit it is necessary to supply to the steam cycle about 902 kJ of an additional amount of energy for each of kWh produced in the generator. The isentropic efficiency of a steam turbine for nominal conditions is equal to 85.1% and it decreases to 79.1% in 40% load. The isentropic efficiency of HP and LP section of steam turbine also decreases with the power load from the 81.5 to 65.2% and from 87.2 to 84.1%, respectively. The only exception is an

Indices	**100% load**		**80% load**		**60% load**		**40% load**	
	EBS	**REF**	**EBS**	**REF**	**EBS**	**REF**	**EBS**	**REF**
Gross power, MW	222.8		179.6		134.9		90.7	
Gross thermal efficiency, %	40.0	39.9	39.6	39.7	38.4	38.6	36.8	36.7
Steam turbine heat rate, kJ/kWh	8119	8100	8164	8175	8358	8380	9021	8999
Isentropic efficiency of turbine, %	85.1	85.2	83.6	83.7	82.1	82.0	79.1	79.0
Isentropic efficiency of HP, %	81.5	81.5	78.1	78.0	74.0	74.3	65.2	65.3
Isentropic efficiency of IP, %	86.6	86.7	86.3	86.5	87.0	87.1	87.6	87.6
Isentropic efficiency of LP, %	87.2	87.0	86.2	86.4	85.2	85.1	84.1	84.0

Table 5. Selected technical-operational parameters of power unit under different load.

isentropic efficiency of IP turbine for which this indices at nominal conditions is equal to 86.6% while in 40% load increases to 87.6%. The thermodynamic analysis of selected power unit performance factors shows that the difference between simulation results and reference data varying from 0.11 to 1.21%. Based on the obtained results it can be concluded that the simulation model of steam turbine cycle accurately confirms the results of the reference performance measurements.

4. Boiler modelling

Boiler modelling was performed using Ebsilon®Professional software with EbsBoiler package. The simulation was made for 100%, 80%, 60% and 40% load of the boiler and results were validated using data from in-situ test campaign. Ebsilon®Professional software allows creating a boiler model using graphical interface embedded in the software. **Figure 9** presents schematic of the reference boiler, with superheaters (SH), reheaters (RH) and water heater (WH) depicted. A number of particular heat exchanger represents the degree of overheating of the steam—SH 5, for instance, is a final superheater with steam outlet temperature equal to about 535°C. **Figure 10** depicts part of the model, that represents combustion chamber and evaporator. Furthermore, simulated processes are controlled in the same way it is done on the reference unit—for instance amount of air supplied to the combustion chamber in the model is controlled by the level of oxygen at the boiler outlet. Values depicted in **Figure 10** present different parameters of the combustion process in full load operation. Fuel flow is equal to 98.697 t/h while total air to combustion is equal to 618012.633 m^3/h. Primary and secondary air flows are modelled as a single stream. However, if more precision in calculations of combustion chamber itself is required, air staging would have to be modelled. Level of oxygen at the outlet of combustion zone is equal to 4.499% while air-fuel ratio is equal to 1.302. The latter value does not represent real stoichiometry of combustion in the reference boiler, due to simplification that was made in case of primary and secondary air streams. **Figure 11** depicts part of the model that represents areas of the boiler (D, D′, D″) from where heat is taken to particular heat exchangers—for instance, heat flows from area D′ to the superheater 4 and 1 subsequently. There is also a water spray injection model, with water flow equal to 3.722 t/h. In steady-state modelling of the boiler, water spray injection is difficult to simulate. In reality, this value varies heavily during operation, therefore it can only be simulated as an average value. In general, this way of modelling requires deep knowledge about the simulated object and its operating conditions.

Results of the simulation indicate boiler behaviour in different load levels, including load 40% which is below minimum safe design load of the reference boiler. **Figure 12** presents result of flue gas temperature distribution inside the boiler, for live steam flow equal to 650 t/h (100% load), 520 t/h (80% load), 390 t/h (60% load) and 260 t/h (40% load). Temperature values depicted in **Figure 12** should be treated as average from given boiler areas (perpendicular to the flue gas flow direction) and not as exact temperature points. What can be seen, is that the difference in temperatures is more significant between 60 and 40% load than between 80 and 60% load.

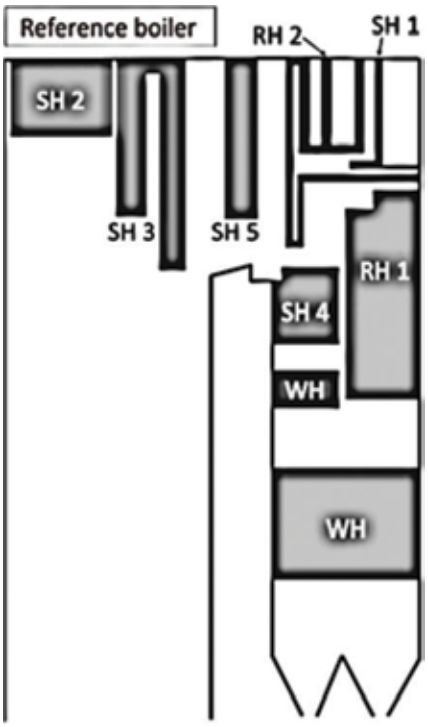

Figure 9. Reference boiler description (SH—superheater, RH—reheater, WH—water heater).

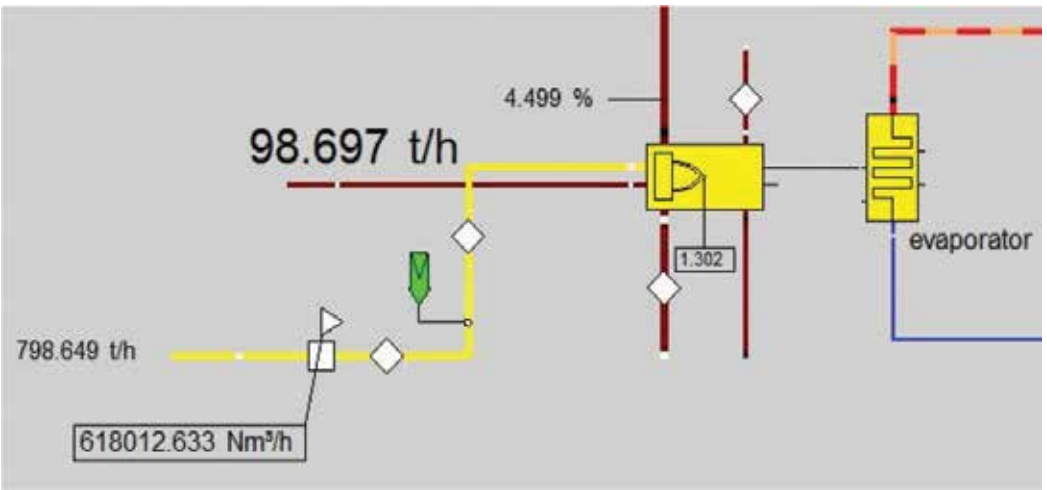

Figure 10. Combustion chamber and evaporator depicted in the model.

Figure 13 presents results of live and reheated steam temperature at the boiler outlet for different load levels. What can be observed, is that both temperatures undergo a steep descent between 60 and 40% load. In the latter case, the live steam temperature is below 520°C and reheated steam temperature falls down below 490°C. Both values are considerably lower than designed

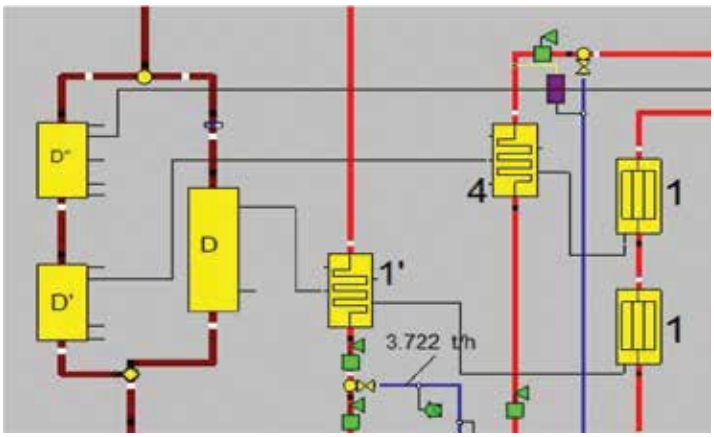

Figure 11. Flue gas path, superheaters and water spray injection depicted in the model.

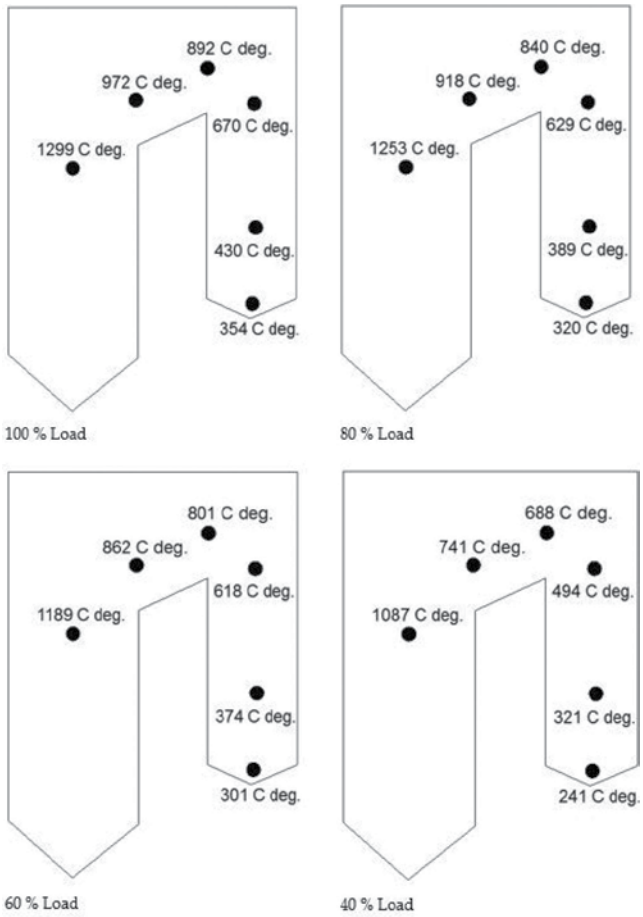

Figure 12. Flue gas temperature distribution inside the boiler for different load levels.

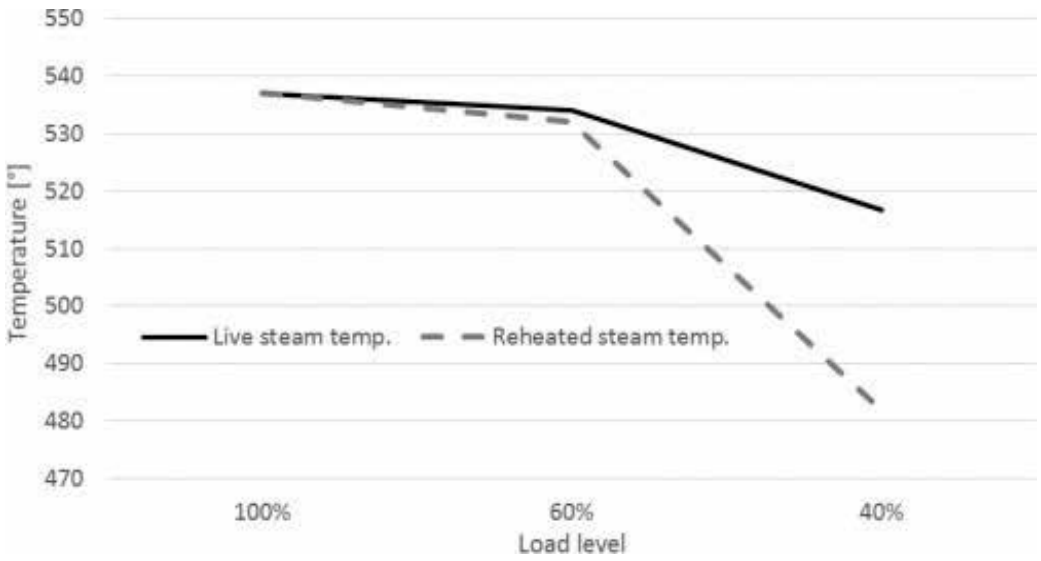

Figure 13. Steam temperatures in different load levels.

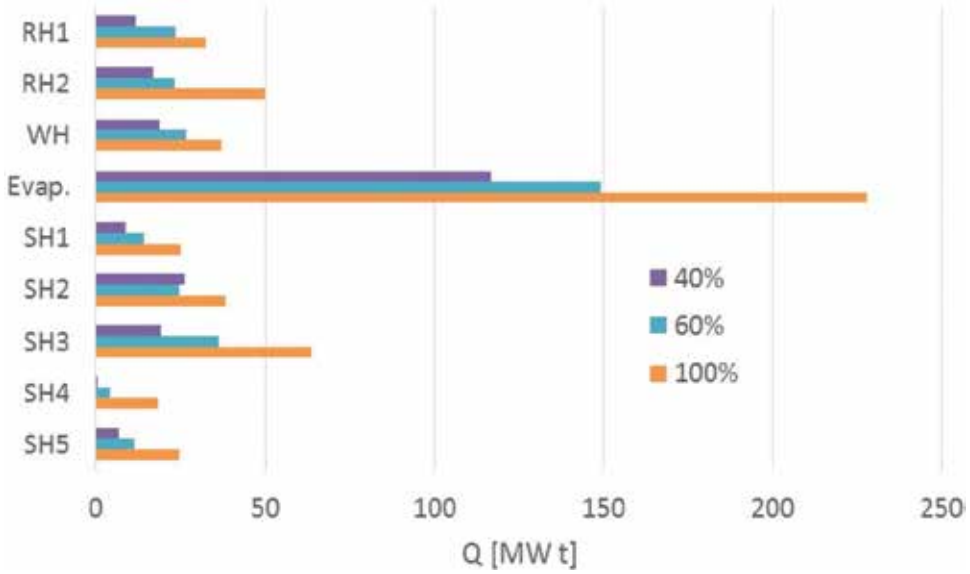

Figure 14. Heating power delivered to each heat exchanger for different load levels (100%, 60%, 40%).

temperature equal to 535°C. **Figure 14** presents results from heating power Q taken by each heat exchanger in the boiler. What is interesting, is that second superheater (SH 2) has got higher power in 40% than in 60% load. Also, power taken by fourth superheater (SH 4) in 40% load is almost negligible. **Figure 15** depicts descend of flue gas temperature at the outlet of air preheater.

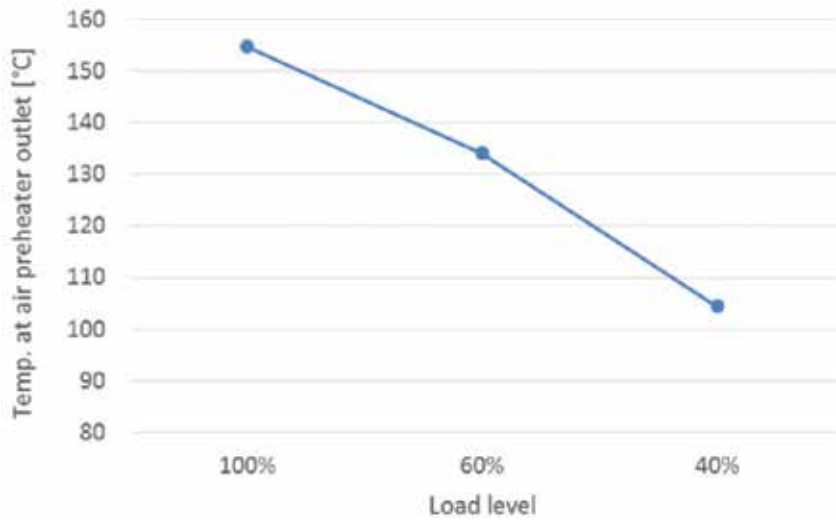

Figure 15. Flue gas temperature at the outlet of air preheater.

5. Discussion

Outcomes from simulation modelling revealed that reference power unit can experience a variety of issues when operating with the decreased minimum safe load. Steam temperatures presented in **Figure 8** indicate, that operation in 40% load is much less efficient than in 60% load. However, there is an economic sense of such configuration when shut down and start-up costs are taken into consideration. Flue gas temperatures presented in **Figure 12** indicate other potential issues. The vastly important threat is related to sulphuric acid (H_2SO_4) condensation. Formation of H_2SO_4 occurs in a temperature range between 200 and 400°C while its content depends on the amount of sulphur trioxide SO_3 and water vapour in the flue gas. The temperature of condensation decreases proportionally to the content of sulphuric acid or water vapour in flue gas and it is in the range of 95–160°C [9–11]. However, roughly 90% of sulphuric acid condenses in a temperature range between 115 and 138°C [12]. According to data presented in **Figures 12** and **15**, in 40% load temperature at the outlet of air preheater is close to 100°C. That increases the probability of sulphuric acid condensation inside the air preheater, which can eventually lead to corrosion problems. Corrosion can also be an issue when it comes to electrostatic precipitator (ESP) operation, however low flue gas temperature is in general favourable here because it decreases dust resistivity [13].

Another concern with low load boiler operation is related to de-NOx installations. Temperature value at the outlet of combustion zone depicted in **Figure 12** decreases from about 1190 to 1090°C. Considering low load operation on boilers equipped with SNCR technology, it must be confirmed that reagent injection system is able to adjust to the new conditions—optimal injection temperature window for NOx removal is roughly between 950 and 1025°C [14]. Regarding

SCR operation, most of the current commercial installations are based on V_2O_5/TiO_2 catalyst, which has considerably high working temperature, roughly between 300 and 400°C. Furthermore, the activity of such catalysts decreases with temperature [15, 16]. SCR installation is normally designed for full load operation temperatures, but it should also work well in minimum load conditions. In case of reference boiler, that would be 60% load. Simulation outcomes reveal, that in 40% load flue gas temperature in SCR relevant region drops below 300°C.

Operation of the steam turbine in part load conditions as well as below current technical minimum involves many technical and economic aspects. The simulation results for a selected different load of power unit shows that analysed power unit can operate stably in the range between 90 and 225 MW. The thermodynamic analysis demonstrates, that the gross thermal efficiency varies between 40.0 and 36.8%. The steam turbine heat rate was calculated to determine the quality of steam turbine performance in off-design conditions. The heat rate of steam turbine cycle increases from 8119 kJ/kWh (for 100% load) to 9021 kJ/kWh (40% load). **Figure 16** shows the course of gross thermal efficiency and steam turbine heat rate. What can be seen, is that the heat rate and efficiency have non–linear characteristic. Presented indices rapidly change in the range between 90 and 135 MW. The thermal efficiency decrease from 38.6 to 36.8% and the steam turbine heat rate increases from 8358 to 9021 kJ/kWh in load range below the current technical minimum.

The simulation calculations reveal that the 225 MW power unit can operate between 40 and 100% load with reasonable efficiency. Power unit operation with reduced minimum load allows decreasing start-up and shut-down operation costs. Reducing the minimum load of

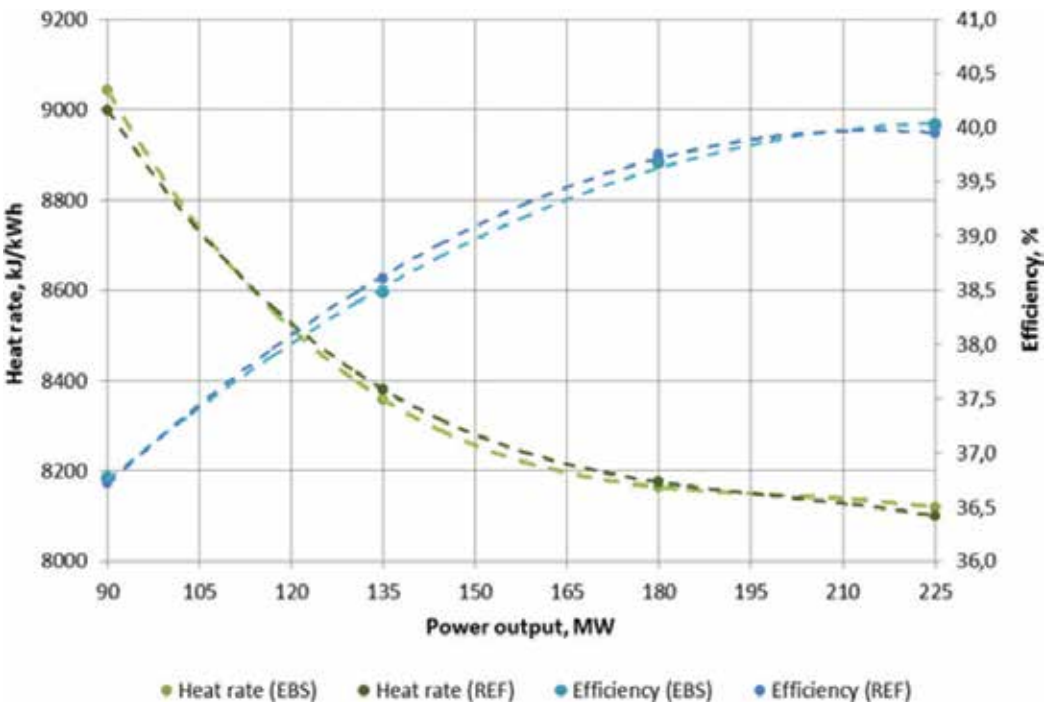

Figure 16. Power unit heat rate and thermal efficiency for part load conditions.

conventional coal-fired power plants strongly influences operation of the steam turbine. The turbine ventilation is one of the main limiting factors in the load range of steam turbine. Insufficient steam flow causes temperature increase and thermal stresses in turbine stages. It is important to revise all of the control loops and measuring devices in case the of power unit operation at low loads to avoid exploitation and performance problems [7, 17]. The steady-state simulation analysis of the power unit model shows a good accordance to reference operating data throughout the power unit operating range. Based on the results of verification process it can be stated that simulation model of steam turbine cycle developed in Ebsilon®Professional can be used as an engineering tool for investigation of power unit performance in off-design conditions.

6. Conclusions

Simulation modelling described in the paper can be recommended as an efficient and accurate method to evaluate power unit operation in different conditions. Authors investigated the operation of '200 MWe' class coal-fired power unit in reduced minimum load regime. Performed tests revealed, that this is a technically feasible way of operation that can improve the flexibility of that sort of units. However, reducing the unit load from designed minimum safe load, can bring about variety of problems. Vastly decreased efficiency, inaccurate measurements and operation problems derived from low flue gas temperature are the most important ones. On the other hand, ability to work in extended load range may decrease number of shut down and start-ups of the unit, which is very desirable from power plant operator point of view. To conclude, it must be said that reference 200 MWe class coal-fired unit, as well as other similar units, have potential of flexibility improvement that is worth considering.

Author details

Piotr Żymełka, Maciej Żyrkowski* and Maciej Bujalski

*Address all correspondence to: maciej.zyrkowski@gkpge.pl

R&D Department, PGE Energia Ciepla S.A., Krakow, Poland

References

[1] Huber M, Dimkova D, Hamacher T. Integration of wind and solar power in Europe: Assesment of flexibility requirements. Energy. 2014;**69**:236-246

[2] Taler J, Węglowski B, Taler D, Sobota T, Dzierwa P, Trojan M, Madejski P, Pilarczyk M. Determination of start-up curves for a boiler with natural circulation based on the analysis of stress distribution in critical pressure components. Energy. 2015;**92**:153-159

[3] Talej J, Dzierwa P, Taler D, Harchut P. Optimization of the boiler start-up taking into account thermal stresses. Energy. 2015;**92**:160-170

[4] STEAG Energy Services GmbH. Ebsilon Professional software. [Online]. December, 2017. http://www.steag-systemtechnologies.com/ebsilon_professional.html

[5] Szega M, Żymełka P. Thermodynamic and economic analysis of the production of electricity, heat and cold in the combined heat and power unit with the absorption chillers. ASME Journal of Energy Resources Technology. 2018;**140**(5)

[6] Alobaid F, Mertens N, Starkloff R, Lanz T, Heinze C, Epple B. Progress in dynamic simulation of thermal power plants. Progress in Energy and Combustion Science. 2017;**59**: 79-162

[7] Madejski P, Janda T, Modliński N, Nabagło D. A combustion process optimization and numerical analysis for the low emission operation of pulverized coal-fired boiler. In: Developments in Combustion Technology. Croatia: InTechOpen; 2016. pp. 33-76

[8] Kotowicz J, Łukowicz H, Bartela Ł, Michalski S. Validation of a program for supercritical power plant calculations. Archives of Thermodynamics. 2011;**32**(4):81-89

[9] Sporl R, Maier J, Scheffknecht G. Sulfur oxide emissions from dust-fired oxy-fuel combustion of coal. Energy Procedia. 2013;**37**:1435-1447

[10] Chen H, Pan P, Shao H, Wang Y, Zhao Q. Corrosion and viscous ash deposition of a rotary air preheater in a coal-fired power plant. Applied Thermal Engineering. 2017;**113**: 373-385

[11] Wei W, Sun F, Shi Y, Ma L. Theoretical prediction of acid dew point and safe operating temperature of heat exchangers for coal-fired power plants. Applied Thermal Engineering. 2017;**123**:782-790

[12] Wang Y, Zhao Q, Zhang Z, Zhang Z, Tao W. Mechanism research on coupling effect between dew point corrosion and ash deposition. Applied Thermal Engineering. 2013;**54**: 102-110

[13] Guo B, Yang D, Su Y, Yu AB. Process modelling of low temperature electrostatic precipitators. Powder Technology. 2017;**314**:567-576

[14] Daood S, Javed M, Gibbs N, Nimmo W. NOx control in a coal combustion by combining biomass co-firing, oxygen enrichment and SNCR. Fuel. 2013;**105**:283-292

[15] Hu X, Shi Q, Zhang H, Wang P, Zhan S, Li Y. NH_3-SCR performance improvement over Mo modified Mo(x)-MnO_x nanorods at low temperatures. Catalysis Today. 2017;**297**:17-26

[16] Tang X, Li C, Yi H, Wang L, Yu Q, Gao F, Cui X, Chu C, Li J, Zhang R. Facile and fast synthesis of novel Mn_2CoO_4@rGO catalysts for the NH_3-SCR of NO_x at low temperature. Chemical Engineering Journal. 2018;**333**:467-476

[17] Richter M, Möllenbruck F, Obermüller F, Knaut A, Weiser F, Lens H, Lehmann D. Flexibilization of steam power plants as partners for renewable energy systems. In: Power Systems Computation Conference (PSCC); 2016. DOI: 10.1109/PSCC.2016.7540840

Chapter 3

Detection of Malfunctions and Abnormal Working Conditions of a Coal Mill

Teresa Kurek, Konrad Wojdan, Daniel Nabagło and Konrad Świrski

Additional information is available at the end of the chapter

http://dx.doi.org/10.5772/intechopen.72952

Abstract

Coal mill malfunctions are some of the most common causes of failing to keep the power plant crucial operating parameters or even unplanned power plant shutdowns. Therefore, an algorithm has been developed that enable online detection of abnormal conditions and malfunctions of an operating mill. Based on calculated diagnostic signals and defined thresholds, this algorithm informs about abnormal operating conditions. Diagnostic signals represent the difference between the measured and the modeled values of two selected mill operating parameters. Models of mill motor current and outlet temperature of pulverized fuel were developed based on the linear regression theory. Various data analysis and feature selection procedures have been performed to obtain the best possible model. The model based on linear regression has been compared with two alternative models. The algorithm validation was carried out based on historical data containing values of operating parameters from 10 months of mill operation. Historical data were downloaded from distributed control system (DCS) of a 200-MW coal-fired power plant. Tests carried out on historical data show that this algorithm can be successfully used to detect certain abnormal conditions and malfunctions of the operating mill, such as feeder blockage, lack of coal and mill overload.

Keywords: predictive maintenance, coal mill, fault detection, digital twin, online diagnostic

1. Introduction

Safety, reliability and flexibility are some of the most important operation features of any power plant. The abnormal operation conditions and malfunctions of coal mills negatively

affect the boiler operation and furthermore can be the cause of emergency boiler shutdown. Coal mills produce the air and pulverized fuel mixture, which is burned in the boiler; hence, abnormal operating conditions can decrease boiler efficiency and increase CO2 and NOx emissions. Undetected at the right time, mill faults are the causes of numerous issues like failing to keep steam parameters, reduction of generated power, and the flame instability in the furnace, which enforces fuel oil burner usage to maintain continuity of combustion; the flame instability can lead to flame loss and that is one of the most dangerous situations that may appear in power plant.

As a consequence of these problems, coal mill control and fault detection have been the main focus in many research activities. General overview of control and fault diagnostic methods are the topics in [1, 2]. The authors in [3] investigated models based on the mass and heat balance together with the energy model. This model has been used in [4, 5]. In [4], observer-based models are developed. The fault detection is based on energy balance analysis, producing fault residuals that are used in detection schemes. It has been shown that the fault (blocked coal inlet pipe) is detected as soon as the fault occurs. A dynamic coal mil model using conservation laws and empirical relations has been developed in [6]. Unknown model parameters are estimated using differential evolution algorithm, and data set contains parameters from 7 days of mill operation. From the validation results, it is concluded that the model fits the on-site measured data very well, but model has not been tested in control or diagnostic application. Non-linear coal mill modeling and its application to model predictive control are presented in [7]. Three system output parameters of vertical roller coal mill (the pressure drop over the mill, power consumed by the mill and outlet temperature) models have been developed and used in non-linear model predictive control with results in improving coal load response time and temperature control. The observer-based approach presented in [3, 4] is compared with the regression-based approach in [8, 9]. The methods have been tested on data with one given fault that is dramatic increasing of the moisture content. Results show that both methods detect faults as it emerges, but the observer-based model detects the tested fault earlier than regression-based model.

In this chapter, a novel coal mill fault detection approach is presented. This is done through applying the linear regression theory to model two mill operating parameters: motor current and outlet temperature of pulverized fuel. Even though the regression theory has been tested and compared in [8], this chapter presents complex approach with high volume of data analysis containing around 2 million of measurements, while model in [8] has been trained on 300 samples. Additionally, the parameter's time delay influence has been tested as it was not used before and the input variables have been selected with the usage of advanced techniques of feature selection. The regression-based models are also compared with two alternative models that are artificial neural network-based models and physical equation-based models. Finally, developed algorithm has been implemented in fault detection algorithm implemented in 200 MW power unit.

The outlier of this chapter is as follows. The coal mill is introduced in Section 2. Real data analysis downloaded from Rybnik power plant is presented in Section 3. Section 4 focuses on feature selection process. In Section 5, moisture content estimation is presented. Developed

models are presented in Section 6, and the comparison between two other models' approaches is derived in Section 7. Section 8 presents the algorithm evaluation, and Section 9 shows algorithm fault detection performance.

2. The coal mill

The work presented in this chapter is based on a MKM-33 ball mill used at Rybnik Unit 4 (rated capacity 220 MW). The mill is one of six mills supplying the 650-k (steam production of 650 t/h) boiler. However, the proposed method in this chapter is so generic that it can be applied to other types of coal mills. The coal mill is illustrated in **Figure 1**.

The coal is fed to the coal mill through the central inlet pipe, where it is pulverized by a series of large balls separated by two types of rings. The pulverized material is carried out in the mill by the flow of air moving through it. The primary air is a mixture of cold air and air heated by the preheaters. The ratio of the hot and cold air flows is used to control the temperature and the flow of the primary air. The size of the pulverized particles released from the grinding section of the mill is determined by a classifier separator. Too large and heavy particles fall back on the gridding table and will be crushed by bowls again.

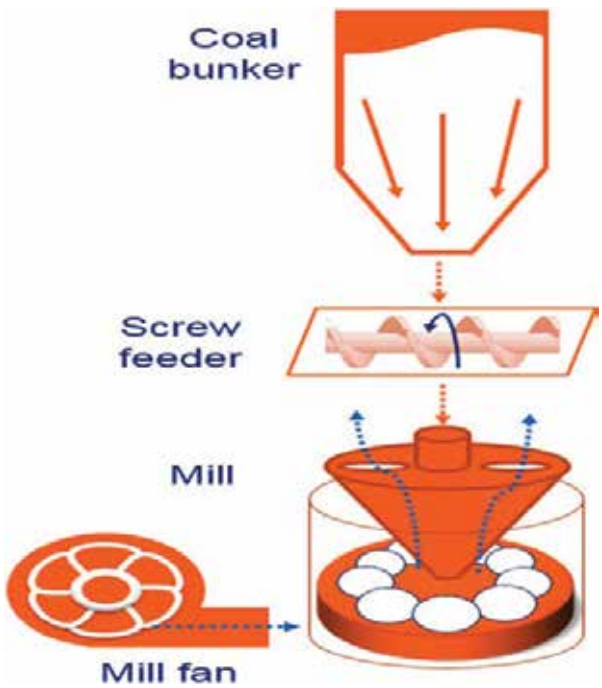

Figure 1. Coal mill scheme.

3. Real data analysis

3.1. Data set

The research has been performed on data set downloaded from Rybnik power plant DCS system. Data contain measurements values of 22 parameters from 10 months of mill operation (January 2014 to October 2014) with 10-s sampling period, except outside temperature and temperature in coal bunker which have 1-min sampling period. All parameters are presented in **Table 1**. In this chapter, variable names presented in **Table 1** have been used.

3.2. Data filtration and distribution analysis

Models presented in this chapter have been developed to describe mill normal working conditions based on historical data. Therefore, from the data set starts up, shuts down and work with feeder speed less than 10% has been removed. Additionally, seven new columns have been added to improve process description. Newly added columns are presented in **Table 2**.

No.	Variables	Description	Units
1	MW	Unit power	MW
2	MW_DMD	Unit power demand	MW
3	TURB_PRESS	Steam pressure at turbine inlet	MPa
4	PRESS_CORR	Corrected pressure demand for the boiler	MPa
5	STEAM_FLOW	Steam flow	t/h
6	FUEL_DMD	Fuel demand	%
7	FAN_DMPR	The fan blade setting	%
8	MILL_IN_PRESS	Primary air inlet pressure	kPa
9	MILL_OUT_TEMP	Temperature of pulverized fuel	°C
10	P_AIR_FLOW_DMD	Primary air flow demand	Nm^3/h
11	P_AIR_FLOW_BIAS	Primary air flow demand correction (manual)	Nm^3/h
12	P_AIR_FLOW	Measured primary air flow	Nm^3/h
13	HOT_AIR_DMPR	The opening of the hot air dumper	%
14	MILL_OUT_TEMP_DMD	Mill outlet temperature demand	°C
15	COLD_AIR_DMPR	The opening of the cold air dumper	%
16	FEEDER_LOAD	Feeder speed	%
17	AMPS	Mill motor current	A
18	TEMP_MILL_IN	Primary air inlet temperature	°C
19	PRESS_FAN_IN_L	Pressure in primary air collector (left side)	Pa
20	PRESS_FAN_IN_R	Pressure in primary air collector (right side)	Pa
21	TEMP_ON_LOAD	Temperature in coal bunker	°C
22	TEMP_OUTSIDE	Ambient temperature	°C

Table 1. Data set variable description.

New variable	Description	Formula
P_PP_IN_AVG_kPa	Pressure difference in primary air [kPa]	$\frac{P\_PP\_IN\_L+P\_PP\_IN\_P}{2}$
P_AIR_FLOW_kgs	Unit change from Nm^3/h to kg/s	$g_{air} = \frac{MILL\_IN\_PRESS}{r*\left(T_{PP_{IN}}+273\right)}$ $\text{P\_AIR\_FLOW\_kgs} = \frac{P_{AIR_{FLOW}}*g_{air}}{3600}$
DELTA_PA_mbar	Pressure difference between mill inlet and primary air collector	$10*(MP\_PP\_IN\_AVG_{kPa} - P\_PP\_IN\_AVG\_kPa)$
FUEL2POWER	Proportion FUEL_DMD/MW, possible estimation of fuel quality	$\frac{FUEL\_DMD}{MW}$
FUEL_DMD_REG	Mean value FUEL_DMD for a given power obtained from linear regression for all historical data	$0.0749435882327*MW + 26.9627419581$
FQUALITY	Difference between FUEL_DMD and FUEL_DMD_REG - second, more accurate fuel estimation quality	$FUEL\_DMD - FUEL\_DMD\_REG$
SUPPLIED_HEAT	Product of STEAM_FLOW and TEMP_ON_LOAD (proportional to the heat supplied)	$STEAM\_FLOW*TEMP\_ON\_LOAD$

Table 2. Added variable.

Finally, an additional column has been added for each input variable (all variables except AMPS and MILL_OUT_TEMP), and newly added columns contained the rolling mean of each column calculated according to the formula 1

$$x_{mean\_3}(t) = \frac{x(t-20s) + x(t-10s) + x(t)}{3} \tag{1}$$

where x is measured value at time t. The final data set contained 56 columns: 27 columns each for one depended variable, 27 columns for theirs means and two columns each for one independent variable. Histogram plots show that we can split data parameters into two groups:

1. Variables with normal distribution
2. Variables with bimodal distribution: MW,

MW_DMD, MILL_OUT_TEMP_DMD, MILL_OUT_TEMP, PRESS_CORR, STEAM_FLOW, FUEL_DMD_REG. Bimodal distribution of power is a result of unit working conditions (high power demand during morning hours, and low power demand during evening hours). Bimodal distribution of outlet temperature is caused by milled fuel type. During periods of coal and biomass co-milling, the mill outlet temperature demand has been set at 115°C. If the mill was gridding, only coal mill outlet temperature demand has been set at 105°C. Histograms are presented in **Figures 2** and **3**.

3.3. Co-correlations between model output and inputs

As presented in Section 2, the process of coal pulverizing in the mill consists of some sub-processes, for example hot and cold air mixtures before entering the mill. Some variable measurements (data set columns) can influence the main process with different time delay. To

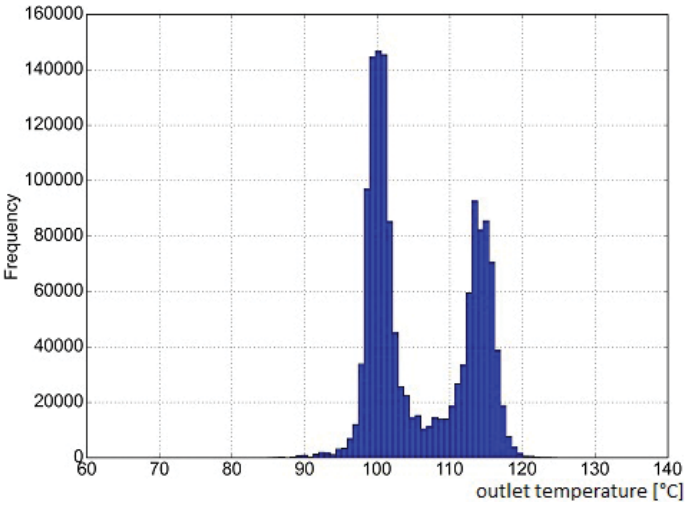

Figure 2. MILL outlet temperature (MILL_OUT_TEMP) histogram.

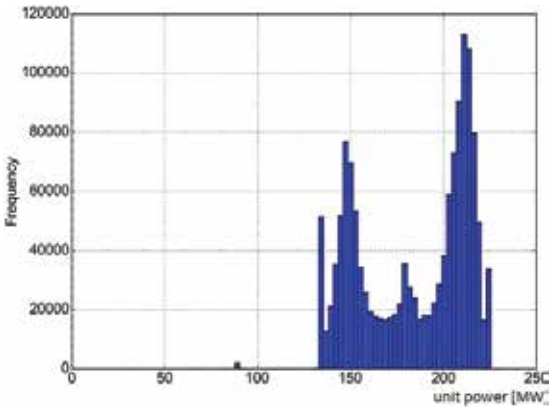

Figure 3. Unit power (MW) histogram.

explore the delay values, the Pearson correlation analysis has been made. Pearson correlation coefficient is a measure of the linear correlation between two variables.

For each depended variable, new columns have been added containing delayed variable values for 10, 20, 30,…,300 s. Afterwards, for each column presented in **Tables 1** and **2** and their mean values, the Pearson correlation coefficient has been calculated and the delay with the highest Pearson coefficient has been chosen. The results are presented in **Tables 3** and **4**.

For MILL_OUT_TEMP, most of the parameters are the best correlated with 6-min delay. This time shows the automatic process control reaction time for mill outlet temperature demand changes. Only the parameters which do not influence directly into demanded outlet temperature are correlated with very slow delay (10, 20 s) For the AMPS variable, the system is reacting for AIR_FLOW_DMD changes with around 6-min delay. However, parameters with strong influence into process are correlated with small delay. The best correlated with AMPS is variable

FEEDER_LOAD_mean3 (correlation value is equal to 0.395). The correlation coefficient higher than 0.3 has also variables: FEEDER_LOAD, FAN_DMPR, MILL_IN_PRESS, P_AIR_FLOW_kgs, DELTA_PA_mbar and theirs means. The best correlated with MILL_OUT_TEMP is variable: MILL_OUT_TEMP_DMD_mean3. With correlation coefficient 0.926 (for the rest of variables, correlation coefficient is not greater than 0.5).

Variables	Delay [s]	Correlation coefficient
FEEDER_LOAD	150	0.393
FAN_DMPR	80	0.390
MILL_IN_PRESS	130	0.369
P_AIR_FLOW_kgs	130	0.347
DELTA_PA_mbar	130	0.340
FUEL_DMD	150	0.289
P_AIR_FLOW_DMD	90	0.287
SUPPLIED_HEAT	30	0.282
FUEL_DMD_REG	20	0.281
MW	20	0.281
MW_DMD	30	0.281
STEAM_FLOW	30	0.276
P_AIR_FLOW	20	0.239
PRESS_CORR	300	0.220
HOT_AIR_DMPR	20	0.208
TURB_PRESS	10	0.199
COLD_AIR_DMPR	300	0.195

Table 3. Variable delays best correlated with AMPS.

Variables	Delay [s]	Correlation coefficient
MILL_OUT_TEMP_DMD	300	0.926
COLD_AIR_DMPR	300	−0.497
TEMP_MILL_IN	300	0.467
P_AIR_FLOW_kgs	300	−0.362
TEMP_OUTSIDE	300	−0.327
DELTA_PA_mbar	10	−0.269
MILL_IN_PRESS	10	−0.259
P_AIR_FLOW_DMD	200	−0.247
P_AIR_FLOW	300	−0.240
TEMP_ON_LOAD	300	−0.202

Table 4. Variable delays best correlated with MILL_OUT_TEMP.

4. Feature selection

So far, input data set used to evaluate models contains all parameters. Obviously, not all of them have the impact on modeling parameters. The process of feature selection has been made to extract all variables with the influence on modeling output. This process is also developed to:

1. simplify the model. Simple models are easier to interpret and maintain;
2. increase the generalization of the model by limiting overfitting, and by that, increasing the quality of the modeling;
3. decrease the model training time.

The main assumption during feature selection is that the initial data set contains variables which are redundant, strongly correlated with one another or irrelevant and, therefore, can be deleted without information losses [10, 11].

The wage of model improvement is determined by model accuracy coefficient, and in this chapter, the root mean square (RMS) coefficient has been used. Forward feature selection has been made with the usage of author algorithms. The comparison between various developed models has been made by comparing calculated model accuracy coefficients. For each model, the following model fitting parameters have been calculated: coefficient of determination (R^2), root mean square (RMS) and mean average percentage error (MAPE). Those parameters have been calculated with the usage of threefold cross-validation technics [12]. Comparison between models has been made by comparing RMS coefficient value.

The determination of unknown regression coefficient has been made with linear and ridge regression usage [13].

In **Table 5**, the reference model is presented. The reference model has been fitted to initial data set containing variables presented in **Tables 1** and **2** and their means (no feature selection process).

Depended variables	R^2	RMS	MAPE
AMPS	0.256	0.707	1.903
MILL_OUT_TEMP	0.85	2.21	1.43

Table 5. Reference models.

Features	Accuracy coefficients	
MILL_IN_PRESS_mean3–120, P_PP_IN_AVG_kPa-30, FUEL2POWER-10, FUEL2POWER_mean3–10	MAPE [%]	1.965
	RMS [A]	0.622
	R^2 [−]	0.179

Table 6. AMPS model.

In **Table 6**, the best model evaluated for AMPS independent variable after feature selection process is presented; the number of features has been decreased from 55 to 4 with minor model accuracy diminution.

The model variables have been chosen from the RFECV feature selection method, with ridge regression model fitting estimator ($\propto$ =1e 07).

In **Table 7**, the best model evaluated for MILL_OUT_TEMP independent variable is presented. The feature number has been decreased from 55 to 15, and the model accuracy has been improved. The features have been chosen from the RFECV feature selection method. The model accuracy has been improved in comparison with the reference model.

The autoregressive models have not been considered because of future model's use that is fault detection. Autoregressive models in case of fault development will model malfunction, and consequently, the fault will be undetected.

Afterwards, few additional hypotheses have been investigated:

Hypothesis 1: Continuous historical data updating can improve model fitting. An assumption has been made that if we will train model progressively based on defined period of historical data, the accuracy of the model will be improved in comparison with model based on all historical data. The hypothesis has been tested by algorithm that idea is presented in **Figure 4**. First model is trained on data located in history window, then the model output prediction is made for samples located in prediction window. Afterwards, data widow is moved by the length of prediction window; then, process of model training and output prediction is repeated. The windows are moved after each iteration until the end of data set.

The algorithm has been implemented to forward feature selection but without particular success (the feature selection algorithm has stopped after first iteration). Furthermore, the algorithm has been used to obtain model coefficient for models presented in **Tables 6** and **7**; for this model, numerous configurations of data history window and data prediction window have been examined. The summary of results is presented in **Table 8**.

The best growth of MAPE coefficient has been observed for short historical data windows (from 14 to 28 days) though training model on such short period of time can be dangerous. If

Features	Accuracy coefficients	
MILL_OUT_TEMP_DMD_mean3–300,FUEL2POWER_mean3–300, P_AIR_FLOW_DMD_mean3–190,COLD_AIR_DMPR-300, TEMP_MILL_IN_mean3–300,P_AIR_FLOW_BIAS_mean3–10, FEEDER_LOAD_mean3–180,COLD_AIR_DMPR_mean3–300, HOT_AIR_DMPR-300, FQUALITY_mean3–300, MW-300,TURB_PRESS_mean3–300, P_AIR_FLOW_DMD-200,PRESS_CORR-300, P_AIR_FLOW_BIAS-10,MW_DMD_mean3–300, STEAM_FLOW-10,P_AIR_FLOW-300, PRESS_FAN_IN_L-300,FUEL_DMD_mean3–300,	R^2[−]	0.930
	RMS[°C]	1.831
	MAPE[%]	1.253

Table 7. MILL_OUT_TEMP model.

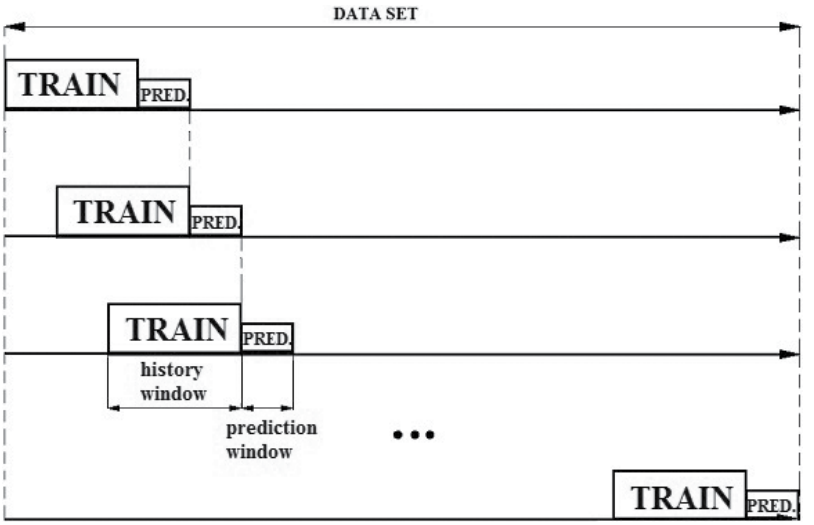

Figure 4. The idea of progressive prediction.

abnormal condition has occurred during this period, the model will fit coefficients into these data obviously; furthermore, model would not achieve its function. It has been assumed that safe historical data length is greater than 800,000 s (around 3 months). For such cases, model accuracy has not improved significantly, and this is why the algorithm has been rejected. Nevertheless, it has to be kept in mind that after some periods, the model coefficient has to be updated, for example in case of mill or boiler renovation. In such cases, it is recommended to train the model on at least 2-month history data set.

Hypothesis 2: The fuzzy regression will improve model accuracy. As shown in Section 3.3, some parameters have bimodal distribution; in such cases, fuzzy regression can be successfully implemented. An algorithm has been developed which creates two linear models, model for high load and model for low load. The model output is the sum of those sub model outputs, multiplied by wages that are depended on load. The formula for wages is presented in Eqs. (2) and (3):

$$\mu_{low\ demand} = \begin{cases} 1 & for\ x < 150 \\ \dfrac{190 - x}{190 - 150} & for\ x\ \epsilon < 150, 190 > \\ 0 & for\ x > 190 \end{cases} \tag{2}$$

$$\mu_{high\ demand} = \begin{cases} 1 & for\ x < 150 \\ \dfrac{x - 150}{190 - 150} & for\ x\ \epsilon < 150, 190 > \\ 0 & for\ x > 190 \end{cases} \tag{3}$$

where x is the unit power. As presented in **Table 9**, the model accuracy has not been improved.

History window (s)	Prediction window (s)	R^2 [−]	RMS [A]	MAPE [%]
50,000	100	0.495	0.488	1.551
100,000	100	0.375	0.543	1.732
100,000	500	0.317	0.568	1.755
5,000,000	100	0.184	0.590	1.890
5,000,000	500	0.164	0.597	1.890
5,000,000	1000	0.142	0.605	1.891

Table 8. AMPS moved historical window.

	RMS	MAPE
AMPS	0.719	1.922
MILL_OUT_TEMP	9.428	1.224

Table 9. Fuzzy regression.

Hypothesis 3: Non-linear input variable transformation may increase model accuracy. Since the processes occurring in the mill are non-linear, some input parameters' manipulation has been investigated. To perform, an algorithm has been created which was adding a new parameter that was obtained by changing selected parameters values according to defined manipulation; however, during one iteration, only one parameter with one manipulation has been investigated; after iteration, the algorithm was returning to initial data set. The parameter modifications have been based on functions such as quadratic function, cubic function, square, natural logarithm, decimal logarithm and exponential function. The results show that for none of the parameter's modification, the model accuracy coefficients have improved significantly.

5. Coal moisture content

To improve model accuracy and abnormal working conditions' detection ability, the estimation of the moisture content has been evaluated. Two main processes, coal gridding and moisture evaporation from the coal dust, are taking place in the mill, and the quality and performance of those processes are highly depended on coal milling quality and moisture content. Online measurements of those parameters are not possible; however, the moisture content can be determined by evaluating the energy balance.

A simple energy balance model of the coal mill is derived based on [2, 3]. The coal mill is considered as one body with the mass m_m, as illustrated in **Figure 5**.

In **Figure 5**, T(t) is the temperature in the mill, Q_air (t) is the energy in the primary air flow, Q_coal (t) is the energy in the coal flow, Q_moisture (t) is the energy in moisture, Q_e (t) is energy losses to environment, Q_pf (t) is energy in air-fuel mixture, Q_steam (t) is energy in steam, Q_evap (t) is energy used to evaporate moisture and Q_cum (t) is accumulated energy

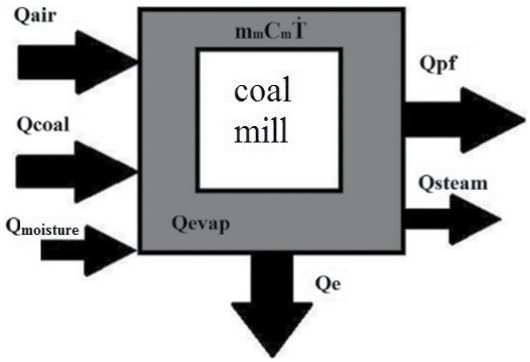

Figure 5. Scheme of coal mill heat balance.

in the mill. The specific heat capacity of the mill is C_m. Even though this assumption is only entirely true for steady state, it is assumed in this chapter for simplifying the model.

The energy balance is given by [2, 3](4):

$$Q_{air}(t) + Q_{coal}(t) + Q_{moisture}(t) = \quad Q_{pf}(t) + Q_{cum}(t) + Q_e(t) + Q_{steam}(t) \tag{4}$$

The Q_cum (t) + Q_e (t) + Q_steam (t) coefficients have been neglected due to relatively small influence into balance or lack of information. The heating and evaporation of the moisture in the coal are modeled by combined heating coefficients. The latent energy of the evaporation dominates the energy required for a few degrees of heating of the moisture. The combined heat coefficient, H_st, is defined as follows: H_st = C_w + L_steam/100, where C_w is the specific heat of the water and L_steam is the latent heat. This combined heat coefficient does not deal with the fact that the specific heats of water and steam are different. However, the model error is due to heat if steam to a couple of degrees above 100°C is negligible in this context. The moisture content has been determined by [4](5):

$$\gamma = \frac{m_{air}Cp_{air}*(T_{air_{in}} - T_{out}) + m_{coal}\, Cp_{coal}\left(T_{on_{load}} - T_{out}\right)}{m_{coal}\, Cp_{coal}\left(T_{on_{load}} - T_{out}\right) + m_{coal}(T_{out} - T_{on\ load}) + m_{coal}h_{ev}} \tag{5}$$

where m_{air} is the primary air flow, m_{coal} is the coal flow into mill, Cp_{air}, Cp_{coal} are specific heat of air and coal, $T_{air_{in}}$ is primary air flow temperature,T_{out} is outlet temperature of pulverized fuel, and $T_{on_{load}}$ is temperature in coal bunker. The modeling results are presented in **Figure 6**.

The moisture content together with the heat accumulation determined by (6) has been added to AMPS model selected features.

$$Q_{acumulated} = Q_{air} + Q_{coal} - Q_{coal\_dust} \tag{6}$$

The model accuracy has been slightly improved, and it has also been noticed that the model presents high differences from measurements during faults.

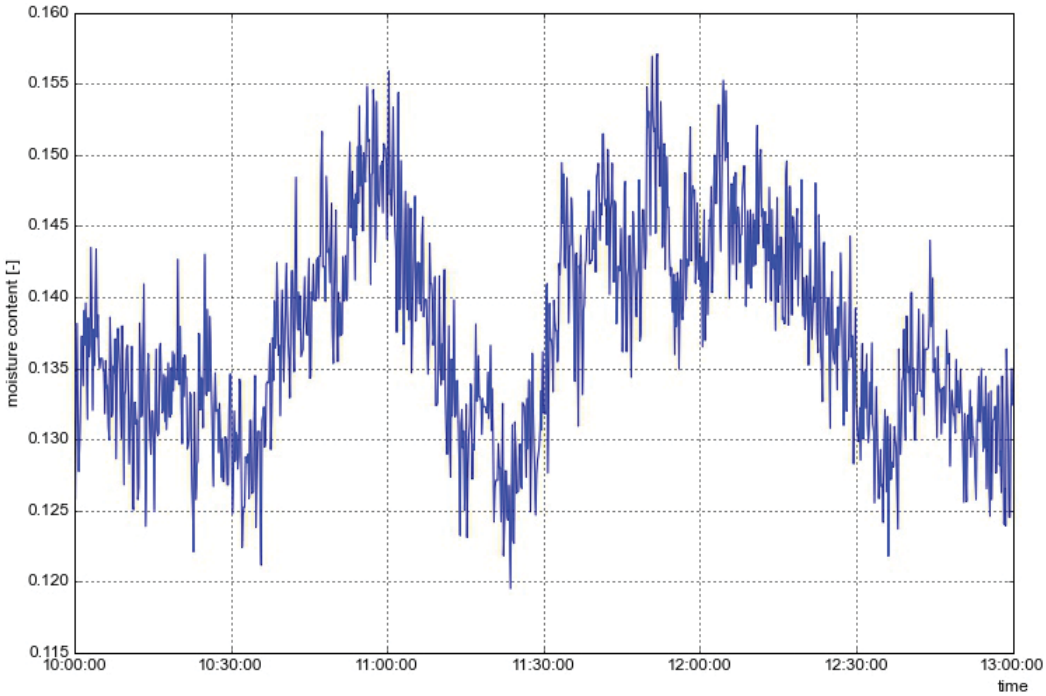

Figure 6. The plot of moisture content estimation.

6. Modeling results

The best obtained models have been based on variables presented in **Tables 7** and **10**. The predicted values are compared with the measured values in **Figures 7** and **8**. From this figure, it can be seen that the models are quite similar to the dynamical changes as the measurements show. However, for periods with co-milling the biomass, model behavior with comparison to measurements is not sufficient. The analyzed power plant does not continue co-firing of biomass with such way; therefore, these periods are not the main focus of this algorithm. It has also been noticed that during fault occurring in data sets, the models have been presenting a noticeable difference from the measurements.

Features	Accuracy coefficients	
MILL_IN_PRESS_mean3–120, P_PP_IN_AVG_kPa-30, FUEL2POWER-10, FUEL2POWER_mean3–10 $\gamma = Q_{acumulated}$	MAPE [%]	1.946
	RMS [A]	0.601
	R^2 [−]	0.21

Table 10. Adding moisture content.

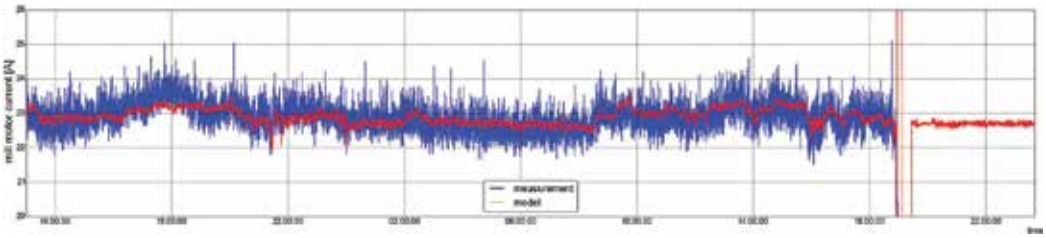

Figure 7. The plot of measured and modeled values of mill motor current (AMPS) date: 15 Feburary 2015, fuel: Coal.

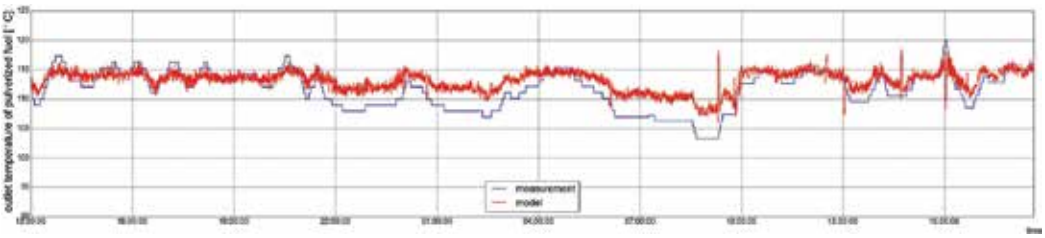

Figure 8. The plot of measured and modeled values of mill outlet temperature (MILL_OUT_TEMP) AMPS 15 Feburary 2015, fuel: Coal.

7. Comparison with artificial neural network and physical model

As presented in Section 1, the mill models have been the subject of investigation by many researches; nevertheless, the main scope of models creation is to develop model as simple as possible without significant model accuracy losses. Processes occurring in the coal mill are dynamic and nonlinear; this is why so many methods have been investigated. The model based on linear regression has been compared with the model based on artificial neural network and the model based on physical equations with genetic algorithm usage to determine unknown parameters.

7.1. Model based on artificial neural network

Artificial neural network (ANN)-based modeling is non-linear statistical technique [14]. Recently, there has been increasing interest in neural network modeling of industrial processes such as gridding in coal mills [19]. The design of ANN includes the choice of architecture, training function and training algorithm. The architecture of a network is determined by the number of hidden layers in the network, the number of neurons and the transfer function in each layer, and how the layers are connected to one another. The basic neural network is shown in **Figure 9**.

The multi-layer perception neural network (MLPNN) is one of the most widely applied neural network topologies, and this topology has been applied to develop non-linear models. The input variables are the features selected and presented in Sections 4 and 5. The values of data

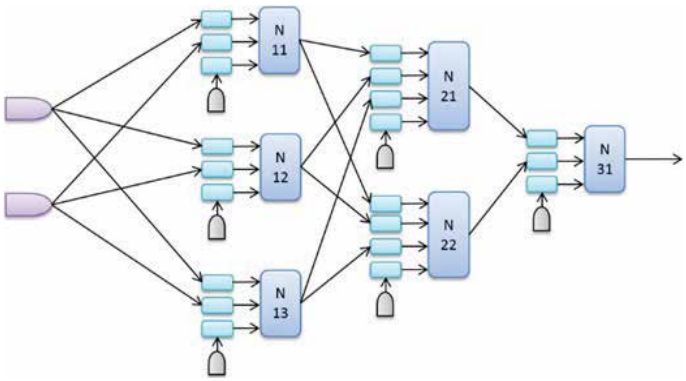

Figure 9. Example of artificial neural network architecture.

Number of neurons		MAPE [%]	
First hidden layer	**Second hidden layer**	**AMPS**	**MILL_OUT_TEMP**
11	8	1.961	1.12
20	6	1.959	1.10
8	2	1.984	1.18
15	0	1.971	1.15
4	0	2.21	1.29

Table 11. ANN modeling results.

set have been standardized [15, 16]. The MPLPNN hidden and output layers are activated with tangent-sigmoid function. Numerous combinations of architecture have been investigated to develop the best possible model. The architecture combinations are presented in **Table 11**. During training and testing procedures, the accuracy parameters have been calculated with cross-validation [12] technique usage. The ANN has been trained with usage of backpropagation supervised ANN learning algorithm. The ANN consists also the bias coefficients. The best obtained structure and results are presented in **Table 11**.

7.2. Model based on physical equations with the use of a genetic algorithm to determine the unknown model coefficients

This method has been developed by [16, 17], and the model is derived through the analysis of energy transferring, heat exchange and mass flow balances. A non-linear mathematical model for a normal mill grinding process was developed in the previous work [16], which was based on the following assumptions: (1) the pulverizing mechanism in the mill is simplified, and coal classification is not considered; (2) grinding and pneumatic transport in the milling process are separated into two stages; and (3) coal size is grouped into only two categories, namely pulverized coal and unpulverized coal. The mill model for the steady-state milling process can

be described by numerous equations [16, 17], containing five algebraic equations describing primary air flow based on pressure differences and air density, coal flow based on feeder speed, pulverized coal flow based on pressure differences and actual amount of pulverized fuel in mill and four differential equations describing mass balance in coal mill based on coal flow, actual coal content in mill, pulverized fuel flow and content in coal mill following equation describing mill motor current, mill pressure differences, and outlet temperature variability.

The main focus in developing this model is unknown coefficients K_i, where i ∈{1,2,3,…,17} definition is such way that the model has the lowest prediction error (the difference between measured and modeled values is minimalized). One approach [16] uses the genetic algorithm to determine unknown coefficients. The same method has been developed and applied to analyzed coal mill [18], and the results are presented in **Table 12**.

7.3. Comparison

In this chapter, three coal mill models' evaluation approaches are presented, and the methods are linear regression (Sections 4, 5 and 6), artificial neural network (Section 7.1) and physical equations with the use of a genetic algorithm to determine the unknown model coefficients (Section 7.2). All mentioned methods have been applied to data set containing values of operating parameters from 10 months of mill operation presented in Section 3. The results presented in **Table 13** show that the AMPS models have similar performance with the MAPE coefficient close to 2%, which is less than 0.5A mean error. The results presented in **Table 14** show that the MILL_OUT_TEMP models have more varied results.

Although ANN-based model of MILL_OUT_TEMP has the best accuracy, and the Ridge regression-based model has lower as it can be seen in **Figures 10** and **11**; the behavior of models, response to parameter changes and places of higher difference from measures are the same. The ANN better adapts to periods with high temperature increasing mainly in case of mill start-up. However, both models have the same sudden changes of predicted value as presented in **Figures 10** and **11**; ANN generates the valued bit proximal to measurement than ridge regression but without significant influence into further application to fault detection. It has been also tested that both models detect abnormal working condition present at nearly the same time. It seems reasonable to use Ridge regression-based models in algorithm since they are easier to train, maintain and adapt.

	MILL_OUT_TEMP [°C]	**AMPS [A]**
MAPE [%]	1.15	2.02

Table 12. Genetic algorithm.

Model based on	**MAPE**
Ridge regression	1.946
Artificial neural network	1.981
Physical equations	2.020

Table 13. AMPS comparison.

Model based on	MAPE
Ridge regression	1.26
Artificial neural network	1.10
Physical equations	1.15

Table 14. MILL_OUT_TEMP comparison.

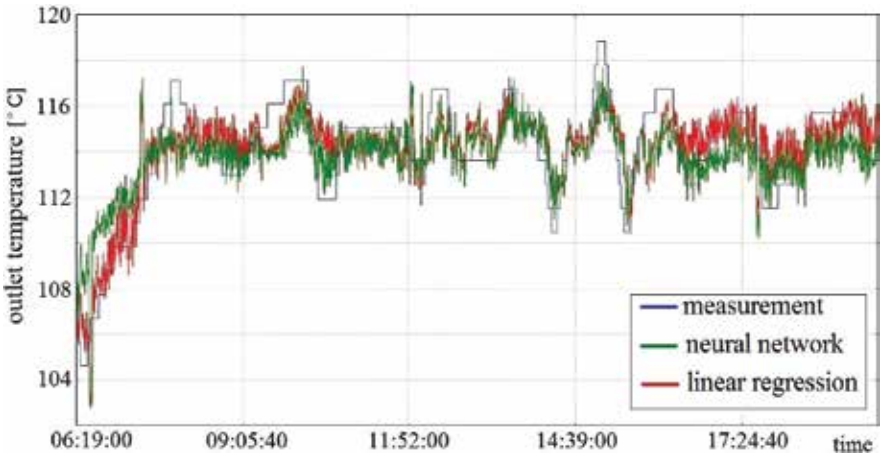

Figure 10. ANN and ridge regression comparison.

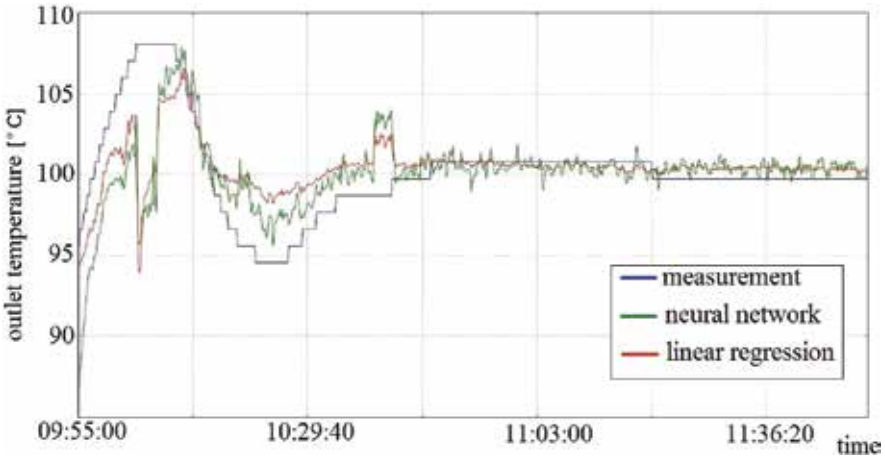

Figure 11. ANN and ridge regression comparison.

The models' application into industrial process control and fault detection usually depends on the model accuracy and the model complexity. As presented in the chapter, the three different approaches of AMPS model evaluations gave comparable model accuracy; however, their complexity differs. It seems natural that the model with the lowest complexity level is implemented, and still, furthermore, complex comparison tests should be performed. Model

based on physical equation is the most understandable, but the process of unknown coefficient estimation is time-consuming and non-deterministic; the neural network-based model is the most complex and the least comprehensible; consequently, its implementation does not seem to be needed. The advantage of regression model is its simplicity and comprehension; therefore, it seems appropriate to implement model in algorithm designed to detect mill faults.

8. Fault detection algorithm

The models presented in **Tables 6** and **7** have been used to develop the algorithm and enabled to detect abnormal operation conditions and malfunction of analyzed mill. The algorithm during mill operation determines diagnostic signals (7) which represents the difference between measured y_measured and predicted y_predicted values of mill current and outlet temperature:

$$r = y_{predicted} - y_{measured} \tag{7}$$

If the value exceeds defined threshold, the algorithm infers about abnormal working condition presence. The predicted values are calculated based on coefficients determined for model presented in **Tables 8** and **10** with consideration of variable delays presented in **Tables 3** and **4**.

8.1. Threshold definition

The appropriate threshold value definition is crucial; if the threshold is low, the algorithm will often falsely infer the presence of abnormal condition; on the other hand, if threshold will be too high, the algorithm may not infer abnormal conditions while it occurs. The threshold values have been determined based on residual valued r, and the distribution of residuals is presented in **Figures 12** and **13**.

After analyzing the model behavior, it has been decided that the algorithm will infer with two levels:

LEVEL 1—abnormal operation conditions.

LEVEL 2—fault.

The thresholds for each level are presented in **Table 15**, and the alarm disabling will occur when the diagnostic signal value is decreased to determine value.

8.2. Fault cause distinction

When algorithm informs about appearance of abnormal working conditions, which mean that at least one diagnostic signal has exceeded the threshold, the most likely cause of these conditions is estimated and provided. There are three main fault causes that algorithm detects: feeder blockage, lack of coal in the mill and mill overload. Inference mechanism combines the algorithm performance and unit operator's experience.

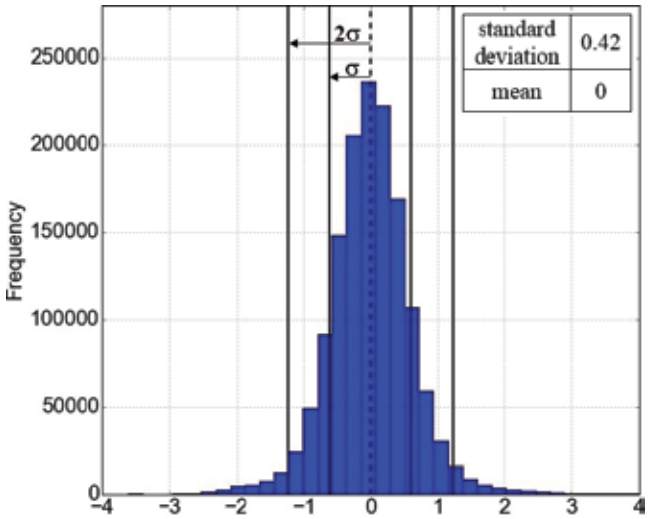

Figure 12. AMPS histogram of residuals.

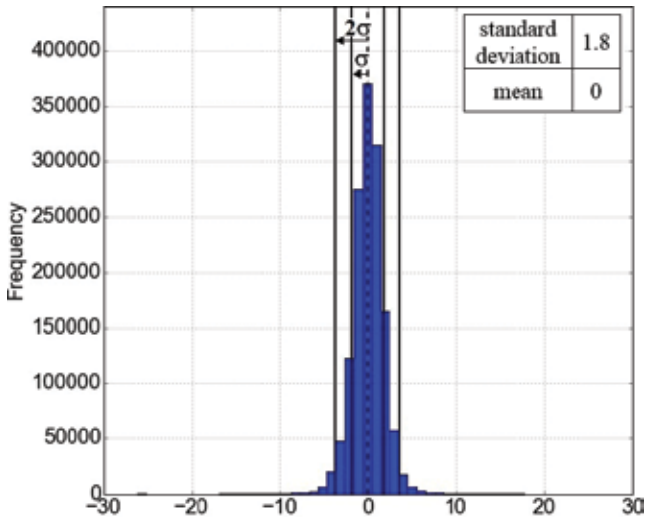

Figure 13. MILL_OUT_TEMP histogram of residuals.

Model	Threshold for level 1	Threshold for level 2	Threshold for disabling
AMPS	1,2	2	0,8
MILL_OUT_TEMP	8	15	6

Table 15. Thresholds.

First, algorithm determines whether in the mill there is too much (r > 0) or too little of coal (r < 0). If there is too little of coal, the second step is to compare temperature in coal bunker. If there is no coal in feeder, the temperature instantly is rising and the feeder motor current is lower that usually. In case of r > 0, the algorithm also is checking the mill inlet presser since it is main parameter observed by operators during mill diagnostic; if the pressure is significantly higher than usual, the algorithm also informs about it. Those mechanisms have been implemented in operator graphic which informs about current mill conditions and estimated risks.

8.3. Algorithm

Algorithm presented in **Figure 14** is designed to inform online about coal mill working conditions. History window contains the measurements from last 5 min (due to input signal time delay), and diagnostic signal is generated in way presented in Section 8. The operators are informed about actual coal mill conditions and estimated risk by dedicated operator graphic containing information about diagnostic signals and estimated risks presented in Section 8.2.

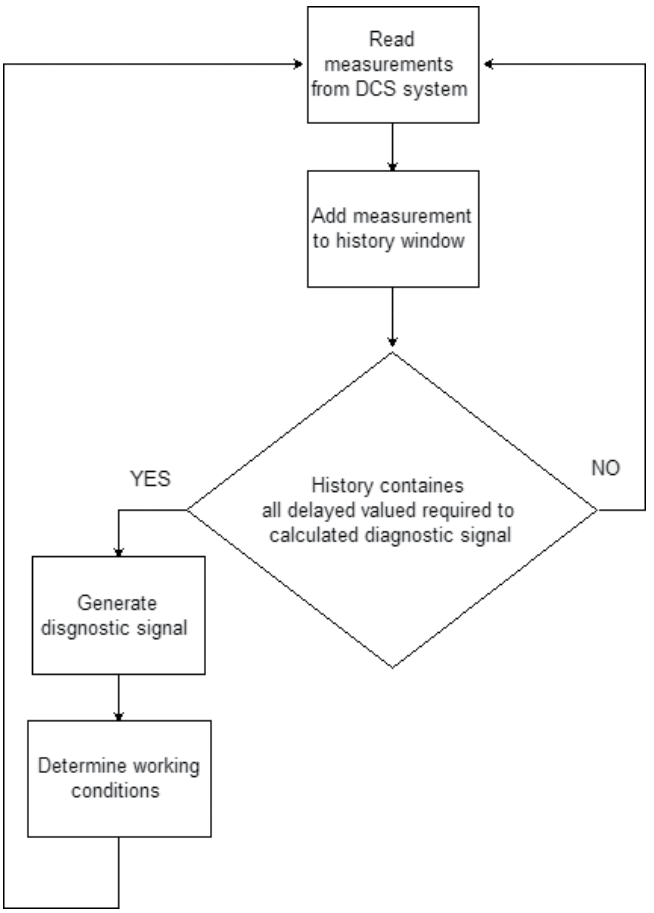

Figure 14. The idea of online diagnostic algorithm.

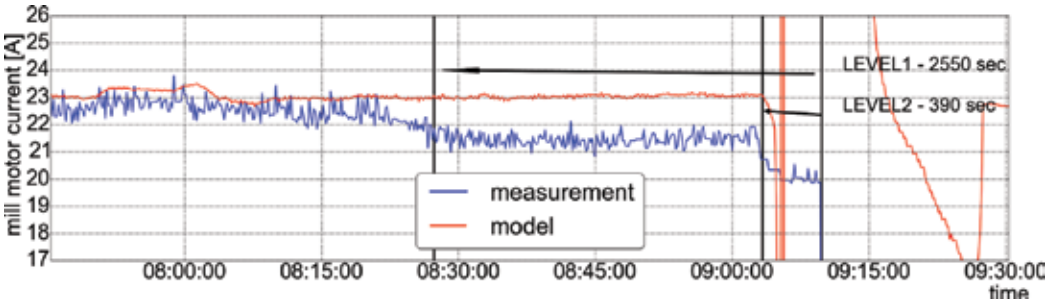

Figure 15. AMPS11 September 2014 fault: Screw blockage.

9. Fault detection performance

The algorithm has been tested to analyze its fault detection performance. In historical data set, the faults occur six times and were caused by lack of coal in coal bunker, feeder blockage and mill overload. For each malfunction type, the algorithm infers abnormal working conditions with some ahead of time. Particularly, the algorithm detects the feeder blockage. For fault in 11 September 2014, the algorithm infers abnormal working conditions around 40 min ahead the mill shutdown and 6 min before mill shutdown algorithm inferring about fault. More detailed times are presented in **Table 16**. It can be seen that the failure has been developing during period between first alarm occupancy at LEVEL1 and LEVEL 2. This gives the unit operators enough time to react safely.

In **Figures 15–16**, the comparison of measured and modeled values is presented. The same type of fault appeared in 22 January 2014, and the LEVELS 1 and 2 appeared at similar time around 11 min before emergency mill shutdown. Details are presented in **Table 17**, and

Model	Level 1	Level 2
AMPS	2550 s	390 s
MILL_OUT_TEMP	240 s	240

Table 16. 11 September 2014 fault: Screw blockage.

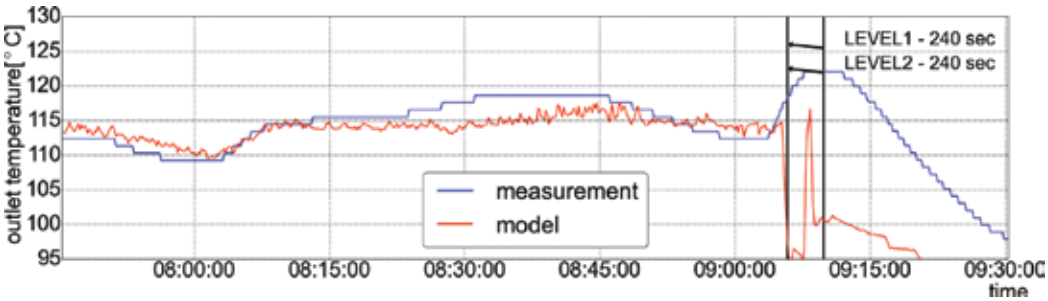

Figure 16. MILL_OUT_TEMP 2014.09.11 fault: Screw blockage.

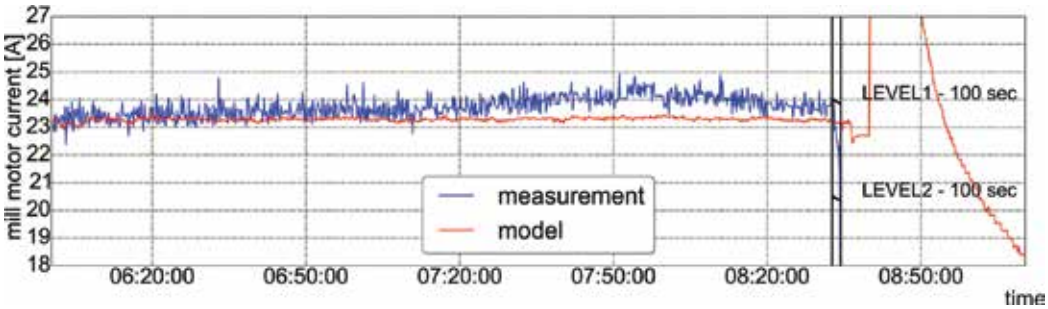

Figure 17. AMPS 12 July 2014 fault: Lack of coal in coal bunker.

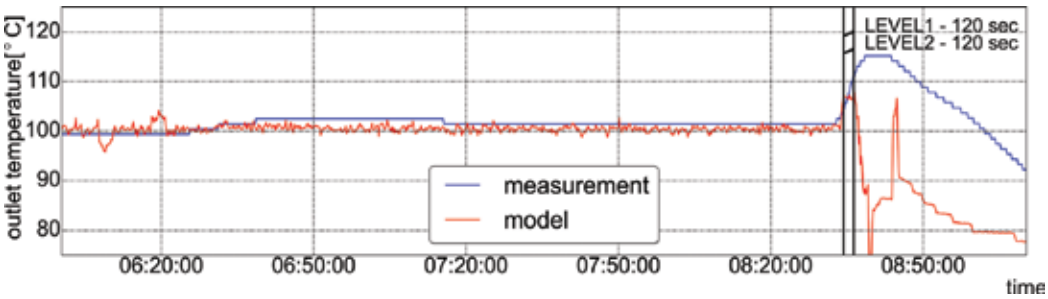

Figure 18. MILL_OUT_TEMP 12 July 2014 fault: Lack of coal in coal bunker.

MODEL	Level 1	Level 2
AMPS	670	600
MILL_OUT_TEMP	590 s	590

Table 17. 22 January 2014 fault: Screw blockage.

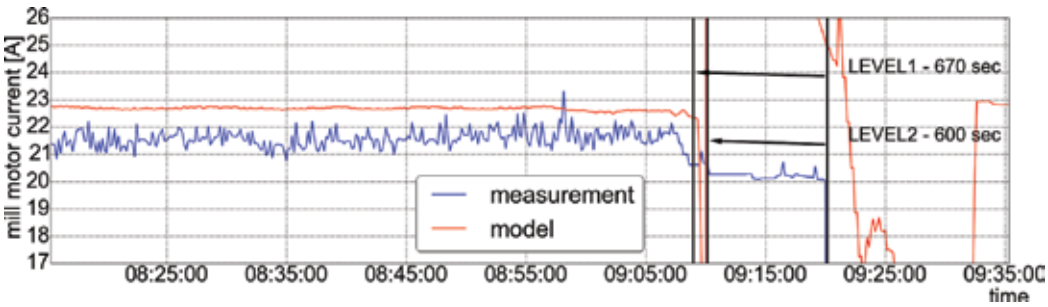

Figure 19. AMPS 22 January 2014. Fault: Screw blockage.

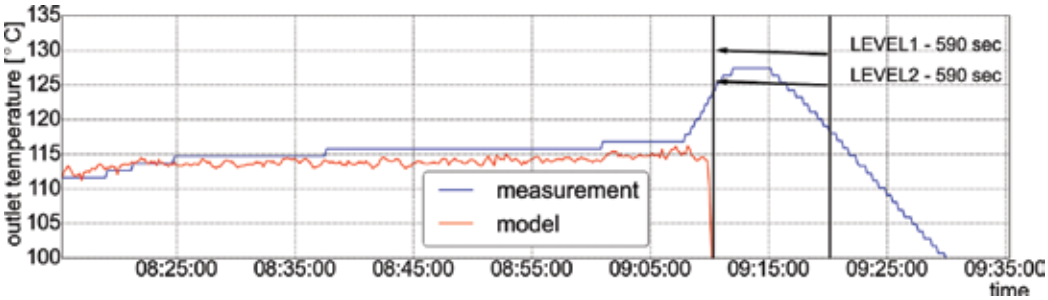

Figure 20. MILL_OUT_TEMP 22 January 2014. Fault: Screw blockage.

MODEL	Level 1	Level 2
AMPS	100	100
MILL_OUT_TEMP	120	120

Table 18. 12 July 2014 fault: Lack of coal in coal bunker.

comparison of modeled and predicted values is presented in **Figures 19** and **20**. It can be seen that the failure occurred suddenly unlike the failure on 11.09 where before failure the mill has been working with abnormal conditions for around 30 min; however, the algorithm has been informing at LEVEL 2 10 min before mill shut down. The fault caused by lack of coal in the bunker is presented in **Figures 17** and **18**, and the times of algorithm abnormal working condition inference are presented in **Table 18**. The algorithm infer at LEVEL 1 and LEVEL 2 around 2 min before emergency mill shutdown; although this is not a lot this types of faults forms and evolve relatively fast and inexpertly and algorithm allows inform and give for the operator a time for propel reaction.

10. Conclusion

This chapter presents the models of two coal mill operation parameters: motor current and outlet temperature of pulverized fuel, implemented in algorithm designed to detect faults and abnormal operating conditions in coal mills. During extended data analysis, it has been shown that some depended variables influence independent variables with certain delay. The models have been developed with usage of multiple regression theory and compared with model based on an artificial neural network and model based on physical equations. It has been demonstrated that regression-based models have comparable model accuracy and fault detection performance. Based on developed models, an algorithm that detects abnormal working conditions and faults of coal mill has been developed. Tests carried out on historical data show that this algorithm can be successfully used to detect certain abnormal conditions and malfunctions of the operating mill, such as feeder blockage, lack of coal and mill overload. The algorithm is implemented in the power plant on 200 MW power unit.

Author details

Teresa Kurek[1]*, Konrad Wojdan[1], Daniel Nabagło[2] and Konrad Świrski[1]

*Address all correspondence to: teresa.bil@itc.pw.edu.pl

1 Institute of Heat Engineering, Faculty of Power and Aeronautical Engineering, Warsaw University of Technology, Warszawa, Poland

2 EDF Polska S.A., Research & Development Department, Krakow, Poland

References

[1] Agrawal V, Panigrahi BK, Subbarao PMV. Review of control and fault diagnosis methods applied to coal mills. Journal of Process Control. 2015;**32**:138-153

[2] Rees NW, Fan GQ. Modeling and control of pulverized fuel coal mills. Institution of Electrical Engineers, Thermal power plant simulation and control: Chapter3. 2003. 63-99

[3] Rees N, Fan F. Modeling and control of pulverized fuel coal mills in Thermal power plant simulation and control. Flynn D, editor. 1st ed. Institution of Electrical Engineers. 2003

[4] Odgaard PF, Mataji B. Observer-based fault detection and moisture estimating in coal mills. Control Engineering Practice. 2008;**16**:909-921

[5] Guo S, Wang J, Wei J, Zachariades P. A new model-based approach for power plant tube-ball mill condition monitoring and fault detection. Energy Convertion and Management. 2014;**80**:10-19

[6] Agrawal V, Panigrahi BK, Subbarao PMV. A unified thermo-mechanical model for coal mill operation. Control Engineering Practice. 2015;**44**:157-171

[7] Cortinovi A. Mercangöz M, Mathur T, Poland J, Blaumann M. Nonlinear coal mill modeling and its application to model predictive control. Control Engineering Practice. 2013;**21**:308–320

[8] Odgaard PF, Lin B, Jorgensen SB. Observer based and regression model-based detection of emerging faults in coal mills. Supervision and Safety of Technical Processes Beijing. 2006;**2006**

[9] Odgaard PF, Mataji B. Fault Detection in Coal Mills Used in Power Plants. Kananaskis, Canada: Power Plants and Power Systems Control; 2006

[10] D'Ambrosio JPR, Dupont P. Kernel methods for heterogeneous feature selection. Neurocomputing. 2015;**169**:187-195

[11] Reif M, Shafait F. Efficient feature size reduction via predictive forward selection. Pattern Recognition. 2014;**47**:1664-1673

[12] Arlot S, Celisse A. A survey of cross-validation procedures for model selection. Statistics Survey. 2010;**4**:40-79

[13] Lium X-Q, H-Y J. Optimal generalized ridge estimator under the generalized cross-validation criterion in linear regression. Linear Algebra and its Applications. 2012;**436**:1238-1245

[14] Guoqiang Zhang, Patuwo BE, Hu MY. Forecasting with artificial neural networks: The state of the art. International Journal of Forecast. 1998;**14**:35-62

[15] Shanker M, Hu MY, Hung MS. Effect of data standardization on neural network training. Omega. 1996;**24**(4):385-397

[16] Zhang YG, Wu QH, Wang J, Oluwande G, Matts D, Zhou XX. Coal mill modeling by machine learning based on on-site measurement. IEEE Transactions on Energy Conversion. 2002;**17**(4):549-555

[17] Wei JL, Wang JH, Wu QH. Further study of coal mill modeling by machine learning based on on-site measurement. In: Proc.. 16th Int. Conf. Syst. Eng. Conf. 2003, Conventry, U.K. 746-741

[18] Krosnicki M. Current diagnosis of coal mill using evolutionary algorithm. WUT Masther thesis. 2015

[19] Guo-you L, Min D. A wavelet and neural networks based on fault diagnosis for HAGC system of strip rolling mill. Journal of Iron and Steel Research, International. 2011;**18**(1):31-35

Chapter 4

Numerical Modeling of Cyclic Creep-Fatigue Damage Development for Lifetime Assessment of Steam Turbine Components

Mariusz Banaszkiewicz

Additional information is available at the end of the chapter

http://dx.doi.org/10.5772/intechopen.73186

Abstract

The paper presents the results of numerical analysis of creep-fatigue damage development in a steam turbine rotor under cyclic duty. Investigations were performed for a full cycle representing the most accurate description of real operation and three simplified cycles representative of different levels of simplification in inelastic strains modeling. It was shown by numerical simulations that significant inaccuracies in creep-fatigue damage predictions, reaching an order of magnitude in deviation of inelastic strains, cannot be excluded when simplified models are used. It is thus concluded that full consideration of creep-fatigue damage at real operating conditions requires proper modeling of stress/strain histories using visco-elastic-plastic material models.

Keywords: creep, low-cycle fatigue, steam turbine, lifetime assessment

1. Introduction

The increasing demand for higher thermal efficiency and higher operational flexibility of modern power generation plants results in severe mechanical and thermal loading conditions experienced by plant components in service [1]. In order to increase the thermal efficiency, it is often necessary to increase the power plant operating temperature, while the higher operational flexibility requires frequent and faster turbine start-ups and shutdowns. The extremely severe service conditions of the plant components are subjected to produce a progressive material deterioration due to the accumulation of creep and fatigue damage and can lead to component failure [2].

Steam turbine components operating at high and highly variable temperatures, e.g., rotors, casings and valve chests, are among the most critical components of power plant units, and their lifetime is already limited at the design stage [3]. Safe and reliable operation of steam turbines can only be ensured with proper monitoring systems, periodic inspections and comprehensive lifetime assessment studies [4–6].

Typical operation cycle of a steam turbine consists of a start-up, steady state, load change, shutdown and natural cooling. During transient phases, the low-cycle fatigue damage is generated, while steady-state operation brings about the creep wear [7]. In order to accurately determine the creep-fatigue life exhaustion, inelastic material models and a proper approach to multiple cycles consideration have to be applied [8].

Traditional methods of lifetime assessment basing on the use of representative operation data and elastic material models can result in significant inaccuracies in damage prediction and lead to non-optimal decisions regarding future operation [9]. That is why the use of inelastic material models and long-term operation data is becoming mandatory for reliable calculation of creep-fatigue damage and residual life prediction.

The paper presents the results of investigations performed for a steam turbine rotor showing possible inaccuracies and, in particular, differences in predicted strain accumulation and damage depending on the material model and cycles analysis method used.

2. Cyclic operation of steam turbines

The lifetime of steam turbine components depends on variable loading conditions resulting in fatigue and creep-fatigue damage. Typical service start-stop cycle includes start-up, full load, part load and shutdown phase, generating variable temperature and stress-strain distributions in turbine components. A schematic illustration of different operation phases and the resulting temperature and stress variations on a rotor surface is shown in **Figure 1**. During turbine run-up, rotor rotational speed increases from turning gear to rated speed (0–1) and steam parameters start rising from the initial values. After unit synchronization (1), turbine loading starts (1–2) with continued increase of steam temperature and pressure, and after some time, all the parameters reach their nominal values. The start-up process is finished and steady-state phase (2–3) with constant process parameters is reached. During steady-state operation, load changes (3–4, 5–6) with different rate can take place, which are accompanied by steam temperature and pressure variations. The operating cycle is closed by the shutdown (7–8) and natural cooling phases when all the process parameters go down.

The corresponding stress variations at a rotor surface are presented in **Figure 1b**. During start-up, the rotor surface temperature increases with a higher rate than the center temperature, which results in compressive stresses at the surface [10]. The stress attains maximum and then slowly decays to a steady-state stress. The following load changes generate transient thermal stresses of different sign, but usually the highest tensile stress is generated on the rotor surface

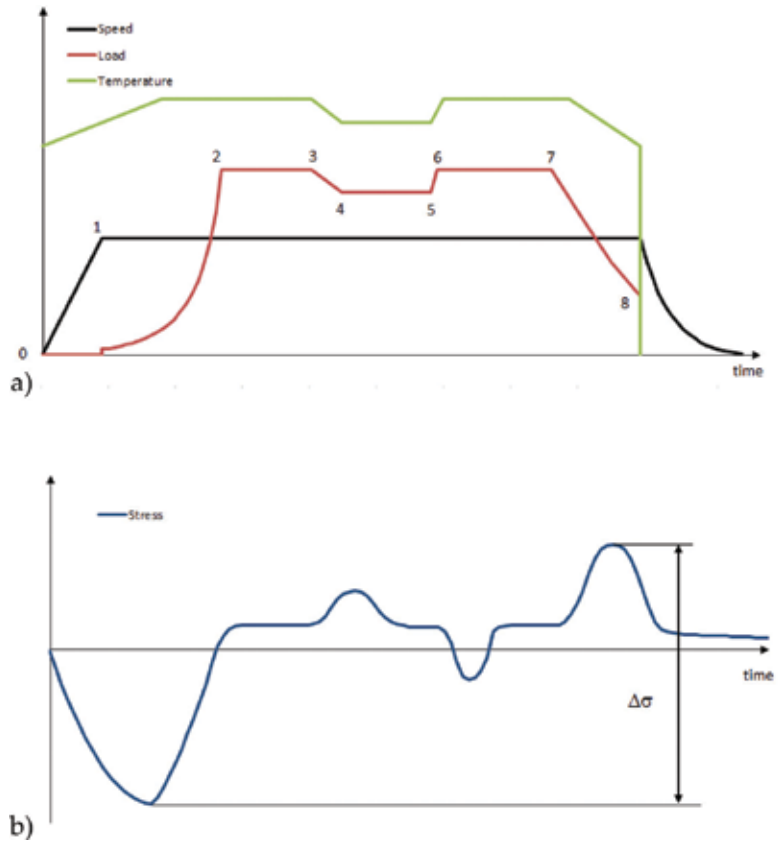

Figure 1. Typical operating cycle of conventional steam turbine unit: (a) process parameters and (b) rotor surface stress.

during the shutdown phase. The major stress range $\Delta\sigma$ is thus formed by the start-up and shutdown stresses, while the minor stress range is defined by the load change stresses.

Full consideration of creep-fatigue damage at real operating conditions requires modeling of long stress/strain histories using visco-elastic-plastic material models. Such a modeling approach is impractical when 2D or 3D models are used to represent the real component geometry and the balance equations solved by means of a finite element method. For the purpose of numerical investigation of creep-fatigue damage development in steam turbine rotors, simplified cycles are defined with different material models prescribed to transient and steady-state phases. It was done in order to investigate the effect of material model applied and number of cycles analyzed on the creep-fatigue damage accumulation. The four cycle types are schematically shown in **Figure 2**. They are as follows:

1. Full multiple cycle: fatigue simulated with elastic-plastic model and creep with viscous model for multiple start-stop cycles.

2. Simplified multiple viscous cycle 1: fatigue simulated with elastic-plastic model for one cycle and creep with viscous model for multiple start-stop cycles.

3. Simplified multiple viscous cycle 2: fatigue simulated with elastic model for one cycle and creep with viscous model for multiple start-stop cycles.
4. Simplified multiple elastic-plastic cycle: fatigue simulated with elastic-plastic model for multiple start-stop cycles and no creep.

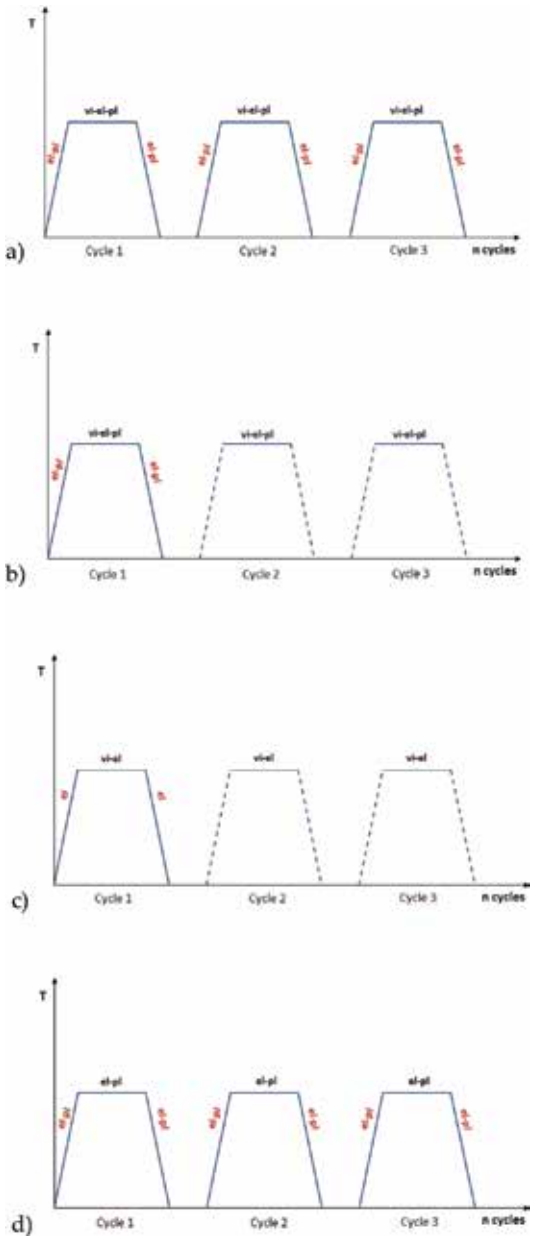

Figure 2. Different cycle types adopted for analyses: (a) full multiple cycle, (b) simplified multiple viscous cycle 1, (c) simplified multiple viscous cycle 2 and (d) simplified multiple elastic-plastic cycle.

The first cycle describes the most realistic representation of actual operating conditions, while the other three cycles represent simplified approaches in terms of material models and number of cycles, which are used in engineering practice.

3. Problem formulation

The problem under consideration is cyclic heating up and cooling down of a steam turbine rotor taking place during start-up and the subsequent shutdown. Rotor heating and cooling are caused by hot steam flow through the turbine with varying temperature, pressure and velocity. Non-stationary heat transfer takes place via forced convection, and the thermal load is a primary load of the rotor [11]. The rotor rotates with a constant rotational speed ω in steady-state operation. Steam pressure and rotational body forces due to rotation are also considered in the model. Non-uniform temperature distribution in the rotor induces thermal stresses due to thermal expansion.

The following assumptions are adopted in the model:

- The rotor material is isotropic and its physical and mechanical properties are temperature dependent.
- Heating and cooling process is described by the linear theory of heat conduction and non-linear convective boundary conditions.
- The resulting thermal stresses are determined from the solution of system of equations of uncoupled thermoelasticity and plasticity.
- Due to the geometrical and load symmetry of the rotor about its axis, the computational region is assumed axisymmetric.
- Mechanical loads are modeled as surface pressure and volumetric body force.

Based on the above assumptions, a boundary problem of heat conduction and thermoelasticity is formulated and solved by means of a finite element method [12].

3.1. Heat conduction problem

Heat conduction in a homogeneous isotropic solid is described by the Fourier-Kirchhoff differential equation [13]

$$\mathrm{div}[k\mathrm{grad}T(x,t)] + g(x,t) = \rho c_p \frac{\partial T(x,t)}{\partial t} \tag{1}$$

where T is the metal temperature, k is the thermal conductivity, g is the heat source, ρ is the density and c_p is the specific heat.

Neglecting the heat source g and assuming heat conduction in the radial and axial direction only, Eq. (1) is rewritten in cylindrical coordinate system as follows:

$$\rho c_p \frac{\partial T}{\partial t} = \frac{1}{\mathrm{r}} \frac{\partial}{\partial r}\left(kr\frac{\partial T}{\partial r}\right) + \frac{\partial}{\partial z}\left(k\frac{\partial T}{\partial z}\right) \tag{2}$$

A non-uniform temperature distribution $T(r,z)$ is assumed as initial condition at $t = 0$. For rotor free surfaces, the boundary conditions are:

$$\left.\frac{\partial T}{\partial r}\right|_{r=r_{in}} = 0 \text{ for } t \geq 0 \tag{3}$$

$$k(z,t)\left.\frac{\partial T}{\partial r}\right|_{r=r_{out}(z)} = -\alpha(z,t)\left(T_s - T_f(z,t)\right) \text{ for } t \geq 0 \tag{4}$$

where $\alpha(z,t)$ is the heat transfer coefficient varying with time and axial co-ordiante, T_s is the metal surface temperature and $T_f(z,t)$ is the fluid temperature depending on time and axial co-ordiante. The outer radius of the rotor $r(z)$ varies with the axial coordinate z defining its outer contour.

The material physical properties are temperature dependent and their variation is described by polynomial functions. The variation of heat transfer coefficient in time and space $\alpha(z,t)$ is considered by the Nusselt number Nu changing in time as a function of the Reynolds number Re and Prandtl number Pr:

$$\mathrm{Nu} = \mathrm{f}(\mathrm{Re}, \mathrm{Pr}) \tag{5}$$

The Nusselt number is defined as follows:

$$\mathrm{Nu} = \frac{\alpha d}{k} \tag{6}$$

where d denotes a characteristic diameter. A detailed form of Eq. (6) depends on the surface type and flow character [11]. The heat transfer model adopted in this study is based on the well-proven formulae for heat transfer coefficients in steam turbine rotors and can be employed in online calculations of temperatures and thermal stresses [14], which is not possible when more advanced thermal FSI (fluid-structure interaction) modeling is adopted [15–18].

Geometrical model of the rotor is shown in **Figure 3**.

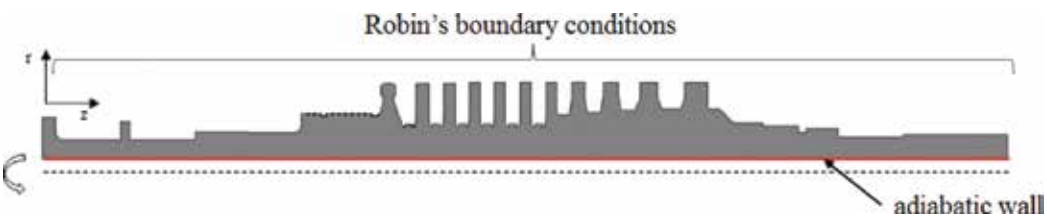

Figure 3. Rotor geometrical model.

3.2. Thermoelasticity problem

Knowing the axisymmetric temperature field in the rotor, a solution of the problem of stress state induced by it can be obtained. The equilibrium conditions written for stresses are transformed, taking into account the relations between stresses, strains and displacements, to obtain differential equations with unknown displacements u and w in the r and z direction, respectively [19]:

$$\begin{gathered}\nabla^2 u - \frac{u}{r^2} + \frac{1}{1-2\nu}\frac{\partial e}{\partial r} + \frac{\rho\omega^2 r}{G} = \frac{2(1+\nu)}{1-2\nu}\frac{\partial\big(\beta(T-T_0)\big)}{\partial r} \\ \nabla^2 w + \frac{1}{1-2\nu}\frac{\partial e}{\partial z} = \frac{2(1+\nu)}{1-2\nu}\frac{\partial\big(\beta(T-T_0)\big)}{\partial z}\end{gathered} \tag{7}$$

where the following definitions were employed:

- Laplacian $\nabla^2 = \frac{\partial^2}{\partial r^2} + \frac{1}{r}\frac{\partial}{\partial r} + \frac{\partial^2}{\partial z^2}$
- Volumetric strain $e = \frac{\partial u}{\partial r} + \frac{u}{r} + \frac{\partial w}{\partial z}$

In Eq. (7), ν is the Poisson's ratio and β is the thermal expansion coefficient.

The system of partial differential equations (7) is solved with the following boundary conditions:

- At the outer cylindrical surfaces of the discs

  $\sigma_r = p_b(z)$—pressure due to centrifugal forces of blades
- At the outer surfaces in contact with steam

  $\sigma_n = -p(z)$—steam pressure acting normal to the surface
- At the left end face
- $w = 0$ at $z = 0$

The relations between strains and displacements for an axisymmetric body in the cylindrical coordinate system are expressed as [19]:

$$\begin{gathered}\varepsilon_r = \frac{\partial u}{\partial r} \\ \varepsilon_\varphi = \frac{u}{r} \\ \varepsilon_z = \frac{\partial w}{\partial z} \\ \gamma_{rz} = \frac{\partial u}{\partial z} + \frac{\partial w}{\partial r}\end{gathered} \tag{8}$$

Stress components are obtained from the solution of the constitutive equation of linear thermoelasticity [13] and for an axisymmetric body in the cylindrical coordinate system they are given as [19]:

$$\begin{aligned}
\sigma_r &= 2G\left\{\varepsilon_r + \frac{1}{1-2\nu}\left[\nu e - (1+v)\beta(T-T_0)\right]\right\} \\
\sigma_\varphi &= 2G\left\{\varepsilon_\varphi + \frac{1}{1-2\nu}\left[\nu e - (1+v)\beta(T-T_0)\right]\right\} \\
\sigma_z &= 2G\left\{\varepsilon_z + \frac{1}{1-2\nu}\left[\nu e - (1+v)\beta(T-T_0)\right]\right\} \\
\sigma_{rz} &= G\gamma_{rz}
\end{aligned} \tag{9}$$

where $G = \frac{E}{2(1+\nu)}$ is the shear modulus and E is the Young's modulus.

Eq. (9) is known as the Duhamel-Neumann relations and has a fundamental importance in thermal stress analysis within the validity of Hooke's law [20].

3.3. Plasticity model

At stress concentration areas, thermal stresses induced by nonuniform temperature field can exceed the material yield stress and give rise to plastic deformation. Instead of estimating the plastic strains based on thermoelastic stresses and using analytical notch stress-strain correction methods [4, 14], a more accurate approach with direct use of elastic-plastic material was adopted. Numerical calculations were performed using Abaqus [21], employing elastic-plastic material model with the Prager-Ziegler linear kinematic hardening. The plasticity surface is defined by the Huber-Mises-Hencky function [22]:

$$F = f\left(\sigma_{ij} - \alpha_{ij}\right) - \sigma_y = 0 \tag{10}$$

where $f\left(\sigma_{ij} - \alpha_{ij}\right)$ is the equivalent stress related to the backstress α_{ij} defining translation of the yield surface. The yield function is traditionally defined as follows

$$f\left(\sigma_{ij} - \alpha_{ij}\right) = \sqrt{\frac{3}{2}\left(s_{ij} - \alpha_{ij}^d\right)\left(s_{ij} - \alpha_{ij}^d\right)} \tag{11}$$

where s_{ij} is a deviatoric part of the stress tensor σ_{ij}, while α_{ij}^d is a deviatoric part of the backstress tensor α_{ij}.

The linear kinematic hardening model assumes the associated plastic flow rule in the form [23]:

$$\dot{\varepsilon}_{ij}^p = \dot{\lambda}\frac{\partial F}{\partial \sigma_{ij}} = \dot{\lambda}\left(s_{ij} - \alpha_{ij}^d\right) \tag{12}$$

where $\dot{\varepsilon}_{ij}^{p}$ is a plastic flow rate and $\dot{\lambda}$ denotes here a plastic work. In the linear kinematic hardening model, translation of the yield surface is described by the backstress tensor α_{ij} whose evolution in time is determined by the Prager-Ziegler linear hardening law

$$\dot{\alpha_{ij}} = \dot{\mu}\left(\sigma_{ij} - \alpha_{ij}\right) \tag{13}$$

where μ is a positive scalar coefficient.

3.4. Creep model

For creep strain predictions, the characteristic strain model proposed by Bolton was employed [24, 25]. The model is simple and effective in description of creep deformation at long times. Based on the analyses of creep test data, Bolton extended the classical Norton model [26] and proposed the following isochronous relation between the stress exponent and stress expressed as a fraction of creep rupture strength σ_R [24]:

$$\frac{\partial \log \varepsilon_c}{\partial log\sigma} = n = \frac{1}{1 - \frac{\sigma}{\sigma_R}} \tag{14}$$

where σ_R denotes the creep rupture strength for a given time at constant temperature. Integrating the above relationship, he obtained an equation for the creep strain ε_C in the form:

$$\varepsilon_C = \frac{\varepsilon_\chi}{\frac{\sigma_R}{\sigma} - 1} \tag{15}$$

where ε_χ is a characteristic creep strain, which is a material constant at a given time and temperature. The characteristic creep strain can be evaluated using Eq. (15) and by knowing two stresses, i.e. the creep rupture strength σ_{R1} at time t_1 and the stress σ_{D1} to produce datum creep strain ε_D at time t_1. With this assumption, the isochronous stress-strain relation of Eq. (15) can be written as:

$$\varepsilon_C = \frac{\varepsilon_D\left(\frac{\sigma_{R1}}{\sigma_{D1}} - 1\right)}{\frac{\sigma_R}{\sigma} - 1} \tag{16}$$

To close the model, a relationship for the rupture strength described by a simple power-law relationship is adopted:

$$\sigma_R = \sigma_{R1}\left(\frac{t_1}{t}\right)^{1/m} \tag{17}$$

where m denotes the exponent in the power-law relationship. The exponent m can be evaluated from two values of rupture strengths at time t_1 and t_2:

$$m = \frac{\log\left(\frac{t_2}{t_1}\right)}{\log\left(\frac{\sigma_{R1}}{\sigma_{R2}}\right)} \tag{18}$$

Finally, combining Eqs. (16) and (17), the model relationship between creep strain and time at a constant stress assumes the form:

$$\varepsilon_C = \frac{\varepsilon_D\left(\frac{\sigma_{R1}}{\sigma_{D1}} - 1\right)}{\frac{\sigma_{R1}}{\sigma}\left(\frac{t_1}{t}\right)^{1/m} - 1} \tag{19}$$

The creep model is thus described by three constants: σ_{R1}—creep rupture strength at time t_1; σ_{R2}—creep rupture strength at time t_2 and σ_{D1}—stress of creep strain ε_D at time t_1, which clearly have physical significance and can be derived from readily available data from standard creep tests.

4. Creep-fatigue damage modeling

Creep damage is assessed on the basis of accumulated creep strain and is calculated using the ductility exhaustion rule [27, 28]. For a given load cycle i of duration t_h, creep damage d_i^{cr} is calculated from the formula [29]

$$d_i^{cr} = \int_0^{t_h} \frac{\dot{\varepsilon}^{cr}}{\varepsilon_R\left(\dot{\varepsilon}^{cr}\right)} dt \tag{20}$$

where ε_R is the creep ductility depending on the creep strain rate. The total creep damage D^{cr} due to n cycles is obtained by summing up the fractional creep damage values:

$$D^{cr} = \sum_{i=1}^{n} d_i^{cr} \tag{21}$$

Fatigue damage is assessed on the basis of accumulated plastic strain. For a given load cycle i, fatigue damage d_i^f is calculated from the formula [30]:

$$d_i^f = \oint \frac{d\varepsilon^{pl}}{\varepsilon_f} \tag{22}$$

where ε_f is the plastic strain at failure. The total fatigue damage D^f due to n cycles is obtained by summing up the fractional fatigue damage values:

$$D^f = \sum_{i=1}^{n} d_i^f \tag{23}$$

According to the linear damage accumulation rule, the total creep-fatigue damage D is a sum of that due to creep and fatigue [31]:

$$D = D^{cr} + D^{f} \tag{24}$$

The total damage D cannot exceed a critical value D_c above which creep-fatigue crack initiation can be expected. The rules of calculating the critical damage are given in different national standards [32–35].

Creep-fatigue damage calculation using the linear damage accumulation rule, creep and plasticity models and the proposed cycle descriptions can be used in lifetime calculations of both new and old turbines that have been in service for a longer period of time. For new machines, the following input data are typically required in order to perform lifetime calculations:

- Number of cold, warm and hot starts that the turbine has to perform.
- Requested operation time with given steam parameters and loads.
- Variation in time of the basic process parameters like steam temperature and pressure, rotor rotational speed and turbine load for cold, warm and hot starts and shutdown (these data are provided in the turbine design start-up diagrams).

Creep-fatigue damage calculations are performed for the cycles defined using the above data.

For old machines, lifetime calculations are carried out in order to determine the current damage and predict the residual life assuming unchanged operating conditions. The accuracy of lifetime calculations strongly depends on the range and quality of operation data provided by the turbine user. In this case, long-term data characterizing turbine operation in the whole operation time or at least representative operation period should be used for computations. The range of data required for such analyses is similar to that required for new machines with the difference that the data were recorded and characterize real operation instead of the ideal operation assumed at the design phase. Creep-fatigue damage calculations are performed for the cycles defined using the real operation data.

The difference between design and real conditions can be high and result in a huge deviation of damage and residual life predictions exceeding an order of magnitude.

5. Damage development in a steam turbine rotor

According to the strain-based damage accumulation rules, damage due to a load cycle depends on the inelastic strain accumulated in the cycle and the strain at failure. For a given material and loading conditions, the failure strain can be assumed as constant, thus the accumulated strain can be adopted as a direct measure of creep or fatigue damage. This property was utilized in the present study to examine creep-fatigue damage development in a steam turbine rotor. In particular, the effect of prior creep and plastic deformation on the creep and plastic strain evolution is investigated, and its impact on damage development is discussed in detail.

5.1. Thermal and elastic analysis

Temperature and elastic stress distributions in the examined rotor were obtained by solving the heat conduction and thermoelasticity equations given in Sections 3.1 and 3.2. Numerical solutions were obtained by means of the finite element method [12] using Abaqus code [21]. Transient and steady-state temperature distributions in the rotor are shown in **Figure 4**. During turbine start-up, highest temperature gradients, predominantly in the radial direction, are present in the rotor hottest region close to the steam inlet (**Figure 4a**). In steady-state, temperature distribution shown in **Figure 4b**, mainly axial temperature gradients are present which result from steam expansion in the turbine steam path and gland system. Transient temperature gradients produce high thermal stresses in the rotor leading to thermal fatigue cracking in stress concentration areas. High temperature in the rotor hottest sections in combination with centrifugal stresses lead to the creep damage which can also be localized in the stress concentration zones [36, 37]. In the examined rotor, the area of highest stress and temperature is located in the gland section where several heat relief grooves are present (**Figure 5**). High elastic stresses are developed at the bottom of the grooves and they frequently exceed the material yield stress. This results in local plastic deformation whose repetitive occurrence leads to thermal fatigue cracking often found in the heat grooves [38]. The heat relief grooves are thus the most critical locations of the rotor and their creep-fatigue damage development is analyzed in detail in the subsequent sections.

5.2. Effect of creep deformation on plastic strain accumulation

Cyclic operation of the turbine and the resulting plastic strain accumulation in the heat grooves were simulated by three start-stop cycles, each consisting of cold start-up, steady-state operation and shutdown followed by natural cooling to the subsequent cold start.

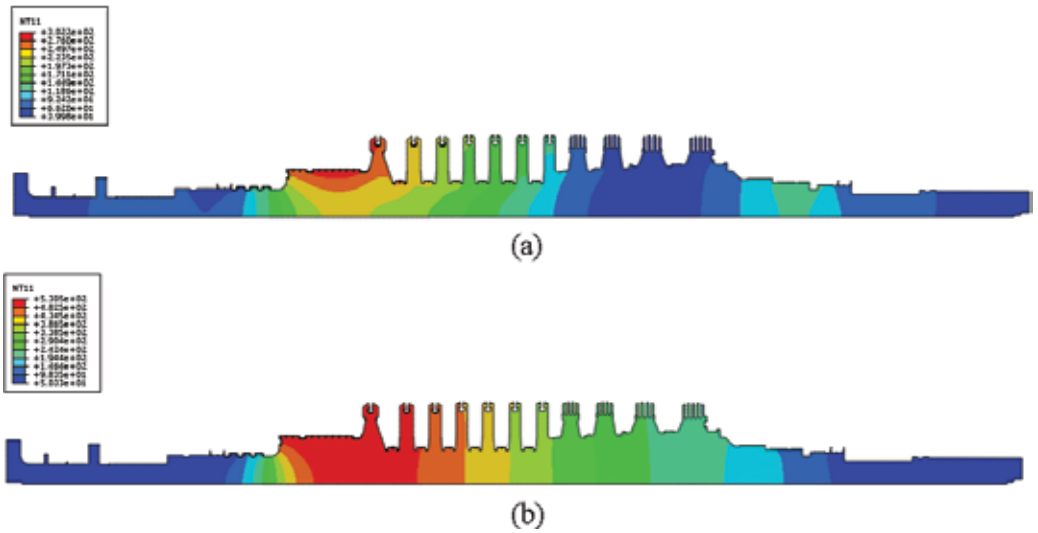

Figure 4. Temperature distribution in the rotor: (a) during cold start at 130 min and (b) at steady-state operation.

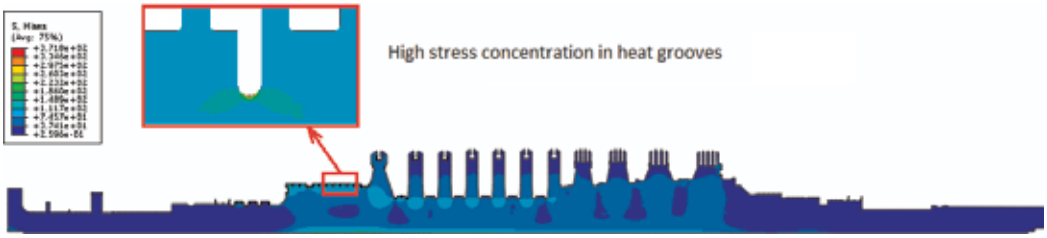

Figure 5. Elastic stress distribution in the rotor during cold start at 130 min.

Throughout the entire analysis, the elastic-plastic material model was enabled with plasticity model defined in Section 3.3. Two types of cycles were utilized in order to examine the effect of creep deformation on plastic strain accumulation, namely full multiple cycle (**Figure 2a**) and simplified multiple elastic-plastic cycle (**Figure 2d**). The former accounts for creep during steady-state operation, whereas the latter cycle neglects the viscous effects and stress relaxation under constant load. The duration of one full cycle was 386 h, which results in the total time to complete three cycles equal 1158 h. The comparison of equivalent plastic strain distribution after each cycle for both types of analysis is shown in **Figure 6**. The zone of plastic deformation increases in size during cycling and its shape remains almost unchanged being close to semi-elliptical. Both models, i.e. elasto-plastic and visco-elasto-plastic, predict similar development of the plastic zone but with slightly higher equivalent plastic strains at the bottom of the groove observed in the elastic-plastic model predictions (without creep effects). The evolution in time of the maximum equivalent plastic strain at the groove is shown in **Figure 7** together with the corresponding temperature cycles. The equivalent plastic strain gradually increases over time and so does the difference between the two models. It is thus found that creep deformation decelerates the plastic strain accumulation, which can be explained by the stress relaxation taking place during steady-state phase. As it is seen from **Figure 7b**, the first deviation in equivalent strains occurs after c.a. 110 h, which corresponds to

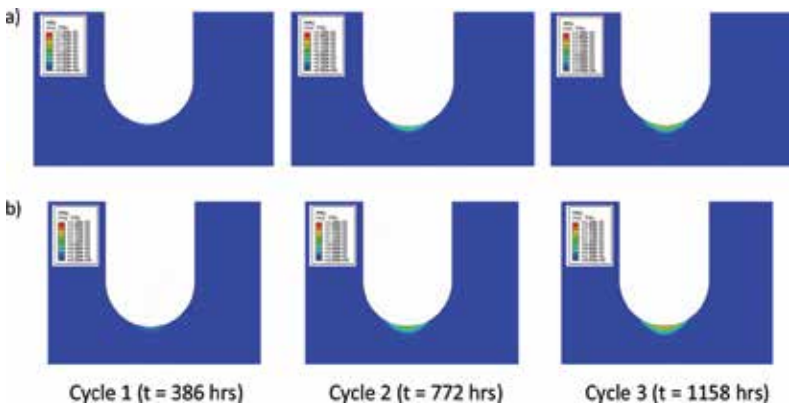

Figure 6. Equivalent plastic strain distribution in heat grooves for: (a) full multiple cycle and (b) simplified elastic-plastic cycle.

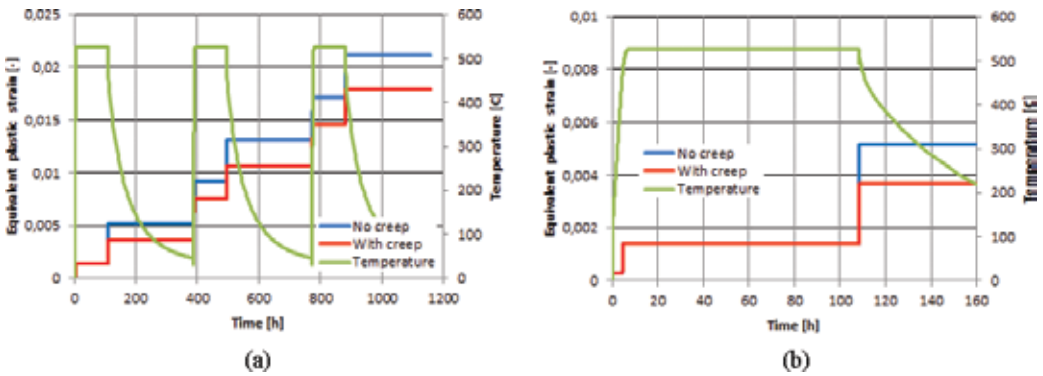

Figure 7. Temperature variation and equivalent plastic strain accumulation in heat groove with and without prior creep: (a) in 3 cycles and (b) in 1 cycle.

the beginning of shutdown phase that started with different stress distributions in the groove computed with and without creep. Creep relaxation has thus a positive effect on the fatigue damage measured by the plastic strain accumulation. By neglecting the viscous effects in the steady-state operation, the plastic strains are overpredicted, and consequently the calculated fatigue damage will be too high as compared with the results of the visco-elastic-plastic model.

Figure 8 presents the evolution of plastic strain components in the groove bottom over 3 cycles. The strain state is very close to plane strain, with the radial and axial components having the same value and opposite sign, and the circumferential plastic strain being close to zero. It is interesting to see that initially the radial and axial strain components have different signs during operation and natural cooling but after the second cycle the radial strain becomes positive and the axial component remains negative.

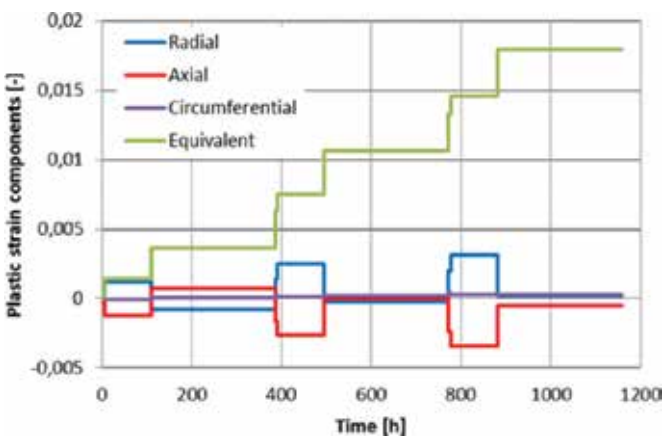

Figure 8. Plastic strain accumulation in heat groove for full multiple cycle.

5.3. Effect of plastic deformation on creep strain accumulation

Similar to the effect of creep deformation on plastic strain accumulation, the effect of plastic deformation on creep strain accumulation can be expected. In order to investigate this phenomenon, different simplified cycles were adopted for analysis, namely simplified multiple viscous cycle 1 (**Figure 2b**) and simplified multiple viscous cycle 2 (**Figure 2c**). The duration of one full cycle was the same as in previous analyses, i.e. 386 h, but creep calculations with viscous model enabled were performed for steady-state phase lasting 100 h. This resulted in the total time of creep strain accumulation in 3 cycles equal 300 h.

The comparison of equivalent creep strain distribution after each cycle for all types of analysis is shown in **Figure 9**. Similar to the behavior of the plastic zone, the zone of creep deformation increases in size during cycling and its shape remains almost unchanged. But this time, the applied models predict visibly different development rate of the creep zone. The largest zone size and equivalent creep strain are obtained for the full multiple cycle (**Figure 9a**), which takes into account both viscous and plastic effects in each individual start-stop cycle (**Figure 2a**). A smaller creep zone size and equivalent creep strain are obtained for the simplified multiple viscous cycle 1 (**Figure 9b**), which includes viscous effects in each individual start-stop cycle but neglects plastic strain development in cycles 2 and 3 (**Figure 2b**). The creep strain zone is nearly invisible in case of the simplified multiple viscous cycle 2, which completely neglects plastic effects.

The differences in creep strain accumulation are better seen from **Figure 10a**, which shows development of the maximum equivalent creep strain at the groove bottom. After the first start-stop cycle, a higher difference in the creep strain reaching 150% is found between the

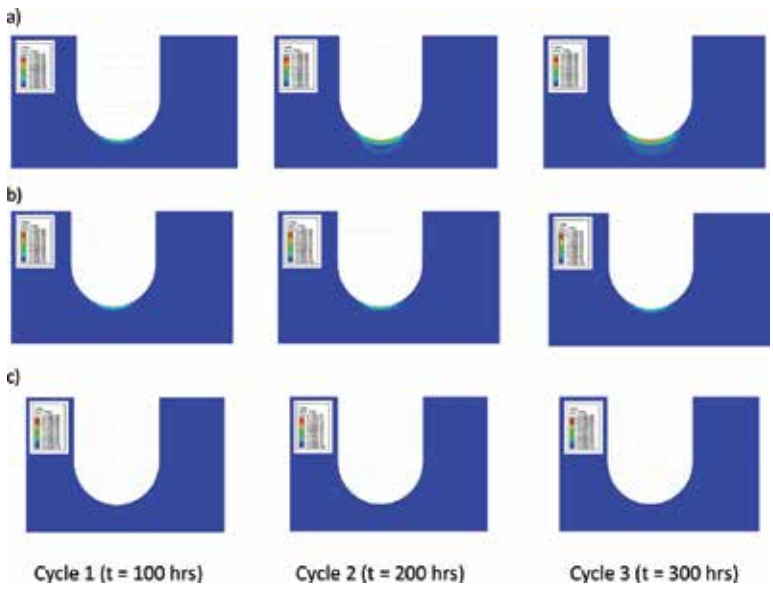

Figure 9. Equivalent creep strain distribution in heat grooves for: (a) full multiple cycle, (b) simplified multiple viscous cycle 1, and (c) simplified multiple viscous cycle 2.

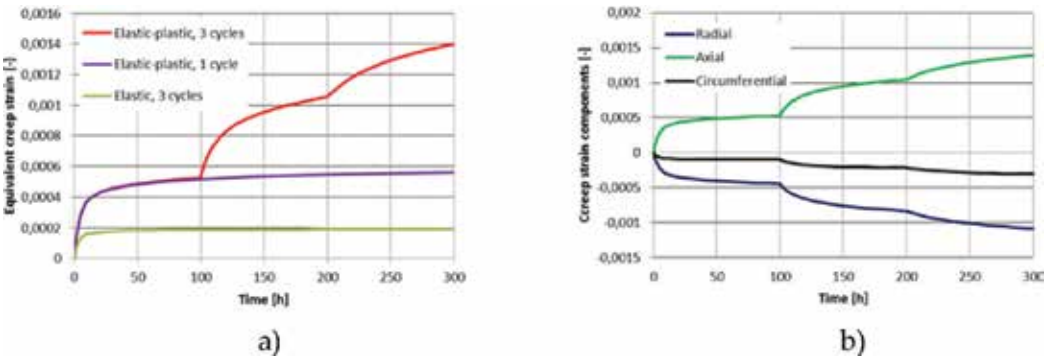

Figure 10. Creep strain accumulation in heat grooves: (a) equivalent creep strain for different cycles and (b) creep strain components for full multiple cycle.

elastic and elastic-plastic models (cycles with and without plasticity). After the second cycle, the deviation increases, but a significant difference in creep strain reaching 100% occurs between the elastic-plastic models, i.e. full multiple cycle and simplified multiple viscous cycle 1. This is due to neglecting the plastic strain development in cycles 2 and 3. It follows from the evolution of the equivalent creep strains that the secondary creep regime is reached already after 100 h (the first cycle) for all simplified modeling approaches, while for the full multiple cycle the heat grooves are still in the primary creep regime after 300 h (third cycle). This qualitative difference is very important from the point of view of creep damage, which on one hand depends on the accumulated creep strain and on the other hand is a function of the failure strain (creep ductility) primarily depending on the creep strain rate, which is very different in the three creep regimes.

The evolution in time of the creep strain components at the groove is shown in **Figure 10b**. The creep strain state at the bottom of the groove is three dimensional with all three components having comparable values. The radial and circumferential strain components are negative, and the axial component is positive and has the largest absolute value. In contrast to the plastic strain components, all the creep strain components increase continuously with continuous slope within the cycle and discontinuous slope change between two subsequent cycles.

6. Summary

Creep-fatigue damage development in a steam turbine rotor in cyclic operation was numerically investigated using different material models and cycle modeling approaches. Creep strain was adopted as a creep damage parameter, and plastic strain was adopted as a damage parameter for fatigue. Four different operation cycles were defined and used in numerical simulations to examine the effect of various simplifications on the creep fatigue-damage prediction. The analyzed multiple cycles included different combinations of material models and number of individual cycles used in damage calculations during steady-state and transient conditions.

Based on the performed investigations, the following observations can be formulated:

- Prior creep deformation affects the plastic strain accumulation by reducing the plastic strain as compared with no creep conditions. The difference in the accumulated plastic strains increases over subsequent cycles.
- Local plastic deformation in heat grooves accelerates the creep strain accumulation during the cycle and over subsequent cycles.
- Neglecting the creep overestimates the fatigue damage (plastic strain) generated during cycling, and neglecting the plasticity in cyclic duty underestimates the creep damage (creep strain) in stationary conditions.

It was shown by numerical simulations that significant inaccuracies in creep-fatigue damage predictions, reaching an order of magnitude in deviation of inelastic strains already after first few cycles, cannot be excluded when simplified models are used. It is thus concluded that full consideration of creep-fatigue damage at real operating conditions requires appropriate modeling of stress/strain histories using visco-elastic–plastic material models. Lifetime assessment studies employing such methodologies ensure the highest possible accuracy of life predictions and optimal decisions regarding units' future operation.

Author details

Mariusz Banaszkiewicz

Address all correspondence to: mbanaszkiewicz@imp.gda.pl

The Szewalski Institute of Fluid-Flow Machinery Polish Academy of Sciences, Gdańsk, Poland

References

[1] Colombo F. Service-Like Thermo-Mechanical Fatigue Characteristic of 1CrMoV Rotor Steel Creep-Fatigue [Dissertation]. Swiss Federal Institute of Technology: Zurich; 2007. 100 p

[2] Viswanathan R. Damage Mechanisms and Life Assessment of High-Temperature Components. ASM International: Ohio; 1989. 497 p

[3] Leyzerovich AS. Steam Turbines for Modern Fossil-Fuel Power Plants. Lilburn: The Fairmont Press Inc.; 2008. 537 p

[4] Banaszkiewicz M. Multilevel approach to lifetime assessment of steam turbines. International Journal of Fatigue. 2015;**73**:39-47

[5] Banaszkiewicz M, Bzymek G, Radulski W. Management and optimization of a steam turbine life by using an on-line monitoring system. Power Engineering. 2015;**8**:519-524

[6] Helbig K, Banaszkiewicz M, Mohr W. Advanced lifetime assessment and stress control of steam turbines. In: PowerGen Europe; June 2016; Milan

[7] Vogt J, Schaaf T, Helbig K. Optimizing lifetime consumption and increasing flexibility using enhanced lifetime assessment methods with automated stress calculation from long-term operation data. In: Proceedings of the ASME Turbo Expo 2013; 3–7 June 2013; San Antonio

[8] Helbig K. Gas turbine plants in the grid dominated by solar and wind energy. In: PowerGen Europe; June 2015; Amsterdam

[9] Schaaf T, Mohr W, Helbig K. Flexibility improvement of steam turbines for conventional and CCPPs. In: PowerGen Europe; 3–6 July 2014; Vienna

[10] Dinh C, Marriner B, Tadros R, Kim SY, Farineau T. Design and Operation of Large Fossil-Fueled Steam Turbines in Cyclic Duty. GE Technical Paper GER4933. July 2016

[11] Chmielniak T, Kosman G. Thermal Loads of Steam Turbines. Warsaw: WNT; 1990

[12] Zienkiewicz OC, Taylor RL, Zhu JZ. The Finite Element Method: It's Basis and Fundamentals. Elsevier Butterworth-Heinemann: Burlington; 2005. 733 p

[13] Hetnarski RB, Eslami MR. Thermal Stresses—Advanced Theory and Applications. Springer; 2009. 559 p

[14] Banaszkiewicz M. Online monitoring and control of thermal stresses in steam turbine rotors. Applied Thermal Engineering. 2016;**94**:763-776

[15] Badur J, Ziółkowski P, Sławiński D, Kornet S. An approach for estimation of Water Wall degradation within pulverized-coal boilers. Energy. 2015;**92**:142-152

[16] Banaś K, Badur J. Influence of strength differential effect on material effort of a turbine guide vane based on a thermoelastoplastic analysis. Journal of Thermal Stresses. 2017;**40**(11):1368-1385

[17] Badur J, Ziółkowski P, Kornet S, Stajnke M, Bryk M, Banaś K, Ziółkowski PJ. The effort of the steam turbine caused by a flood wave load. In: AIP Conference Proceedings; 2017

[18] Badur J, Ziółkowski P, Zakrzewski W, Sławiński D, Kornet S, Kowalczyk T, Hernet J, Piotrowski R, Felicjancik J, Ziółkowski PJ. An advanced thermal-FSI approach to flow heating/cooling. In: Journal of Physics: Conference Series 530; p. 012039

[19] Orłoś Z. Thermal Stresses. Warsaw: PWN; 1991

[20] Nowacki W. Thermoelasticity. Warsaw: PWN; 1986

[21] Abaqus User's Manual. Dassault Systems; 2008

[22] Kleiber M, Kowalczyk P. Introduction to Non-linear Mechanics of Deformable Bodies. IPPT PAS: Warsaw; 2011. 360 p

[23] Olszak W, Perzyna P, Sawczuk A. Theory of Plasticity. Warsaw: PWN; 1965

[24] Bolton J. A 'characteristic strain' model for creep. Materials at High Temperature. 2008;**25**:101-108

[25] Bolton J. Analysis of structures based on a characteristic-strain model of creep. International Journal of Pressure Vessel and Piping. 2008;**85**:108-116

[26] Norton FH. The Creep of Steel at High Temperatures. London: McGraw-Hill; 1929

[27] Webster GA, Ainsworth RA. High Temperature Component Life Assessment. London: Chapman & Hall; 1994. 327 p

[28] Binda L, Holdsworth SR, Mazza E. The exhaustion of creep ductility in 1CrMoV steel. International Journal of Pressure Vessel and Piping. 2010;**87**:319-325

[29] Holdsworth SR. Creep-Fatigue Failure Diagnosis. Materials. 2015;**8**:7757-7769

[30] Socha G., Dietrich L. Evolution of damage for P91 steel under cyclic load. In: 1–5 September 2014; Zakopane

[31] Holdswoth SR. Creep-fatigue interaction in power plant steels. Materials at High Temperatures. 2011;**28**(3):197-204

[32] ASME. Boiler and Pressure Vessel Code, Section III, Division 1 – Subsection NH, Class 1 Components in Elevated Temperature Service. New York: ASME; 2001

[33] TRD 508, Annex 1: Additional Tests on Components – Methods for the calculation of components having time-dependent design strength values, edition July 1986

[34] RCC-MR, Design and Construction Rules for Mechanical Components of Nuclear Installations; AFCEN: Paris, France, 2007

[35] R5 Panel, Revision 3 (as Amended); An Assessment Procedure for the High Temperature Response of Structures. Barnwood, UK: EDF Energy Nuclear Generation Ltd.; 2003

[36] Banaszkiewicz M. Analysis of rotating components based on a characteristic strain model of creep. Journal of Engineering Materials and Technology. 2016;**138**:031004-1-031004-1

[37] Chmielniak T, Kosman G, Rusin A. Creep of Thermal Turbines Components. Warsaw: WNT; 1990

[38] Banaszkiewicz M. Numerical investigations of crack initiation in impulse steam turbine rotors subjected to thermo-mechanical fatigue. Applied Thermal Engineering [Accepted for publication]

Chapter 5

Ti Microholes Potential for Thermal Power Plants Application Punched by WC/Co Micropunch

Kelvii Wei Guo and Hon Yuen Tam

Additional information is available at the end of the chapter

http://dx.doi.org/10.5772/intechopen.73308

Abstract

The use of microholes is a potential approach to enhance fluid flow and heat exchange within thermal power plants, especially for the turbines. Ascribed to eco environmental competition, micropunching is extremely suitable for the mass production of micro features with friendly eco effects. Therefore, the morphology variation of micropunch and microhole during the punching with WC/Co micropunches was investigated by scanning electron microscopy (SEM), energy dispersive spectrometer (EDS) and confocal laser. Results reveal that due to the optimal joint contribution of WC and Co, the formed microholes satisfy with the practical requirements in the quasi stable period. Moreover, the serious wear of micropunch occurs with the wear loss both of Co and WC when the punching number exceeds 1525. With the further increment in punching numbers, the dominant factors of the wear loss would mainly rely on the easily peeled off WC due to the serious loss of Co. In addition, the microholes can be adequately processed after about 30 min by natural sand grains. The quality of the hole would decrease with further increase in processing time and sand accumulation becomes severe.

Keywords: microhole, thermal power plants, WC/Co, micropunch, morphology

1. Introduction

It is well known that the thermal power plants can be classified by the source of the energy used to generate the steam that it is expanded in the turbine to produce electricity, which are listed as follows classified by heat source: (1) heat sources for fossil fuel power stations: (i) a steam turbine generator and (ii) the natural gas-fired plants. They may use a combustion turbine. To date, a coal-fired power station produces heat by burning coal in a steam boiler. The steam drives a steam turbine coupled to a generator producing electricity. It is well known that the fossil fuel power stations are still currently the dominating plants for generation

of energy production around the world. (2) A nuclear power plant is a steam turbine plant where the steam is generated by a nuclear reactor. Up to now, about 10% of all electric generation worldwide is produced by nuclear power plants. It should be noted that after the Fukushima disaster, all the plants are scheduled to be shut down in a few years, and the rest of the world is very hesitant with respect to what role nuclear energy should have in future energy planning. (3) Geothermal power plants use steam extracted from hot underground rocks. This kind of energy plant only contributes a minor energy output compared with the global demand. (4) Biomass-fueled power plants are fueled with wood pellets, wood chips, straw and waste from the agricultural industry such as sugar cane and nut scale, municipal solid waste, landfill methane or other forms of bio gas. (5) In integrated steel mills, blast furnace exhaust gas is a low cost, although low energy-density, fuel. This recycled gas is available to produce about 60% of the total electricity consumption. (6) Waste heat from industrial processes is occasionally concentrated enough to use for power generation, usually in a steam boiler and turbine. (7) Solar thermal electric plants use sunlight to boil water and produce steam, which turns the generator. (8) IGCC (integrated gasification combined cycle) with carbon capture and storage (CCS) technology allows coal to be used to generate power as cleanly as natural gas [1, 2].

In most of the countries, thermal power plants are playing an important role in the energy production. Therefore, the research work should be taken enough attention toward the optimization of these power plants. In the developing countries, energy supplies are less secure because of its costlier price. Indeed, there is a need to reconsider lowest cost energy options and the relevant techniques. Since, from an energy performance point of view, first law analysis has been found to be insufficient. So, in thermodynamic analysis of various thermal processes and plant systems, exergy analysis is getting its own importance. It is well known that the total conversion of heat into work is not possible.

Consequently, that part which is available for conversion is termed as exergy. It is a property associated with the state of system and environment, nowadays a useful tool to differentiate between internal irreversibility and energy losses in a process [2]. Thermal power plant performance can be evaluated through energetic performance criteria, which are electrical power and thermal efficiency. In recent decades, exergy analysis of plant has been found as a useful method in the design, evaluation, optimization and improvement of thermal power plants [3–5]. Exergy analysis helps in finding the losses taking place in a system. By this method, energy conversion at different points, various component efficiencies and points of largest losses are easily obtainable and hence it helps in taking necessary action to decrease them [6, 7].

Some researchers have contributed review paper on exergy analysis, which helps the young researchers to get in touch with the previous year's problems [8]. In power plants, insights have been provided into various energy and exergy efficiencies which are helpful for design engineers [9, 10]. As a result, improvement in thermal performance of power generation units and consuming devices can be achieved significantly by combining exergy analyses with the related techniques upgraded.

In recent years, microtechnology has become one of the key disciplines with a significant effect on the development of new products and production technologies [11–14].

It is well known that microtechnology describes the technological approach, directed to the miniaturization of components and systems, down to micrometer scale. Microtechnological components, such as distributed holes, bear the potential to provide further functionality, for example, enhancing fluid flow and heat exchange within thermal power plants, especially for the turbine blades [15–18].

Up to now, the ever increasing demand for smaller, higher quality and lower priced products from almost all fields of industry, household equipment and entertainment electronics involves the optimisation of already existing and the development of new manufacturing methods which are tailor-made for the micro systems technique with higher precision [19, 20].

However, these kinds of micro devices are mainly fabricated by using micromachining technique, and fabrication technology with stable and low cost as one of the important issues [11, 12, 14, 19].

Therefore, the microholes formed by micropunching at low cost and in large quantities, applied for thermal power plants application and micro-parts fabrication have been researched. This research aims at investigating the wear characteristics of micropunch (150 μm in diameter) and the morphology variation of microholes formed by punching pure titanium (Ti) in various processing periods to overcome current problems in the micro-metal-forming technology. In the long run, this research can lead to making microholes distributed in the thermal power materials (both non-metals and metals) at low cost and in large quantities with this eco-friendly technique.

2. Experimental materials and procedures

2.1. Experimental material

Micropunch with 75% volume fraction WC particle and 25% volume fraction Co particle of 50 μm mean size, 150 μm in diameter, is shown in **Figure 1**. **Figure 2** shows the surface texture of micropunch. Pure titanium sheet with 200 μm in thickness was used as the substrate.

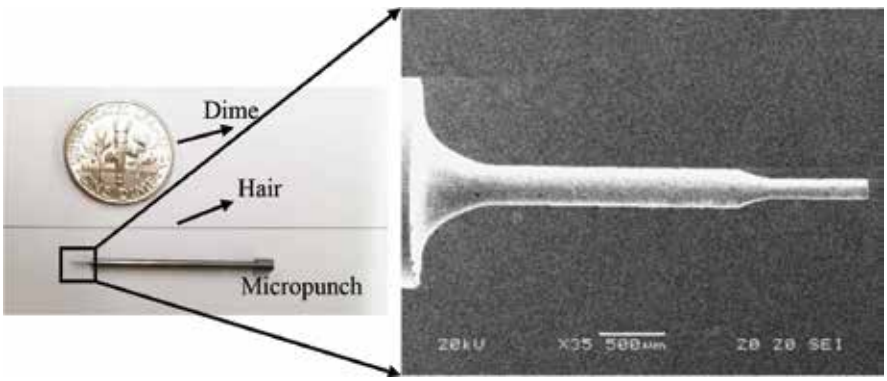

Figure 1. Profile of micropunch.

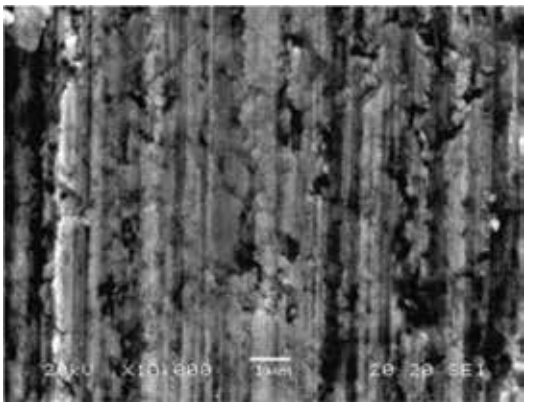

Figure 2. Surface texture of micropunch.

2.2. Experimental procedures

In order to clean the contaminants in the prepared pure titanium sheet, it was carefully washed by acetone and pure ethyl alcohol before putting into the microdie. After that, the microprocessing machine MP50 (made in Japan) was taken to punch the titanium sheet with 20 pulses per minute, and feedrate of 2 mm.

The wear of the micropunch and the variation of the morphology of microholes in different processing periods were investigated using confocal microscopy, scanning electron microscopy (SEM), energy dispersive spectrometer (EDS) and confocal laser.

3. Results and discussion

3.1. Initial wear characteristic of micropunch

The relationship between the wear loss of micropunch and punching numbers is shown in **Figure 3**. It illustrates that the weight of micropunch (each for five times) has an obvious decrease with the increment of punching number in the initial. Its corresponding surface texture is expressed in **Figure 4**. It depicts that the particles distributed more uniformly than that of parent material (cf. **Figures 2** and **4**).

According to **Figures 3** and **4**, it shows that the wear of micropunch in the initial increases significantly, and WC particles cannot be easily observed. Consequently, the dominant factor of the wear loss in the initial period is mainly due to Co. The morphology of the formed microhole is expressed in **Figure 5**. Some substrate debris is distributed sparsely in the backside as shown in **Figure 5b**, and its EDS results are illustrated in **Figure 6**.

3.2. Quasi stable wear characteristic of micropunch

With the increment of punching numbers, the phenomena of the initial distinct wear of micropunch disappears, the wear loss of the micropunch becomes relatively stable with a little variation

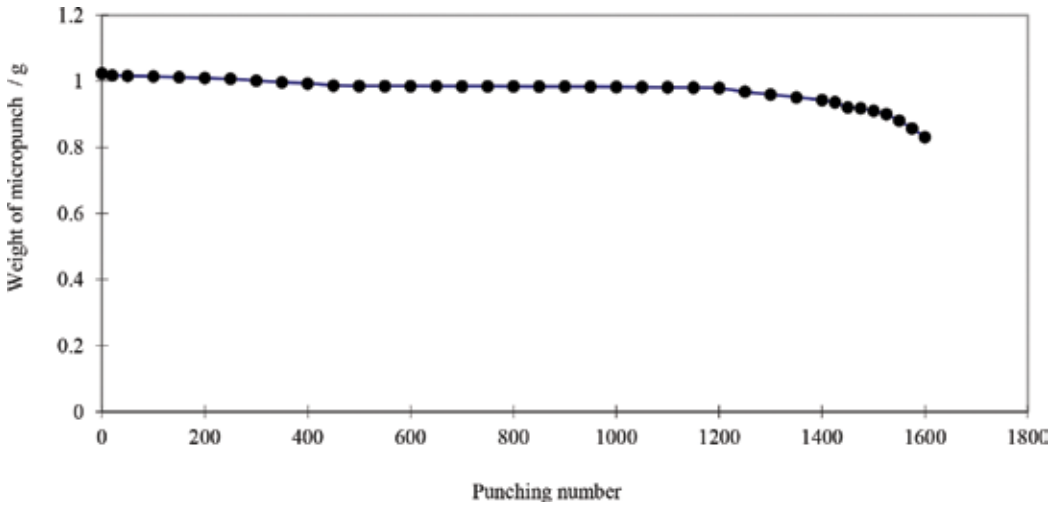

Figure 3. Relationship between wear loss of micropunch and punching numbers.

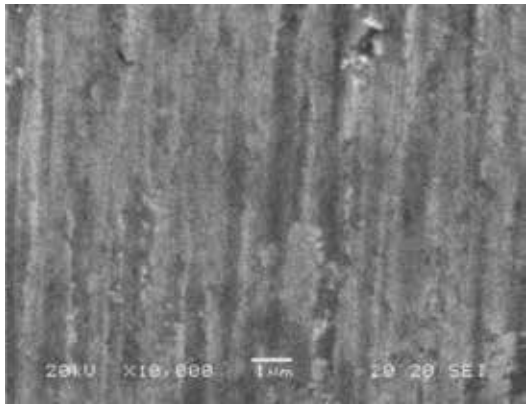

Figure 4. Surface texture of micropunch in the initial condition (punching number lower than 500).

as depicted in **Figure 3**, particularly for punching number from 500 to 1200. The surface texture of micropunch is shown in **Figure 7** correspondingly. It expresses small pieces of WC particles on the surface. Meanwhile, WC particles distribute uniformly on the micropunch surface.

The morphologies of the formed microhole are shown in **Figure 8**. It expresses that although some substrate debris still distribute in the backside (**Figure 8b**), the quality of the quasi stable-period-microhole is definitely superior to the initial period (compared **Figure 5** with **Figure 8**). It illustrates that because of the joint contribution of WC and Co, the wear loss of micropunch in the quasi stable period is little.

3.3. Severe wear characteristic of micropunch

The surface texture of micropunch with punching number over 1525 is shown in **Figure 9**. It shows that large amounts of WC particles distributes on the micropunch surface because of

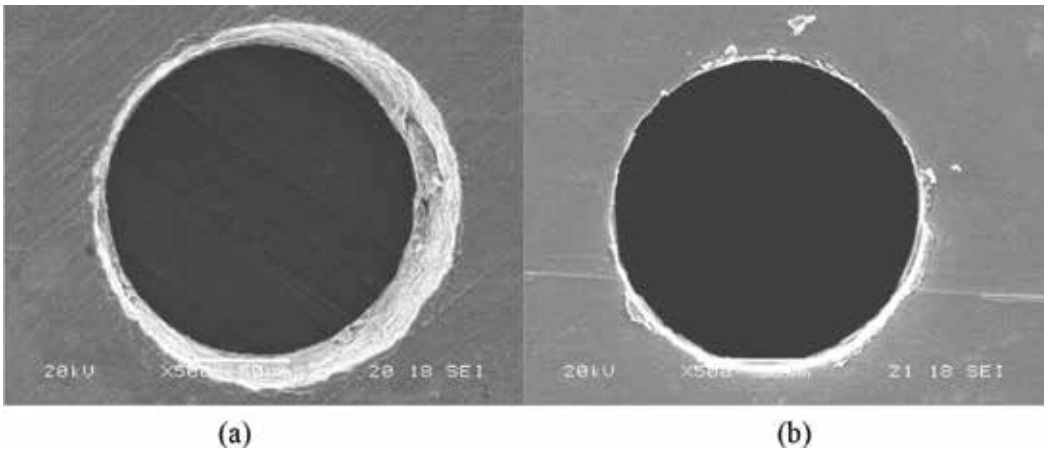

Figure 5. Morphology of microhole. (a) Front side, (b) back side.

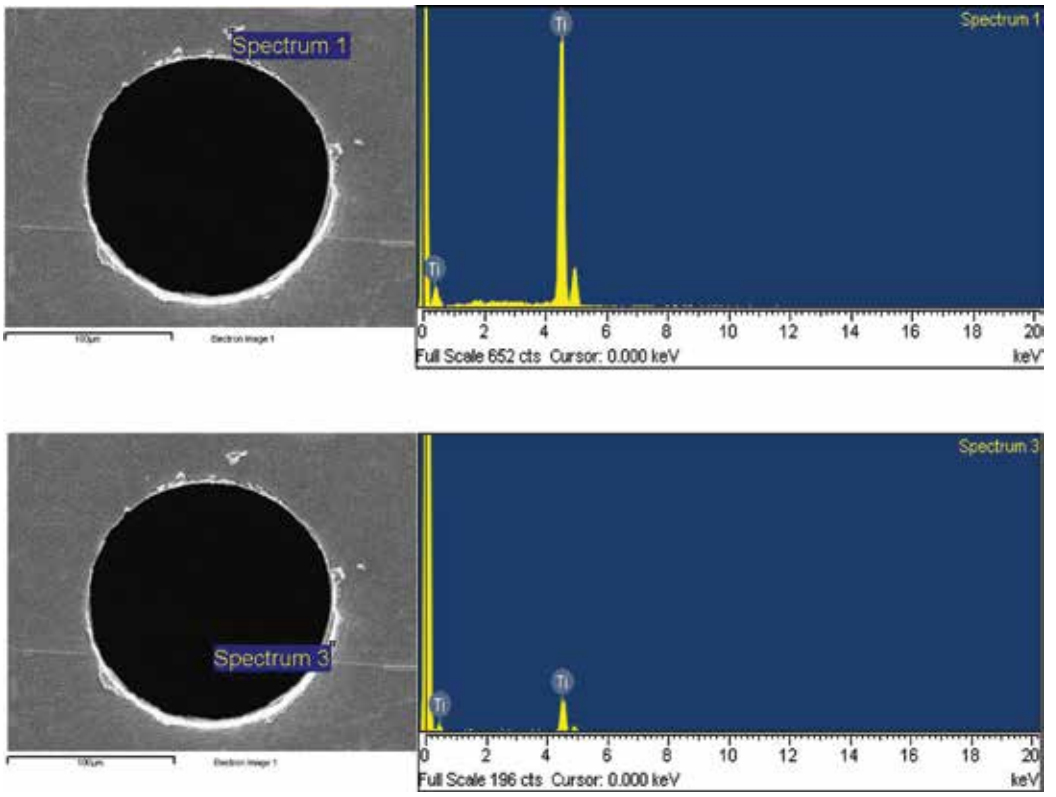

Figure 6. EDS results of debris in the backside.

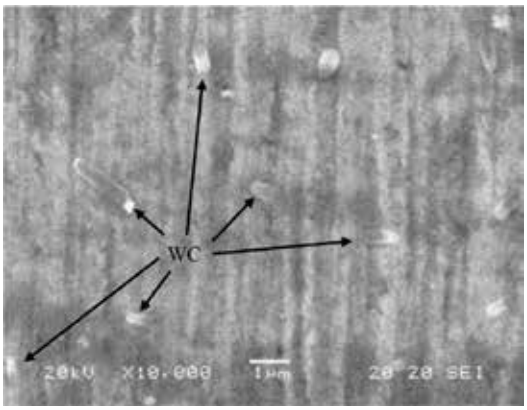

Figure 7. Surface texture of micropunch with punching number between 500 and 1200.

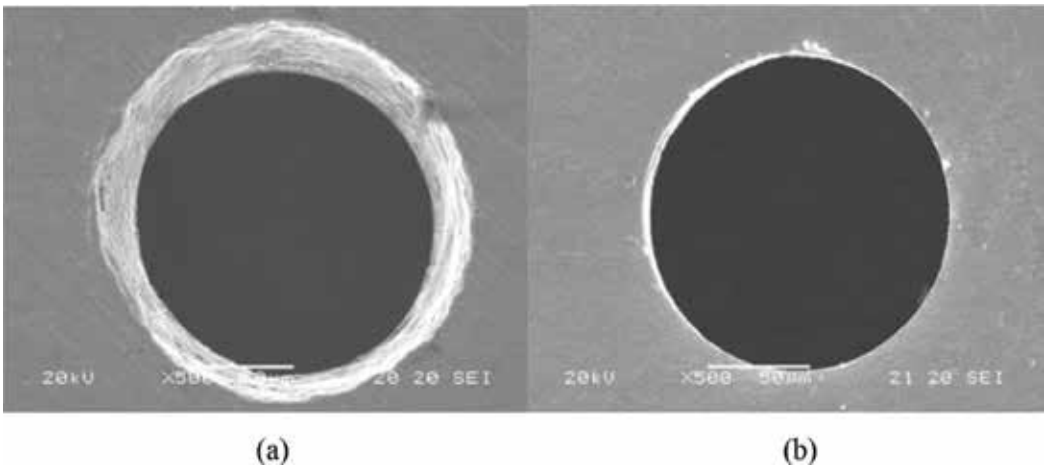

Figure 8. Morphology of microhole. (a) Front side, (b) back side.

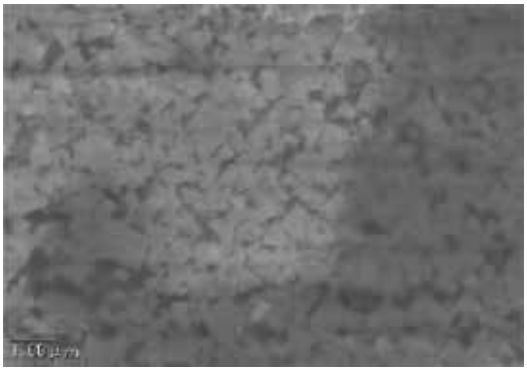

Figure 9. Surface texture of micropunch in the severe wear condition.

serious wear loss of Co, which matches well with **Figure 3**. As a result, the wear of micropunch increases distinctly (**Figure 3**). Furthermore, with the punching numbers increasing further, the dominant factors of the wear loss would mainly rely on WC (which is easily peeled off during the micropunching) as shown in **Figure 9**. Meanwhile, the quality of the machined microhole decreases distinctly (cf. **Figures 5**, **8**, **10** and **11**). It illustrates that a large amount of micropunch materials are peeled off and adhered to the Ti substrate. At the same time, the substrate material could not be punched successfully and it would stick to the substrate. Also, with the effect of feedrate, the unsuccessfully removed materials would be sheared and form the larger debris as shown in **Figure 11**.

3.4. Profile of the microhole punched by micropunch

The diameter of the punched microhole by micropunch was measured by LEXT confocal laser-OLS3000 as shown in **Figure 12**. Its corresponding results (each for five times) are shown in

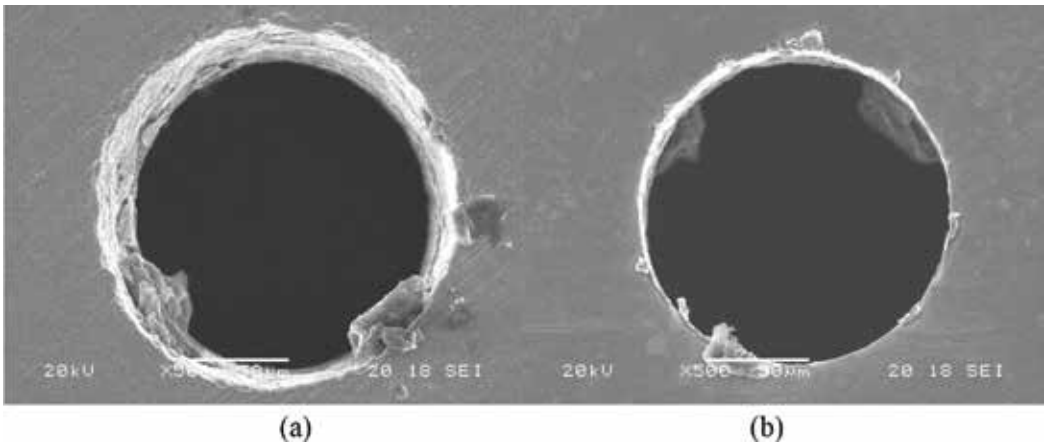

Figure 10. Morphology of microhole in the severe wear condition. (a) Front side, (b) back side.

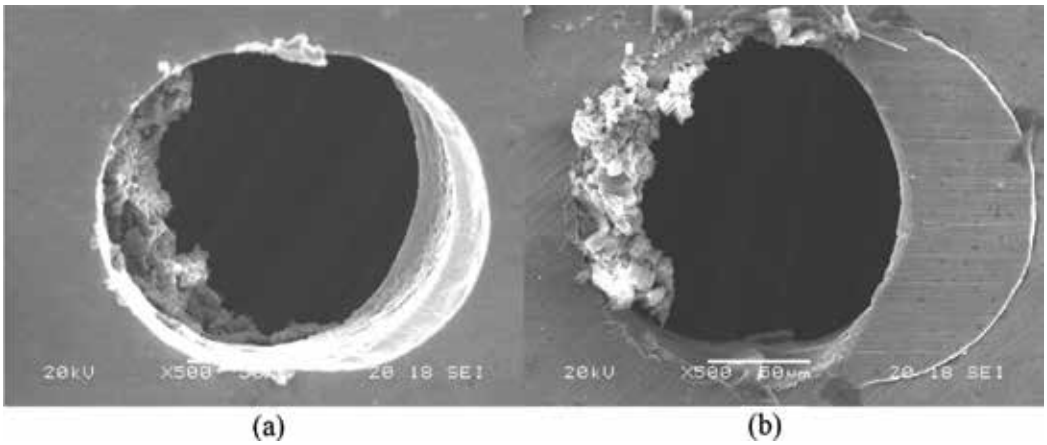

Figure 11. Morphology of microhole in the intensively severe wear condition. (a) Front side, (b) back side.

Figure 13. Compared with **Figure 3**, it indicates that the diameter of microhole changes in the different micropunching periods. At the beginning of the micropunching, the obvious decrement of the diameter of microhole varies with the punching number increasing, which surely matches well with results expressed in **Figure 3**. The attractive results are addressed with the relatively stable diameter of microhole when the micropunching number varies from 500 to 1200. When the punching number increases further, the obvious decrement of the diameter of microhole becomes more and more clear on account of the serious Co loss, especially for the punching number over 1525 as depicted in **Figure 13**. As a result, in the severe wear period of micropunching, due to the serious loss of bonding material Co, the wear of micropunch mainly relies on the easily peeled off WC particles. Simultaneously, because the temperature of the micropunch increases with the increment of the punching number, WC particles are more easily detached off from the micropunch. Consequently, the wear loss of the micropunch becomes more intensive. Furthermore, if the pulses per minute increases, the wear of micropunch will drastically lose. In order to improve the quality of the micropunch, besides the abovementioned, the microstructure of micropunch should be considered further with the composition of the micropunch, especially for the distribution of WC and Co particles.

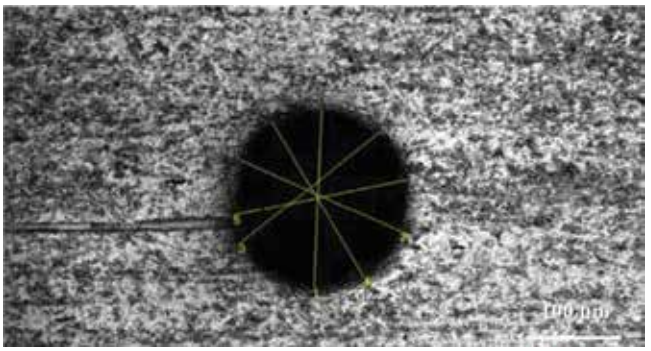

Figure 12. Profile of microhole punched by micropunch measured by OLS3000.

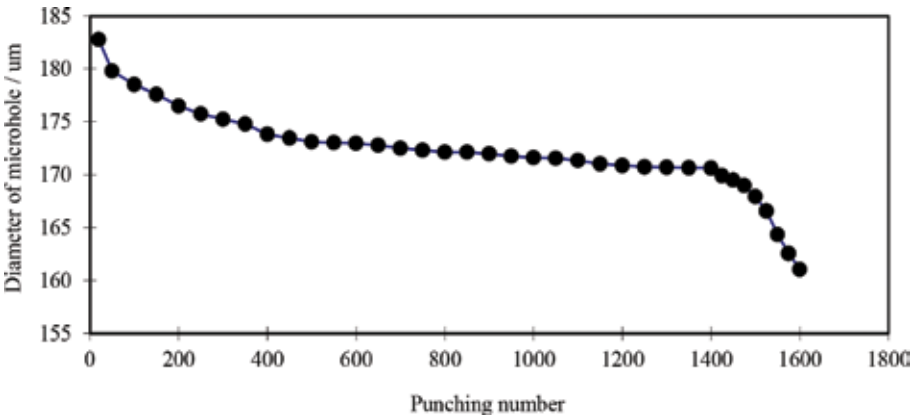

Figure 13. Relationship between diameter of microhole and punching number.

4. Post-treatment for microholes by natural sand grains

Features of microholes (such as **Figures 5** and **8**) in the micropunching include debris (for example, shear marks and burrs). Because of the combination of shear and ductile fracture in the micropunching, the debris produced. Moreover, the property of the processing materials is also one of the crucial effective influence factors on the final features of the microhole. In the meantime, the uniformity of the clearance can affect the microhole features during the micropunching (cf. **Figures 5**, **8**, **10** and **11**). The debris can hinder the normal functionality of micro features and prevent the proper assembly of micro components to form micro systems. Therefore, the microholes shall be post treated to improve its finishing.

Figure 14 shows the post treated microhole realized with the agitation of abrasive grains through planetary stirring, where natural sand was used as the abrasive due to its environmental

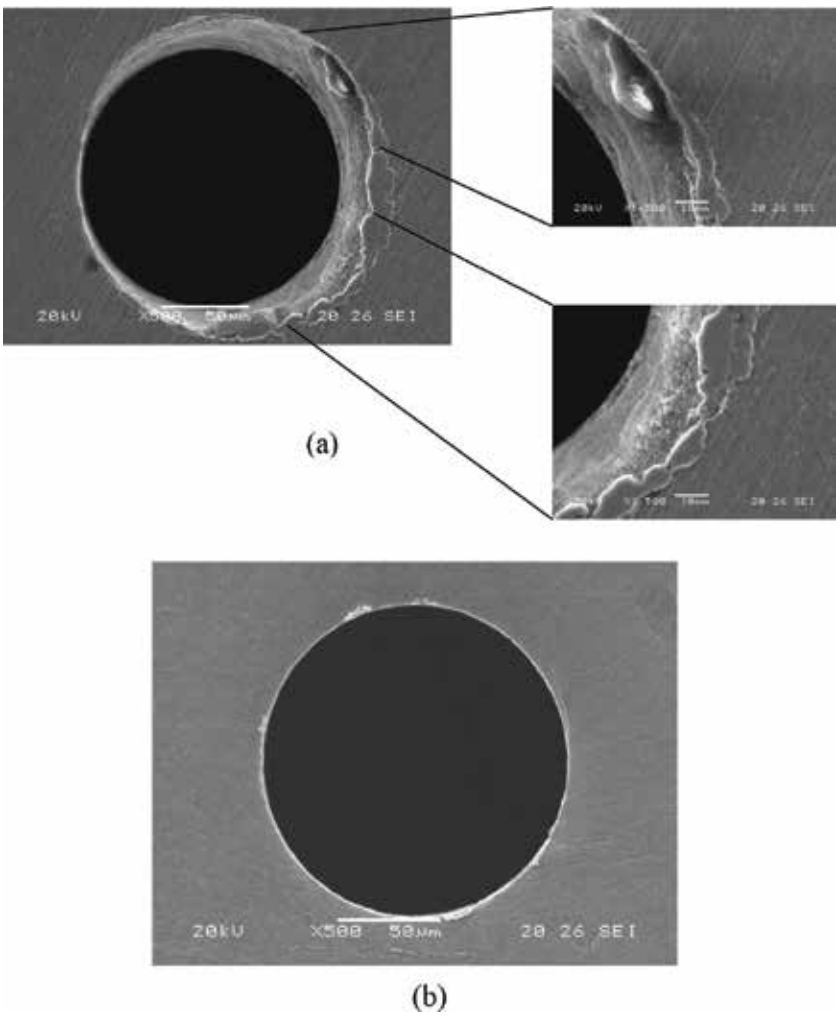

Figure 14. Morphology of a microhole after 20 min processing. (a) Front side, (b) back side.

friendliness. It expresses the results of a 20 min processing microhole. The hole is basically free from loosely attached debris. Burrs at the back side edge are further lowered. Those flattened fragments are slimmer than before. More aggregation of the microscopic grains is observed, both the fragment regions and the edge regions (**Figure 14a**, insets). Their sizes range from the micron to sub-micron. Continued aggregation might possibly be on account of van der Waals or inter-molecular forces.

With further increment of the processing time, the quality of the hole continues to improve. **Figure 15** reveals that the burrs in the back side edge are no longer existed, except for some small isolated pieces (**Figure 15b**, inset). Burrs are protrusions from the edge. Their bonding with the substrate is much stronger than that of the re-attached debris. Tiny burrs are particularly hard to be removed. It is well known that the impact energy from a grain of sand depends on the grain size besides its velocity. Those burrs could not be effectively cleaned by the impact from smaller grains. Yet, the chance that tiny burrs are impacted by the larger sand grains is relatively low.

The fragment terraces on the front side become very thin. As a result, they are noticeable mainly under higher magnification (**Figure 15a**, right inset). In addition, more grains are gathered around the edge of the hole as well as stuck to the inner wall of the hole through attraction forces (**Figure 15a**, left inset).

The quality of the holes cannot improve with further processing. Spontaneously, more sand aggregates after 40 min (**Figure 16**). The attachment of sand grains to the edge regions and inner wall could be visible from the back side as well as from the front side.

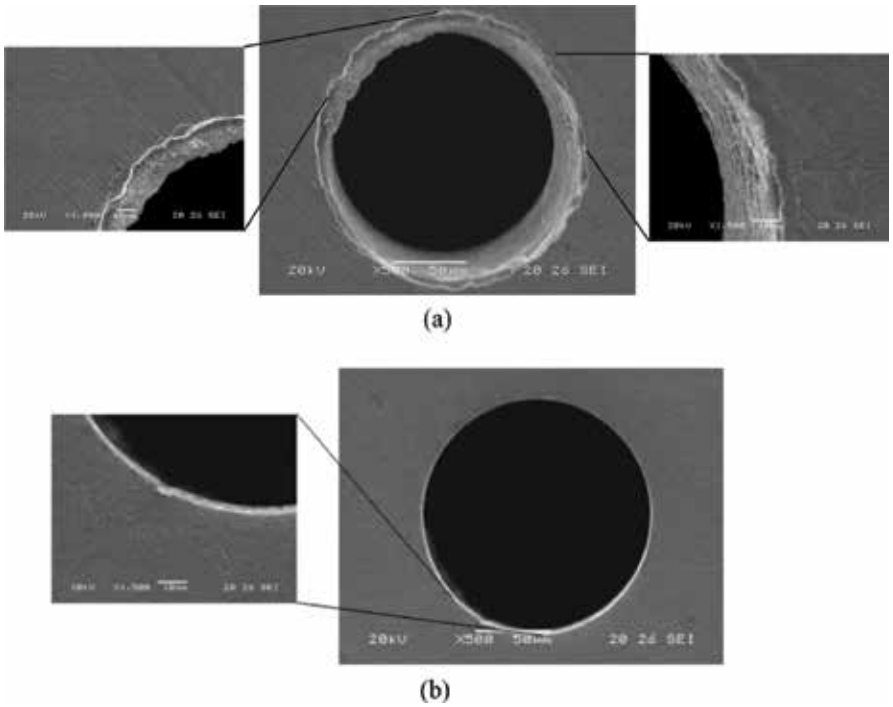

Figure 15. Morphology of a microhole after 30 min processing. (a) Front side, (b) back side.

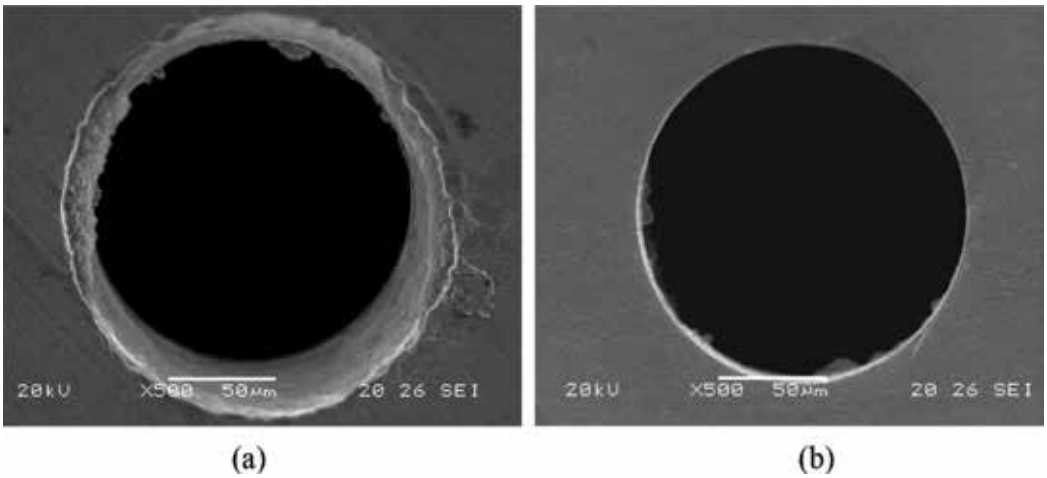

Figure 16. Morphology of a microhole after 40 min processing. (a) Front side, (b) back side.

A band of jagged foil material is detected around the front surface near the edge of the hole. It is mainly produced as substrate material breaks from the punch when it is pulled back from the hole. It cannot be clearly detected before because (1) the feature size is relatively small compared with those fragments detected at earlier times and (2) parts of the band are rolled back against the surface of the substrate material. Apparently sand abrasion could only reduce the width of the band to a few microns. Occasionally, parts of the band are bent toward the microhole. On account of the support of sand gathered underneath, it is unlikely that their posture could be reversed in subsequent processing.

5. Conclusion

The wear characteristic of the WC/Co micropunch used for micromachining microhole potential for thermal power plants application had been researched. It shows that the wear of micropunch increases significantly in the initial and the dominant factor of the wear loss mainly relies on Co. With the punching number increasing, the quasi stable wear of WC/Co micropunch varies with a little wear loss. However, when the punching number exceeds 1525, the serious wear loss of Co and WC of micropunch takes place. Moreover, with the increment of the punching numbers further, the dominant factor of the wear loss would mainly rely on the easily peeled off WC. Meanwhile, the quality of microhole decreases intensively. In addition, the microholes can be adequately processed after about 30 min by natural sand grains. The quality of the hole would decrease with further increase in processing time and sand accumulation becomes severe and no further improvement is observed.

Acknowledgements

The work is supported by the Strategic Research Grant (SRG) from City University of Hong Kong (Grant No.: 7004860).

Author details

Kelvii Wei Guo* and Hon Yuen Tam

*Address all correspondence to: kelviiguo@yahoo.com

Department of Mechanical and Biomedical Engineering, City University of Hong Kong, Hong Kong

References

[1] Bogmansa CWJ, Dijkemab GPJ, van Vliet MTH. Adaptation of thermal power plants: The (ir)relevance of climate (change) information. Energy Economics. 2017;**62**:1-18

[2] Utlu Z, Hepbasli A. A review on analyzing and evaluating the energy utilization efficiency of countries. Renewable & Sustainable Energy Reviews. 2007;**11**(1):1-29

[3] Wang LG, Voll P, Lampe M, Yang YP, Bardow A. Superstructure-free synthesis and optimization of thermal power plants. Energy. 2015;**91**:700-711

[4] Alobaid F, Mertens N, Starkloff R, Lanz T, Heinze C, Epple B. Progress in dynamic simulation of thermal power plants. Progress in Energy and Combustion Science. 2016;**59**: 79-162

[5] Gonzalez-Salazara MA, Kirstena T, Prchlik L. Review of the operational flexibility and emissions of gas- and coal-fired power plants in a future with growing renewables. Renewable and Sustainable Energy Reviews. 2018;**82**:1497-1513

[6] Dincer IY, Cengel Y. Energy, entropy concepts and their roles in thermal engineering. Entropy. 2001;**3**(3):116-149

[7] Rosen MA, Bulucea CA. Using exergy to understand and improve the efficiency of electrical power technologies. Entropy. 2009;**11**(4):820-835

[8] Sciubba E, Wall G. A brief commented history of exergy from the beginnings to 2004. International Journal of Thermodynamics. 2007;**10**(1):1-26

[9] Kanoglu M, Dincer I, Rosen MA. Understanding energy and exergy efficiencies for improved energy management in power plants. Energy Policy. 2007;**35**(7):3967-3978

[10] Verkhivker GP, Kosoy BV. On the exergy analysis of power plants. Energy Conversion and Management. 2001;**42**(18):2053-2059

[11] Madou MJ. Microfabrication challenge. Analytical and Bioanalytical Chemistry. 2004; **378**:11-14

[12] Mark JJ. Microfabrication and Nanomanufacturing. Boca Raton, FL: CRC/Taylor & Francis; 2006

[13] Beau V, Chabassier G. Metrology of large optical components for high-power lasers. Microsystems Engineering: Metrology and Inspection III. SPIE. 2003;**4411**:197-203

[14] Fecht HJ, Werner M. The Nano-micro Interface: Bridging the Micro and Nano Worlds. Weinheim: Wiley-VCH; 2004

[15] Horn A, Weichenhain R, Albrecht S, Kreutz EW, Michel J, Niessen M, Kostrykin V, Schulz W, Etzkorn A, Bobzin K, Lugscheider E, Poprawe R. Microholes in zirconia coated Ni-superalloys for transpiration cooling of turbine blades. High-Power Laser Ablation III. SPIE. 2000;**4065**:218-226

[16] Lugscheider E, Bobzin K, Moes M, Lackner K, Poprawe R, Kreutz EW, Willach J. Laser drilled microholes in zirconia coated surfaces using two variants to implement the effusion cooling of first stage turbine blades. Advanced Engineering Materials. 2005;**7**(3):145-152

[17] Kaur N, Kumar M, Sharma SK, Kim DY, Kumar S, Chavan NM, Joshi SV, Singh N, Singh H. Study of mechanical properties and high temperature oxidation behavior of a novel cold-spray Ni-20Cr coating on boiler steels. Applied Surface Science. 2015;**328**:13-25

[18] Moon HW, Yoon YJ, Park JH, Myung BS, Kim DE. Dynamic wetting and boiling characteristics on micro-structured and micro/nano hierarchically structured surfaces. Experimental Thermal and Fluid Science. 2016;**74**:19-26

[19] Knobloch H, Kaminorz Y. MicroNano Integration. Berlin Heidlberg: Springer-Verlag; 2004

[20] Mohamed GH. The MEMS Handbook. Boca Raton, FL: CRC/Taylor & Francis; 2006

Chapter 6

A Review on Supercritical Fluidization

Youjun Lu, Liping Wei and Jikai Huang

Additional information is available at the end of the chapter

http://dx.doi.org/10.5772/intechopen.68180

Abstract

Supercritical water fluidized bed (SCWFB) has been used to gasify biomass, coal and solid waste to produce gas fuel. Supercritical carbon dioxide fluidized bed ($SCCO_2FB$) was applied in the coating industry. Both the two fluidized bed treats the supercritical fluids as fluidization medium. The fluidization behaviours of particles in the supercritical fluids are quite important issues for achieving the basic two phase flow pattern. Few research institutions have conducted experimental and numerical investigations on the fluidization in supercritical conditions. The authors try to establish a comprehensive insight of fluid dynamics of the supercritical fluidized bed. For the SCWFB, the fluidization transitions of fixed bed, homogeneous bed expansion and bubbling were demarcated by discrimination number D_n. A flow pattern map of Reynolds number vs. Archimedes number was available for describing the flow patterns and their boundaries of the $SCCO_2FB$. Ergun equation was acceptable for calculating the fixed bed pressure drop for both SCWFB and $SCCO_2FB$. Wei and Lu correlations of the minimum fluidization velocity, minimum bubbling velocity and homogeneous bed expansion rate are suggested to design the SCWFB. Wen and Yu equation of the minimum fluidization velocity, Vogt et al. correlation of the homogeneous bed expansion rate and their method for determining the minimum bubbling velocity, Nakajima et al. equation of transition velocity, and Bi and Fan correlation of turbulent velocity were recommended to calculate $SSCO_2FB$.

Keywords: supercritical fluids, fluidized bed, flow pattern, simulation, experiment

1. Introduction

Supercritical fluidized bed fluidizes solids with supercritical fluids. The supercritical fluids is the fluid phase, and the solid particles including silica sand, biomass, coal or some coating particles are used in specific applications. Normally, supercritical fluidized bed can be divided into two types according the different supercritical fluids: supercritical water (SCW) and supercritical

carbon dioxide ($SCCO_2$). The critical point of SCW and $SCCO_2$ is T_c = 374°C and P_C = 22.1 MPa, and T_c = 31.26°C, P_C = 7.36 MPa, respectively. The properties including density, viscosity, conductivity, and specific heat capacity vary with operating temperature and pressure. The properties of water are calculated by ISAWP-IF97 equations based on the operating temperature and pressure [1]. The drastic and fast variation of property under temperatures near the pseudo-critical temperature greatly affects the multiphase flow and heat transfer processes [2, 3].

1.1. Applications of supercritical fluidized bed

The supercritical water fluidized bed (SCWFB) has been used for gasifying biomass and coal for hydrogen production. The concept of SCWFB reactor was proposed first by Matsumura and Minowa [4]. In 2008, State Key Laboratory of Multiphase Flow in Power Engineering (SKLMF) of Xi'an Jiaotong University developed a SCWFB reactor for hydrogen production by gasifying wet biomass [5]. The reactor could avoid plugging, increase the hydrogen yield and improve gasification efficiency. Then, SKLMF successfully applied the SCW fluidized bed reactor to gasify coal and established pilot plant for gasification of biomass or coal [6]. In addition, the water fluidized bed operating in high pressure and temperature is a promising reactor for other high temperature water reactions to produce gas or liquid fuels.

The $SCCO_2$ is treated as a solvent and fluidization medium in the fluidized bed. Coating some inert substrate or pharmaceutical particle within the supercritical carbon dioxide fluidized bed ($SCCO_2$FB) can help to improve the material performance or control the release processes of the active substance. The $SCCO_2$FB coating processes have many advantages: narrow particle size distribution, simple process step, simple solvents, moderate temperatures, and easily controlling the particle fluidizations. A further advantage is that they offer control over solid state properties, producing either amorphous or crystalline material and sometimes polymorphs [7].

1.2. Challenges of supercritical fluidized bed

One of the challenges for industrial applications of chemical technology of the supercritical fluidized bed is the reliability of continuous running of the reactor. Another challenge of the supercritical fluidized bed is enlargement. The inner diameter or size of the fluidized bed are limited to the operating high temperature and high pressure. An increase in the inner diameter leads to larger wall thickness, which may reduce the heat transfer coefficient. The unclear flow pattern and transitions processes may affect the chemical reaction efficiency. The theories of optimal matching of mass, momentum, heat, and chemical reaction are still not perfect.

1.3. Important issues within the supercritical fluidization

The design and operation of the fluidized bed reactor are greatly dependent on the understanding of the two-phase flow characteristics in the fluidized bed. An exact determination of flow patterns in fluidized bed reactor will help to keep the chemical reaction under suitable conditions. The evolution of flow patterns, key design parameters (minimum fluidization

velocity, minimum bubbling velocity, bed expansion rate, etc.) of the supercritical fluidized bed are important issues for perfecting the theory of the supercritical fluidized bed.

Although the experimental investigations of the supercritical fluidized bed are still limited, the flow patterns and their boundaries of the supercritical fluidized bed have been gradually obtained, and the correlations of the minimum fluidization velocity, homogenous bed expansion rate and minimum bubbling velocity, transition velocity and turbulent velocity were also partially proposed based on the experimental data. They can help readers to understand the basic two-phase flow characteristics and achieve a calculation of design work.

2. Experiment and simulation

2.1. Experiment study

Tarmy et al. [8] studied the three-phase flow characteristics of fluidized beds under a pressure of 17 MPa and temperature of 450°C. Jiang et al. [9] investigated bed contraction and expansion in a gas–liquid–solid fluidized bed at pressures from 0.1 to 17.4 MPa and temperatures from 20 to 94°C. Liu et al. [10] operated a CO_2-fluidized bed system from ambient to 9.4 MPa. The fluidized bed is a stainless steel column with 25 mm i.d. and 1.2 m height. They experimentally studied the fluidization of Geldart Group A, B, and D particles in CO_2 under ambient to supercritical conditions. They found that fluidization of the supercritical CO_2 fluidized bed was intermediate between the classical aggregative (gas-solid system) and particulate (liquid-solid system) fluidizations. Marzocchella and Salatino [11] fluidized Geldart Group A and B particles by CO_2 at temperature of 35°C with pressure ranging from 1 to 8 MPa. The fluidization column consisted of a lower section made of a polycarbonate pipe with height of 600 mm and inner diameter of 30 mm and a higher stainless steel upper section with height of 700 mm. The temperature of CO_2 varies from ambient to 80°C. The pressure varies from ambient to 100 bar and regulated by a back pressure regulating valve. The maximum flow rate was up to 100 kg h^{-1}. Pressure drop transducer and a hot wire anemometer were applied to measure the fluctuations signals, pressure drop, and average voidage. The fluidization regimes of fixed bed, homogeneous bed expansion, bubbling zone, and turbulent regime were mapped. Vogt et al. investigated the fluidization behaviors of supercritical CO_2-fluidized bed with pressure up to 30 MPa [12]. The experimental system was designed with a maximum operating pressure of 35 MPa and a maximum CO_2 flow of 50 kg $\cdot$ h^{-1}. The largest steel autoclave had a volume of 2.5×10^{-3} m^3 with inner diameter of 39 or 21 mm. They provided a comprehensive picture for the supercritical CO_2-fluidized bed when the superficial velocity was not very high. Potic et al. [13] visually studied the fluidization process of Geldart Group A particles in high pressure water within a cylindrical quartz reactor with an internal diameter of 1.0 mm in the range of 0.1–24.4 MPa and 20–500°. Lu et al. [14] experimentally obtained the minimum fluidization velocity by measuring the pressure drops of a SCWFB with a diameter of 35 mm for temperature ranging from 360 to 420°C and pressure ranging from 23 to 27 MPa. Wei and Lu [15] built a SCWFB fluid dynamics teasing systems; the fluidized bed section is made of stainless steel with 1.2 m height and 35 mm inner diameter. It is designed for the temperature up to 550°C and the pressure up to 30 MPa. A porous metal foam with bore diameter of 30 μm

is used as the distributor of the fluidized bed test section, and a metal foam filter is installed in the exit of the fluidized bed to avoid the escape of the bed materials. They measured the fixed bed pressure drop, minimum fluidization velocity, and bed expansion, minimum fluidization bubbling velocity of a water-solid fluidized bed from ambient to supercritical conditions, and they proposed a flow pattern map of the SCWFB.

2.2. Simulation advance

The fluidization of particles in the supercritical fluidized beds has been simulated by few researchers. Potic et al. [13] applied a DPM model to qualitatively simulate a micro-fluidized bed with an inner diameter of 1 mm. The model provided consistent flow structures with the tested results in the sub-critical and supercritical zones. Vogt et al. [16] developed a compromised model to compute the movement of bubbles in a $SCCO_2FB$ on the basis of empirical correlations. The model describes local fluid dynamics within the $SCCO_2FB$ by treating the surrounding emulsion phase as a continuum and bubble as the other phase. Rodriguez-Rojo and Cocero [17] simulated a $SCCO_2FB$ with an Eulerian two-flow model incorporating the classical drag model of Gidaspow. Wei et al. [18] simulated the feeding methods of a SCW fluidized bed reactor based on the Eulerian two-flow model incorporating particle kinetic theory. Bubbling phenomenon of Geldart Group B particles was observed in the simulation results. Lu et al. [19] derived a non-sphere drag equation to determine the momentum transfer between non-sphere particles and fluid in a dilute suspension system. A combination drag of the non-spherical particle drag model and the Ergun equation has been validated by comparing experimental data of the SCWFB. More recently, Lu et al. [20, 21] studied the fluidization process of Geldart Group B particles in SCW by a CFD-DEM model. Fluidization transition of fixed–homogeneous-bubbling zone was observed in the simulation work. The two-fluid model and CFD-DEM model are two effective simulation method to investigate the fluid dynamics of the supercritical fluidized bed.

3. Flow dynamic in the supercritical fluidized bed

Fixed bed pressure drop, minimum fluidization velocity, minimum bubbling velocity, homogenous expansion rate, bubble properties and transitions, and turbulence flow regimes of the supercritical fluidized bed are summarized. The flow characteristics of each flow regime are analyzed. The correlations for the key parameters are proposed. In this part, the results of measured method or simulated method for obtaining these parameters are discussed. The properties of SCW and $SCCO_2$ used in the experiments were shown in **Tables 1** and **2**, respectively.

P/MPa	27	27	27	27	27	25	23	23
T/°C	201	350	400	430	479	386	421	406
ρ_f/kg.m$-^3$	880.1	616.1	200.0	150.5	108.2	283.8	112.2	136.5
μ_f/10$-^5$ Pa·s	13.5	7.16	3.12	2.96	3.04	3.67	2.71	2.75

Table 1. Properties of SCW.

P/MPa	0.1	2	4	6	8	9.1	10.1	14.8	17.9	24.8
T/°C	18	35	35	35	35	54	57	56	57	57
ρ_f/kg.m^{-3}	1.8	36	85	150	480	266.8	316.4	637.2	707.1	799.1
μ_f/10^{-5}Pa·s	1.46	1.65	1.73	1.91	4.18	2.25	2.49	4.92	5.77	7.13

Table 2. Properties of $SCCO_2$.

3.1. Fixed bed pressure drop

Fixed bed pressure drop is greatly affected by properties of fluid (density and viscosity), solid properties (diameter, density, and shape factor), and superficial velocity and operation conditions. The description of the fixed bed pressure drop is a key element in the calculation of the minimum fluidization velocity. The calculation of fixed bed pressure drop can be achieved by Ergun equation,

$$\frac{\Delta P}{L} = a\frac{(1-\varepsilon)^2}{\varepsilon^3} \times \frac{\mu u}{(\psi d_p)^2} + b\frac{1-\varepsilon}{\varepsilon^3} \times \frac{\rho_f u^2}{\psi d_p} \tag{1}$$

where ΔP is the pressure drop, μ is the viscosity of fluid, ρ_f is the density of fluid, ε is the fixed bed voidage, d_p is the equivalent volume diameter of the particle, and ψ is the sphericity. The parameters a and b are 1.50 and 1.75, respectively, which are from the investigations of Ergun [22]. Ergun equation has been accepted to calculate the fixed bed pressure drop widely in literature [23].

Figure 1(a) shows the bed pressure drop vs. superficial velocity at temperature from ambient to supercritical zone. The pressure drop increased with an increase in the superficial velocity. An elevated temperature greatly affects bed pressure drop, and the main reason is the density and viscosity of high pressure water decrease with an increase in temperature. **Figure 1(b)** shows the simulated instantaneous bed pressure drop under each superficial velocity was time-averaged, and the relationship between bed pressure drop and fluidization number (superficial velocity divided by u_{mf}). When the superficial velocity is below the minimum fluidization velocity u_{mf}, the bed pressure drop increases with the increasing superficial velocity. When the superficial velocity is above the minimum fluidization velocity, the curve of the bed pressure become flat. Wei and Lu [15] found the deviation of Ergun equation was about ±30%, which was suitable for predicating fixed bed pressure drop in the sub-critical and supercritical zones.

Figure 2 shows the pressure drop of $SCCO_2$-fluidized bed. The experimental data are provided by Marzocchella and Salatino [11], and Vogt et al. [12]. It was found that Ergun equation was generally giving a good description of the measured relationship between pressure drop and superficial velocity. Considering the different supercritical fluids and operating pressures and temperature from ambient to supercritical zone, Ergun's equation is also well applicable for fixed bed flow with a supercritical fluid.

3.2. Minimum fluidization velocity

The minimum fluidization velocity serves as a critical parameter for the design and operation of fluidized bed. The determination of minimum fluidization velocity is conventionally based on the

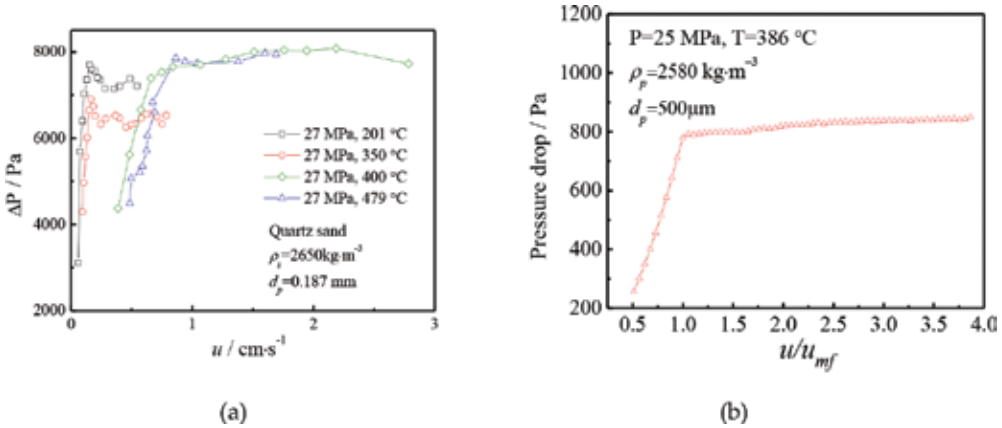

Figure 1. Bed pressure drop vs. superficial velocity for water-solid fluidized bed: (a) experimental data [15] and (b) simulation results by CFD-DEM model [20].

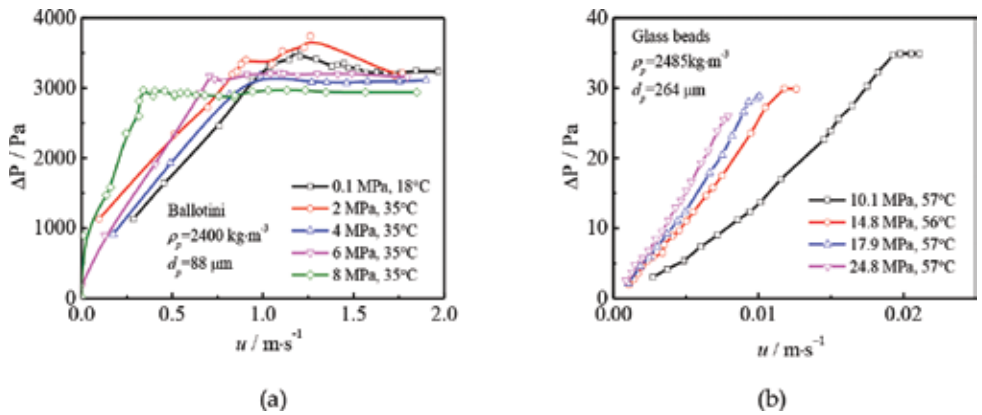

Figure 2. Bed pressure drop vs. superficial velocity for $SCCO_2$ fluidized bed: (a) Marzocchella and Salatino [11], and (b) Vogt et al. [12].

curve of experimentally measured pressure drop vs. superficial velocity. The minimum fluidization velocity was determined by the turning point of the curves, as shown in **Figures 1** and **2**. The minimum fluidization velocity is a function of temperature and pressure for Geldart-A and Geldart-B particles. The minimum fluidization velocity increased with an increase in temperature. The results are attributed to the decrease in density and viscosity of water induces a larger relative velocity for achieving force balance of particles in fluidization. Wei and Lu [15] proposed that an empirical equation of minimum fluidization velocity was achieved for fluidization of Geldart-B and Geldart-A particles in water from ambient zone to supercritical zone. The correlation combined the experimental data in supercritical zone and the expression is shown as follows

$$Re_{\mathrm{mf}} = 6.17\times10^{-4}Ar^{0.9324},\ 70 < Ar < 52000 \tag{2}$$

where Ar is the Archimedes number $Ar = g d_p^3 \rho_f(\rho_s - \rho_f)/\mu_f^2$.

In literature, Wen and Yu [24] equation has been usually used to calculate the minimum fluidization velocity of fluidized bed, even at high pressure conditions. Vogt et al. [12] found Wen and Yu equation predicated the minimum fluidization velocity with an average error of 14.3% in a $SCCO_2$ fluidized bed. Rodríguez-Rojo and Cocero [17] also used Wen and Yu equation to determine the minimum fluidization velocity in the simulation work. Marzocchella and Salatino [11] used Chitester et al. [25] equation to calculate the minimum fluidization velocity of the supercritical CO_2 fluidized bed. Wei and Lu [15] have examined the applicability of those reported correlations in SCW fluidized bed. It was found that Wen and Yu equation predicated acceptable minimum fluidization velocity from ambient to supercritical conditions, and the deviations of most predicated results are within ±30%. However, Chitester et al. equation predicated much higher minimum fluidization velocities than the experimental data.

Chitester et al. equation

$$Re_{\mathrm{mf}} = \sqrt{(28.7)^2 + 0.0494Ar} - 28.7 \tag{3}$$

Wen and Yu equation

$$Re_{\mathrm{mf}} = (33.7^2 + 0.0408Ar)^{0.5} - 33.7 \tag{4}$$

3.3. Bed expansion

Figure 3 shows the curves of bed voidage vs. superficial velocity in typical operating conditions for the SCW fluidized bed. The slopes of the curves after the turning point were obviously lower than that before the turning point. Similar phenomena were also observed in the $SCCO_2$ fluidized bed, as shown in **Figure 4**. The turning points of the voidage curves indicated bubbling occurrence in the fluidized bed. The homogenous bed expansion existed before the turning point and after which bubbling was formed. The experimental results show that the transitions from homogenous to bubbling occur in several supercritical conditions for both Geldart A and B particles.

Figure 5 shows the relation curve of bed pressure drop and superficial velocity vs. time. It can be observed that the curve of bed pressure drop vs. time can be divided into three stages.

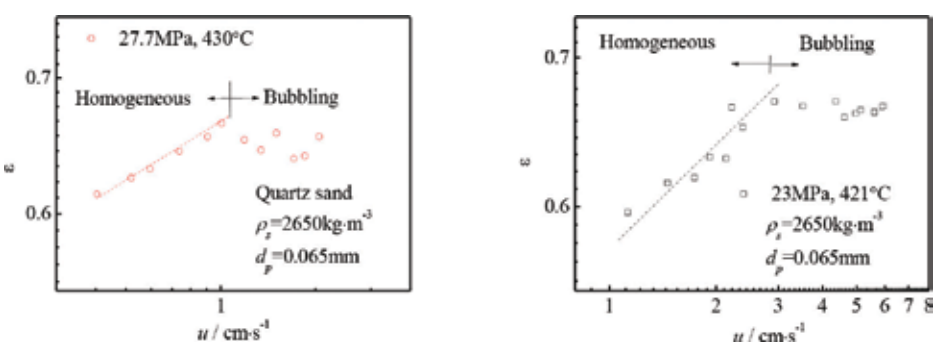

Figure 3. Typical results of voidage vs. superficial velocity for the SCW fluidized bed [20].

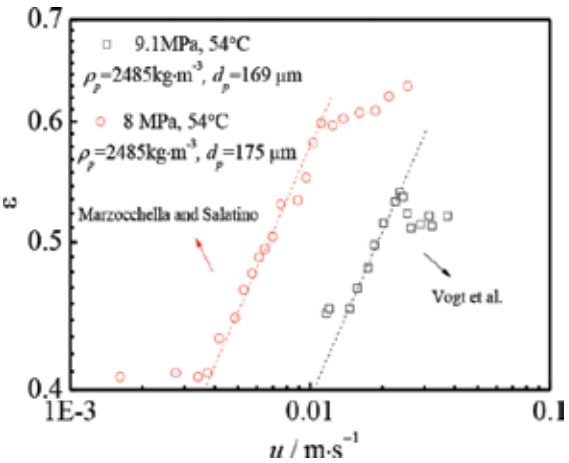

Figure 4. Typical results of voidage vs. superficial velocity for the $SCCO_2$ fluidized bed Vogt et al. [12], and Marzocchella and Salatino [11].

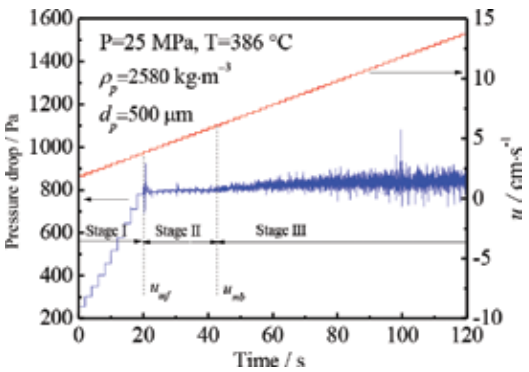

Figure 5. Bed pressure drop and superficial velocity vs. time for the SCW fluidized bed [21].

Stage I, the bed pressure drop increases step by step with the superficial velocity and without fluctuation when $u < u_{mf}$. Stage II, the pressure drop stops increasing with superficial velocity and fluctuates around a fixed value and decays rapidly when $u_{mf} < u < u_{mb}$. Stage III, the pressure fluctuates more violently with the increasing of superficial velocity when $u > u_{mb}$.

Figure 6 shows three snapshots of particles in the three stages. **Figure 6(a)** shows the fixed bed almost no particle moves. **Figure 6(b)** shows the homogeneous fluidization regime without bubbling fluidization in SCW fluidized bed. **Figure 6(c)** shows a bubble fluidization. Bubbles are quite small and scattered in SCW fluidized bed and the bed expansion is more obvious. The distribution characteristics of bubbles benefit the mixing state of fluid phase and solid phase.

For predicating the homogenous bed expansion rate at supercritical pressure, Richardson and Zaki equation [26] was modified based on the experimental data. The basic equation was given:

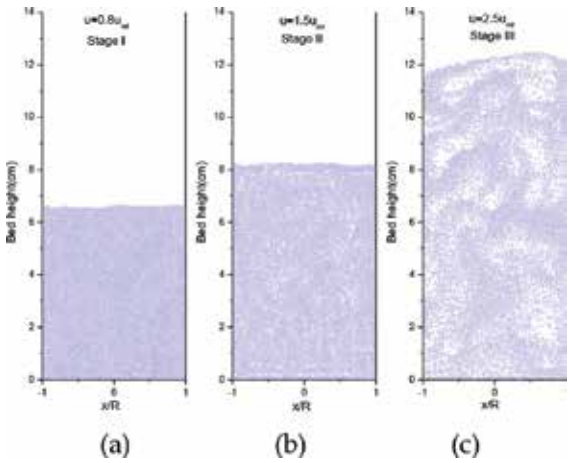

Figure 6. Snapshots of particles in various fluidization regimes [20].

$$u = u_t \varepsilon^n \tag{5}$$

where u_t is the terminal velocity, which can be calculated by correlation from Haider and Levenspiel [27].

Vogt et al. [12] proposed an empirical correlation for homogeneous bed expansion in the $SCCO_2$ fluidized bed, which was given:

$$n = 11.8 Re_t^{-0.23} \tag{6}$$

Wei and Lu [15] provided a modified correlation for homogeneous bed expansion in the SCW fluidized bed, which is shown as follows,

$$n = 10.364 \mathrm{Re}_t^{-0.09973},\ 2 < Re_t < 270 \tag{7}$$

The exponent n obtained from linear fitting of experimental data, thus they diverge each other greatly. The deviation of Eqs. (6) and (7) may indicate that the effects of fluid properties or operating conditions on bed expansion rates are remarkable. Care should be taken to use the bed expansion correlation. The correlation should be carefully used for the design of sub- and supercritical water or $SCCO_2$ fluidized bed.

The Gibilaro's equation [28] was used to predicate the bed expansion of $SCCO_2$ fluidized bed in literature [17].

$$\Delta \mathrm{P} = \left(\frac{18}{Re_p} + 0.33\right) \cdot \frac{\rho_f u^2 H}{d_p} (1 - \varepsilon) \varepsilon^{-4.8} \tag{8}$$

3.4. Bubbling fluidization

3.4.1. Minimum bubbling velocity

The minimum bubble velocity can be obtained from the figure of the standard deviation σ of pressure drop and heat transfer coefficient vs. superficial velocity in the vicinity of the incipient fluidization and incipient bubbling velocities. **Figure 7** shows the simulated and experimentally measured method of the minimum bubbling velocity. As shown in **Figure 7**, before bubbling, the standard deviations kept nearly invariable with an increase in the superficial velocity. After bubbling, an approximately linear relationship between the standard deviation σ and superficial velocity were observed. The onset increase in σ was related to the bubble occurrence. Based on the two methods, the minimum bubbling velocities were obtained.

For the classical gas-solid fluidized bed, Abrahamsen and Geldart correlation is usually used to calculate the minimum bubbling velocity [29]. However, Vogt et al. [12] found Abrahamsen and Geldart correlation predicated a much higher minimum bubbling velocity for the $SCCO_2$ fluidized bed. They suggested to use Foscolo and Gibilaro [30] criterion to predicate the ε_b, and then use Eqs. (5) and (6) to calculate the minimum bubbling velocity by intruding the minimum

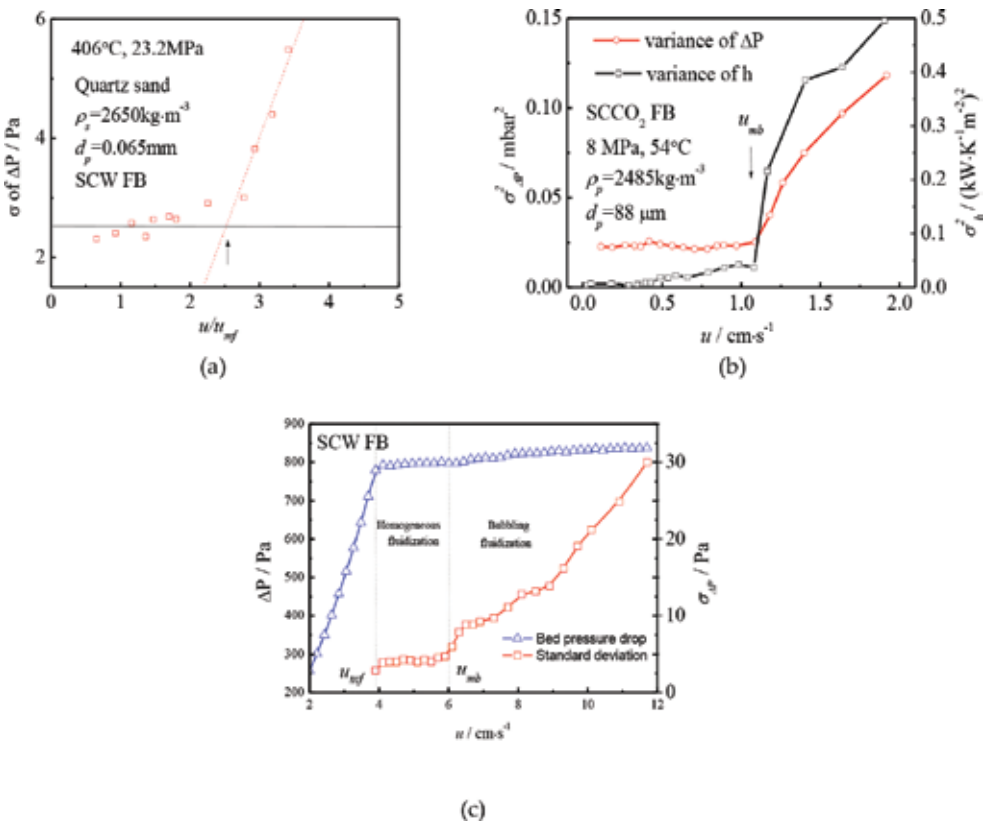

Figure 7. Typical results of variance of variables in the vicinity of incipient fluidization and bubbling: (a) SCW fluidized bed [15], (b) $SCCO_2$ fluidized bed [11], and (c) SCW fluidized bed by CFD-DEM simulation [21].

fluidization velocity and minimum fluidization voidage. Foscolo and Gibilaro found system is homogeneous when the kinematic wave velocity is higher than the dynamic wave velocity, otherwise bubble occurs. When the two velocities are equal, the limit of stability of the system is reached. The criterion is expressed as:

$$\frac{U_d - U_k}{U_k} = \begin{cases} + : \text{Homogeneous} \\ 0 : \text{Stability limit} \\ - : \text{ Bubbling} \end{cases} \tag{9}$$

The kinematic wave speed is

$$U_k = nu_t(1-\varepsilon)\varepsilon^{n-1} \tag{10}$$

The dynamic wave velocity is

$$U_d = \sqrt{3.2gd_p(1-\varepsilon)(\rho_s - \rho_f)/\rho_s} \tag{11}$$

However, Wen and Lu [15] evaluated the adaptability of Foscolo and Gibilaro criterion for the water-solid fluidized bed from ambient to supercritical conditions. They found that Foscolo and Gibilaro's criterion qualitatively predicated bubbling occurrence, the transformation processes of homogenous to bubbling were not captured. Therefore, it was difficult to use Foscolo and Gibilaro's criterion to predicate the minimum bubbling velocity for the SCW fluidized bed. They provided a polynomial function of Archimedes number for calculating the minimum bubbling velocity for the SCWFB.

$$Re_{\text{mb}} = 2\times10^{-8}Ar^2 - 9\times10^{-8}Ar + 1.4608,\ 700 < Ar < 34000 \tag{12}$$

3.4.2. Visible bubble flow rate

Based on the investigations of Vogt et al. [12], the visible bubble flow is multiplying the bubble gas holdup with the local mean bubble rise velocity,

$$V_b = \varepsilon_b u_b \tag{13}$$

The linear relationship between the visible bubble flow and the excess velocity was observed in **Figure 8**.

$$V_b = \phi(u - u_{mb}) \tag{14}$$

where ϕ = 0.6. When the emulsion phase voidage and bed average voidage are known, the bubble voidage can be obtained $\varepsilon_b = (\varepsilon - \varepsilon_e)/(1-\varepsilon_e)$. Then the bubble rising velocity can be calculated by Eq. (13). Eq. 14 reflects a linear relationship between the visible bubble flow and the excess velocity, which is adapted to the ambient conditions. Although the correlation has not been validated for the SCWFB, the equation is suggested to evaluate bubble rising velocity in the situation of lack of reliable formula for predication.

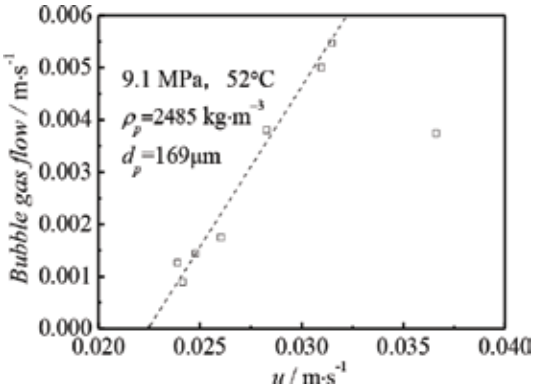

Figure 8. Visible bubble flow for glass beads in the $SCCO_2$ fluidized bed [12].

3.4.3. Effects of fluid states on the bubbling fluidization

Based on the Eulrian two fluid models and non-spherical particle drag model, the fluidized processes of the SCWFB were simulated [19]. **Figure 9** shows the solid distribution of the fluidized bed using different states of water as the fluidization medium and the properties of the SCW were shown in **Table 3**. The superficial velocity was set as 3.5 u_{mf}. **Figure 9(a)–(c)** describes the ambient and sub-critical water-solid system, in which particulate fluidization and homogeneous bed expansion are two typical characteristics. **Figure 9(g)** and **(h)** represents the flow characteristics of the vapor-solid system. **Figure 9(d)–(f)** represents the SCW-solid flow system. In the SCW zone, the pseudo-homogeneous expansion of the bed was similar to the liquid-solid system, but the bubbles occurrence was similar to the gas-solid system. Liu et al. [10] stated that the fluidization in the supercritical CO_2 fluidized bed was an intermediate state between bubbling and homogeneous fluidization through an experimental analysis. The

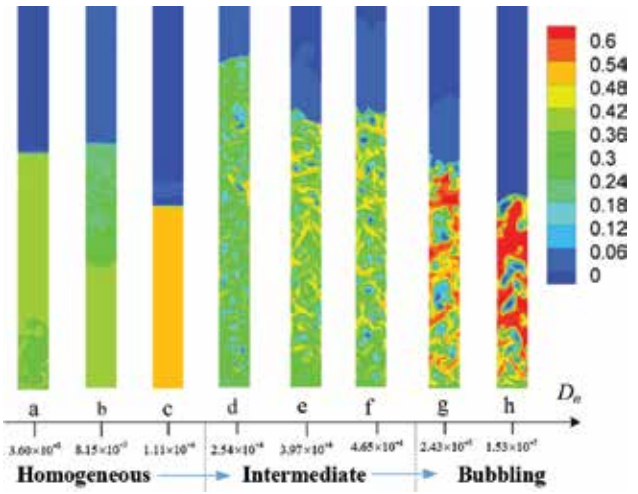

Figure 9. Solid distribution of fluidized bed at different states of water with u / u_{mf} = 3.5 [19].

Fluid states	Ambient	Subcritical		SCW			Steam	
No.	(a)	(b)	(c)	(d)	(e)	(f)	(g)	(h)
P/MPa	0.1	6.3	25.1	25.4	25.2	25.5	6	0.1
T/°C	20	207	224	387	403	428	400	400
ρ_f/kg.m^{-3}	998.2	859.9	854.1	296.7	162.9	128.7	21.1	0.322
μ_f/10^{-5} Pa·s	100.1	13.06	12.48	3.787	2.913	2.87	2.437	2.446

Table 3. Simulation conditions and parameters in **Figure 9**.

intermediate fluidization has the characteristics of the two-phase flow in both bubbling and homogeneous fluidization. Obviously, the present simulation results showed an intermediate state of the SCW fluidized bed, which was a pseudo-homogeneous expansion with a large number of small bubbles. With an increase in the discrimination number D_n, the fluidization of water-solid system evolved from particulate to intermediate to aggregative.

3.5. Turbulence fluidization and transition zone

Marzocchella and Salatino [11] observed the $\sigma^2_{\Delta P1}/\Delta P_1^2$ vs. u pattern of the $SCCO_2$ fluidized bed is the well-known bell-shaped curve, as shown in **Figure 10**. With an increase in superficial velocity, $\sigma^2_{\Delta P1}/\Delta P_1^2$ increase first and then decrease. Gas superficial velocities at which $\sigma^2_{\Delta P1}/\Delta P_1^2$ is at a maximum and at which it levels off, have been assumed, respectively, as the beginning U_C and the end U_k of the transition to the turbulent fluidization regime. Note that no detectable decrease in the pressure drop across the bed was observed over several minutes of operation of the bed even at fluid superficial velocities over U_k. Based on the experimental investigations, Marzocchella and Salatino [11] suggested Nakajima et al. [31] equation to calculate the transition velocity, and Bi and Fan [32] correlation to determine the turbulent velocity.

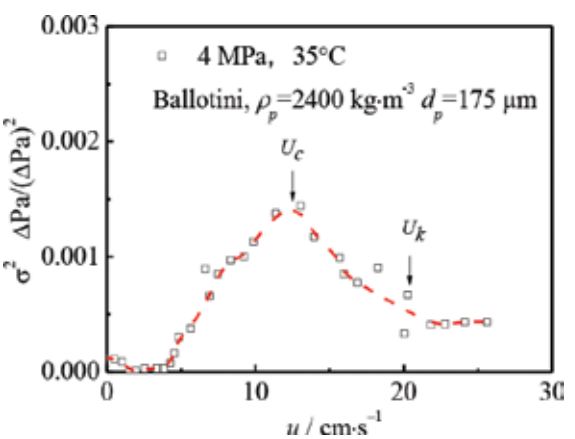

Figure 10. Dimensionless variance of the bed pressure drop vs. superficial fluid velocity for the $SCCO_2$ fluidized bed.

Nakajima et al. equation is,

$$Re_c = 0.663Ar^{0.467} \tag{15}$$

Bi and Fan correlation is,

$$Re_k = \begin{cases} 0.601Ar^{0.695} & Ar \leq 125 \\ 2.28Ar^{0.419} & Ar > 125 \end{cases} \tag{16}$$

4. Flow pattern maps of supercritical fluidized bed

Mapping flow pattern based on experimental data is a useful method to characterize the flow regimes and transitions. For the classical gas-solid or liquid-solid fluidized bed, maps of pressure drop vs. supercritical velocity, slip velocity vs. solid fraction, voidage vs. supercritical velocity, DP standard deviations vs. voidage, non-linear parameters vs. supercritical velocity, dimensionless diameter vs. dimensionless gas velocity, and Reynolds number vs. Archimedes number have been investigated [33, 34, 35]. Those maps can be classified into two groups: dimension and dimensionless. Obviously, the dimensional flow pattern maps are hard to be used in present situation because the fluid state varies greatly from ambient to supercritical conditions. For example, although a plot of velocity vs. fluid density shows a clear physical meaning, it cannot include all the cases for different particles. The dimensionless flow pattern maps are promising to solve the shortcoming. The horizontal ordinates of dimensionless gas velocity or Archimedes number in the traditional flow maps have been proved effective to the classical fluidized bed. However, they are useless for present situations because they cannot discriminate the different transitions of flow regimes. The transitions of flow regimes are mainly depending on the properties of each phases and operating parameters. Obviously, just using Archimedes number cannot reflect effects of both sides. The main obstacle of mapping the flow pattern is describing the horizontal ordinates reasonably.

4.1. SCWFB

Wei and Lu [15] drew the flow pattern maps with abscissa D_n demarcating the three transitions processes and ordinate charactering the operating parameters. The discrimination number D_n was proposed by Liu et al. [10] to demarcate the fluidization quality.

$$D_n = \left(\frac{Ar}{Re_{mf}}\right)\left(\frac{\rho_s - \rho_f}{\rho_f}\right) \tag{17}$$

The discrimination umber shows the effect of properties of two phases in $Ar \cdot \left(\frac{\rho_s - \rho_f}{\rho_f}\right)$, and the effect of operating parameters in $\frac{1}{Re_{\mathrm{mf}}}$. This paper found the discrimination number D_n can demarcate the flow pattern evolution processes. Based on the experimental analysis, fluidization state of fixed-homogeneous (F-H), fixed-homogeneous-bubbling (F-H-B) and fixed-bubbling (F-B) was summarized as follows:

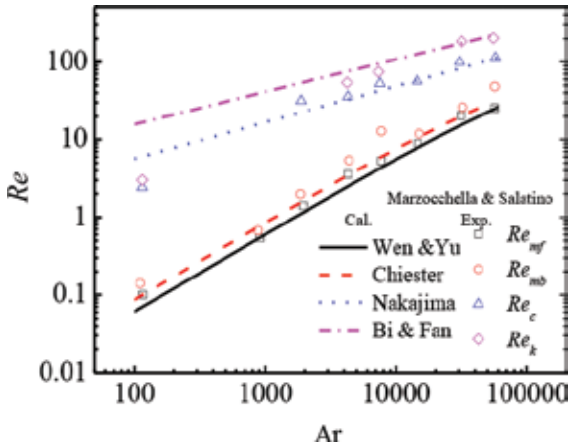

Figure 11. Flow pattern for the $SCCO_2$ fluidized bed.

$$\begin{cases} D_n < 1.2\times10^4 & F-H \\ 1.2\times10^4 \le D_n < 6.4\times10^4 & F-H-B \\ D_n \ge 6.4\times10^4 & F-B \end{cases} \tag{18}$$

The discrimination number D_n of 1.2×10^4 is little higher than the experimental results by Liu et al. [10]. The boundary of F-H fluidization can be determined by the minimum fluidization velocity correlation Eq. (2), and the boundary of F-B and H-B fluidization can be calculated by the minimum bubbling velocity correlation Eq. (12).

4.2. $SSCO_2FB$

Marzocchella and Salatino [11] gave a flow pattern map of Reynolds numbers *Re* vs. Archimedes number for the $SCCO_2$ fluidized bed. In the original map, they calculated Re_{mf} according to Chitester et al. [25] correlation, Re_c by Nakajima et al. [31] correlation, and Re_k could be calculated by Bi and Fan [32]. Here, the map was redrawn by adding the Wen and Yu equation to evaluate the minimum fluidization velocity as shown in **Figure 11**. What's more, the minimum bubble velocity is suggested to be determined according to Foscolo and Gibilaro's criterion.

5. Conclusion

Supercritical bed is a kind of new and promising reactors. This work tries to conduct a comprehensive study on supercritical fluidized bed to provide information of basic two-phase flow and theories of design and operation. A review of main research progress is illustrated and important results were summarized. The main conclusions are obtained as follow:

1. Fixed bed pressure drop in supercritical conditions can be predicated by Ergun equation.
2. Wei and Lu correlation Eq. (2) was suggested as a new correlation for minimum fluidization velocity of water-solid fluidized bed in high pressure, near-critical and supercritical conditions. Wen and Yu equation Eq. (4) was acceptable for calculating the minimum fluidization velocity of the SCWFB and $SCCO_2FB$.
3. The homogeneous bed expansion rate of supercritical fluidized bed can be described by modified Richard and Zaki equation. The index function n can be correlated by Wei and Lu equation Eq. (7) and Vogt et al. equation Eq. (6) for the SCWFB and $SCCO_2FB$, respectively.
4. The bubbling fluidization was found for both Geldart A and B particles in the supercritical fluidized bed. An empirical correlation of minimum bubbling velocity in Eq. (12) was achieved by Wei and Lu for the SCWFB. Vogt et al. provided a method to determine the minimum bubbling velocity of the $SCCO_2FB$ by using Foscolo and Gibilaro criterion.
5. The fluidization state of the supercritical fluidized bed can be viewed as an intermediate between classical gas-solid and liquid-solid fluidizations. The visible bubble flow rate can be predicated by Vogt et al. equation Eq. (14).
6. For the SCWFB, discrimination number D_n was used to determine the fluidization regimes from ambient to supercritical conditions. Fluidization of F-H was found when D_n was below 1.2×10^4; fluidization of F-H-B was found when D_n was between 1.2×10^4 and 6×10^4, and fluidization of F-B was found when D_n was above 6×10^4. As suggested by Marzocchella and Salatino [11], Nakajima et al. [31] equation was used to calculate the transition velocity, and Bi and Fan [32] correlation was applied to determine the turbulent velocity of the $SSCO_2FB$. A flow pattern map of Reynolds numbers Re vs. Archimedes number has been provided for the $SSCO_2FB$.

Acknowledgements

This work is currently supported by the National Natural Science Foundation of China through contract No. 91634109, 51676158, and 51606153.

Nomenclature

Ar	Archimedes number ($Ar = gd_v^3\rho_f(\rho_s - \rho_f)/\mu_f^2$)
d	Particle diameter (m)
d_b	Bubble equivalent diameter (m)
D_n	Discrimination number
FB	Fluidized bed
g	Acceleration due to gravity (m s^{-2})
n	Index function

P	Pressure (Pa)
Re	Reynolds number
Re_p	Particle Reynolds number
Re_t	Terminal Reynolds number
SCW	Supercritical water
$SCCO_2$	Supercritical carbon dioxide
t	Time (s)
T	Temperature (K or °C)
u	Superficial fluid velocity (m s^{-1})
u_{mb}	Minimum bubbling velocity (m s^{-1})
u_{mf}	Minimum fluidization velocity (m s^{-1})
u_t	Terminal velocity (m s^{-1})

Greek letters

ε	Voidage
ρ	Density

Subscripts

c	Transition
f	Fluid
k	Turbulence
o	Initial state
s	Particle phase
t	Terminal state

Author details

Youjun Lu[1]*, Liping Wei[1,2] and Jikai Huang[1]

*Address all correspondence to: yjlu@mail.xjtu.edu.cn

1 State Key Laboratory of Multiphase Flow in Power Engineering (SKLMF), Xi'an Jiaotong University, Xi'an, Shaanxi, China

2 School of Chemical Engineering, Northwest University, Xi'an, Shaanxi, China

References

[1] Wagner W, Kruse A. Properties of water and steam-the industrial standard IAPWS-IF97 for the thermodynamic properties and supplementary equations for other properties: tables based on these equations. Berlin: Springer Verlag; 1998

[2] Wei L, Lu Y, Wei J. Numerical study on laminar free convection heat transfer between sphere particle and high pressure water in pseudo-critical zone. Thermal Science. 2014;**18**(4):1293-1303

[3] Yang CY. Numerical simulation of convection heat transfer for supercritical carbon dioxide in tube. Beijing: North China Electric Power University; 2013

[4] Matsumura Y, Minowa T. Fundamental design of a continuous biomass gasification process using a supercritical water fluidized bed. International Journal of Hydrogen Energy. 2004;**29**(7):701-707

[5] Lu Y, Jin H, Guo L, Zhang X, Cao C, Guo X. Hydrogen production by biomass gasification in supercritical water with a fluidized bed reactor. International Journal of Hydrogen Energy. 2010;**31**(7):822-831

[6] Guo L, Jin H. Boiling coal in water: Hydrogen production and power generation system with zero net CO_2, emission based on coal and supercritical water gasification. International Journal of Hydrogen Energy. 2013;**38**(29):12953-12967

[7] Leeke G A, Lu T, Bridson R H, et al. Application of nano-particle coatings to carrier particles using an integrated fluidized bed supercritical fluid precipitation process. Journal of Supercritical Fluids. 2014;**91**(7):7-14

[8] Tarmy, B, Chang, M, Coulaloglou C, Ponzi, P. Hydrodynamic characteristics of three phase reactors. Chemical Engineer. 1984;**407**:18-23

[9] Jiang P, Luo X, Lin T J, et al. High temperature and high pressure three-phase fluidization—bed expansion phenomena. Powder Technology. 1997;**90**(2):103-113

[10] Liu D, Kwauk M, Li H. Aggregative and particulate fluidization—The two extremes of a continuous spectrum. Chemical Engineering Science. 1996;**51**(17):4045-4063

[11] Marzocchella A, Salatino P. Fluidization of solids with CO_2 at pressures from ambient to supercritical. Aiche Journal. 2000;**46**(5):901-910

[12] Vogt C, Schreiber R, Brunner G, et al. Fluid dynamics of the supercritical fluidized bed. Powder Technology. 2005;**158**(1–3):102-114

[13] Potic B, Kersten S, Ye M, et al. Fluidization with hot compressed water in micro-reactors. Chemical Engineering Science. 2005;**60**(22):5982-5990

[14] Lu Y, Zhao L, Han Q, et al. Minimum fluidization velocities for supercritical water fluidized bed within the range of 633–693K and 23–27MPa. International Journal of Multiphase Flow. 2013;**49**(3):78-82

[15] Wei L, Lu Y. Fluidization behavior in high-pressure water at temperature from ambient to supercritical. Powder Technology. 2016;**304**:89-100

[16] Vogt C, Hartge E, Werther J, et al. Simulation of particle coating in the sueprcrtical fluidized bed. Particuology. 2005;**3**(Z1):113-124

[17] Rodríguez-Rojo S, Cocero M. Supercritical fluidized bed modeling. Journal of Supercritical Fluids. 2009;**50**(1):54-60

[18] Wei L, Lu Y, Wei J. Hydrogen production by supercritical water gasification of biomass: Particle and residence time distribution in fluidized bed reactor. International Journal of Hydrogen Energy. 2013;**38**(29):13117-13124

[19] Lu Y, Wei L, Wei J. A numerical study of bed expansion in supercritical water fluidized bed with a non-spherical particle drag model. Chemical Engineering Research & Design. 2015;**104**:164-173

[20] Lu Y, Huang J, Zheng P. Fluid hydrodynamic characteristics in supercritical water fluidized bed: A DEM simulation study. Chemical Engineering Science. 2014;**117**(1):283-292

[21] Lu Y, Huang J, Zheng P, et al. Flow structure and bubble dynamics in supercritical water fluidized bed and gas fluidized bed: A comparative study. International Journal of Multiphase Flow. 2015;**73**:130-141

[22] Ergun S. Fluid flow through packed columns. Journal of Materials Science & Chemical Engineering. 1952;**48**(2):89-94

[23] Luckos A, Bunt J. Pressure-drop predictions in a fixed-bed coal gasifier. Fuel. 2011;**90**(3): 917-921

[24] Wen C, Yu Y. Mechanics of fluidization. The Chemical Engineering Progress Symposium Series. 1966;**62**:100-111

[25] Chitester D, Kornosky R, Fan L, et al. Characteristics of fluidization at high pressure. Chemical Engineering Science. 1984;**39**(2):253-261

[26] Richardson J, Zaki W. Sedimentation and fluidisation: Part I. Transactions of the Institution of Chemical Engineers. 1954;**32**(35):35-53

[27] Haider A, Levenspiel O. Drag coefficient and terminal velocity of spherical and nonspherical particles. Powder Technology. 1989;**58**(1):63-70

[28] Gibilaro L. Fluidization dynamics. Oxford: Butterworth Heinemann, 2001

[29] Abrahamsen A, Geldart D. Behaviour of gas-fluidized beds of fine powders part I. Homogeneous expansion. Powder Technology. 1980;**26**(1):35-46

[30] Foscolo P, Gibilaro L. A fully predictive criterion for the transition between particulate and aggregate fluidization. Chemical Engineering Science. 1984;**39**(12):1667-1675

[31] Nakajima M, Harada M, Yamazaki R, et al. Bubble fraction and voidage in an emulsion phase in the transition to a turbulent fluidized bed. Kagaku Kogaku Ronbunshu. 1990;**16**(2): 322-328

[32] Bi H, Fan L. Existence of turbulent regime in gas-solid fluidization. Aiche Journal. 1992, **38**(2):297-301

[33] Bi H, Grace J, Zhu J. Regime transitions affecting gas-solids suspensions and fluidized beds. International Journal of Multiphase Flow. 1996;**22**(97):154-161

[34] Bai D, Shibuya E, Nakagawa N, et al. Characterization of gas fluidization regimes using pressure fluctuations. Powder Technology. 1996;**87**(2):105-111

[35] Zhu J, Karamanev D, Bassi A, et al. (Gas-) liquid-solid circulating fluidized beds and their potential applications to bioreactor engineering. Canadian Journal of Chemical Engineering. 2009;**78**(1):82-94

Chapter 7

Introductory Review on an Engineering Approach for Fast-Bed Modeling in Mimic to Bubbling Bed Practice

Ming-Chuan Zhang and Chu Zhang

Additional information is available at the end of the chapter

http://dx.doi.org/10.5772/68107

Abstract

Based on the downward-penetrating particle flow through clusters and the analogy between a falling cluster and a rising bubble identified by the authors, a "type-A-choking-oriented separate-phase-coexistence model" for the upper dilute region of fast beds was established first. Without any model parameter adjustment, the unified model predicted successfully the type C choking, the solids holdup of upper dilute region, and transitions to the high-density fast bed and the dense suspension up-flow.

The model was then integrated with the sub-models of "cluster rebound at the dense bottom," "the momentum flux balances for acceleration and transition zones" in the lower and middle parts of the bed. The integrated model predicted successfully the axial solids holdup distributions of literature data under extremely wide operation conditions covering dilute-phase transportation, the premature fast bed, the classical fast bed, and the high-density fast bed.

Keywords: fast fluidization, separate-phase model, type A choking, cluster rebound, solids holdup distribution

1. Introduction

After several decades of development, fast fluidization or circulating fluidized bed (CFB) has been applied widely, nowadays, in different industries, such as chemical, metallurgy, and energy engineering [1–3]. Thanks to the particle agglomeration in CFB risers, small particles could be fluidized under quite high gas velocity, resulting in very high rates of heat and mass transfers in the bed. A unique feature of a fast fluidized bed is its nonuniform axial distribution of particle concentration. On top of the bed, the solids holdup is small, while it is large at the bottom. To form a fast fluidized bed, both of the two conditions are usually required [4]: (i) the

solid circulating rate G_s is larger than the minimum value of that G_{sm}; (ii) and at a given solid circulating rate $G_s > G_{sm}$, the superficial gas velocity u_f should be higher than the critical velocity for type C choking, but lower than that for type A choking, that is, $u_{ch,C} < u_f < u_{ch,A}$.

To predict the two-phase flow characteristics in this very special flow regime, different kinds of modeling methods have been developed. They are, for examples, two-fluid modeling based on kinetic theory established by Gidaspow [5], two-fluid modeling with energy minimization multiscale (EMMS) approach suggested by Li and Kwauk [6], CFD modeling coupled with discrete element method (DEM) [7], CFD modeling with multiphase particle-in-cell (MP-PIC) approach [8], and so on. Nowadays, these methods have been developed to an extent that three-dimensional (3D) simulation of large-scale reactors including the full-solids loop, heat and mass transfer, and reaction kinetics can be realized [9]. However, all these methods expend great amount of computer efforts, sometimes super computers are even needed [9], which is usually not affordable for engineering application.

To overcome the problems met in practice, an engineering approach for fast fluidization dynamics was proposed by the authors recently [10, 11]. This paper will give an introductory review on this approach as follows.

2. Analogy between fast beds and bubbling beds

2.1. Analogy of flows around a cluster and a bubble

To explain how a cluster is formed in a CFB riser, the wake effect was applied quite often in the literature. Recently, He et al. [12] conducted an excellent PIV investigation in a CFB riser, shown in **Figure 1(a)** and **(b)**, from which some details of this phenomenon can be seen clearly. They declared in their article, "it can be easily seen that a cluster is followed by a wake, in which particles move downward quickly," and "when a cluster is passing by, the particles are dragged down at a higher velocity." It is very clear that those particles move toward the cluster at quite high velocities, which will cause a notable deposition, yet not the one negligible, on the back side of the cluster. Considering the size limitation for a stable cluster, the same quantity of particles must be poured out from its nose. Therefore, the continuous deposition and pour out of those particles together with the downward displacement inside can be viewed as an integrated penetration of particles through the cluster. From this point of view, the phenomenon was thought quite analogous to what happens around a rising bubble in a bubbling bed, shown as in **Figure 1(c)** [13].

It can be seen that the flow patterns of the two are quite similar, except their directions being opposite-down. Moreover, the following correspondences could be easily recognized if phase-reversing is applied: (1) a rising bubble with null or few particles against a falling cluster with concentrated particles; (2) the relatively downward dense particle flow around the bubble against the upward dilute flow around the cluster; and (3) the upward-penetrating gas flow through the bubble against the downward-penetrating particle flow through the cluster. The scenarios in a CFB riser described are very close to the detailed numerical simulation results using two-fluid model combined with EMMS approach [14], that is, "the particles tend to enter

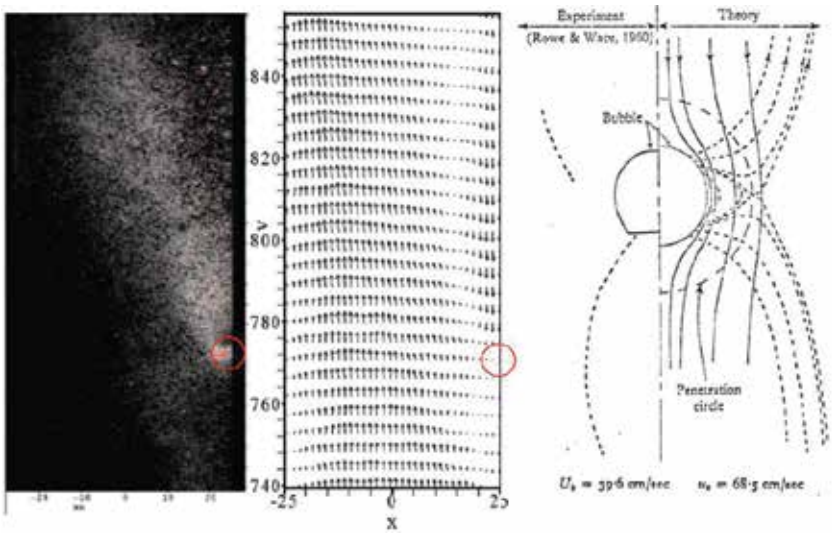

(a) (b) (c)

Figure 1. PIV measurement of particle moving in a CFB riser [12] compared with the flow field around a rising bubble [13]: (a) snapshots of instantaneous particle positions when a falling cluster (denoted by the small circle on the right wall) passing by; (b) corresponding particles' velocity field; and (c) flow pattern around a rising bubble.

into clusters instead of suspending in dilute broth (phase), whereas the gas tends to pass around, instead of penetrating through, the dense cluster phase" [14]. Thus, it might be possible that some results obtained from bubbling beds could be applied also to the fast fluidization, as depicted below.

2.2. Modeling strategies learned from bubbling beds

In the research progress of traditional fluidization, though people understood the phenomenon of minimum fluidization and its prediction method long time ago [15], the knowledge on fluidization had not been an applied science, to some extent, until Davidson and Harrison's bubble model appeared in 1963 [13]. This excellent model explained successfully many important phenomena of bubbling beds, and based on that, a series of reactor models of this type, that is, "bubble models," were developed [9].

What can we learn from the research success of bubbling beds? First, to grasper the critical boundary of this flow regime, that is, minimum fluidization (or minimum bubbling) in this case, is extremely important, since predicting the flow characteristics of a bubbling bed from its boundary not far away is much easier than extrapolating the flow transformation from the force analysis with a single particle. It can be seen clearly that the corresponding boundary in fast fluidization is the type A choking. And at a given gas velocity u_f, the saturation-carrying capacity or the solid flux at type A choking in a riser G_s^* corresponds to the superficial gas velocity for minimum fluidization u_{mf}. Thus, the critical boundary condition of fast fluidization, that is, the type A choking, should be studied carefully first.

Secondly, the classical two-phase theory of fluidization, that is, "above the minimum fluidization velocity, all the extra gas passes through the bed in the form of bubbles, while the rest part of the bed remains at the minimum fluidization condition" [13], is probably one form of a general law caused by the agglomeration nature of gas-solid systems. The appearing form of the general law in fast beds should be further excavated, too. It will be shown later that the formation of clusters at $G_s > G_s^*$ corresponds to the formation of bubbles at $u_f > u_{mf}$. And also, when clusters are formed, in the case of fast bed, the upward dilute flow will still be at the solid-saturated condition, as if at type A choking. All these ideas will be used for the derivation of our model below.

3. Constitutive equations for solid-saturated up-flow

3.1. Yang's formula for type A choking

To predict the happening of type A choking, much research work was carried out in the past. Among the different types of methods developed, the form of Yang's formula [16, 17] looks the one most reasonable, as the formula was derived from two simple theoretical deductions. The first one is used to calculate the terminal velocity u_t' for uniformly suspended particles with voidage ε in a riser of diameter D_t, in relative with the original value u_t for a single particle

$$u_t' = u_t\sqrt{\left(1+\frac{f_p u_p^2}{2gD_t}\right)\times\varepsilon^{4.7}}. \tag{1}$$

where $u_p = G_s/[\rho_s(1-\varepsilon)]$ stands for the particle velocity, and f_p is the solid-wall friction factor. The formula is theoretically correct, and the detailed derivations of that can be found in the series work of Yang from 1973 to 1975 [16, 18, 19].

The second deduction is that the terminal velocity of a particle suspension in a finite diameter riser u_t', that is, the slip velocity between gas and solid, is just equal to the terminal velocity of a single particle in the infinity u_t, when type A choking occurs [16, 17]

$$u_t' = u_t. \tag{2}$$

In the derivation of Yang's predictive equation (Eq. (3)), this deduction was actually applied [16, 17], yet not declared clearly

$$\frac{2D_t g(\varepsilon_{ch}^{-4.7}-1)}{(u_{ch}-u_t)^2} = f_p. \tag{3}$$

The original value of solid-wall friction factor f_p was taken as 0.01 in 1975 [16], but it was changed in 1983 to the present form as [17]

$$f_p = 6.81\times10^5\left(\frac{\rho_g}{\rho_s}\right)^{2.2}. \tag{4}$$

3.2. Physical essence of Yang's formula

From Eq. (1), it can be easily recognized that the influence of wall friction on u'_t is reflected by the first item with square root sign $\sqrt{[1+f_p u_p^2/(2gD_t)]}$, since for an infinitely wide riser it will always be unity. With a decrease of D_t, the wall friction increases, then u_t' increases. And the influence of bed voidage, that is, the influence of surrounding particles, is reflected by the second item with square root sign $\sqrt{\varepsilon^{4.7}}$. With an increase of particle concentration $(1-\varepsilon)$, ε decreases, and then u_t' decreases. This is because when the concentration of particles increases, the real gas velocity $(1/\sqrt{\varepsilon^2})$ increases, and the flow path of gas around the particle considered becomes more flexuous, and then the drag force coefficient will increase $(1/\sqrt{\varepsilon^{2.7}})$, too [14].

To quantitatively analyze further the overall force balance for a uniform suspension of particles in a gas flow, we can resolve the increased fluid drag into the basal fluid drag on a single particle F_f and the surplus F_s due to the surrounding particles. Then, we have

$$F_f + F_s = G + W, \tag{5}$$

where G is the gravity of particle suspension, while W stands for the friction of riser wall.

If we compare the values of F_s and W, we will have two different situations. When the suspension is quite dilute, the surplus drag force is relatively small. Then, we will have $F_s < W$, and $F_f > G$. The latter means that subtracting particle gravity the basal fluid drag F_f still have something rest with its own freedom, resulting in $F_f - G = W - F_s$ and a simple dynamic system centered on each single particle. That is the case of normal dilute transportation, because the relatively independent movement of these particles will let themselves disperse uniformly. On the other hand, if we have $F_s > W$ and $F_f < G$, the basal fluid drag F_f will no longer be able, by itself, to support the particle but requires help from surrounding particles, as $F_f + (F_s - W) = G$. That makes the dynamic system more complex and easier to lose its uniformity, since the force balance of any single particle depends more on the others.

Therefore, the criteria of $F_s = W$ or $F_f = G$ can be used to separate the two different situations just mentioned. Clearly, this critical condition is the type A choking, where the influence of bed voidage on u_t' is just compensated by the influence of riser wall, leading to $u_t' = u_t$. At this unique condition, a moving particle looks as if there is neither surrounding particles nor the riser wall. From the authors' opinion, this is the real physical essence of type A choking. Then, the functional dependence of the bed voidage on the superficial gas velocity at type A choking, that is, Eq. (3), could be used as the "constitutive equation" for solid-saturated up-flow.

3.3. Reconstruction of Yang's formula

According to a comprehensive review paper on choking for vertical conveying systems by Xu et al. [20], the prediction accuracy of Yang's formula is not satisfactory for type A choking, though it was suggested to be applied for a pretty long time [21]. In conserving its form, the solid-wall friction factor f_p in Yang's formula was recorrelated by the authors [10] with the data collected by Xu et al. [20], resulting in

$$f_{\mathrm{p}} = 0.01\left(\frac{u_{\mathrm{f}} - u_{\mathrm{t}}}{u_{\mathrm{t}}}\right)^{\alpha}\left(\frac{gD_{\mathrm{t}}}{0.8u_{\mathrm{t}}^2}\right)^{\vartheta} \tag{6}$$

$$\alpha = -(1.0723 + 0.0017\mathrm{Ar}). \tag{7}$$

When $gD_{\mathrm{t}}/u_{\mathrm{t}}^2 > 0.8$, $\vartheta = 0.71$; while $gD_{\mathrm{t}}/u_{\mathrm{t}}^2 < 0.8$, $\vartheta = -1.27$, as shown in **Figure 2**. This correlation is applied with Ar = 1–1000, $u_{\mathrm{ch,A}}/u_{\mathrm{t}}$= 3–40, and $gD_{\mathrm{t}}/u_{\mathrm{t}}^2 = 0.2$–1000. And the values of f_{p} should range from 0.001 to 0.1. As can be seen in **Figure 3**, the predicted saturation-carrying capacities G_{s}^* are in good consistency with the experimental data, if some observation delays in these experiments are considered.

The dependence of dimensionless solid-wall friction factor $\tilde{f}_{\mathrm{p}}$ on dimensionless riser diameter $gD_{\mathrm{t}}/u_{\mathrm{t}}^2$ changes abruptly at $gD_{\mathrm{t}}/u_{\mathrm{t}}^2 = 0.8$, which corresponds to the transit of general flow pattern from confined slugging to free bubbling [10]. It further confirms that type A choking is a riser-diameter-dependent phenomenon, as we discussed before. However, most of the previous work ignored this dependence except Xu et al. [20], showing that the influence of

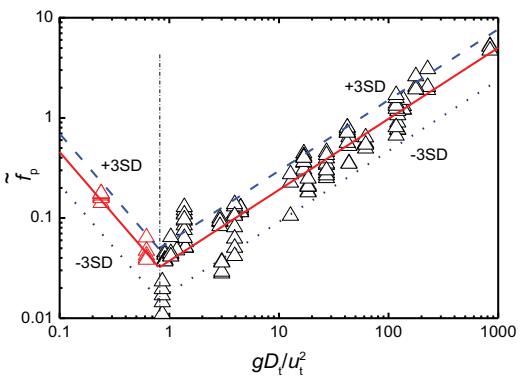

Figure 2. Log-log plot of $\tilde{f}_{\mathrm{p}}$ with $gD_{\mathrm{t}}/u_{\mathrm{t}}^2$ for experimental data collected by Xu et al. [20].

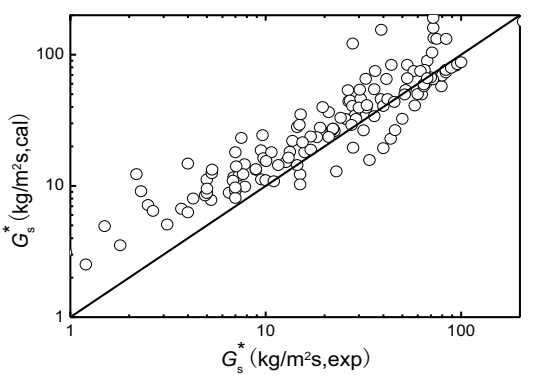

Figure 3. Predictions of G_{s}^* for type A choking compared with experimental data of [20].

riser diameter on type A choking velocity was not monotonic. Since the new correlation is given in a dimensionless form and the application ranges are quite wide, it is hoped that this correlation could be used, to some extent, in practically large units. For instance, if the particle terminal velocity is around 0.3 m/s (typical in CFB boilers), the riser diameter could be used up to 10 m.

4. Separate-phase-coexistence model for fast bed

4.1. Physical description of the model

Described above, Eq. (3) gives the functional dependence of bed voidage ε_{ch} on superficial gas velocity u_{ch} under solid-saturated conditions. For a given fluidizing system, with an increase of u_{ch}, ε_{ch} decreases and $(1-\varepsilon_{ch})$ increases, and then the solid flux at type A choking G_s^* will increase more rapidly

$$G_s^* = \rho_s(u_{ch} - u_t)\frac{1-\varepsilon_{ch}}{\varepsilon_{ch}}. \tag{8}$$

Taking an FCC-air fluidizing system as an example, **Figure 4** shows the calculated $(1-\varepsilon_{ch})$ and G_s^* varied with u_f. Thanks to this special dependence of G_s^* on u_f (u_{ch} in the equation), the system will not completely collapse when the circulating solid flux is greater than G_s^* corresponded to the superficial gas velocity u_f. Some particles will segregate from the gas stream to form a free-sedimentary dense phase, that is, the so-called cluster. The fluidizing system then runs in a more complicated separate-phase-coexistence mode. The cluster occupies a part of the cross-sectional area of the riser, but without any outer gas invading in. Meanwhile in the rest part of the riser, all gas squeezes into the dilute phase and carries much more particles upward.

Let β stand for the fraction of cross-sectional area occupied by the falling clusters, and m_s^- for the solid flux downward, while m_s^+ represent the solid flux upward in the dilute phase. Both

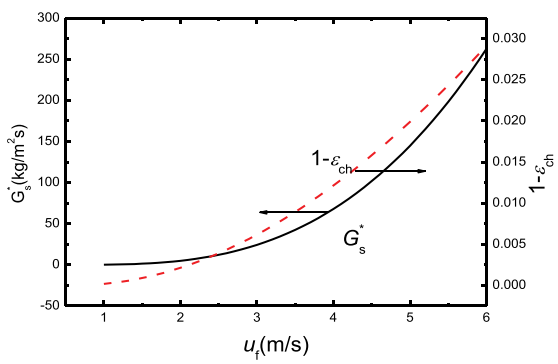

Figure 4. Dependences of solid flux G_s^* and its concentration $(1-\varepsilon_{ch})$ at type A choking on superficial gas velocity u_f for an FCC-air system (ρ_s= 1620 kg/m^3, d_p= 100 μm, D_t= 0.1 m).

m_s^+ and m_s^- are calculated based on the total cross-sectional area of the riser, but not their own occupied. Then, the circulating solid flux in the riser G_s should be

$$G_s = m_s^+ - m_s^-. \tag{9}$$

Figure 5 shows the schematic diagram of m_s^+ and m_s^- calculated for varied β at a given gas velocity.

This figure shows when

$$\left.\frac{dm_s^+}{d\beta}\right|_{\beta=0} > \left.\frac{dm_s^-}{d\beta}\right|_{\beta=0}, \tag{10}$$

more particles, compared with those at type A choking, can be transported upward in the separate-phase-coexistence mode, that is, $G_s = m_s^+ - m_s^- > G_s^*$. However, when β increases to a critical value β_{ch}

$$\left.\frac{dm_s^+}{d\beta}\right|_{\beta=\beta_{ch}} = \left.\frac{dm_s^-}{d\beta}\right|_{\beta=\beta_{ch}}, \tag{11}$$

the net solid flux transported upward reaches its maximum value $G_{s,max}$. Beyond that point, the system will be abruptly collapsed, that is, the case of type C choking.

Therefore, the basal requirement for separate-phase-coexistence mode should be

$$\left.\frac{dm_s^+}{d\beta}\right|_{\beta=0} >= \left.\frac{dm_s{}^-}{d\beta}\right|_{\beta=0}. \tag{12}$$

This criterion will be applied later to predict G_{sm}, the minimum solid flux for fast bed.

"Without outer-gas invaded in clusters" is a primary assumption used in our model. Its necessary condition is met by the downward penetration of solid particles into the cluster, in

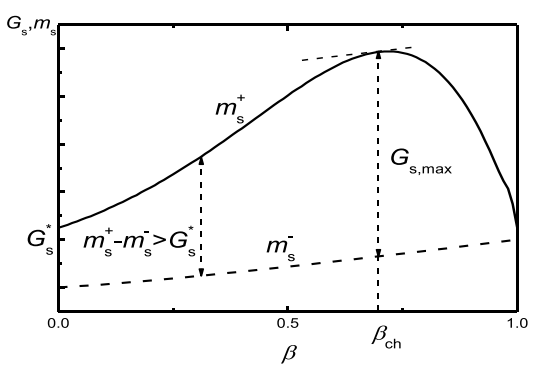

Figure 5. Schematic diagram of $m_s^+$and m_s^-changed with β at given gas velocity.

which there is always an upward interstitial gas flow subject to the pressure gradient of the bed. There have not been direct experimental evidences for the sufficient condition, that is, the two opposite flows should be completely compensated with each other. However, it is speculated that this situation could be the one with least flow resistance for a gas-solid two-phase system with agglomerative nature, and then tends to be most possible. In analogy with the bubbling beds, "no outer-gas invading clusters" is surely corresponding to "no solid particles falling into bubbles."

4.2. Mathematical model kernels

4.2.1. Model kernels

At the very beginning of cluster formation ($\beta \approx 0$), the terminal velocity of a single particle u_t can still be used as the gas-solid slip velocity, the same value at type A choking. It is surely expected, when clusters visibly appear, the gas-solid slip velocity will increase due to the impact of falling clusters. To facilitate the calculation, this impact can be realized with decreasing the effective gas velocity of dilute phase by an effective velocity factor of $F(\beta) < 1$. Therefore, the upward solid flux based on unit dilute-phase area should be

$$G_s^+ = \rho_s \left[\frac{u_f F(\beta)}{1-\beta} - u_t \right] \frac{1-\varepsilon_{ch}}{\varepsilon_{ch}}. \tag{13}$$

Meanwhile, the solid-saturated dilute-phase voidage ε_{ch} and the nominal gas velocity $u_{ch}^* = u_f F(\beta)/(1–\beta)$ should still fit the revised Yang's formula. Then, the kernel model for dilute phase, that is, the superficial upward solid flux based on unit cross-sectional area of the riser, is expressed as

$$m_s^+ = \rho_s [u_f F(\beta) - u_t(1-\beta)] \frac{1-\varepsilon_{ch}}{\varepsilon_{ch}}. \tag{14}$$

The form of the kernel model for dense phase or falling clusters is quite simple as

$$m_s^- = \rho_s \beta u_{cl} (1-\varepsilon_{cl}). \tag{15}$$

Meanwhile, to keep the outer-gas flow within the cluster being zero, the modified Richardson-Zaki's equation [22] must be satisfied for the cluster voidage ε_{cl} and its falling velocity u_{cl}. Then, we have

$$u_{cl} = u_t \left(\frac{\varepsilon_{cl}}{1} \right)^m = u_t \varepsilon_{cl}^m. \tag{16}$$

Here,

$$m = \lg\left(\frac{u_{mf}}{u_t} \right) \Big/ \lg \varepsilon_{mf}, \tag{17}$$

and the value of voidage at minimum fluidization $\varepsilon_{mf} = 0.45$ was taken in later calculations.

4.2.2. Empirical closures for F(β) and ε_{cl}

To make the kernel model for dilute phase closed, an empirical expression for the effective velocity factor $F(\beta)$ was given as [10]

$$F(\beta) = 1 - [1 - F(1)]\beta^n, \tag{18}$$

where $F(1)$ is the value of $F(\beta)$ at β=1 and can be calculated as

$$F(1) = \left(1 - \frac{u_t}{u_f}\right)\frac{1 - \varepsilon_{ch,A}}{\varepsilon_{ch,A}}\frac{\varepsilon_{sl}}{1 - \varepsilon_{sl}}, \tag{19}$$

ε_{sl} and $\varepsilon_{ch,A}$ are the bed voidages for slugging (β=1) and type A choking (β=0), respectively.

Here,

$$\varepsilon_{sl} = 1 - (1 - \varepsilon_{mf})/2. \tag{20}$$

To make the kernel model for dense phase closed, Harris's correlation [23] for solid concentration in clusters $\varepsilon_{s,\ cl}$ was suggested be applied [11].

$$1 - \varepsilon_{cl} = \varepsilon_{s,cl} = \frac{0.58(\varepsilon_s^*)^{1.48}}{0.013 + (\varepsilon_s^*)^{1.48}}, \tag{21}$$

where ε_s^* is the solids holdup in upper dilute region, which will be discussed in Section 4.4. Or, an even rough estimation directly from ε_{ch} could be used as

$$1 - \varepsilon_{cl} = 2(1 - \varepsilon_{ch}) + 0.45\beta. \tag{22}$$

With these equations derived, the calculation procedure is quite straightforward. (i) Type A choking velocity $u_{ch,A}$ is calculated for a given solid flux $G_s > G_{sm}$. (ii) Decreasing superficial gas velocity to make $u_f < u_{ch,A}$; then, m_s^+ and m_s^- are calculated by using different β until $G_s = m_s^+ - m_s^-$ is satisfied; the voidage of upward dilute phase ε_{ch} at the operating gas velocity u_f is then determined. (iii) Repeating the steps above until type C choking occurs, the type C choking velocity $u_{ch,C}$ is finally obtained.

Using different model parameter n, the variations of dilute-phase voidage ε_{ch} with operating gas velocity u_f for an FCC-air system are shown in **Figure 6**. It can be seen from the figure that when the operating gas velocity u_f is close to $u_{ch,C}$, a small reduction of gas velocity will cause a great increase of solid concentration ($1-\varepsilon$) and then pressure drop of the bed. Thus, it can be recognized as the occurrence of type C choking.

The figure also shows that the type C choking velocity calculated decreases with an increase of n used. Since Yousfi and Gau's empirical correlation for type C choking [24] (Eq. (23)) had been considered as the best in the literature [20], it was applied to estimate the proper value of n

$$\frac{u_{ch,C}}{\sqrt{gd_p}} = 32\mathrm{Re}_t^{-0.06}\left(\frac{G_s}{\rho_g u_{ch,C}}\right)^{0.28}. \tag{23}$$

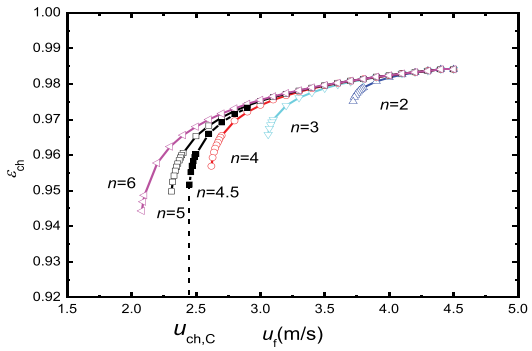

Figure 6. Variations of dilute-phase voidage ε_{ch} with gas velocity u_f calculated from different n for an FCC-air system (D_t= 0.1 m, ρ_s= 1620 kg/m^3, d_p= 100 μm, G_s= 100 kg/(m^{2}s)).

From this kind of "calibration," the model parameter $n = 4.5$ was chosen for a simplified version of the model without iteration. **Figure 7** shows comparisons between the model predicted $u_{ch,C}$ with $n = 4.5$ and those given by Eq. (23), for both FCC-air and sand-air systems with different particle sizes (50, 100, 150, and 200 μm) and solid fluxes (50, 100 and 200 kg/(m^{2}s)) in a riser of 0.1 m, typical scale in laboratories. The result looks quite satisfactory.

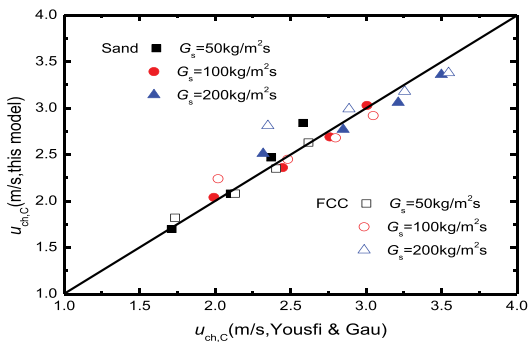

Figure 7. Comparison of model predictions for type C choking ($n = 4.5$, D_t= 0.1 m) and those from Yousfi and Gau [24].

4.2.3. Mechanistic closures for F(β) and ε_{cl}

From a meso-scale analysis in mimic to bubbling beds [10], the effective velocity factor in dilute phase $F(\beta)$ was determined as

$$F(\beta) = 1 - \frac{3u_{pen}}{u_f} \cdot \frac{1-\varepsilon_{cl}}{\varepsilon_{cl}} \cdot \frac{\varepsilon_{ch}}{1-\varepsilon_{ch}} \cdot \beta \cdot \varphi, \tag{24}$$

where u_{pen} stands for the superficial percolation velocity in a packed bed of voidage ε_{cl} under pressure gradient of the bed, and φ is the influence factor of penetrating particles in clouds

$$\varphi = \left(\frac{u_{cl} + 2u_{sd,\infty}}{u_{cl} - u_{sd,\infty}} - 1\right)\frac{\beta}{1-\beta}. \tag{25}$$

Detailed definitions and calculation methods of these parameters in Eqs. (24) and (25) can be found in Ref. [10].

It will be discussed later in Section 5.1, the weight of clusters should be balanced by the inter-phase drag between the dilute and the dense phases. This requirement can be used to determine the cluster voidage ε_{cl} independently, rather than using Harris's correlation. Certainly, all these calculations need iterations.

As an example, **Figure 8** shows that the meso-scale model determined $F(\beta)$ compared with those with constant n for an FCC-air system. It can be seen that $n = 4.5$ is a pretty good approximation for the simplified version without iterations. And **Figure 9** shows the solid concentration of clusters predicted by inter-phase balance compared with Harris's correlation. It can be seen that they are also in agreement with each other pretty well.

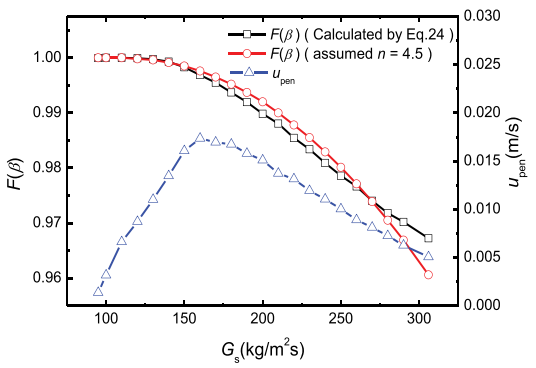

Figure 8. F(β) calculated by Eq. (24) compared with constant n (FCC-air system, $\rho_s = 1600$ kg/m^3, $d_p = 70$ μm, $D_t = 0.1$ m, $u_f = 6$ m/s).

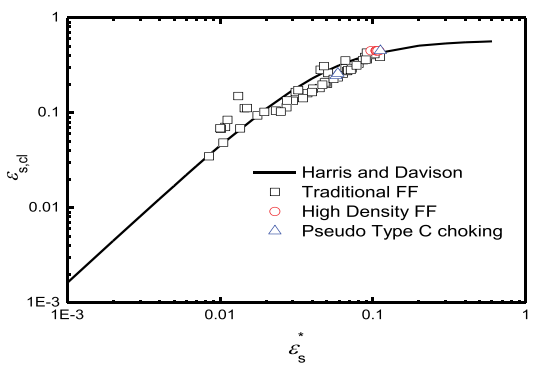

Figure 9. Predicted solid concentration of clusters $\varepsilon_{s,cl}$ compared with Harris's correlation [23].

As a first check, **Figure 10** shows the solid flux G_s^C at type C choking predicted by the mechanistic model. The model predictions were compared with the experimental data collected by Xu et al. [20]. Noting that some data points of type B choking due to blower and/or standpipe limitation of the system [21] could also be included, the accuracy of model prediction is reasonably accepted.

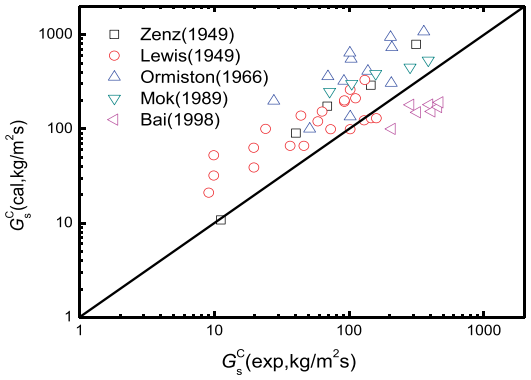

Figure 10. Predictions of G_s^C for type C choking compared with the experimental data collected by Xu et al. [20].

4.3. Minimum solid flux for fast bed

As mentioned before, the critical requirement for separate-phase-coexistence mode is

$$\left.\frac{\mathrm{d}m_s^+}{\mathrm{d}\beta}\right|_{\beta=0} = \left.\frac{\mathrm{d}m_s^-}{\mathrm{d}\beta}\right|_{\beta=0}, \tag{12a}$$

which can be used for the determination of G_{sm}, the minimum solid flux for fast bed. And we have already

$$m_s^+ = \rho_s[u_f F(\beta) - u_t(1-\beta)]\frac{1-\varepsilon_{ch}}{\varepsilon_{ch}} \tag{14a}$$

$$m_s^- = \rho_s \beta u_{cl}(1-\varepsilon_{cl}). \tag{15a}$$

The derivation of Eq. (15a) is quite straightforward, that is,

$$\left.\frac{\mathrm{d}m_s^-}{\mathrm{d}\beta}\right|_{\beta\to 0} = \rho_s u_{cl}|_{\beta\to 0}(1-\varepsilon_{cl})|_{\beta\to 0}. \tag{26}$$

And, as we have also [11]

$$(1-\varepsilon_{cl})|_{\beta\to 0} = 2(1-\varepsilon_{ch,A}) \tag{27}$$

$$u_{cl}|_{\beta\to 0} = u_t \times (\varepsilon_{cl}|_{\beta\to 0})^m = u_t[1-2(1-\varepsilon_{ch,A})]^m \approx u_t. \tag{28}$$

The first statement means that at the very beginning of phase separation, the original formation of cluster is due to a noncollided convergence of two dilute solid pockets. The second statement with equal signs is required for the force balance of gas and particles inside the clusters settled freely, that is, the modified Richardson-Zaki equation should be fitted [11]. Because the solid concentration of the originally formed cluster is very small, the voidage is

close to unity, its falling velocity can then be estimated as the particle terminal velocity u_t. Putting Eqs. (27) and (28) into Eq. (26), we have approximately

$$\frac{\mathrm{d}m_s^-}{\mathrm{d}\beta}\Big|_{\beta\to 0} \approx 2\rho_s u_t(1-\varepsilon_{ch,A}). \tag{29}$$

To obtain the derivative of m_s^+ with respect to β directly is difficult, since both $F(\beta)$ and ε_{ch} in Eq. (14a) change with β in very complicated manners. However, the expression for m_s^+ can be linearized, under conditions of very small β ($\beta \approx 0$) as

$$m_s^+|_{\beta\approx 0} = (1+k\beta)G_s^*. \tag{30}$$

Here, k stands for an unknown coefficient to be determined numerically later. Then, the derivative can be written as

$$\left.\frac{\mathrm{d}m_s^+}{\mathrm{d}\beta}\right|_{\beta\approx 0} = kG_s^* \quad \begin{aligned} &= k\rho_s(u_{ch,A}-u_t)\frac{1-\varepsilon_{ch,A}}{\varepsilon_{ch,A}} \\ &\approx k\rho_s(u_{ch,A}-u_t)(1-\varepsilon_{ch,A}) \end{aligned}. \tag{31}$$

Let the terms on the right side of Eqs. (29) and (31) be equal, we have

$$k^*\rho_s(u_{ch,A}^* - u_t) \approx 2\rho_s u_t. \tag{32}$$

Here, $u_{ch,A}^*$ and k^* are $u_{ch,A}$ and k evaluated at the minimum solid flux G_{sm}, respectively. Therefore, we obtain

$$u_{ch,A}^* \approx \left(\frac{2}{k^*}+1\right)u_t. \tag{33}$$

The values of k can be calculated numerically for different small values of β, according to the definition of $k = (m_s^+/G_s^+ - 1)/\beta$. Taking 60-μm FCC particles fluidized in a 0.1−m diameter riser as an example, the results obtained are shown in **Figure 11**. From reasonable extrapolation,

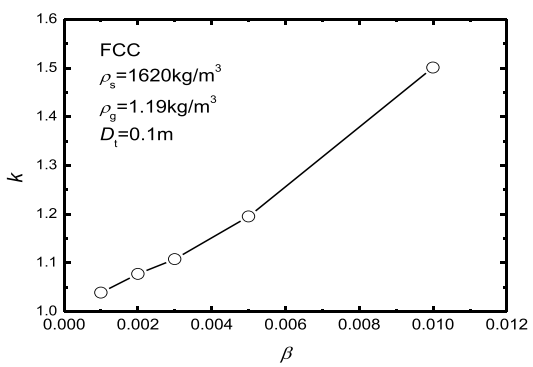

Figure 11. Variation of coefficient k in Eq. (30) with β for 60-μm FCC particles in a 0.1-m diameter riser.

it can be concluded that the coefficient k under the condition of $\beta \to 0$ is approximately one, that is, $k^* \approx 1$. Finally, we have a very simple result, that is,

$$u^*_{\mathrm{ch,\,A}} \approx 3u_{\mathrm{t}}. \tag{34}$$

Correspondingly, the minimum solid flux G_{sm} for fast fluidization can be estimated by the revised Yang's formula at superficial gas velocity of $3u_{\mathrm{t}}$.

Figure 12 shows comparison between the values of G_{sm} determined from $3u_{\mathrm{t}}$ and those from $u_{\mathrm{ch,C}}$ and $u_{\mathrm{ch,A}}$ becoming equal, for 60-μm FCC particles in a 0.1−m diameter riser. It can be seen from the figure that the comparison is quite satisfactory.

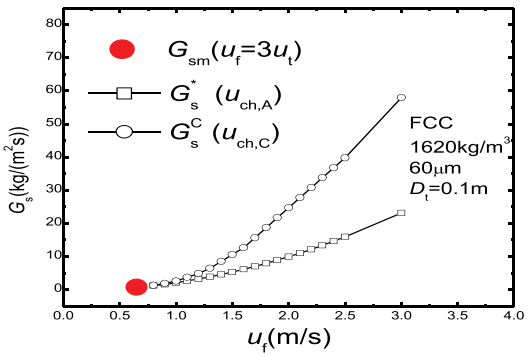

Figure 12. G_{sm} determined from $3u_{\mathrm{t}}$ compared with $u_{\mathrm{ch,C}}$ and $u_{\mathrm{ch,A}}$ becoming equal, for 60-μm FCC particles in a 0.1-m diameter riser.

The minimum solid flux for fast bed is generally more important in theory than in practice, since in most practical circulating fluidized bed systems the solid flux is usually much higher than G_{sm}. However, there might be a potential practical application for circulating fluidized bed combustion of coal, where particle size distribution is quite wide, but the gas velocity is relatively low. Therefore, it is possible that the gas velocity is higher than the minimum value required for fast fluidization with respect to the average particle size $3u_{\mathrm{t}(d\mathrm{p,ave})}$, but not high enough for some coarse particle fractions. In this case, the value of $u_{\mathrm{t}(d\mathrm{p,crit})} = u_{\mathrm{f}}/3$ may be used as a criterion, by which the whole particle size distribution can be divided into two relatively narrow groups, $d_{\mathrm{p}} \le d_{\mathrm{p,crit}}$ and $d_{\mathrm{p}} > d_{\mathrm{p,crit}}$. It is suggested that only the finer particle group with its own average size be calculated with the model, while the coarse particle group be treated as a stationary fluidized bed.

4.4. Solids holdup in upper dilute region

As we mentioned earlier, Eq. (1) was proposed by Yang to amend the terminal velocity of a uniform particle suspension in a CFB riser u'_{t} [16, 17]. The influence of wall friction on u_{t}' appears in the form of $\sqrt{[1+f_{\mathrm{p}}u_{\mathrm{p}}^2/(2gD_{\mathrm{t}})]}$. In a finite diameter riser, besides the particle gravity the gas drag at u_{t}' will also conquer the wall friction. Considering the influence of wall friction as additional particle gravity, the equivalent gravity factor is determined as

$$k_w = \left(1 + \frac{f_p u_p^2}{2gD_t}\right). \tag{35}$$

The concept of k_w can also be applied to the case of separate-phase-coexistence if the falling clusters are considered as a moving wall, in which the dilute-phase flows upward. In this case, the slipping velocity of those particles relative to the "cluster wall" will increase from u_p to

$$u_p' = u_p + \beta u_{cl} = \frac{G_s^+}{\rho_s(1 - \varepsilon_{ch})} + \beta u_{cl}. \tag{36}$$

Meanwhile, the equivalent diameter of the flow path will decrease from D_t to D_t', which is determined as [10, 11]

$$\frac{1}{D_t'} = \frac{1}{D_{t1}} + \beta\left(\frac{1}{D_{t2}} - \frac{1}{D_{t1}}\right), \tag{37}$$

where D_{t1} is the equivalent flow-path diameter for very small cluster fraction β, while clusters tend to move close to the wall

$$D_{t1} = D_t\sqrt{1 - \beta}. \tag{38}$$

And D_{t2} is the equivalent flow-path diameter for very big cluster fraction β, while clusters have to distribute uniformly in the riser

$$D_{t2} = \frac{4F}{U} = D_t \frac{1 - \beta}{1 + 1.5\beta\frac{D_t}{D_{cl}}}, \tag{39}$$

where F and U are the cross-sectional area and the wetted perimeter of the "tubing" dilute flow, respectively, while Dcl is the diameter of cluster, which can be estimated from the empirical correlation given by Harris and Davidson (Eq. (40)) [23] or the dimensionless form suggested by the authors (Eq. (41)) [10] (see also **Figure 13**).

$$D_{cl} = \frac{1 - \overline{\varepsilon}}{40.8 - 94.5(1 - \overline{\varepsilon})}\,[\mathrm{m}] \tag{40}$$

$$\frac{D_{cl}}{D_t} = 27.34(1 - \overline{\varepsilon})^{1.26}\left(\frac{gD_t}{2u_t^2} + 1.5\right)^{-1}, \tag{41}$$

where ε^- is the average voidage of the upper dilute region.

The reason that we could treat the meso-scale drag using the concept of equivalent wall friction with viscous drag only, same as the riser wall, is due to the suppression effect of penetrating particles on the wake separation behind the cluster, which is discussed in detail in Ref. [11].

By using the concept of equivalent gravity, the pressure gradient in the upper dilute region can be expressed as [10]

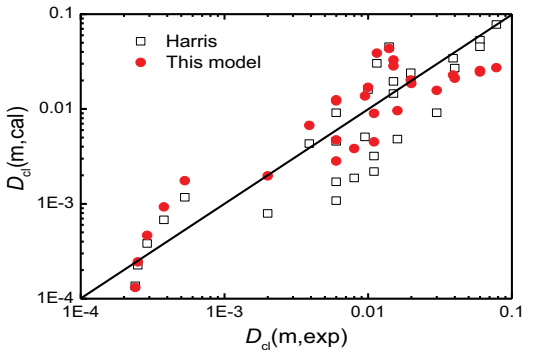

Figure 13. Cluster size predictions from different correlations compared with experimental data collected by Harris et al. [23].

$$-\frac{\mathrm{d}p}{\mathrm{d}z} = (1-\varepsilon_{\mathrm{ch}})\rho_{\mathrm{s}}g\left(1+\frac{f_{\mathrm{p}}u_{\mathrm{p}}'^{2}}{2gD_{\mathrm{t}}'}\right)(1-\beta), \tag{42}$$

where $\varepsilon_{\mathrm{ch}}$ is the dilute-phase voidage calculated by this model. In the equation, $(1-\varepsilon_{\mathrm{ch}})\rho_{\mathrm{s}}g$ is the particle weight in dilute phase, $(1-\varepsilon_{\mathrm{ch}})\rho_{\mathrm{s}}g\times f_{\mathrm{p}}u_{\mathrm{p}}'^{2}/(2gD_{\mathrm{t}}')$ is the equivalent "wall" friction, while $(1-\beta)$ represents the time fraction when the upward dilute phase is sensed by the pressure probe.

From the analysis above, the apparent solids holdup in the upper dilute region can be easily predicted as

$$\varepsilon_{\mathrm{s}}^{*} = -\frac{\mathrm{d}p}{\mathrm{d}z}/(\rho_{\mathrm{s}}g) = \varepsilon_{\mathrm{s,ch}}\left(1+\frac{f_{\mathrm{p}}u_{p}'^{2}}{2gD_{\mathrm{t}}'}\right)(1-\beta). \tag{43}$$

Here, $\varepsilon_{\mathrm{s,ch}}=(1-\varepsilon_{\mathrm{ch}})$ is the solid concentration in upward dilute phase. Since the calculation of D_{cl} (Eqs. (40) or (41)) involves $(1-\bar{\varepsilon}) = \varepsilon_{s}^{*}$, iterations should be applied. The initial value of $(1-\bar{\varepsilon})$ for iteration is suggested as $(1-\bar{\varepsilon})_0 = \varepsilon_{\mathrm{s,ch}}+0.25\beta$.

There were quite a lot of theoretical and experimental investigations on the solids holdup of the upper dilute region in the literature. Among them, Ouyang and Potter compiled abundant data available at that time [25], where the solids holdups of the upper dilute regions and the corresponding operating conditions were both reported in detail. Using the operating conditions provided, the solids holdups of the upper dilute regions were calculated with the model and compared with the experimental data in **Figure 14**. In the figure, symbols of 1–4 indicate the conditions of dilute transportation, traditional fast fluidization, high-density fast fluidization (HDFF) (to be discussed later in Section 5), and pseudo type C choking, respectively. The figure shows that the predictions for traditional fast fluidization, high-density fast fluidization, and pseudo type C choking are reasonably good. However, predicted ε_{s}^{*} for dilute transportation (denoted as hollow squares in the figure) are all lower than those from experiments. The reason for under-prediction of ε_{s}^{*} in those cases might be under-evaluation of the terminal velocity u_{t}. It would often be met for particles with certain size distribution.

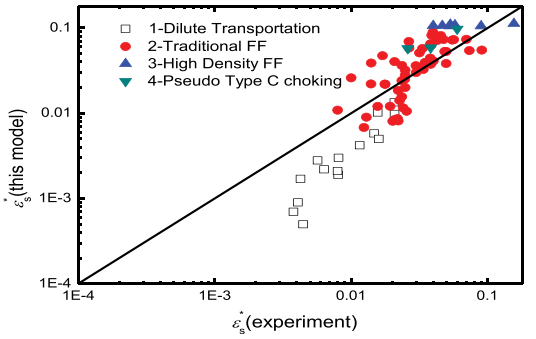

Figure 14. Predictions of solids holdup for the upper dilute region ε_s^* compared with experimental data collected by Ouyang and Potter [25].

5. Transition to high-density fast bed

5.1. Force balance of falling clusters

As discussed above, besides its gravity the upward dilute phase should also conquer the equivalent "wall" friction F_w in a fast-bed riser [10]

$$F_w = (1 - \varepsilon_{ch})\rho_s g \frac{f_p u_p'^2}{2gD_t'}. \tag{44}$$

The equivalent friction is caused by both falling clusters and the riser wall. The latter can be estimated from the wall friction at the type A choking F_{w0}, since falling clusters have not yet formed at that moment

$$F_{w0} = (1 - \varepsilon_{ch,A})\rho_s g \frac{f_p u_p^2}{2gD_t}. \tag{45}$$

Then, the net inter-phase drag between the upward dilute phase and falling clusters can be estimated as

$$\Delta F_w = F_w - F_{w0}. \tag{46}$$

On the other hand, the gravity of falling clusters is easily calculated as

$$G_{cl} = \beta(1 - \varepsilon_{cl})\rho_s g. \tag{47}$$

As we mentioned above in Section 4.2.3 (closure to dense phase model), the weight of clusters should always be balanced with the inter-phase drag. By using the initial value of $\varepsilon_{cl,0}$ (Eq. (22)), the inter-phase drag ΔF_w calculated is usually not just equal to the cluster gravity G_{cl}. Then, sequence adjustments for u_{cl} and/or ε_{cl} will be done with iterations until a new balance of $\Delta F_w = G_{cl}$ is reached. At a relatively low-operating velocity of gas, the adjustment of u_{cl} and ε_{cl} is reciprocally supported. With an increase of G_s, the cluster-falling velocity u_{cl} and

its voidage ε_{cl} decrease simultaneously, until type C choking happens. This is the case of traditional fast fluidization, where clusters settle down freely as we discussed above.

5.2. Secondary fluidization of clusters

On the other hand, if the operating velocity of gas is high enough, the situation could be different. When G_s increases to a certain value of G_s^{**}, the cluster voidage ε_{cl} reaches its minimum value $\varepsilon_{cl,min}$, the minimum voidage of clusters. In the case of $G_s > G_s^{**}$, the adjustments of u_{cl} and ε_{cl} are no longer reciprocally supported, since the voidage of clusters is fixed to $\varepsilon_{cl,min}$. Therefore, the adjustment for $\Delta F_w = G_{cl}$ can be performed by reducing the cluster-falling velocity along. Compared with its original value, that is, the one determined by the modified Richardson-Zaki's equation for the voidage $\varepsilon_{cl} = \varepsilon_{cl,min}$, the minus adjustment for falling velocity of clusters can be signed as (-)u^*. To keep the relative velocity of gas and particles inside the cluster unchanged, a small quantity of outer gas has to invade into the cluster at the same velocity u^*. As a result, the cluster gets a tendency of moving upward, but no longer be free settling. This phenomenon might be termed as "secondary fluidization of clusters" (SFC), somewhat similar to the fluidization of packed particles.

Detailed model modifications for $G_s > G_s^{**}$ can be found in Ref. [10], in which the most important ones are listed below:

$$m_s^+ = \rho_s[(u_f - \beta u^*)G(\beta) - u_t(1-\beta)]\frac{1-\varepsilon_{ch}}{\varepsilon_{ch}} \tag{48}$$

$$m_s^- = \rho_s \beta(u_{cl} - u^*)(1-\varepsilon_{cl}). \tag{49}$$

Here, $G(\beta)$ stands for the modified effective velocity factor of dilute phase for $G_s > G_s^{**}$

$$G(\beta) = 1 - \frac{3(u_{pen} - u^*)}{u_f} \cdot \frac{1-\varepsilon_{cl}}{\varepsilon_{cl}} \cdot \frac{\varepsilon_{ch}}{1-\varepsilon_{ch}} \cdot \beta \cdot \varphi \text{ for } 0 < u^* < u_{pen}, \tag{50}$$

$$G(\beta) = \frac{u_f - \beta u_{pen}}{u_f - \beta u^*} \text{ for } u^* > u_{pen}. \tag{51}$$

5.3. Prediction to transition of HDFF

The model predictions to Issangya's experiment [26] for $u_f = 6$ m/s are shown in **Figure 15(a)**. It can be seen from the figure that the model properly predicted the unique feature of high-density fast fluidization, that is, the solids holdups of the upper dilute region and the bottom-dense region do not change obviously with further increase of $G_s > G_s^{**}$. And **Figure 15(b)** shows that the final falling velocity of clusters $u_{cl}^* = u_{cl}$-u^* (opposite direction of u_f as positive) decreases continuously with an increase of G_s. When $u^* > u_{cl}$, u_{cl}^* becomes negative, this means all the clusters will move upward. This is the flow regime defined by Grace et al. as "dense suspension up-flow" (DSU) [27].

According to Issangya's experiment [26], the solid-gas mass ratio at the onset of high-density fast fluidization was about 40. And Grace et al. proposed a more general correlation for the onset of dense suspension up-flow as [27]

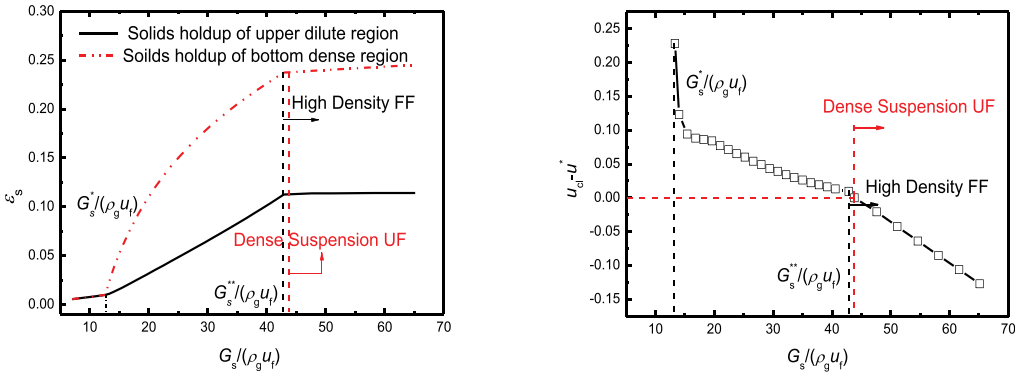

(a) (b)

Figure 15. Transition from traditional fast bed to HDFF for an FCC-air system ($\rho_s = 1600$ kg/m^3, $d_p = 70$ μm, $D_t = 0.076$ m, $u_f = 6$ m/s): (a) solids holdups of upper dilute region and bottom-dense region; (b) falling velocity of clusters.

$$U_{DSU} = 0.0113 G_s^{1.192} \rho_g^{-1.064} [\mu_g g(\rho_s - \rho_g)]^{-0.064}. \tag{52}$$

The model predictions to the onsets of high-density fast bed and dense suspension up-flow for FCC and sand particles fluidized by ambient air are compared with those given by Issangya et al. [26] and Grace et al. [27] in **Figure 16**, respectively. The results are also reasonably good.

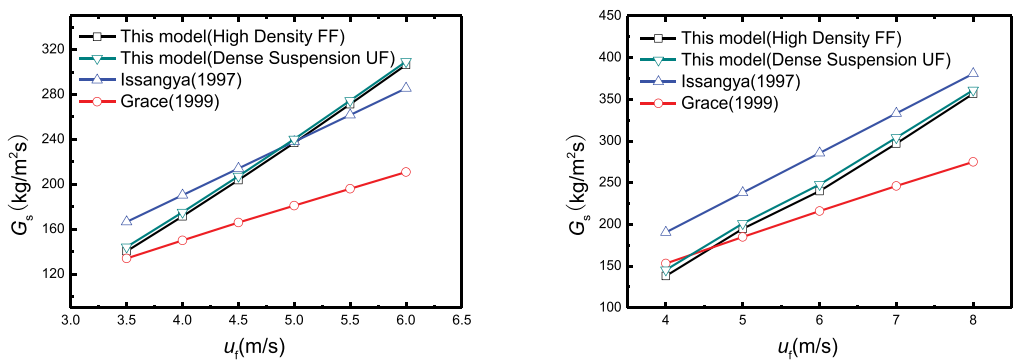

(a) (b)

Figure 16. Comparisons of onsets of HDFF and DSU predicted from different models or criteria: (a) FCC-air, $\rho_s = 1600$ kg/m^3, $d_p = 70$ μm, $D_t = 0.076$ m; (b) sand-air, $\rho_s = 2500$ kg/m^3, $d_p = 100$ μm, $D_t = 0.1$ m.

6. Submodels for bottom-dense region

6.1. Cluster rebound at dense bottom

Unlike the upper dilute region, the dense bottom region of a fast bed was less investigated in the past. And significant controversies appeared in the literature on the actual mechanism of

this region. However, it is generally agreed that two different types of axial solids holdup distributions can be found in this region, that is, the S-shaped distribution and the one exponentially decayed with height. According to Bai and Kato's systematical studies, the two different distributions would happen in a riser depending on the circulated solid flux, whether greater or smaller than the so-called "saturated carrying capacity of gas" G_s^{Bai} (in their paper noted as G_s^*) [28].

It is also agreed that fluctuations, with respect to both time and space, in the bottom dense region are very strong. Based on their measurements, Bai et al. [29] described the bottom dense region as "a more radial homogeneous cluster-dominating turbulent pattern," while Brereton and Grace [30] called it as "the cluster-like structure" indicated by its high intermittency index. Very detailed experimental investigations to the bottom region of a CFB riser were also carried out by Zhu and Zhu [31]. From their investigations, the solid concentrations at the intermittent peaks were much higher than those in free-settled clusters. Even more, in the near-wall region, the values at some plateaus reached around 0.45.

On the basis of the investigations, the authors of the paper put forward a new hypothetic model called "cluster rebound at the dense bottom" [11]. The model declares that (1) during the time that a cluster falls down and decelerates in the dense bottom, it will still absorb surrounding particles from its wake, but there will be no more particles pouring out from its nose, because of the high-flow resistance there. Thus, the solid concentration inside the cluster will increase continuously until a determinate value of $\varepsilon_{s,cl}^{d}$ is reached; (2) thanks to very strong mixing and interaction with the upward-moving gas-solid flow in the bottom, the much denser cluster will then be "bounced back" and leave the bottom at its original falling velocity $|u_{cl}|$ yet in the opposite direction; (3) just because of this unbalanced cluster rebound, the gas flow will gain an additional carrying capacity in this region at the basis of a uniformly saturated suspension, that is, the solid flux at type A choking G_s^*. Then, we obtain

$$G_s = G_s^* + \beta \rho_s u_{cl} (\varepsilon_{s,cl}^{d} - \varepsilon_{s,cl}), \tag{53}$$

where ρ_s is the particle density. From this equation, the solid concentration in rebounding clusters $\varepsilon_{s,cl}^{d}$ can be determined; (4) when the solid concentration in the rebounding clusters reaches its maximum value $\varepsilon_{s,cl}^{max} = 0.45$, the average value of the loosest parked beds suggested by Leva [15]; the total solid flux reaches a critical value, the saturated solid flux with once-through cluster rebound at the bed bottom

$$G_s^{rb} = G_s^* + \beta \rho_s u_{cl} (\varepsilon_{s,cl}^{max} - \varepsilon_{s,cl}); \tag{54}$$

(5) above G_s^{rb}, the gas flow will have no more ability to carry over all solid particles passing through the bottom directly. Yet, some of the particles will stay longer in this region, causing built-up of a higher dense bottom; (6) therefore, the saturated solid flux with once-through cluster rebound at the bottom G_s^{rb} can be used as a criterion to distinguish the two different distributions of axial solids holdup in the bottom region, thus it is comparable to G_s^{Bai} in Ref. [28].

6.2. Average solids holdup in dense bottom

According to the hypotheses proposed above, the modeling method for average solids holdup in the dense bottom of the bed was established as follows [11]:

1. Calculate the solid concentration in rebounding clusters $\varepsilon_{s,cl}^{d}$ and the corresponding solids holdup in the dense bottom $\varepsilon_{s,d}^{-}$, as

$$\varepsilon_{s,cl}^{d} = \varepsilon_{s,cl} + \frac{G_s - G_s^*}{\beta \rho_s u_{cl}} \tag{55}$$

$$\overline{\varepsilon}_{s,d} = \beta \varepsilon_{s,cl}^{d} + (1-\beta)\varepsilon_{s,ch}; \tag{56}$$

2. Calculate the solids holdup in the dense bottom $\varepsilon_{s,d}$, corresponding to the maximum solid concentration in rebounding clusters $\varepsilon_{s,cl}^{max} = 0.45$:

$$\varepsilon_{s,d} = \beta \varepsilon_{s,cl}^{max} + (1-\beta)\varepsilon_{s,ch}; \tag{57}$$

3. Compare the values calculated from Eqs. (56) and (57) and take the smaller one as the average solids holdup for the dense bottom;
4. At a given superficial gas velocity, repeat steps 2 and 3 with an increase of solid flux, and get the curves of $\varepsilon_{s,d}^{-}$ and $\varepsilon_{s,d}$ crossed, which determines G_s^{rb}, the saturated solid flux with once-through cluster rebound at the bottom.

The postulated behaviors of particle movement in the bottom region, that is, "once-through" or "stay longer," are also well consistent with the experimental visualizations using PEPT imaging in Ref. [32]. To distinguish the two different cases easily, we will call the case of S-shaped solids holdup distribution as a "classical" fast bed ($G_s > G_s^{rb}$), while call the case of exponentially decayed solids holdup as a "premature" fast bed ($G_s \le G_s^{rb}$). Both the classical and premature cases are "traditional" fast beds in comparison with the "high-density" fast bed characterized in Ref. [26].

Based on the above analysis, increasing solid flux G_s continuously at a constant gas velocity will lead to transitions from dilute transportation, through the premature fast bed, to the classical fast bed. Taking Bai and Kato's experiment [28] as an example, **Figure 17** gives the predicted variation of bottom solids holdup with solid flux, showing clearly these kinds of transition. The bottom solids holdup calculated by Bai and Kato's empirical correlations and the so-called "saturated carrying capacity of gas" G_s^{Bai} [28] are also given in the figure. From the figure, it is clear that the $\varepsilon_{s,d}$–G_s curves are deflected indeed near G_s^{rb} or G_s^{Bai}, but the curves are not flattened for $G_s > G_s^{rb}$ or G_s^{Bai}. The curves will be flattened at a much higher solid flux G_s^{**} with the onset of high-density fast bed, as explained before in Section 5.3. To avoid confusing this deflection with type A choking, it is better to call G_s^{rb} in its full termination "saturated solid flux with once-through cluster rebound at the bottom" or simply "saturated solid flux with cluster rebound," while calling "saturation carrying capacity" only for type A choking.

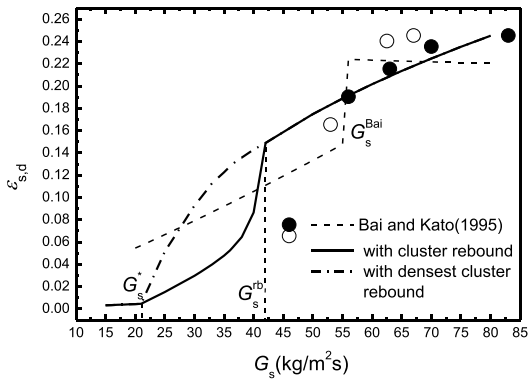

Figure 17. Predicted variation of bottom solids holdup with solid flux, and compared with Bai and Kato's experimental data and correlations [28].

6.3. Height of built-up section in dense bottom

The mechanism of how a vertical section with nearly constant solids holdup is built-up in the dense bottom has seldom been investigated. Li [33] ever tried to explain and model this process by a dynamic balance of the elutriated solid particles from the bottom region with the particles accumulated in it, which were in turn proportional to the "height of the built-up section," or simply "the dense bottom height". Using this assumption, a semi-empirical correlation between the solid flux G_s and the dense bottom height h was established [33].

The above-depicted mechanism is simple enough and looks reasonable. However, from our understanding, the solid flux to be correlated ought to be (G_s-G_s^{rb}), the extra portion beyond G_s^{rb}, but not the total one G_s. Using the data collected by Ouyang and Potter [25], the rate constant for elutriation was then reregressed [11], shown as in **Figure 18**.

$$k' = 10^{2.366}\left(\frac{\rho_g}{\rho_s - \rho_g}\right)^{1.581}\left[\frac{(u_f - v_s)^2}{d_p g}\right]^{0.471}. \tag{58}$$

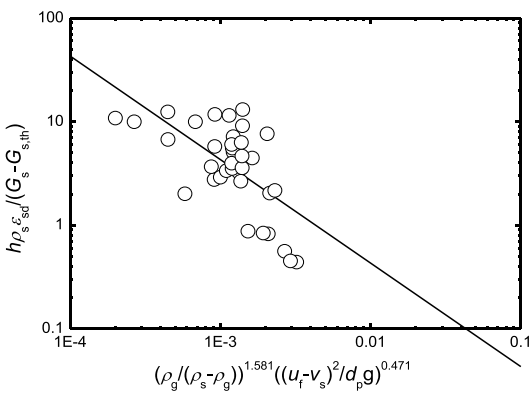

Figure 18. Multiregression result for dense bottom height h using the data collected by Ouyang and Potter [25].

And finally, the height of the built-up dense bottom can be calculated as

$$h = 10^{-2.366}\left(\frac{\rho_s - \rho_g}{\rho_g}\right)^{1.581}\left[\frac{d_p g}{(u_f - v_s)^2}\right]^{0.471} \times \frac{G_s - G_s^{rb}}{\rho_s \varepsilon_{s,d}}, \tag{59}$$

where u_f stands for the superficial gas velocity, ρ_g for gas density, while $v_s = G_s/(\rho_s \varepsilon_{s,d})$ is the nominal particle velocity in the dense bottom.

7. Axial solids holdup distribution

7.1. Momentum balance for acceleration/transition zones

In addition to the fully developed upper dilute region described in Section 4.4 and the built-up dense bottom region we have just discussed, there are also two less important zones in a classical fast bed. They are a transition zone between the two regions and an acceleration zone prior to the built-up dense section. In the acceleration zone, the particles recycled from the standpipe should be accelerated from their original downward movement to a finite upward velocity. It was assumed that in a premature fast bed, the axial solids holdup distribution decayed exponentially with height was a direct conjunction of the two zones with null built-up section in between [11].

As selecting an adequate drag coefficient is very difficult for those complicated gas-solid flows, the detailed flow mapping from commercial CFD software is usually less reliable. However, the most important principle involved in the software, that is, the momentum conservation, can still be applied when those integrated zones are considered. Compared with the solid phase, the momentum of gas and the wall friction can be neglected; the conservation of momentum between the inlet and the outlet cross sections is then written as

$$M_{out} - M_{in} = \Delta P - G, \tag{60}$$

where M_{out} and M_{in} are the solid momentum fluxes at the outlet and inlet cross sections, respectively, while ΔP stands for the pressure difference of the two sections, and G for the solid gravity per unit area within the zone.

The apparent solids holdup $\varepsilon_{s,t}^{-}$ averaged in the zone can be used to calculate the pressure difference between the lower and the upper cross sections of the acceleration/transition zones, that is, $\Delta P = h_t \rho_s g \varepsilon_{s,t}^{-}$, where h_t is the height of the zone. And the real solid concentration $\varepsilon'_{s,t}$ averaged can be used to calculate the solid gravity per unit area within the zone, that is, $G = h_t \rho_s g \varepsilon'_{s,t}$. It is supposed that $\varepsilon'_{s,t} = \eta \varepsilon_{s,t}^{-}$, where η can be considered as the contribution factor of gravity for the pressure drop. Then, we obtain

$$M_{out} - M_{in} = h_t \rho_s g(\overline{\varepsilon}_{s,t} - \varepsilon'_{s,t}) = h_t \rho_s g \overline{\varepsilon}_{s,t}(1 - \eta). \tag{61}$$

Therefore, the height of acceleration/transition zones can be calculated from the momentum flux deference between the inlet and the outlet, and the average apparent solids holdup $\varepsilon_{s,t}^{-}$ as

$$h_t = \frac{M_{out} - M_{in}}{\rho_s g \overline{\varepsilon}_{s,t}(1-\eta)}. \tag{62}$$

Putting the expressions of M_{in} and M_{out} for acceleration/transition zones, respectively, in, we have

$$h_{t1} = \frac{m_s^+ V_s^+ + m_s^- V_s^- - G_s V_d}{\rho_s g \overline{\varepsilon}_{s,t1}(1-\eta)} \text{ for transition zone,} \tag{63}$$

$$h_{t2} = \frac{G_s V_d (1+\delta)}{\rho_s g \overline{\varepsilon}_{s,t2}(1-\eta)} \text{ for acceleration zone,} \tag{64}$$

where δ stands for the coefficient of the converse momentum flux caused by the recycled solid particles moving downwards. And velocities in the equations are

$$V_s^+ = \frac{m_s^+}{\rho_s(1-\beta)\varepsilon_{s,ch}} \tag{65}$$

$$V_s^- = u_{cl} \tag{66}$$

$$V_d = v_s = G_s/(\rho_s \varepsilon_{s,d}). \tag{67}$$

Then, the equivalent momentum balance heights based on the average solids holdup of dense bottom $\varepsilon_{s,d}$ can be calculated as

$$H_{t1} = \frac{m_s^+ V_s^+ + m_s^- V_s^- - G_s V_d}{\rho_s g \varepsilon_{s,d}(1-\eta)} \text{ for transition zone,} \tag{68}$$

$$H_{t2} = \frac{G_s V_d (1+\delta)}{\rho_s g \varepsilon_{s,d}(1-\eta)} \text{ for acceleration zone.} \tag{69}$$

Adding the two equivalent momentum balance heights for the acceleration and transition zones together, we get the total momentum balance height as

$$H_t = H_{t1} + H_{t2}. \tag{70}$$

7.2. Functional description of acceleration/transition zones

As depicted in the above section, the axial solids holdup distribution exponentially decayed with height in a premature fast bed can be considered as a special case of a classical fast bed with null built-up section. Therefore, it is possible that the functional description of the acceleration/transition zones for both classical fast bed and premature fast bed can be unified to a single one. Actually, this attempt can be easily realized by the ordinate transfer from z to (z-h) for the transition zone of a classical fast bed, where h stands for the height of built-up section in the bottom. Thus, the commonly accepted exponential decay of solids holdup with bed height for the premature fast bed can be used for the unified functional description of the acceleration/transition zones as

$$\varepsilon_s = \varepsilon_{s0} e^{-\gamma z}, \tag{71}$$

where ε_{s0} stands for the solids holdup just above the air distributor of the riser, and γ for the decay constant.

Since the equivalent momentum balance heights of acceleration/transition zones have been determined above, we can simply transfer the values to the actual solids holdup distributions, in accordance with their equal impacts on the total bed pressure drop.

By some mathematical deduction, the final expressions for ε_{s0} and γ were obtained as [11]

$$\varepsilon_{s0} = \frac{\varepsilon_{s,d} - m'\varepsilon_s^*}{1 - m'} \tag{72}$$

$$\gamma = \frac{\varepsilon_{s0} - \varepsilon_{s,d}}{\varepsilon_{s,d} H_{t2}} = \frac{1}{H_{t2}}\left(\frac{\varepsilon_{s0}}{\varepsilon_{s,d}} - 1\right), \tag{73}$$

where $m' = H_{t2}/H_t$, and ε_s^* stands for the solids holdup of the upper dilute region.

Under the same conditions of experiments in Ref. [25], the heights of transition zones were calculated with $\delta = 0$ assumed. Then, a proportionality coefficient $(1-\eta) = 0.212$ was determined from comparing those results with experimental data [25], shown as in **Figure 19**. From that, $\eta = 0.788$ was obtained, which meant that the particle gravity contributed roughly four-fifths of the total pressure drop for the zone. Now, the method to predict the axial solids holdup distribution of fast beds has been established completely.

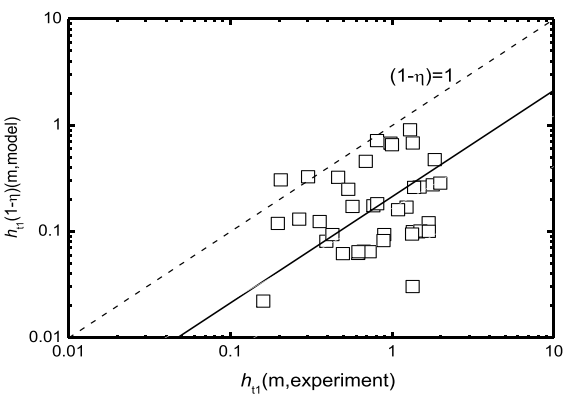

Figure 19. Comparison of the predicted heights of transition zones and the experimental data collected by Ouyang and Potter [25].

7.3. Prediction of axial solids holdup distribution

Though there were quite a lot of experimental data available in the literature, Issangya's investigation [26] for axial solids holdup distributions seemed the most systematical. FCC particles of 70 μm in diameter and 1600 kg/m^3 in density were fluidized by ambient air in a

riser of 0.076-m inner diameter. The operating conditions varied from dilute transportation, through the premature fast bed, the classical fast bed, until the high-density fast bed [26].

The coefficient of converse momentum flux $\delta = 2$, for the recycled particles, was applied in the calculation. As an example, **Figure 20** shows the comparisons of model predictions and the experimental data [26] for a constant gas velocity u_f= 4 m/s yet different solid fluxes of 18, 44, 68, 138, 200, and 240 kg/(m^{2}s), respectively. It can be seen from the figure that the results are somewhat reasonable.

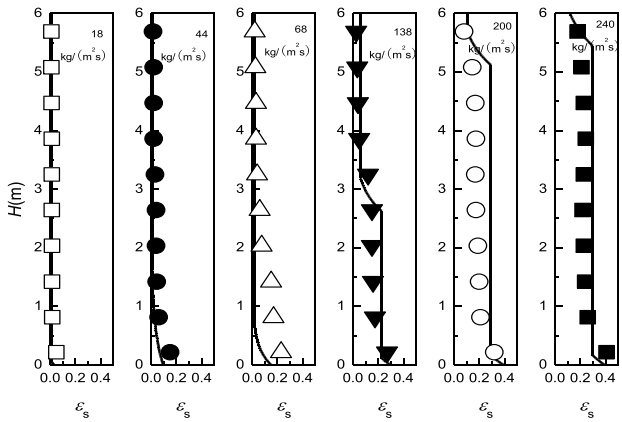

Figure 20. Axial solids holdup distributions from present model and Issangya's data, u_f= 4 m/s [26].

8. Conclusions and outlook

Based on the downward-penetrating particle flow through clusters and the analogy between a falling cluster and a rising bubble identified by the authors, a "type-A-choking-oriented separate-phase-coexistence model" for the upper dilute region of fast beds was established first. The model was then integrated with the sub-models of "cluster rebound at the dense bottom," "the momentum flux balances for acceleration and transition zones" in the lower and middle parts of the bed. The integrated model predicted successfully the axial solids holdup distributions of literature data under extremely wide operation conditions covering dilute-phase transportation, the premature fast bed, the classical fast bed, and the high-density fast bed.

To make the model system for fast fluidization have even sounder theoretical basis, more fundamental studies are expected in the future, especially those to explain further the reasons for "the four simplest integer numbers" as: "0"—in the regime of traditional fast fluidization, clusters settle down freely without outer-gas invasion; "1"—at type A choking, the terminal velocity of a particle suspension in a finite diameter riser is just equal to the terminal velocity of a single particle in an infinite fluid; "2"—at the very beginning of particle aggregation, the solid concentration in clusters is twice that in the dilute phase; "3"—the minimum solid circulating flux for fast fluidization corresponds to the type A chocking at the gas velocity of triple particle terminal velocity.

Acknowledgements

The authors would like to acknowledge the financial support from the Chinese National Natural Science Fund, Grant No. 50676062.

Author details

Ming-Chuan Zhang* and Chu Zhang

*Address all correspondence to: mczhang@sjtu.edu.cn

School of Mechanical Engineering, Shanghai Jiao Tong University, Shanghai, China

References

[1] Dry R, Beeby C J. Applications of CFB technology to gas-solid reaction. In: Grace J R, Avidan A A & Knowlton T M, editors. Circulating Fluidized Beds. London: Black Academic & Professional; 1997, Chapter 12

[2] Avidan A A. Fluid catalytic cracking. In: Grace J R, Avidan A A & Knowlton T M, editors. Circulating Fluidized Beds. London: Black Academic & Professional; 1997, Chapter 13

[3] Masten J M. Design and scale-up of CFB catalytic reactors. In: Grace J R, Avidan A A & Knowlton T M, editors. Circulating Fluidized Beds. London: Black Academic & Professional; 1997, Chapter 14

[4] Du B, Warsito W, Fan L S. Behavior of the dense phase transportation regime in a circulating fluidized bed. Industrial and Engineering Chemistry Research. 2006;**45**: 3741-3751

[5] Gidaspow D. Multiphase Flow and Fluidization: Continuum and Kinetic Theory Descriptions. Boston: Academic Press, 1994

[6] Li J, Kwauk M. Particle-Fluid Two-Phase Flow—The Energy-Minimization Multi-Scale Method. Beijing: Metallurgical Industry Press, 1994

[7] Zhu H P, Zhou Z Y, Yang R Y, Yu A B. Discrete particle simulation of particulate systems: Theoretical developments. Chemical Engineering Science, 2007;**62**:3378-3396

[8] Snider D M. An incompressible three-dimensional multiphase particle-in-cell model for dense particle flows. Journal of Computational Physics, 2001;**170**:523-549

[9] Werther J, Hartge E. Bridges between industrial practice and fundamental research in fluidization technology. In: Proceedings of CFB-11. Beijing: Chemical Industry Press; 2014. p. 1-21

[10] Zhang M C, Zhang C. A type-A-choking-oriented unified model for fast fluidization dynamics. Powder Technology, 2013;**241**:126-141

[11] Zhang M C, Zhang C. Further integration of the type-A-choking-oriented unified model for fast fluidization dynamics. Powder Technology, 2015;**286**:132-143

[12] He Y, Deen N G, ven Annaland S, Kuipers J A M. Gas-solid turbulent flow in a circulating fluidized bed riser: Experimental and numerical study of mono-disperse particle system. Industrial and Engineering Chemistry Research. 2009;**48**:8091-8097

[13] Davidson J F, Harrison D. Fluidised Particles. Cambridge: University Press, 1963

[14] Yang N, Wang W, Ge W, Wang L N, Li J H. Simulation of heterogeneous structure in a circulating fluidized bed riser by combining the two-fluid model with the EMMS approach. Industrial and Engineering Chemistry Research. 2004;**43**:5548-5561

[15] Leva M. Fluidization. New York: McGraw-Hill Book Company, 1959

[16] Yang W C. A mathematical definition of choking phenomenon and a mathematical model for predicting choking velocity and choking volume fraction. AIChE Journal. 1975;**21**:1013-1015

[17] Yang W C. Criteria for choking in vertical pneumatic conveying lines. Powder Technology, 1983;**35**:143-150

[18] Yang W C. Estimating the solid particle velocity in vertical pneumatic conveying lines. Industrial and Engineering Chemistry Fundamentals. 1973;**12**:349-352

[19] Yang W C. Correlations for solid friction factors in vertical and horizontal pneumatic conveyings. AIChE Journal. 1974;**20**:605-507

[20] Xu G, Nomura K, Gao S, Kato K. More fundamentals of dilute suspension collapse and choking for vertical conveying systems. AIChE Journal. 2001;**47**:2177-2196

[21] Bi H T, Grace J R, Zhu J X. On types of choking in vertical pneumatic systems. International Journal of Multiphase Flow, 1993;**19**:1077-1092

[22] Richardson J F, Zaki W N. Sedimentation and fluidization: Part I. Trans. Inst. Chem. Transport Bed. Chemical Engineering Science. 1954;**40**:259-267

[23] Harris A T, Davidson J F, Thorpe R B. The prediction of particle cluster properties in the near wall region of a vertical riser. Powder Technology, 2002;**127**:128-143

[24] Yousfi Y, Gau G. Aerodynamique de l'ecoulement vertical de suspensions concentrees gaz-solides-I: regimes d'ecoulement et stablilite aerodynamique. Chemical Engineering Science, 1974;**29**:1939-1946

[25] Ouyang S, Potter O E. Consistency of circulating fluidized bed experimental data. Industrial and Engineering Chemistry Research. 1993;**32**:1041-1045

[26] Issangya A S, Bai D, Bi H T, Lim K S, Zhu J, Grace J R. Suspension densities in a high-density circulating fluidized bed riser. Chemical Engineering Science. 1999;**54**:5451-5460

[27] Grace J R, Issangya A S, Bai D, Bi H, Zhu J. Situating the high-density circulating fluidized bed. AIChE Journal. 1999;**45**:2108-2116

[28] Bai D, Kato K. Quantitative estimation of solids holdups at dense and dilute regions of circulating fluidized beds. Powder Technology, 1999;**101**:183-190

[29] Bai D, Shibuya E, Masuda Y, Nakawaga N, Kato K. Flow structure in a fast fluidized bed. Chemical Engineering Science, 1996;**51**:957-966

[30] Brereton C M H, Grace J R. Microstructure aspects of the behavior of circulating fluidized beds. Chemical Engineering Science, 1993;**48**:3565-2572

[31] Zhu H, Zhu J. Characterization of fluidization behavior in the bottom region of CFB risers. Chemical Engineering Journal, 2008;**141**:169-179

[32] Chen C W, Seville J, Yang Z, Baeyens J. Particle motion in the CFB riser with special emphasis on PEPT-imaging of the bottom section. Powder Technology, 2009;**196**:318-325

[33] Li Y C. Introduction of Fluidization Process Engineering (in Chinese). Beijing: Science Press; 2008

Chapter 8

Economic Future of Concentrating Solar Power for Electricity Generation

Enas Raafat Maamoun Shouman

Additional information is available at the end of the chapter

http://dx.doi.org/10.5772/intechopen.74334

Abstract

Worldwide, the climate change is a major universal concern. CO_2 is the main cause of international warming, and at least 85% emission results of CO_2 came from conventional energy depleted sources (oil, natural gas and coal) for energy generation. Hence, renewable energy has been the focal point of most regulations of governments to aim at greenhouse gas reduced. In Egypt, greenhouse gas emissions from rural activities amount to some 25% of national greenhouse gas emissions, amounting to approximately 27 million t CO_2 equivalent annually. Moreover, these emissions are supposed to increase rapidly in the coming decades, more than doubling in the next 15 years, as rural populations grow and activities become increasingly energy intensive. The Mediterranean region embraces Europe, North Africa and Middle East and has enormous potential in solar energy. It has abundant solar radiation, cheap land and high electricity demand, which could make this region the universal hub for concentrating solar power (CSP) generation. This chapter discusses the Egypt market potential of CSP. The chapter covers recent CSP trends and discusses in detail the CSP market development. The chapter aims to obtain the data sources to compare the CSP and levelized electricity cost. Enas Shouman presents a strategy for CSP plant market entrance in Egypt and a comparison between the electricity cost for Egypt model case and the cost evolution of CSP plants on the basis of expectations for the expansion as an international level. This chapter proposes a concept strategy for management CSP in Egypt. The chapter included two applied parts. The first part is to calculate the generating electricity cost from conventional power sources and its expansion in the future. Then, the second part will be followed by identifying the CSP cost and its growth in the future.

Keywords: solar energy, CSP, renewable energy, economics, levelized cost, electricity

1. Introduction

1.1. Outlook for CSP in Europe and MENA

The solar direct normal irritation (DNI) plays a great role for the of electricity generation amount from CSP plants. Europe has vast variations in solar radiation unlike the Middle East and North Africa. It has enormous potential for generating electricity from solar energy, with great average solar energy irradiance (**Figure 1**). This allows the Middle East and North Africa to export energy to Europe [1, 2].

This would open up new opportunities for economic and technical cooperation between the two regions and protect environmental considerations by reducing the CO_2 emissions in Europe. World energy demand is growing by over 50% up to the year 2030; **Figure 2** shows the energy consumption per capita up to the year 2050 [3, 4].

The CSP economic potential is limited to Spain, Portugal, Greece, Turkey and the Mediterranean Islands and amounts to 1570 TWh/y of which 1280 TWh/y are located in Southern Spain. Mediterranean Sea is a more attractive site for CSP, with direct solar irradiance of about 2800 kWh/m^2/y.

1.2. Universal cumulative installed CSP capacity

 Spain and the USA have 69 and 29% of installed capacity, respectively, and they have dominated the market; United States used to be a leader actor in solar power generation until 2007 when Spain design its first plant (PS10).

 Spain developed 1.9 GW of CSP, and it dominates the market with 69% of the universal installed capacity.

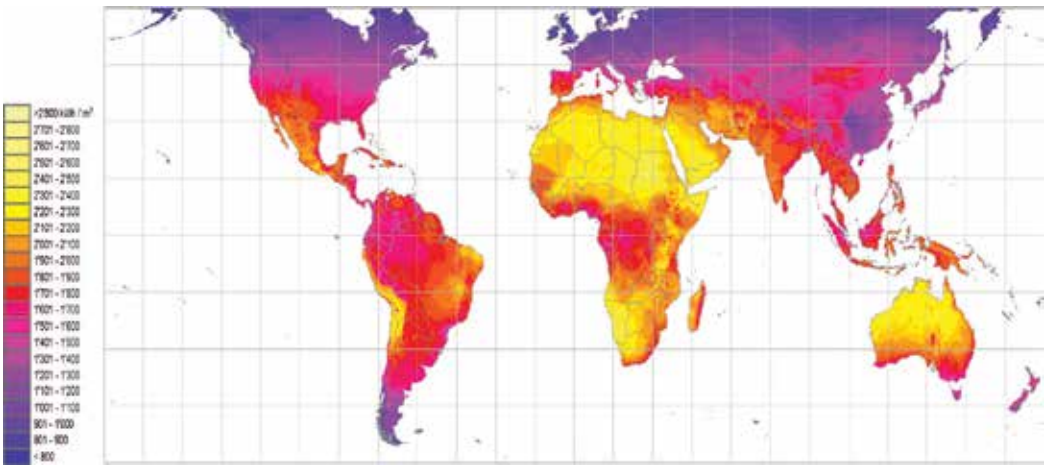

Figure 1. Sum of universal irradiation annually [1, 2].

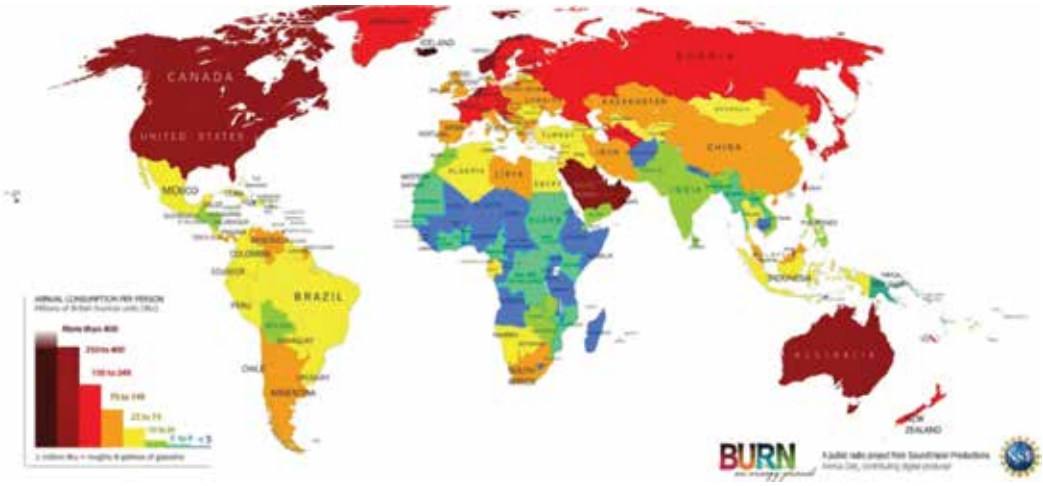

Figure 2. Energy consumption per capita [3, 4].

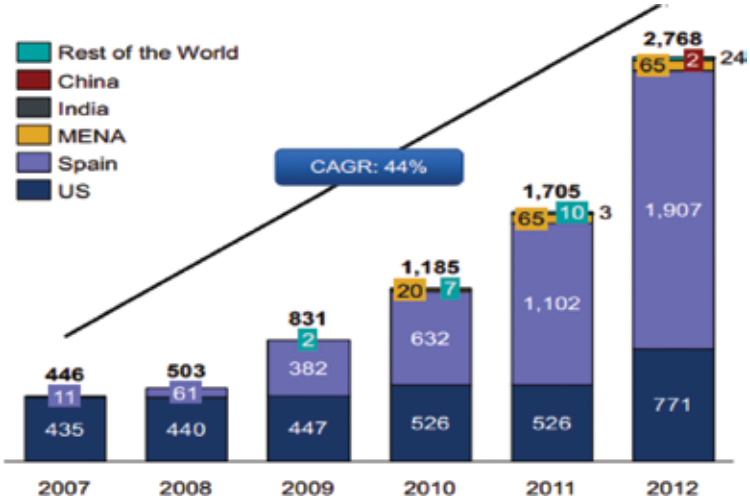

Figure 3. Universal cumulative installed CSP capacities, MW, 2007–2012 [5, 6].

- Between 2010 and 2011, Middle Eastern and African countries (Algeria, Morocco and Egypt) have generated 65 MW. The UAE has a 100 MW plant (Shams 1) which is established in 2013.

- China and India have started to generate CSP since 2010, and at the end of 2012, their installed capacity was about 1.5 and 2.5 MW, respectively (**Figure 3**).

- Australia, France, Thailand, Germany and Italy have developed CSP plants with nominal capacities of 1–9 MW.

1.3. CSP deployment beyond 2030

By 2040, the universal installed CSP capacity will be about 715 GW, with an average capacity factor of 45% (3900 h/year), thereby providing 2790 TWh yearly. The solar share of 85%, or 2370 TWh, represents 8.3% of universal electricity generation [7, 8]. By 2050, the universal installed capacity will reach 1089 GW, with an average capacity factor of 50% (4380 h/y). In the year 2010, the total electricity demand for 30 countries in Europe was 3530 TWh/y, which is projected to reach a maximum of 4310 TWh/y in 2040 [9, 10].

Figure 4 represents the future electricity demand expected in Europe in 2050, which would cover the demand with a surplus of 45%. However, it must be considered that about 30% of the countries which have been analyzed show considerable deficits, while on the other side considerable surpluses are concentrated in seven countries as shown in **Figure 4**.

Figure 5 shows where CSP electricity will be produced and consumed by 2050. North America would be the leader in producing solar energy, followed by Africa, India and the Middle East. Africa would be the largest exporter and Europe the largest importer. Indeed, the Middle East and North Africa are the largest reproducers when all solar products are considered [11].

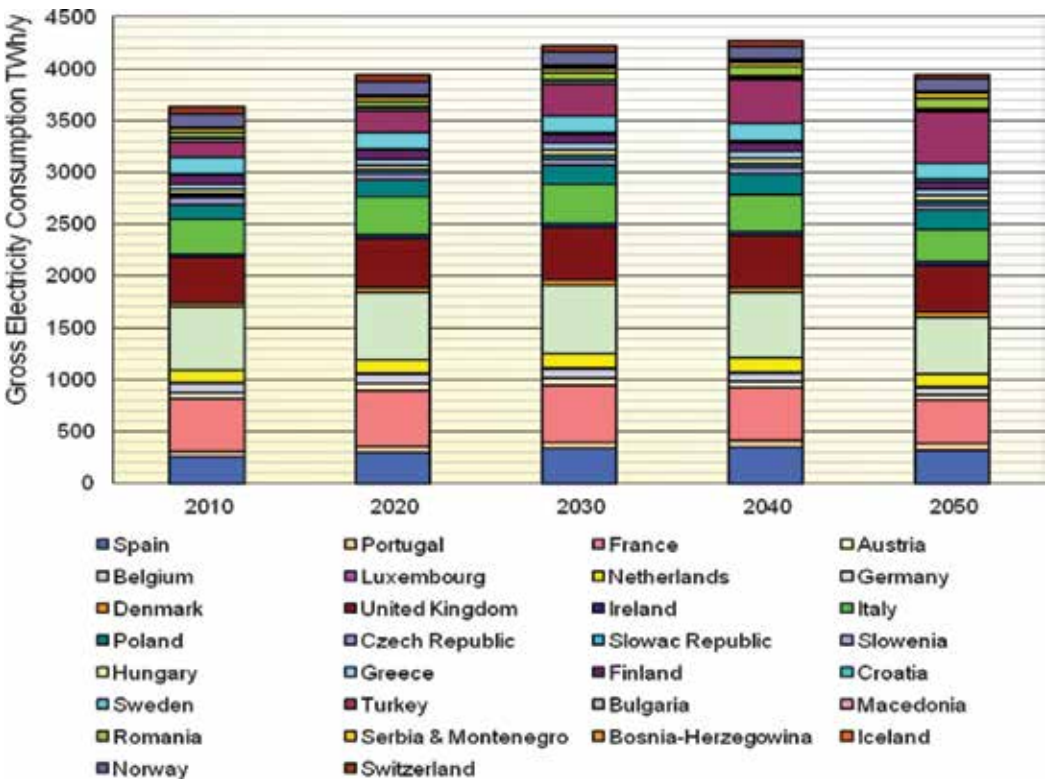

Figure 4. Electricity consumption of European countries between 2010 and 2050.

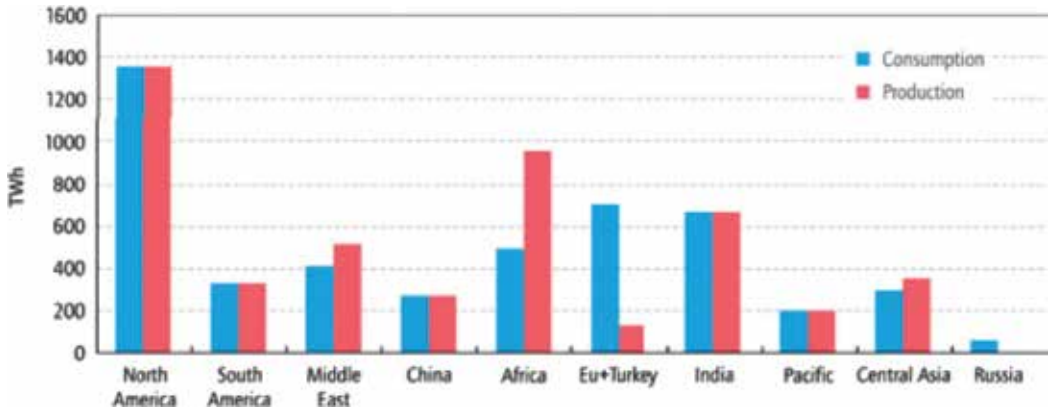

Figure 5. Production and consumption of CSP electricity by 2050 (in TWh) [12, 13].

2. Future energy demand

2.1. World electricity consumption

In North Africa, as a result of increasing population from 150 million in 2005 to a projected 250 million in 2050, an increasing electricity demand and production is expected.

Total electricity consumption is prospective to increase at a compound yearly growth rate of 3.17% with a rise in population. Total installed generating capacity is also expected to rise at a compound annual growth rate of 3.28% to meet the growing demand of electricity and to fill the shortfall of supply and demand. **Figure 6** represents electricity production by different sources from 2000 to 2050.

Total electricity generation from CSP has been supposed to increase to contribute by more than 40% of the total electricity produced in North Africa by 2030 through efficiencies

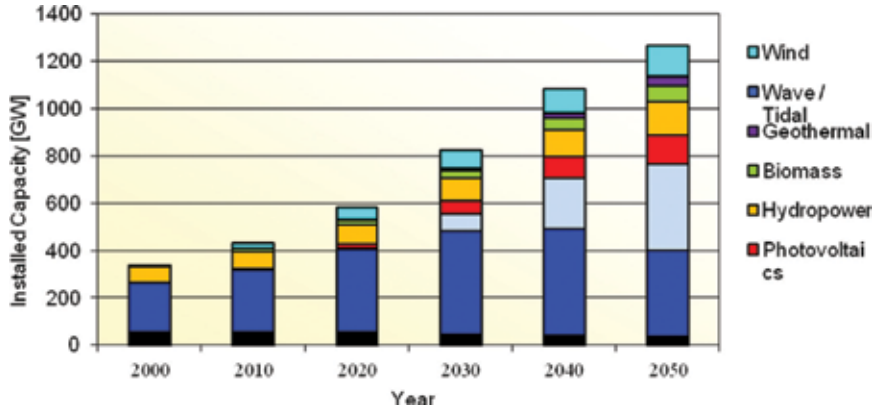

Figure 6. MENA region installed capacity by sources.

achieved on account of advancements in CSP technology [14]. **Figure 7** shows MENA region renewable energy resources.

Figure 8 shows the comparison between El-Kharga in Egypt and different areas in Europe and North Africa. **Figure 8** represents the monthly electricity yield of a best-case CSP plant with 24-h storage capacity throughout the year.

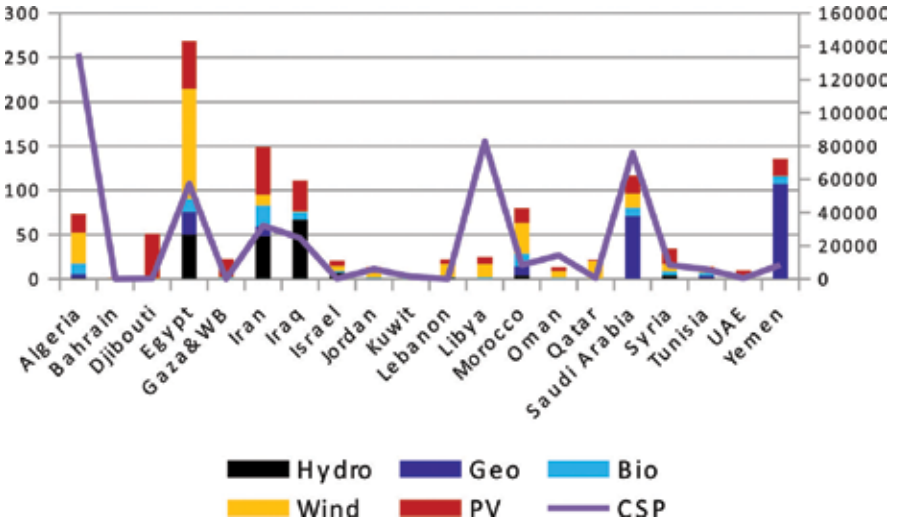

Figure 7. Renewable power generation potential by sources in TWh/y [15].

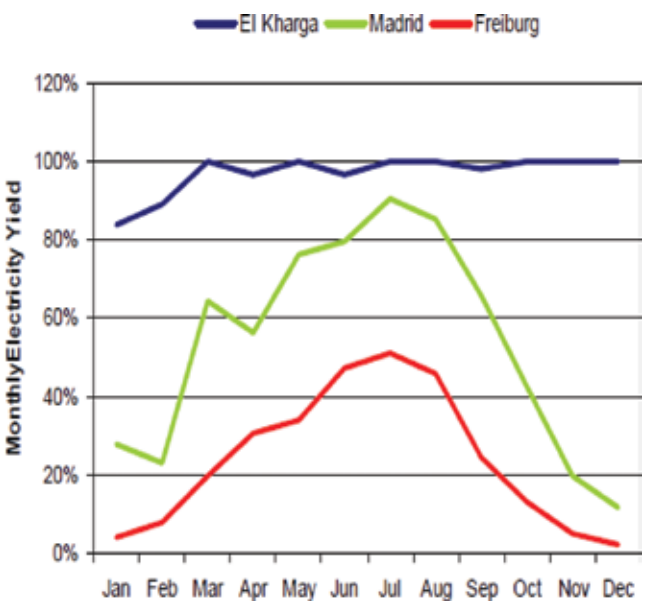

Figure 8. Proportional monthly electricity generation simulation of CSP plant with 24-h storage for equivalent annual full load hours in different sites with different DNI, Freiburg in Germany 2260 h/y, Madrid in Spain 5150 h/y, El Kharga in Egypt 8500 h/y/May 2005/.

2.2. Egypt electricity consumption

The German Aerospace Center has produced statistic studies on forecasted electricity consumption for Egypt up until 2050. Egypt will largely depend on CSP to satisfy the electricity demand due to the unpredictable population increase as well as the prospective economic growth (**Figures 9** and **10**). In 2020, in Egypt, electricity generated from CSP will likely contribute more than 30% and will reach 55% in 2050 [16, 17].

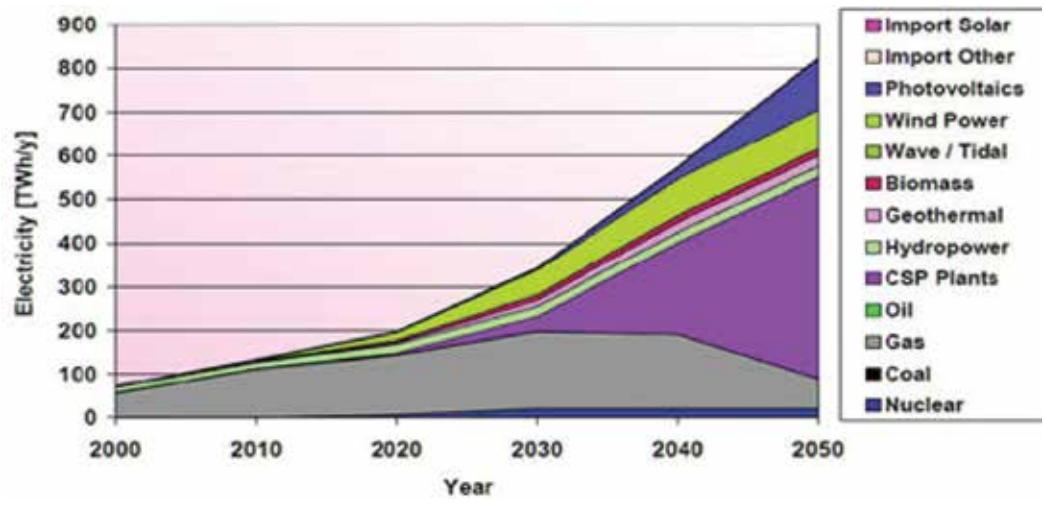

Figure 9. Electricity scenarios by primary energy sources for power generation in Egypt [16, 17].

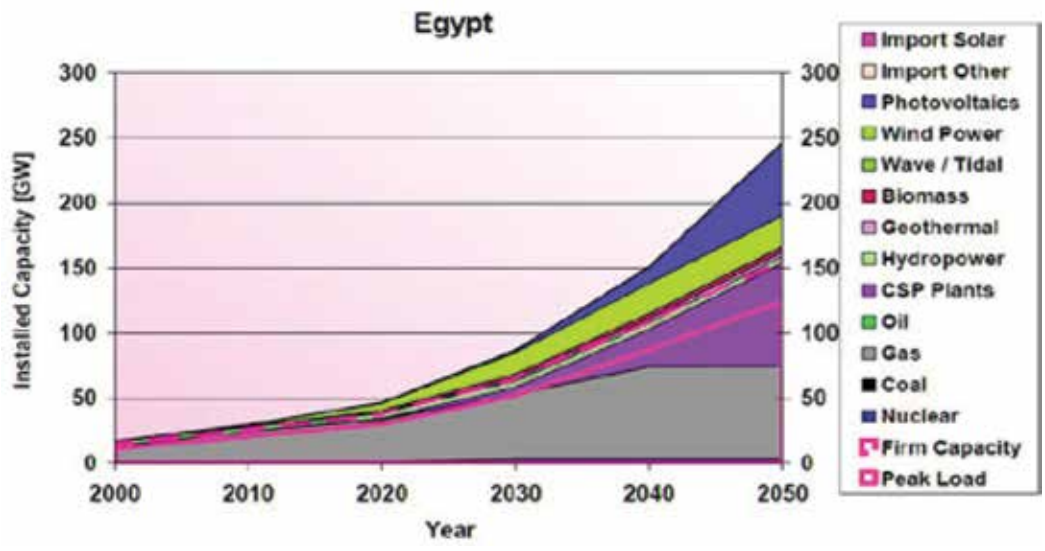

Figure 10. Installed capacities required for the electricity supply in Egypt [16, 17].

3. Economic methods for solar energy financial analyses

There are five economic methods of financial analysis for making investment decisions. Enas R. Shouman et al. have mentioned different methods including payback analysis (Annex 1), saving-to-investment ratio (SIR) (Annex 2), life-cycle cost (LCC) (Annex 3) and an adjusted internal rate of return (AIRR) (Annex 4). These studies evaluated the economics of PV applications by using these financial methods [18].

3.1. Levelized cost of electricity generation

The most significant parameters that determine at 2011 the levelized cost of electricity (LCOE) of CSP plants are as follows:

- Cost of initial investment, including location design for plants, with component costs, structure, grid connection and capitalized costs;
- CSP power plant capacity and efficiency factor.
- Level of DNI at the project location;
- Operation and maintenance (O&M) ($/y) costs (including insurance) costs; and.
- The capital cost, economic lifecycle, etc.

The economics of CSP technologies are substantially different from that of fossil fuel power technologies. Solar energy has high investment costs, modest operation and maintenance costs and very low or no fuel costs when compared to conventional fossil fuel power which is only very sensitive to the price volatility of the fossil fuel international markets. On the other hand, solar energy technologies are more sensitive to change in the capital and financing condition costs. The levelized cost of electricity of CSP plants is strongly correlated with DNI. Supposing a base of 2100 kWh/m^2/year (a typical value for Spain), the estimated LCOE of a CSP plant is declined by 4.5% for every 100 kWh/m^2/year that the DNI exceeds 2100 (**Figure 11**). In Egypt, the estimated average value of the DNI is around 2500.

Egypt is in an advantageous position for generating solar energy. It enjoys 2900–3200 h of sunshine annually with annual direct normal energy density 1980–3200 kWh/m^2 and technical solar-thermal electricity generating potential of 73.6 PWh, so the CSP is a promising technology in Egypt.

CSP capacity growth and cost learning curves from different project locations were taken as a basis for the modeling of the levelized CSP for generating the cost of electricity plants. The chapter uses Spain as a reference value for the successful market in 2010–2011 which its electricity tariff is around 27 €ct/kWh and define an equivalent value for MENA region in US($) currency. Supposing an exchange rate of 1.19 $/€ and Egypt DNI reference of about 2500 kWh/m^2/a compared to Southern Spain DNI of about 2900 kWh/m^2/a, our equivalent demand tariff for CSP in the model case reached to 28 UScent/kWh in 2010 [19, 20] (**Figure 12**).

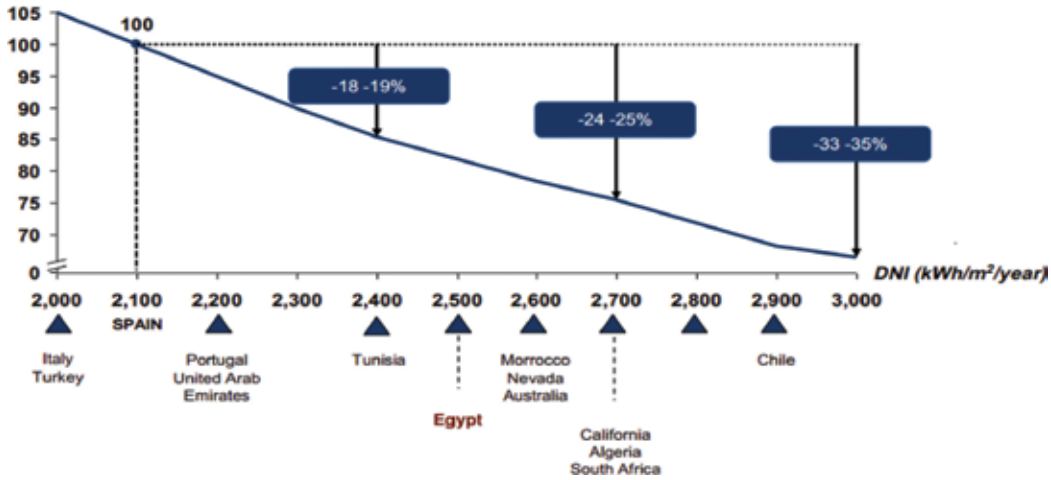

Figure 11. LCOE of CSP plants as a function of DNI [19].

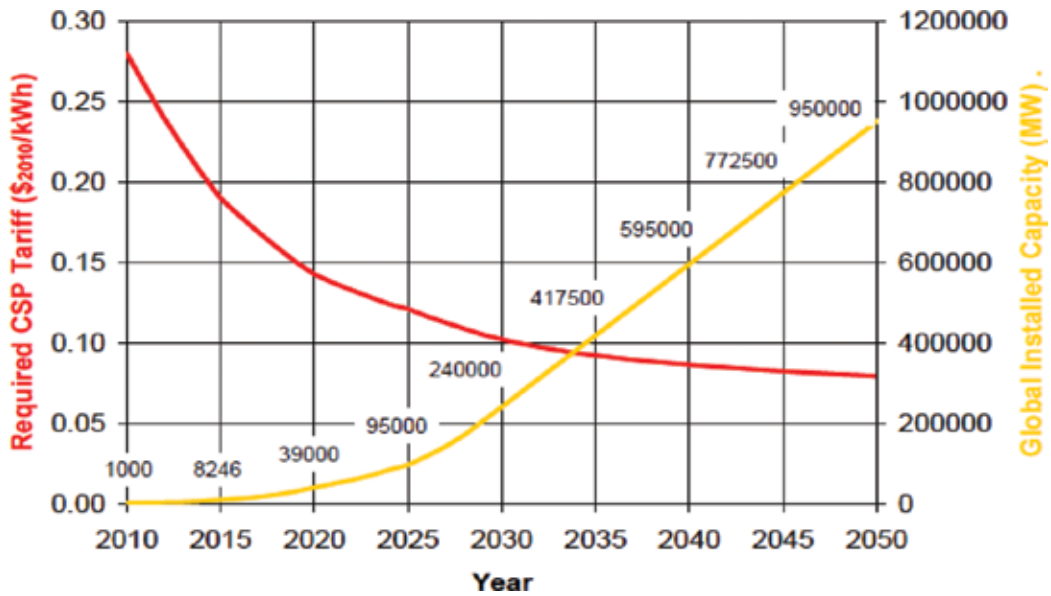

Figure 12. Expansion of universally installed CSP capacity and resulting reduction of demand tariff for the model parameters shown in **Table 1**.

CSP capacity is expected to increase from 20,000 MW to 150,000 MW by 2020 and about 230,000–340,000 MW by 2030. In 2050, expectation range for installed CSP capacity will be from 850,000 MW to 1,500,000 MW worldwide. In order to calculate the cost of decreased effects for the model reference case, we have selected a moderate universal expansion scenario, reaching about 39,000–240,000 MW in 2020–2030. This assumption will be the basis for the cost model scenario. In 2050, about 950,000 MW is supposed to be installed. The

Preference LCOE of CSP in 2010	$/kWh	0.280
Preference DNI	kWh/M2/a	2400
CSP progress ratio	%	88.0%

Table 1. Installing CSP model parameters for capacity.

demand tariff for CSP is decreased according to the universal installed capacity, with a progress ratio of about 0.88 according to a model by Neij, that the cost is cut the price by 12% every time worldwide installed capacity doubles [21]. In 2020, with these conditions the required CSP tariff will cut the price to 14 and 10 cent/kWh by 2030. In the long term, a cost below 8 cent/kWh is achieved.

3.2. A strategy for CSP finance in Egypt

3.2.1. Calculating levelized cost parameter of electricity (LCOE)

3.2.1.1. Assuming the electricity output per capita

For this model, the electricity output per capita is needed, while only the total electricity output value is known, which is 101,898 GWh/a [1, 2]. From the reference model for MENA region, the share of each capita could be calculated and supposed to be the same distribution in Egypt. Multiplying this share by the total annual electricity output will give us the electricity output per capita as shown in **Table 2** [22].

3.2.2. Cost of fuel (CoF)

The objective of the coming calculations is to determine the Cost of fuel for the different segments (peak-, medium, and base load). In the annual report of the EEHC a case was given that showed savings of 581 million EGP, when 3195 k toe were saved in the year 2008–2009, fuel cost [EGP/toe] was 181.84 according to the following equation [22].

$$\text{Specific fuel cost [EGP/Toe]} = (fuelcost[EGP])/fuel[ktoe] \tag{1}$$

The fuel cost could be about 7.19 $/MWh according to the following equation, taking into consideration the value proposition in Eq. (1), as well as knowing the total fuel consumed in

Study [23]	**Egypt**			
	Installed capacity (MW)	**Electricity (GWh/a)**	**Share of electricity (%)**	**Electricity (GWh/a)**
Peak load	1000	2000	5	4852
Medium load	2500	10,000	24	24,261
Base load	4000	30,000	71	72,784
Total	7500	42,000	100	101898

Table 2. Electricity output/capita in Egypt.

electricity generation of about 22,179 ktoe and total electricity generation of about 101,898 GWh/a [22].

$$\textbf{Specific fuel cost}\,[\textbf{USD}/\textbf{MWh}] = \frac{fuelconsumption[toe]*fuelcost\frac{\left[\frac{EGP}{toe}\right]*USD}{EGP}}{Electricityoutput[MWh]} \tag{2}$$

Eq. (3) will be followed to measure efficiency which plays a significant role in consumption and fuel cost. The equation would calculate the fuel cost estimated for the medium load and peak load with the fuel efficiency of 35 and 30%, respectively.

$$\mathbf{COF_{medium/peak}} = \mathbf{COF_{base}}^{*}\,\frac{\eta base}{\eta medium/peak} \tag{3}$$

where η is the efficiency (%). This will result in a cost of fuel (CoF) medium load of 8.2 USD/MWh and cost of fuel peak load of 9.6 USD/MWh.

3.2.3. Investment cost of the conventional power plants

The investment cost of the conventional energy plants has three main types of energy generation: combined cycle plants, gas turbine plants and steam turbine energy plants. By multiplying the installed capacity and the share of the production of each type and then these costs with the share of the installed capacity as shown in **Table 3**, we calculate the weighted average for the CSP plant investment cost of 1114.77 USD/kW [23] which is very significant to determine the LCOE.

3.2.4. Cost of operation and maintenance

The fixed O&M costs vary between the different types of generation, as Combined Cycle Charge around 2 US/kW, Gas about 13 USD/kW while the most expensive ones are the Steam energy plants with 28 USD/kW. Using the weighted average according to the, respectively, installed capacity about 7178, 1641 and 11,458 MW, the average fixed operation and maintenance cost could be calculated as 17.58 USD/kW/year [23].

3.3. LCOE for conventional power in Egypt

Figure 13 shows the levelized cost of electricity (LCOE) calculated as in Annex 5 for the peak load, medium load and base load segments as well as for the resulting weighted average cost of electricity.

Type of energy generation	Combine cycle	Gas turbines	Steam turbine energy plants
Investment cost (USD/kW)	800	500	1400
Share of the installed capacity	35%	8%	57%

Table 3. Weighted average for the CSP plant investment cost.

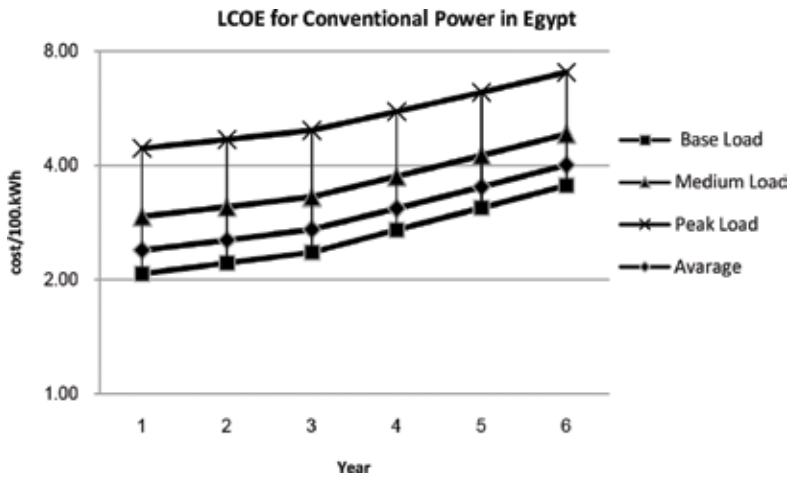

Figure 13. LCOE for conventional power in Egypt.

For rising economies with high demand rise rates, the fuel cost escalation and fuel consumption of installed power capacity are greatly relevant, as it will directly affect economic development negatively. For the Egypt model case, we have assumed a rather moderate 3.6% growth of electricity demand, while growth rates of over 7% yearly.

Egypt has a technical potential exceeding 2800 kWh/m^2/y, while the newly identified project location of Kom Ombo in Egypt has DNI average of about 2500 kWh/m^2/y [24]. Therefore, this DNI value could be used as an indicator for DNI in Egypt in this model and this indicator compared with Spain with only a DNI level of 2090 kWh/m^2/y [7, 8, 11]. These data could be used for calculating C0 [11].

$$\mathbf{C_{o\ Egypt}} = (\mathbf{CSP})_{\mathbf{ain}^*} \frac{DNIspain}{DNIEgypt} * \mathbf{\$/€} \tag{4}$$

Assuming a USD–EUR exchange rate of 1.19, C0 Egypt is equal to 26.86 ct$/kWh (Annex 6) (C0Egypt = 26.86 ct$/kWh), which is in the lower half of estimated CSP costs worldwide by the IEA of (20–30) ct$/kWh in 2010 [8]. The cost which is shown in **Figure 14** depends on the yearly solar radiation, and Egypt has high direct normal irradiance. Applying equation to the following data (**Table 4**), **Figure 14** shows the results for Egypt CSP cost curve, which decreases from 26.88 to 7.56 ct$/kWh from 2010 to 2050, respectively.

In Egypt, CSP potential is about 73,000 TWh/year. Egypt is the highest one in the region. Other promising characteristics are a high DNI which is around 19,870–3200 kWh/m^2/year, few cloudy days, high sun duration hours (9–11 h), huge expanses of vacant desert land, and an outstretch national electric grid. All of these elements make Egypt a perfect location for CSP projects.

The chapter aims to obtain a range of data for economic CSP energy. The chapter explains international CSP economic methods with financial analyses on the basis of expectations for the increase of solar energy in Egypt.

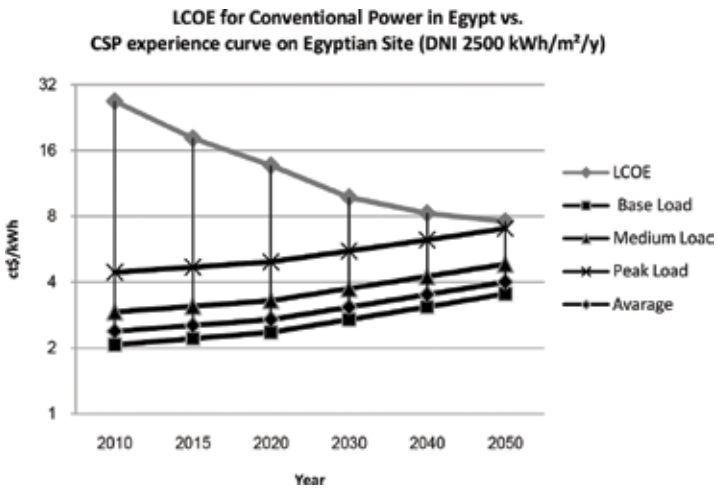

Figure 14. EgyptLCOE (CSP) vs. conventional power.

CSP progress ratio [22]	0.88
Egypt DNI [kWh/m^2/y]	2500
LCOE for CSP in Egypt in 2010 [ct$/kWh]	26.86

Table 4. Levelized cost of electricity (LCOE) for CSP in Egypt parameters.

More concern should be devoted to solar energy, especially CSP, by establishing a special sub-authority to support solar energy field. The responsibility of this entity is to measure DNI and also to identify a specific location for solar energy plant project and stand by feasibility studies. They would also assign and acquire land for solar energy plant projects, provide technical support and set a part business partners.

The major objective of this chapter is to create a continuous flow of the required data to be used as a base for taking decisions and to provide sufficient information about project needs. Project specifications, the other similar project in a different site, accurate information market and cost changes help the decision maker to determine and achieve the right target with minimum cost.

The aim is to facilitate the creation in the highest level of decision makers' community to serve the scientific project and to maximize scientific findings and overcome existing barriers of perspective, culture, geography and time. There is a need for scientists, as individuals or as groups, to develop a diversity of data analysis strategies, to clearly identify key target audiences, and to learn how to execute an effective project.

Annex

Annex 1

Payback period is the minimum time it takes to recover investment costs. The payback method is often used as a rough evidence to cost performance. The payback period for the

solar energy project is calculated as the total cost of investment divided by the income of the first year from the energy produced. If the payback period analysis is less than the expected power system life, the projects of the power system are potential to be cost-effective evidence. Projects of power system with short payback periods are considered to have lower risks. **Table 5** shows the equation for payback calculation indicated by Enas R. Shouman et al. [1, 18].

where Y = summation from years 1 to Y; E = reduction in electricity costs in year j;

M = differential maintenance and repair costs in year j; S = differential salvage value in year j;

R = differential replacement costs; and P = differential purchase and installation costs.

Annex 2

Savings-to-investment ratio (SIR) can be used to compare savings to costs of one energy system relative to an alternative power system. For a good result for net savings, the saving-to-investment ratio (SIR) should be greater than one. The higher the ratio, the greater the savings realized relative to the investment. **Table 6** represents the SIR methods in financial analysis by Enas R. Shouman et al. [1, 18].

Annex 3

Life-cycle cost analysis (LCC) shows a summation of all relevant present and future costs to build the system for CSP energy system. These costs include energy, installation, acquisition, operations and maintenance, repair, inflation, replacement (less salvage value) and the discount rate for the life of the investment.

Financial analysis	General formulas: All costs expressed as present value	Evaluation criteria
Discounted payback period (DPB) Minimum time it takes to recover an investment	**DPB = Find Y, such that** **Y** $\sum (EJ - MJ - RJ + SJ)$ **=P** ***j* = 1** $Payback \quad Period = \frac{Overalcostofthepowersystem}{Totalcostofthefuelgeneratoratfristyear}$	Payback period is less than the power system project life time

Table 5. Payback period general formulas.

Financial analysis	General formulas: Costs of present value	Criteria evaluation
Savings-to-investment ratio (SIR) The ratio represents how many times savings exceed costs and recompensing for the time value of money.	SIR = (E-M) (P−S + R)	SIR>1

Table 6. Savings-to-investment ratio general formulas and evaluation criteria.

If the life cycle cost analysis is lower than that for the base case and in other aspects is equal, then the life cycle cost meets the objectives of investor and budget constraints. It is considered as cost-effective and the preferred investment. **Table 7** shows the equation to calculate LCC [18].

LCC general formulas present value sum of costs and benefits of power system over lifetime which is (LCC = P1−S1 + M1 + R1 + E1) for evaluation criteria to compare LCC among exclusive alternatives. Minimum LCC and LCC1 < LCC2.

where P1 is the purchase and installation cost; S1 the salvage value; M1 the maintenance and repair costs;

R1 the replacement costs; and E1 the electricity costs.

Annex 4

Adjusted internal rate of return (AIRR) is a discounted cash flow technique that measures the yearly yield from a solar energy project, taking into account the reinvestment of tentative receipts at a specified rate. The cost-effectiveness of power project estimating adjusted internal rate of return (AIRR) includes comparisons between the projects calculated AIRR and the investor's minimum acceptable rate of return (MARR). **Table 8** represents the cost-effectiveness if the AIRR is greater than the MARR.

where TV is terminal value of all cash flows except investment costs,

PVI the present value of investment, c the costs, and 1/*n* the *n*th root of the ratio of TV/PVI.

Method financial analysis	General formulas: All costs expressed as present value	Evaluation criteria
Life cycle cost (LCC) **Present value sum of costs and benefits over life of a system**	**LCC = P1−S1 + M1 + R1 + E1** P1, S1, M1, R1, E1	Compare LCC among mutually exclusive Alternatives. Minimum LCC LCC1 < LCC2

Table 7. Life Cycle Cost guidelines are to define cost-effectiveness.

Method of financial analysis	General formulas: All costs expressed as present value	Evaluation criteria
Adjusted internal rate of return (AIRR) measures annual yield from a project assuming reinvestment of interim proceeds at the MARR	AIRR = Find the *n*th root of the ratio of the terminal value of all cash flows (except investment costs) to the present value of investment costs and subtract 1 **AIRR = (TV/PVI)1/*n* − 1**	AIRR must be equal to or greater than the investor's minimum rate of return

Table 8. General formulas and evaluation criteria for adjusted internal rate of return.

Annex 5

Levelized cost of electricity (LCOE) estimation follows the following calculations.

$$\mathbf{LCOE} = \frac{\sum_{t=1}^{n} \frac{I_t + M_t + F_t}{(1+r)^t}}{\sum_{t}^{n} 1 \frac{E_t}{(1+r)^t}}$$

where LCOE is the average lifetime levelized cost of electricity.

generation; It the investment expenditures in the year t; Mt. the operation and maintenance expenditures in the year t; Ft the fuel expenditures in the year t; Et the electricity generation in the year t; r the discount rate; and n the life of the system.

Annex 6

The cost experience curve function is

$$c_x = c_0 \left(\frac{P_x}{P_0} \right)^{\frac{\log PR}{\log 2}}$$

where PR is the progress ratio, Cx is the specific investment at point x, C0 is the specific investment at reference point 0, Px is the cumulated capacity at point x, and P0 is the cumulated capacity at reference point 0 [11, 16, 17].

Author details

Enas Raafat Maamoun Shouman

Address all correspondence to: shouman@hotmail.com

Information Systems Department, Engineering Division, National Research Centre, Giza, Egypt

References

[1] Shouman ER, Hesham Ezz. Forecasting transition electricity solar energy from MENA to Europe. Journal of Engineering and Applied Sciences. March 2016;**11**(5)

[2] Burn, Energy Journal. http://burnanenergyjournal.com/

[3] http://meteonorm.com/images/uploads/demo_uploads/ghi_world_mn71.png. March 2015

[4] Trieb F et al. Concentrating Solar Power for the Mediterranean Region, MED (CSP). BMU, Germany: German Aerospace Center (DLR); 2005. http://www.dlr.de/tt/med-Concentrating Solar Power (CSP)

[5] Kearney AT, ESTELA. Solar Thermal Electricity 2025. Brussels: ESTELA; 2010. http://www.estelasolar.eu/index.php?id=22 and EASAC 2011, "Concentrating Solar Power"

[6] NREL Solar Paces database (http://www.nrel.gov/Concentrating Solar Power (CSP)/solarpaces/by_project.cfm). BNEF Database. Protermosolar (http://www.protermosolar.com/)

[7] OECD/IEA, International Energy Agency Technology Roadmap Concentrating Solar Power; 2010

[8] Shouman ER, Khattab NM. Future economic of concentrating solar power (CSP) for electricity generation in Egypt. Renewable and Sustainable Energy Reviews. 2015;**41**: 1119-1127

[9] Technology Roadmap Concentrating Solar Power. Paris: International Energy Agency; 2010. www.iea.org

[10] http://www.seda-eg.com/content/advantages-egypts-geographical-position-global-sun-belt

[11] CSIR, ESKOM, DME. 2004. http://www.watersafe.co.za/2010/08/20/why-solar-energy-in-south-africa

[12] International Energy Agency (IEA). Technology Roadmap Concentrating Solar Power

[13] http://newenergynews.blogspot.com/search?q=(CSP)+economic+

[14] EIA. Annual Energy Outlook Online. 2006. Available at: www.eia.doe.gov/oiaf/aeo

[15] German Aerospace Center (DLR). Concentrating Solar Power for the Mediterranean Region. [Online]. 2005. Available at: http://www.dlr.de/tt/en/desktopdefault.aspx/tabid-2885/4422_read-6575 Includes data from: Algeria, Libya, Morocco, Tunisia

[16] Renewable Energy Sector in egypt. Final Report, IMC; 2006

[17] Trieb F et al. Combined Solar and Desalination Plants: Techno-Economic Potential in Mediterranean Partner Countries. MED CSD. Final Report; 2010. p.21

[18] Shouman ER, El Shenawy T, Khattab NM. Market financial analysis and cost performance for photovoltaic technology through international and national perspective with case study for Egypt. Journal of Renewable and Sustainable Energy Reviews. 2016;**57**: 540-549

[19] Kearney AT, ESTELA. Solar Thermal Electricity 2025. Brussels: ESTELA; 2010. http://www.estelasolar.eu/index.php?id=22

[20] IEA. Technology Roadmap Concentrating Solar Power. International Energy Agency, Paris. 2010, 2010. www.iea.org

[21] Neij L et al. Experience Curves: A Tool for Energy Policy Assessment: Lund University, European Commission, Lund; 2003. http://www.iset.unikassel.de/extool/Extool_final_report.pdf

[22] Egyptian Electricity Holding Company: 2008/2009. Arab Republic of Egypt: Ministry of Electricity & Energy

[23] Trieb F, Müller-Steinhagen H, Kern J. Financing concentrating solar power in the Middle East and North Africa. Elsevier; 2011

[24] Loosen A et al. Pre-Feasibility Study Report- KomOmbo. EMPower Program, Phase II; United Nations Environment Program; German Ministry of Economic Cooperation and Development (BMZ) represented by KfW. 2010

Edited by Paweł Madejski

The demand for electricity and heat production is still largely covered by conventional thermal power plants based on fossil fuel combustion. Thermal power stations face a big challenge to meet the environmental requirements constantly keeping high process efficiency and avoiding lifetime shortening of critical components. In recent years, many activities have been observed to reduce pollutant emissions and optimize performance in thermal power plants.

Increased share of renewable sources of energy in domestic markets enforces flexible operation and fast adjustment to actual demand. Gas power plants start to play a very important role in this process, allowing for rapid change of load and emission reduction. Operation under changing load together with keeping emissions at the accurate level requires constantly introducing new solutions and technologies as well as carrying out many research and development activities for optimization of the electricity and heat production process.

The edited book is aimed to present new technologies, innovative solutions, measurement techniques, tools and computational methods dedicated to thermal power plants in the light of new trends and challenges.

Published in London, UK

IntechOpen

ISBN 978-1-83881-408-3
9 781838 814083